Techniques to Measure Biophysical Properties of Lipid Membranes and Lily Flowers

Gunnar J. Goetz

A dissertation
submitted in partial fulfillment of the
requirements for the degree of

Doctor of Philosophy

University of Washington

2025

Reading Committee:

Sarah L. Keller, Chair
Joshua C. Vaughan
Jesse G. Zalatan

Program Authorized to Offer the Degree:

Department of Chemistry

University of Washington

Abstract

Techniques to measure biophysical properties of
lipid membranes and lily flowers

Gunnar J. Goetz

Chair of the Supervisory Committee:

Professor Sarah L. Keller

Department of Chemistry

Complex biophysical phenomena can be broken down into building blocks that can be probed and manipulated through experiment to expand our understanding of those phenomena. To define and characterize the building blocks, experimentalists choose techniques to measure the underlying biophysical properties that influence the phenomena. Each technique has advantages and disadvantages and may come with underlying assumptions that should be confronted in order to strengthen scientific results. In this dissertation, we will discuss two biophysical systems: phospholipid membranes and lily flowers. In the first discussion, we pare down the compositional organization of biological membranes, focusing on the utility of model membranes for isolating the independent, biophysical contributions of each constituent lipid. We evaluate an assumption that model membranes have the same composition of lipids as the stock from which they are made. Model membranes are then used to elucidate the effect of PE-lipids on micron-scale, liquid-liquid phase separation in membranes with a ternary lipid composition. In the second discussion, we shift to a much larger biophysical system and characterize rippling and blooming phenomena in lily flowers using a combination of physical, spectroscopic, and computational techniques. While our experimental results with lily flowers are motivated and inspired by previous work and simulations, we expect that our experimental results for the phase behavior of model membranes containing PE-lipids will inspire new theory and simulations.

Table of Contents

Acknowledgements

First and foremost, I want to extend my deepest gratitude to my Ph.D. advisor, Dr. Sarah Keller. From the moment that I met Sarah on my visit to the University of Washington as a prospective student, she has been one the most encouraging, understanding, thoughtful, optimistic, diligent, hardworking, and admirable people with whom I have ever had the pleasure to collaborate. From the initial excited emails about the opportunities awaiting me at UW and as a possible member of her research group, to the vast amounts of time she afforded to me to discuss my academic progress, career goals, and experimental tribulations, I could not have asked for nor hoped for a better advisor. Sarah has always prioritized my success, as well as the success of everyone in the Keller Lab. I hope to be as incredible a mentor as Sarah is one day. Even if I can be half as good, that will still be an incredible feat of which I will be proud.

Thank you to my committee members, Dr. Sharona Gordon, Dr. Joshua Vaughan, and Dr. Jesse Zalatan. Your questions during my exams have helped me to think about my research with a more critical and discerning eye, and I am thankful for both your responsiveness as my mentors and your efforts to help me expand my connections as I explored different career opportunities. I am also grateful for many of the faculty members in the Chemistry Department at the University of Washington with whom I taught undergraduate chemistry as a Teaching Assistant, helping me to improve myself as an instructor and allowing me to pursue greater responsibilities as a Lead Teaching Assistant.

To my friends and colleagues in the Keller Lab, both past and present, thank you for your camaraderie through the entirety of the experience. Regular group meetings, trips to the Biophysical Society Conference, berry picking, cookie baking, and Ethiopian food; these interactions in retrospect were probably a considerable chunk of the social activity that I had during my Ph.D. I am forever grateful for these small but important breaks to the sometimes grueling stretches of doing science. Most importantly, thank you for your encouragement, criticisms, and celebrations of success, your inputs have undoubtedly made me a better, more equipped scientist.

I also want to thank some of my previous mentors who have helped introduce me to the world of scientific research. From the psychology of magic with Dr. Anthony Barnhart, to bacteriophages with Dr. Deborah Tobiason, to analyzing green teas with HPLC with Dr. Dan Choffnes, to microfluidic green chemistry with Dr. David Brownholland, all of you helped feed my curiosity and start me on the scientific path. I want to thank my mentors at Brandeis University, Nikita Alimov and Bruce Goode, for my first opportunity to do summer NSF-funded research, and my mentors, Thomas Litschel and Petra Schwille, at the Max Planck Institut für Biochemie in Germany where I began my career in biophysics and made my first vesicles.

I want to extend a heartfelt thanks to my undergraduate advisor Dr. David Brownholland. Alongside his scientific mentorship, he instilled in me that one can always reinvent themselves after graduate school. That guidance meshed well with my broad and numerous interests and emboldened me to pursue a Ph.D. without fear of limiting my future career path. A testament to his word, I secured a postdoctoral fellowship with NOAA Fisheries investigating the impacts of contaminated stormwater runoff on salmon populations, a completely new and exciting chapter in my scientific career.

I am incredibly thankful for all the friends and roommates who have been a part of my life throughout graduate school. A side effect of my studies was that I leaned heavily into the introverted side of my personality. In spite of that, you all consistently reached out to chat and invited me to gatherings, thwarting (thankfully) my attempts to be a complete recluse. Thank you to Alex Smith, a lifelong friend, for your efforts to keep in touch and for long phone calls to help pass time imaging on the microscope. A special thanks to Coire Gavin-Hanner and Nicole Panek, whose offerings of food and nudges to play Catan helped keep my batteries above empty in the final weeks. And an extra special thanks to their cat, Simba, for keeping me company on late nights and reminding me that it is good to be present in and enjoy the moment.

A warm and loving thank you goes to my family. I am immensely grateful for my parents, Bill and Kirsten, who have supported me in every way they can in all aspects of my life. So many things were made possible through their encouragement, wisdom, and generosity. I can always count on them for a place to come home to. Thank you to my brother and sister, Anders and Annika.

You both mean the world to me, from our numerous memories growing up all the way through to our endeavors and successes here in the present; we have always cheered each other on.

And finally, to my partner in life, Sonja Katt. I extend my deepest gratitude for your selfless and compassionate support, spirit of optimism, and for being my very best friend. You have endured the most difficult moments right beside me, remaining a guiding light, nonetheless. I am filled with gratitude for the life we have carved out for ourselves here in the PNW. Now that I'm nearing the end of a long and laborious journey, allow yourself to take a breath. It's time for me to return the favor for your journey.

Chapter 1

Introduction

Like many scientists, biophysicists strive to break down the complexity of natural systems into understandable building blocks. For example, the function of a protein can be broken down this way into a combination of simple machines and one-step, chemical transformations. Consider the cell membrane and its hundreds of constituent lipids: the chemical and physical properties of each individual lipid species contribute to the overall behavior of the membrane. Or zoom out to the macrobiological scale of a plant's growth: water pressures and distributions of cells give rise to the myriad of morphologies plants may adopt. Once the building blocks themselves are understood, biophysicists must then uncover how the building blocks fit together and interact, giving rise to the complex phenomena that are observed in living, biological systems. To this end, biophysicists propose hypotheses and perform tests on individual building blocks and collections thereof, motivating further hypotheses and tests. It is this ubiquitous cycle of theory and experiment—a hallmark of the scientific endeavor—that contextualizes the scientific contributions of each biophysicist.

In this dissertation, I will examine two examples of how biophysical complexity can be pared down into simpler building blocks, and discuss the experimental techniques used to probe them. The first example will focus on compositional organization within biological membranes. Model phospholipid membranes comprised of binary and ternary lipid mixtures provide a means by which to attribute characteristics of a membrane's behavior to its individual lipids. The second example will focus on rippling and blooming of lily flowers. Ripple evolution at the edges of lily petals can be described by physics principles, and simple models of lily buds used to simulate blooming are compared against measurements of actual lily buds, obtained through a straightforward, physical tomography technique.

1.1 Lipids and Model Membranes.

Biological membranes are made up primarily of molecules called lipids. Lipids that form membranes are amphiphilic, containing a region that is hydrophilic, or "water-loving," and a region that is hydrophobic, or "water-fearing" (Fig. 1.1A). These two characteristics are necessary for lipids to assemble into membranes in water. In a membrane, amphiphilic lipids pack side-by-side to form two apposed leaflets called monolayers. Together, the leaflets form a bilayer. Hydrophilic lipid headgroups face outwards and interact favorably with water, while hydrophobic lipid tails are pointed inwards to sequester them away from unfavorable interactions with water (Fig. 1.1B). Membranes serve as a boundary around cells and many organelles.

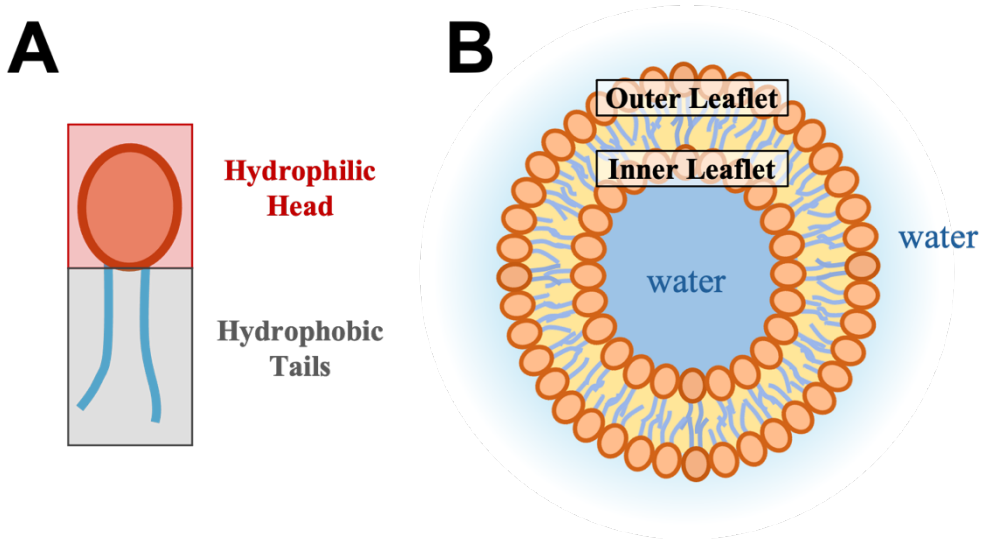

Figure 1.1. Lipids can form bilayers in water. A) A cartoon of an amphiphilic lipid known as a phospholipid. The hydrophilic region is located on the lipid headgroup while the hydrophobic region is located on the lipid tails. For molecular structures of different phospholipids, see Figs. 2.2 and 3.1. **B)** A cartoon of a single-component membrane formed by the self-assembly of two leaflets of amphiphiles into a spherical shell. The hydrophobic tails point inwards while the hydrophilic heads point outwards and interact favorably with water.

Phospholipids are a type of lipid with three major components: 1) a phosphate headgroup, 2) one or more hydrocarbon tails, and 3) a glycerol backbone that covalently links the headgroup and tails. Headgroups have a significant impact on the properties and overall structure of a phospholipid. For example, phosphocholine (PC) and phosphoethanolamine (PE) both include positively charged moieties on the phosphate headgroup, resulting in an overall neutral lipid at

physiological pH. However, the amine in choline is methylated whereas the amine in ethanolamine is not, so PC-lipids are shaped like cylinders whereas PE-lipids are shaped more like cones (1, 2). The length and saturation of the hydrocarbon tails influence the melting temperature (T_{melt}) of a phospholipid and how tightly its tails pack together in a lipid bilayer. Longer carbon chains with no double bonds are more ordered (e.g., lipid tails are more extended, aligned, and packed closely together), and the membrane is more rigid. In contrast, shorter carbon chains with one or more double bonds are more disordered (e.g., lipid tails are kinked, misaligned, and have more space between them). Membranes comprised of disordered lipids are more fluid as a result, and diffusion coefficients of lipids are higher than those of lipids in membranes with higher rigidity (3, 4).

Since cellular membranes contain hundreds of unique lipid types (5), researchers have sought ways to characterize the qualities that individual lipids impart to the membrane. Model membranes have proven to be exceptionally useful as a simplification tool because they can be tailored to suit a broad range of experimental conditions such as composition, size, and shape. Giant unilamellar vesicles (GUVs) are valued for being free-floating, unilamellar, and readily synthesized. Some of the prominent techniques to form GUVs include gentle hydration (6), electroformation (7, 8), and emulsion transfer (9). Typically, researchers who work with model membranes have assumed that those model membranes retain the same composition as the lipid stock solutions from which they are made. In Chapter 2, we will confront this assumption and confirm that it holds true for several techniques and lipid compositions, though there are a few caveats.

1.2 Phase Separation in Model Lipid Membranes.

One of the first models of the cell membrane, proposed by Singer and Nicolson in 1972, described the membrane as a “fluid mosaic” of lipids and proteins (10). This mosaic of proteins and lipids had long been known to be nonuniformly distributed across the surfaces of cell membranes. In 1997, Simons and Ikonen developed a new way of thinking about these distributions by introducing their “raft hypothesis” in which they asserted that some lipids and proteins were enriched in distinct membrane regions called rafts (11). A subsequent explosion of interest in the lipid raft field (12) fueled efforts to simplify and reconstitute raft-like domains in model membranes. Raft formation is likely influenced by the same lipid properties that drive liquid-liquid

phase separation. Our lab identified that ternary mixtures of a low T_{melt} lipid, high T_{melt} lipid, and cholesterol produce GUVs with robust regions of liquid-liquid phase separation. Using fluorescence microscopy, our lab characterized micron-scale, liquid-liquid phase separation in GUVs made from a collection of ternary mixtures of phospholipids and cholesterol (13, 14), and mapped the ternary phase diagrams for several of these mixtures (Fig. 1.2).

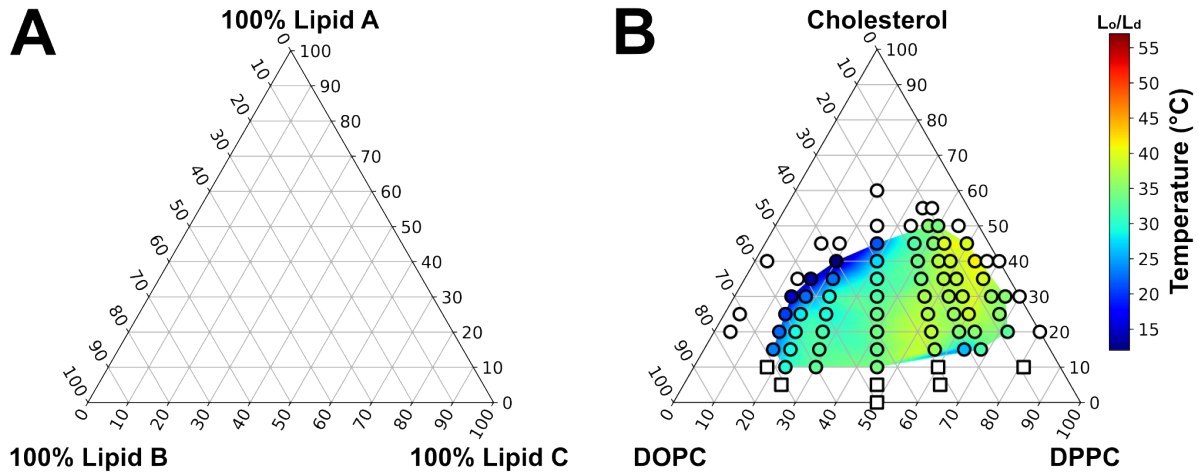

Figure 1.2. Gibbs phase diagrams are used to map phase transitions in a three-component membrane. A) A blank ternary phase diagram. The top, left, and right vertices of the triangle represent compositions with 100% of lipid A, lipid B, or lipid C respectively. Each edge of the triangle represents binary compositions of the lipids at the adjoining vertices. Points within the triangle represent ternary compositions of all three lipids. **B)** A phase diagram mapped for GUVs containing a ternary composition of the lipids DOPC, DPPC, and cholesterol, adapted from (14). For further discussion, see Fig. 3.3 and section 3.4 of Chapter 3.

Fluorescence microscopy has also been used to observe micron-scale liquid domains in membranes of vacuole organelles within living yeast cells (15), and phase separation of the vacuole was further shown to help yeast cells metabolize lipid droplets during nutrient deprivation in the stationary phase of their growth (16). Yeasts can actively tune their membrane compositions so that the vacuole membrane phase separates at temperatures that scale with their growth temperature (17); similar tuning had previously been found in zebrafish (18). In these cases, phase separation can be observed and characterized in living systems, but the identities of the lipids that are in each phase is not known. Mapping phase diagrams for model systems with only two or three lipids enables more direct attribution of the membrane phases and their biophysical properties to specific lipid constituents.

Considerable progress has been made on mapping phase diagrams for a variety of lipid compositions; a few examples include PC-lipids (14, 19, 20), charged PS- or PG-lipids (21, 22), and sphingomyelins (23, 24). Although PE-lipids are a relatively abundant lipid class found in cellular membranes (5), PE-lipids have not received much attention, owing to their conical shape and propensity to form inverted hexagonal phases rather than stable lamellar phases (25). The miscibility phase behavior of GUVs containing PE-lipids is only now being mapped thoroughly. In Chapter 3, we explore the phase diagrams for two ternary lipid mixtures that contain a PE-lipid.

1.3 Rippling and Blooming in Lily Flowers.

The flowers of plants undergo morphological transformations as they bud, grow, and bloom. For example, some types of lilies develop ripples along the edges of their petals. These beautiful transformations are likely due to a combination of causes such as genetic encoding, differential cell growth rates, environmental stimuli, and more. Focusing on one of these factors, some groups have applied growth hormones to the edges of plant leaves to induce ripple formation (26). Others have simulated the blooming of a lily bud by modeling it as a thin, lenticular shell (27).

Inspired by the previous work on lily rippling and blooming, we take time-lapse videos of lilies as they ripple, and we apply and improve upon a simple scaling law used to describe ripples in torn plastic sheets (28). We also employ a straightforward, surgical tomography technique to slice lily buds, measure petal thicknesses, and compare those thickness measurements to models used in simulations. The work on rippling and blooming in lilies will be discussed in Chapter 4.

Chapter 2

Several common methods of making vesicles (except an emulsion method) capture intended lipid ratios

*This chapter was first published in the *Biophysical Journal* in 2024. It was written in collaboration with Heidi M. J. Weakly, Kent J. Wilson, Emily L. Pruitt, Amy Li, Libin Xu, and Sarah L. Keller.

Weakly, H. M. J., K. W. Wilson, G. J. Goetz, E. L. Pruitt, A. Li, L. Xu, S. L. Keller. 2024. Several common methods of making vesicles (except an emulsion method) capture intended lipid ratios. *Biophys. J.* 123:3452-3462.

2.1 Abstract.

Researchers choose different methods of making giant unilamellar vesicles in order to satisfy different constraints of their experimental designs. A challenge that arises when researchers use a variety of methods is that each method may produce vesicles with a different average lipid ratio, even if all experiments use lipids from a common stock mixture. Here, we use mass spectrometry to investigate ratios of lipids in vesicle solutions made by five common methods: electroformation on indium tin oxide slides, electroformation on platinum wires, gentle hydration, emulsion transfer, and extrusion. We made vesicles from either five-component or binary mixtures of lipids chosen to span a wide range of physical properties: di(18:1)PC, di(16:0)PC, di(18:1)PG, di(12:0)PE, and cholesterol. For a mixture of all five of these lipids, ITO electroformation, Pt electroformation, gentle hydration, and extrusion methods result in only minor shifts in lipid ratios ($\leq$ 5 mol%) relative to a common stock solution. In contrast, emulsion transfer results in ~80% less cholesterol than expected from the stock solution, which is counterbalanced by a surprising overabundance of saturated PC-lipid relative to all other phospholipids. Experiments using binary mixtures of saturated and unsaturated PC-lipids and cholesterol largely support results from the five-component mixture. In general, our results imply that experiments that increment lipid ratios in small steps will produce data that are highly sensitive to the technique used and to sample-to-

sample variations. For example, sample-to-sample variations are roughly ±2 mol% for five-component vesicles produced by a single technique. In contrast, experiments that explore larger lipid ratio increments or that seek to explain general trends and new phenomena will be less sensitive to sample-to-sample variation and the method used.

2.2 Introduction.

Many methods have been developed to produce giant unilamellar vesicles (GUVs) (29), where each meets different experimental constraints. For example, researchers may prioritize vesicle size (30–32), number of lamellae (33–35), compositional asymmetry (36–38), membrane charge (6, 21) and encapsulation of solutes (39, 40). Similarly, researchers may use different mixtures of molecules to produce GUVs ranging from simple models of minimal membranes to complex mimics of living cells.

However, when scientists use different methods to make GUVs, an uncomfortable question arises: do the vesicles produced by each method contain the same ratio of lipids as the stock solution from which the vesicles were made? If not, do all methods alter the intended lipid ratio in the same way, or does each method yield different ratios? These straightforward questions have huge impact: researchers who use different methods cannot compare their results unless they know that their vesicle compositions are similar or unless they know how to estimate the magnitude of the offset in lipid composition they might observe.

Concerns that different vesicle-making methods may incorporate different ratios of lipids into membranes are well-founded, especially when one of the lipids is a sterol. The solubilities of sterols in membranes of giant vesicles are sensitive to experimental conditions and to the identities of the other lipids in the membrane (41–44). Even when the mole fraction of cholesterol is below its membrane solubility limit, extrusion of vesicles may perturb the cholesterol fraction (45). Cholesterol levels are known to be especially low in vesicles made by emulsion transfer techniques (46–48). Challenges also arise in incorporating sufficient lipids with high melting temperatures (12), high charge (21, 49) or high spontaneous curvature (33) into membranes of giant vesicles.

Here, we used mass spectrometry to directly measure population-averaged mole fractions of lipids in vesicle solutions made by multiple methods (Fig. 2.1). We chose four common techniques of producing GUVs: electroformation on slides coated with indium tin oxide (ITO), electroformation on platinum (Pt) wires, emulsion transfer, and gentle hydration (Fig. 2.1). We also included a common technique of converting giant vesicles into smaller vesicles: extrusion across a porous membrane filter. For each technique, we chose only one instance of experimental conditions commonly in use. (Other labs may employ different conditions, so may observe different results.) Each technique has advantages. Electroformation produces stable GUVs that span a wide range of sizes, frequently up to 100 μm (8). Emulsion transfer is valued for high encapsulation efficiency (9). Gentle hydration incorporates (and often requires) charged lipids in GUVs (6). Extrusion converts GUVs into vesicles of smaller and more uniform sizes.

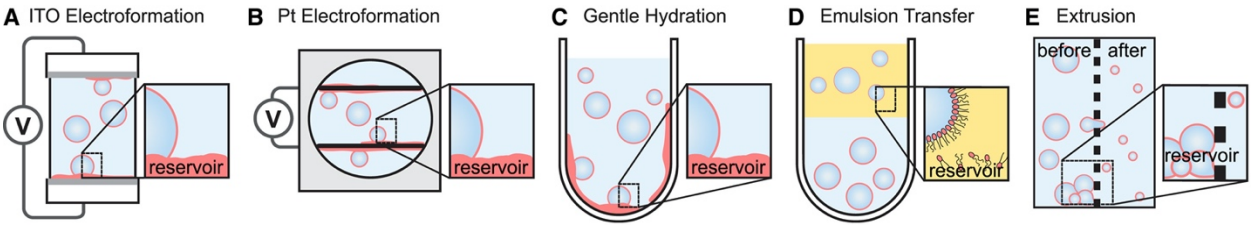

Figure 2.1. Five methods of producing vesicle solutions. A) In ITO electroformation, an alternating field is applied across a hydrated lipid film on slides coated with indium tin oxide. Afterward, a reservoir of lipid remains on the slide. **B)** In Pt electroformation, an alternating field is applied across a hydrated film on platinum wires. Afterward, a reservoir of lipids remains on the wires. **C)** In gentle hydration, vesicles form spontaneously from a hydrated lipid film on a glass surface. Afterward, a reservoir of lipids remains on the glass. **D)** In emulsion transfer, lipids from an oil solution assemble at water/oil interfaces to form emulsion droplets, which then pass through a second interface to form vesicles. Afterward, a reservoir of lipids remains in the oil. **E)** In extrusion, smaller vesicles are made by passing giant vesicles through a porous filter. Afterward, a reservoir of lipids and vesicles remains on the filter. Figures are not to scale.

Our use of mass spectrometry to measure average lipid compositions of vesicle solutions complements recent advances in using Nanoscale Secondary Ion Mass Spectrometry (NanoSIMS) to directly measure vesicle-to-vesicle variations in lipid compositions (50). The two techniques are synergistic. Whereas current NanoSIMS analyses excel at measuring relative compositions in individual vesicles, the technique currently has low sample-to-sample reproducibility for vesicle populations (50). Our mass spectrometry technique does the opposite. It excels in reproducibly evaluating average lipid ratios in vesicle populations and does not evaluate compositions of

individual vesicles. By using population averages, we address the question of how the lipid composition of vesicle solutions varies across multiple techniques.

To produce our vesicle solutions, we chose lipids with a range of features that characterize broad classes of lipids (Fig. 2.2). Specifically, we chose cylindrical, zwitterionic lipids with both low and high melting temperatures (di(18:1)PC and di(16:0)PC), a charged lipid (di(18:1)PG), a cone-shaped lipid (di(12:0)PE), and a sterol (cholesterol).

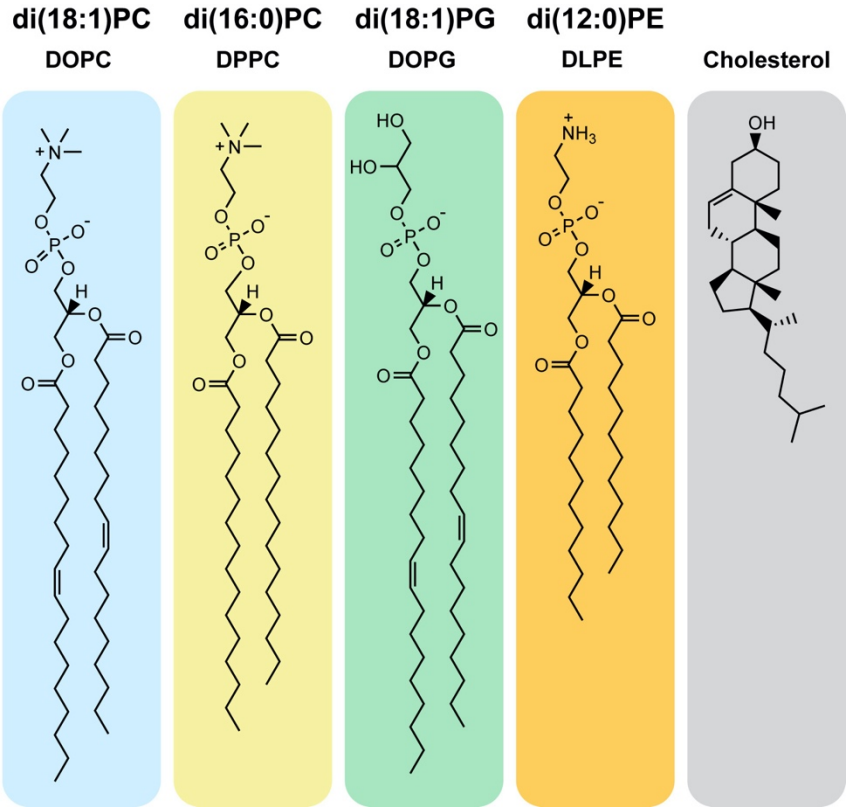

Figure 2.2. Structures of lipid types used to form GUVs. Lipids were chosen to represent five important lipid characteristics: saturated tails, unsaturated tails, charged headgroup, non-cylindrical shape, and sterol structure. Formal names of lipids reflect the length and unsaturation of the acyl chains and the headgroup type, whereas common names reflect historical sources. For example, di(18:1)PC (commonly called DOPC) is a zwitterionic lipid with a phosphatidylcholine (PC) headgroup and two 18-carbon chains, each with one double bond, whereas di(16:0)PC is saturated, with 16 carbons in each chain. Di(18:1)PG is a charged and unsaturated lipid with a phosphatidylglycerol (PG) headgroup. Phosphatidylethanolamine (PE) headgroups, as in di(12:0)PE, are smaller than PC headgroups, so PE-lipids are typically cone-shaped. Cholesterol has a hydroxyl moiety as a headgroup and a fused, four-ring structure with an 8-carbon chain.

Each lipid was included for a different reason. PC-lipids produce stable membranes and are the most abundant lipid in mammalian cells (1, 5, 51). PG-lipids are abundant in mycobacteria (52). Their low pKa (53) and subsequent charge can increase the yield of vesicles made by gentle hydration, as do charged phosphatidylserine (PS) lipids (6). PE-lipids are one form of non-cylindrical lipids; PE-lipids facilitate membrane fusion and are abundant in the inner leaflet of red cell membranes (1, 5, 54). Cholesterol, in addition to facilitating membrane fusion (55), enables large-scale, liquid-liquid phase separation in membranes (56) and constitutes a large fraction (up to ~40 mol%) of lipids in mammalian membranes (5).

We tested five-component and 2-component (binary) lipid mixtures. In the five-component mixture, the ratio of each lipid was selected to promote high vesicle yields for every method. High vesicle yields facilitate our central goal of comparing average lipid compositions across vesicle solutions made by each method. In detail, we included high fractions of PC-lipids to produce stable membranes. We added saturated (rather than unsaturated) PE-lipids in low fractions to avoid hexagonal phases and to minimize tubule formation (1). Because vesicles with high fractions of charged lipids are challenging to form by electroformation (21), we chose to include only a low fraction of PG-lipid. We ensured that fractions of cholesterol were well below its membrane solubility limit (41–44). To minimize vesicle-to-vesicle differences in composition, we chose all lipids to have melting temperatures ≤50˚C (12). To answer key questions that arose from our experiments with the five-component mixture, we then conducted experiments with membranes comprised of binary mixtures of lipids. For all measurements, we compared the ratios of lipids in vesicle solutions directly to ratios in lipid stock solutions to minimize potential error due to concentration variations across manufacturer lots.

2.3 Materials and Methods.

i. Chemicals.

PC-lipids, PG-lipids, PE-lipids, and phospholipid standards were obtained from Avanti Polar Lipids; cholesterol was obtained from Sigma-Aldrich; and d7-cholesterol standard was obtained from Kerafast. All lipids were used without further purification and without verifying concentrations because our experiments focus on measuring relative deviations in lipid

composition from pre-mixed stock solutions rather than absolute concentrations in stocks. Lipid names reflect their headgroup (e.g., "PC", "PG", or "PE"), the number of carbon chains (e.g., "di" = 2), and each chain's number of carbons and unsaturation (e.g., "18:1"). Specific lipids in our samples include dioleoyl-phosphocholine (di(18:1)PC or DOPC, T_{melt} = -18.3 ± 3.6°C (57)), dipalmitoyl-phosphocholine (di(16:0)PC or DPPC, T_{melt} = 41.3 ± 1.8°C (57)), 1,2-dipalmitoleoyl-sn-glycero-3-phosphocholine (di(16:1)PC or DPoPC, T_{melt} = -35.5°C (58)), dioleoyl-phosphoglycerol (di(18:1)PG or DOPG, T_{melt} = -18°C (59)), and dilauroyl-phosphoethanolamine (di(12:0)PE or DLPE, T_{melt} = 49.3 ± 1.7°C (25)). Lipid standards for mass spectrometry include di(15:0)PC, (16:0/18:1)PC, di(15:0)PE, di(15:0)PG, and d7-cholesterol. Cholesterol (Sigma-Aldrich) and a fluorescently labeled lipid (Texas Red DPPE, Life Technologies) were dissolved in chloroform at 10 mg/mL and 1 mg/mL, respectively. Mineral oil (light, bioreagent, 0.84 g/mL, 14.2-17.2 cSt at 40°C) was from Sigma Aldrich.

ii. Master Stocks.

Seven master stock solutions of lipids (which included 0.8 mol% of the fluorescent dye Texas Red DPPE) were prepared in chloroform. Each stock was stored at –20°C in a vial sealed with Teflon tape, parafilm, and electrical tape. Lipid compositions of all master stocks were measured by HILIC-IM-MS as a baseline for direct comparisons between stocks and vesicle samples. The first of the seven stock solutions contained five lipid components (DOPC/DPPC/DOPG/DLPE/cholesterol). The second, third, and fourth contained binary mixtures that isolated the effects of unsaturation (DPPC/DPoPC), chain length (DPoPC/DOPC), and sterol content (DPoPC/cholesterol). The fifth, sixth, and seventh added 5 mol% DOPG to the binary mixtures, since charged lipids were required for the gentle hydration technique.

iii. Electroformation on ITO Slides.

Electroformation followed standard procedures (8). Briefly, for each sample, 0.25 mg of total lipid (29 μL of master stock solution) was heated to 60°C and spread across two ITO-coated glass slides using the side of a glass Pasteur pipette. The slides were placed under vacuum for ~30 min to allow residual chloroform to evaporate. An electroformation chamber was made by sandwiching 0.3 mm thick Teflon spacers between the ITO-coated slides. The chamber was filled with 300 mM sucrose (~300 μL) and sealed with vacuum grease. The chamber was then attached to metal electrodes

using stainless steel binder clips. An AC voltage of 1.0 V was applied across the electrodes at 10 Hz for 2 h at 60°C. The temperature of 60°C is roughly 20°C above the highest lipid T_{melt} in the system. To minimize variability, all experiments using ITO slides were conducted by the same researcher.

iv. Electroformation on Platinum wires.

A chamber was adapted from previous designs (60). Briefly, a vertical hole of 15 mm diameter was cut in a 25 mm x 25 mm x 5 mm block of Teflon. Two holes of ~0.25 mm diameter were cut horizontally through the chamber, separated by 2.5 mm. Two 0.25-mm platinum wires were inserted into the two holes. Before each use, the wires and chamber were cleaned with chloroform. The bottom of the Teflon chamber was sealed with a glass cover slip, and the chamber was placed on a 60°C hot plate. Next, 5.7 µL of master stock solution was deposited in evenly spaced 0.5 µL drops on both wires. The interior of the chamber was filled with 1 mL of 300 mM sucrose solution, and the top was sealed with a glass cover slip. An AC voltage of 2.5 V was applied at 10 Hz for 2 h at 60°C. To minimize variability, all experiments using Pt wires were conducted by the same researcher.

v. Gentle Hydration.

For each sample, 0.2 – 0.8 mg of total lipid from the master stock was transferred into a glass test tube. The test tube was placed in a water bath at > 50°C while chloroform was removed from the lipid solution by a steady stream of N_2 gas to form a lipid film. To remove residual chloroform from the film, the test tube was placed under vacuum for ≥ 1 h. After drying, the lipid film was rehydrated by adding 0.2 - 0.8 mL of 300 mM sucrose, so that the test tube contained 1 mL of solution for every 1 mg of lipid. The test tube was sealed with parafilm and maintained in an oven at 50°C for 24 h. while vesicles formed. To minimize variability, all experiments using gentle hydration were conducted by the same researcher.

vi. Emulsion Transfer.

The procedure was adapted from standard protocols (9, 47, 61) and was conducted at room temperature (20-25°C). First, a volume of master stock equivalent to 0.4-0.6 mg of total lipid mass was added to a chloroform-rinsed test tube. A lipid film was formed inside the test tube by drying

the lipid solution under a gentle stream of nitrogen gas and placing the test tube in a vacuum chamber for ≥ 30 min. The test tube and a sealed container of mineral oil were quickly transferred to a glove box (Techni-Dome 360° Glove Box Chamber), which was then purged with nitrogen gas until humidity reached ≤ 25% (ThermPro Digital Indoor Thermometer). The container of mineral oil was opened only in the glove box, and 200-300 µL of mineral oil was added to the lipid film inside the test tube, resulting in a final lipid concentration of 2 mg/ml in mineral oil. The test tube was sealed with Teflon, parafilm, and electrical tape, removed from the glove box, and sonicated in a water bath (CO-Z Digital Ultrasonic Cleaner Model 10A, 40 kHz) for two or more intervals of 30 min at 50°C until no visible lipid film remained on the glass surface and the red color of the dye within the lipid-in-oil solution was homogenous. Between each 30 min sonication step, samples were gently vortexed to improve solubilization of the lipid film. The resulting lipid-in-oil solution was mixed with 20-30 µL (10% of the oil volume) of an aqueous, 300 mM sucrose solution by vigorous pipetting to create an emulsion. Approximately 200-300 µL of the emulsion was layered above 300 µL of an aqueous, 300 mM glucose solution in a 1.5 mL microcentrifuge tube and then centrifuged at 9000 x g for 30 min to drive dense, sucrose emulsion droplets through the oil/water interface. The supernatant was removed without disturbing the vesicle pellet until minimal solution covered the pellet. The pellet was resuspended in 600-800 µL of 300 mM glucose by gentle pipetting, using tips that had been cut to larger diameters to minimize shearing. To minimize variability, all experiments using emulsion transfer were conducted by the same researcher.

vii. Vesicle Sedimentation and Storage.

To maximize the yield of lipids in vesicles relative to lipids in aggregates, GUVs made by electroformation and gentle hydration were sedimented in an osmotically matched glucose solution. Briefly, 200 µL of vesicle solution was added on top of 800 µL of glucose solution in a 13 x 1000 glass test tube (Fisher Scientific). Vesicles sank to the bottom of the tube for 10 min. Then 150 µL of vesicle solution was transferred from the bottom of the tube to a new microcentrifuge tube for storage. For emulsion transfer, vesicles were also sedimented after resuspension in 600-800 µL of a glucose solution. For all methods, enriched vesicle solutions were stored at –20°C in parafilm-sealed 1.5 mL microcentrifuge tubes. A schematic of the method is shown in Fig. S2.17.

viii. Vesicle Imaging.

Vesicle solutions were imaged between glass slides on a Nikon Eclipse ME600L upright epifluorescence microscope using a Hamamatsu C13440 camera at room temperature (20–25°C).

ix. Extrusion.

Vesicle solutions were prepared by gentle hydration and enriched in solution (relative to vesicle aggregates) by sedimenting. The sedimented vesicle solution was split into two samples of equal volume. The first sample was reserved for "Before" extrusion measurements and the second sample was extruded to obtain an "After" measurement. To minimize loss of solution due to dead volume of the miniextruder (Avanti Polar Lipids), the filter supports and 0.1 μm polycarbonate filter were prewet by passing 1 mL of a sucrose solution through them prior to loading the sample. The complete extruder assembly (the heat block, the syringe with the vesicle solution, and the empty syringe) was maintained at 50 °C for 30 min before extrusion. Finally, the vesicle solution was passed through the filter nine times and collected for analysis.

x. Internal Standards.

Cholesterol concentrations were normalized to the internal standard d_7-cholesterol, which was dissolved in benzene at a concentration of 2.5 μg/mL. Phospholipids in five-component samples were normalized to the following internal standards: both di(16:0)PC and di(18:1)PC were normalized to di(15:0)PC, di(12:0)PE was normalized to di(15:0)PE, and di(18:1)PG was normalized to di(15:0)PG. For binary samples, PC-lipids were normalized with respect to saturation: di(16:0)PC was normalized to di(15:0)PC, and both di(16:1)PC and di(18:1)PC were normalized to (16:0/18:1)PC. All phospholipid internal standards were 1 μM in samples.

xi. Lipid extraction.

To enable quantification of each lipid class, internal phospholipid standards dissolved in chloroform and the d7-cholesterol internal standard dissolved in benzene were added to master stocks (in chloroform) and vesicle samples (in aqueous solution) before solutions were extracted for analysis. To maximize accuracy in comparing mass spectrometry data, sample concentrations were adjusted. Lipids were extracted from vesicle solutions by the method of Bligh and Dyer (62).

Extracts were dried in a vacuum concentrator and reconstituted in 2:1 acetonitrile-methanol. Assuming each method of making vesicles incorporates 10% of the initial lipid mass into vesicles, vesicle solutions were diluted to achieve concentrations of ~1 μM for the least prevalent lipid in the acetonitrile-methanol solution. A schematic of the method is shown in Fig. S2.17.

xii. HILIC-IM-MS Analysis of Phospholipids.

Phospholipid analysis was conducted using hydrophilic interaction liquid chromatography (HILIC) coupled with ion mobility-mass spectrometry (IM-MS) in positive electrospray ionization mode (Waters Synapt XS HDMS; Waters, Milford, MA). This technique relies on the presence of ionizable groups, which are present in lipids (and not in the hydrocarbons of mineral oil used in emulsion transfer techniques). Chromatographic separations were carried out using a Phenomenex Kinetex HILIC column (50 x 2.1 mm, 1.7 μm) with 95% acetonitrile/5% water/5 mM ammonium acetate as mobile phase A and 50% acetonitrile/50% water/5 mM ammonium acetate as mobile phase B (Waters Acquity FTN UPLC; Waters). Collisional cross-section calibration and IM-MS analysis were conducted as described previously (63–65). Data alignment and peak detection were performed in Progenesis QI (Nonlinear Dynamics; Waters). Retention time calibration and lipid identification were performed with the LiPydomics Python package (66). Lipid abundances were normalized to their internal standards and compared to the background. For only two types of samples (membranes produced by emulsion transfer in the main text that evaluate binary mixtures of lipids that differ in chain length and in PC-lipid versus cholesterol), lipid abundances were deemed indistinguishable from the background. For these samples, extracts were concentrated by a factor of 5 and re-analyzed by HILIC-IM-MS.

xiii. UHPLC-MS/MS Analysis of Cholesterol.

Extracts were analyzed through ultra-high performance liquid chromatography-tandem mass spectrometry (UHPLC-MS/MS) using atmospheric pressure chemical ionization (Sciex QTRAP 6500; SCIEX, Framingham, MA or Waters Xevo TQ-XS; Waters) (67). Reversed-phase chromatography separations were carried out using a Phenomenex Kinetex C18 column (100 x 2.1 mm, 1.7 μm) with a 90% methanol/10% water/0.1% formic acid mobile phase. Quantitation methods and peak integration were performed using Analyst software (SCIEX Analyst 5.1, SCIEX) or MassLynx and TargetLynx software (Waters Corp.). Concentrations of cholesterol were

obtained using peak ratios relative to d_7-cholesterol (67) and a calculated average relative response factor (RRF) (for further information on RRF, see Tables S2.12, S2.16, and S2.18). Cholesterol abundances in emulsion transfer samples that evaluate binary mixtures of a PC-lipid and cholesterol were measured after concentration by a factor of 5.

xiv. Analysis and Plotting.

Phospholipid abundances are raw values obtained from the mass spectrometry measurements. To calculate lipid composition as mole percentages, the abundance of each lipid (normalized to a lipid standard) was divided by the total lipid abundance for each sample (Tables S2.11-2.20). Cholesterol abundances are raw values divided by the experimental RRF. The mean percentage of each lipid type and the standard deviation were calculated for three independent samples. Ternary plots were generated using the open-source Python library, python-ternary (https://github.com/marcharper/python-ternary).

2.4 Results and Discussion.

Our experiments answer four types of questions: 1) Do all methods produce giant vesicles with sufficient yield? 2) How do the ratios of lipids in vesicle solutions produced by each method differ from ratios in vesicle solutions produced by the other methods? 3) How do those ratios differ from the stock solution? 4) How reproducible is each method? We begin with a five-component mixture of lipids and then conduct targeted experiments in binary mixtures.

i. All methods produce sufficient vesicles from the five-component mixture.

As expected, all five methods produce vesicles. Vesicles produced by electroformation (on ITO slides and platinum wires) are predominantly unilamellar (Figs. S2.2 and S2.3) and are at sufficient yield for mass spectrometry. Vesicles produced by electroformation on Pt wires were smaller and less numerous than vesicles from electroformation on ITO slides (Fig. S2.3), which is consistent with fewer moles of lipids being deposited on Pt wires than on ITO slides. Vesicles made by gentle hydration consistently have more lamellae or are nested (Fig. S2.4), and vesicles made by emulsion transfer show membrane defects or nested vesicles (Fig. S2.5). Vesicles extruded through 100 nm membrane filters are too small to be resolved by traditional fluorescence microscopy (Fig. S2.6).

Collecting and measuring lipids exclusively from vesicles is challenging. Although sedimentation successfully enriches solutions in vesicles, some lipid aggregates remain and are included in extractions, as in Fig. S2.1. For all techniques, some lipids remain in reservoirs after vesicles are formed (Fig. 2.1), either as residues on surfaces or dissolved in oil (Figs. S2.7-2.10). The lipid compositions of the sedimentation supernatant and the lipid reservoirs were not analyzed.

Vesicles made by electroformation and gentle hydration exhibit liquid-liquid phase separation of their membranes, consistent with the tendency for membranes to demix when they contain mixtures of high-T_{melt} lipids, low-T_{melt} lipids, and cholesterol (12). In contrast, the vesicles prepared by emulsion transfer did not exhibit liquid-liquid phase separation at room temperature, indicating that the lipid composition of emulsion transfer vesicles differed from the composition of the other vesicles (Fig. S2.5).

ii. Electroformation and gentle hydration create vesicles with minor offsets in lipid ratios.
Our central result is that three methods of producing giant vesicles (electroformation on ITO slides, electroformation on platinum wires, and gentle hydration) result in similar population-averaged percentages of lipids in the membranes. Moreover, these percentages are similar to that of the master stock solution. These similarities are shown in the first four stacked bars in Fig. 2.3A.

Another way to visualize the minor differences in lipid ratios between the three methods is to zoom into a region of the pseudo-ternary diagram in Fig. 2.3B. Symbols for the three independent experiments of each method (circles for ITO electroformation, triangles for Pt electroformation, and squares for gentle hydration) cluster around the single star denoting the master stock solution. Fig. 2.3B shows that electroforming vesicles on ITO slides and on platinum wires shifts lipid mole ratios from the master stock solution by roughly 4 mol% and 1.5 mol%, on average. Similarly, gentle hydration of vesicles shifts lipid mole ratios by roughly 5 mol% on average, in the direction of increasing cholesterol. When expressed as a percent change, the gentle hydration method incorporated ~20% more than the expected amount of cholesterol in the five-component sample.

The data in Fig. 2.3 also show that reproducibility of these three methods is high, based on the close clustering of data from three independent experiments: the range of sample-to-sample lipid ratios for each method is within ± 2 mol%.

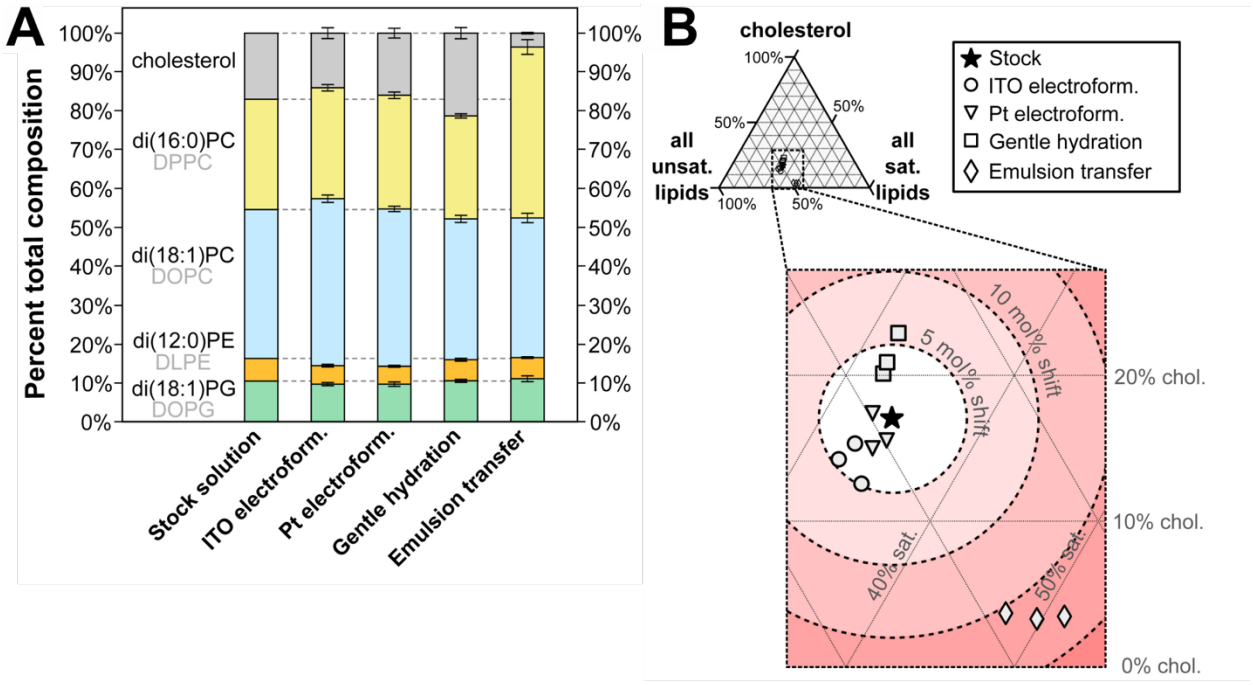

Figure 2.3. Lipid percentages in five-component vesicle solutions produced by different methods. **A)** Percent of each lipid in a five-component stock solution and averages from three independent vesicle solutions made from the stock solution by each technique. Error bars above each section of the bar chart are standard deviations of the three independent experiments. Full data appear in Tables S2.1, S2.11, and S2.12. **B)** Lipid percentages for each independent experiment plotted on a pseudo-ternary diagram, where the three vertices represent cholesterol, the sum of the saturated lipids (di(16:0)PC and di(12:0)PE), and the sum of the unsaturated lipids (di(18:1)PC and di(18:1)PG).

Our result that electroformation and gentle hydration reproducibly create vesicles with similar mole fractions of cholesterol is consistent with reports that the maximum amount of cholesterol that can be incorporated into membranes is roughly equivalent for vesicles made by electroformation (between 65 and 70 mol% (44)), gentle hydration (61 mol% (68) or ≤ 63 mol% (41)), and a third method, rapid solvent exchange (66 ± 1 mol% (41)). Recent NanoSIMS data disagree, but have low reproducibility: between two independent experiments, the amount of cholesterol in GUVs made by electroformation was either ~1/4 or ~2/3 of that in GUVs made by gentle hydration (50).

Shifts in lipid compositions in Fig. 2.3 are largely due to different mole fractions of cholesterol in vesicles with respect to the master stock solution. In contrast, only small shifts of ~1 mol% occur in PE-lipid and PG-lipids (Fig. S2.11). These shifts are the same magnitude as sample-to-sample differences of independent experiments. The small shift in di(12:0)PE seems surprising in light of previous studies using lipid mixtures extracted from rabbit sarcoplasmic reticulum: PE-lipids were grossly over-represented in the lipids left behind on a glass substrate (33). The particular lipid we use, di(12:0)PE, may integrate better into vesicles than other PE lipids because it is in a liquid, lamellar phase (rather than a solid phase or an inverted hexagonal phase). In contrast, the small shift in the charged PG-lipid is not surprising, at least with respect to gentle hydration of samples with high fractions of PG-lipids. Blosser et al. found agreement between the mole fraction of diphytanoyl-PG-lipids in a stock solution and in vesicles that were made by gentle hydration, for molar ratios of > 66% (21). Similarly, for a lipid mixture with ≥ 4% charged PS-lipids, Angelova found no significant difference in the mole fractions of the charged and uncharged lipids between a vesicle solution made by gentle hydration and a lipid film left behind on a glass surface (33).

How will the minor shifts in lipid ratios we observe in Fig. 2.3 impact how the biophysics community interprets data from GUVs? It depends on how experiments are designed. Broad conclusions derived from experiments that increment stock lipid compositions by ~5 mol% will likely apply equally well to vesicles electroformed on ITO slides or on platinum electrodes, and may slightly differ when applied to vesicles made by gentle hydration. In contrast, detailed conclusions that depend on incrementing lipid compositions by only ~1 mol% will likely apply only to vesicles made by a single method and will likely be affected by sample-to-sample differences. More detailed conclusions are difficult to extract from the data in Fig. 2.3 because only the percentages of the lipids (rather than their absolute values) are relevant. For example, an increase in the ratio of cholesterol to phospholipids could be due to an absolute increase in cholesterol, an absolute decrease in phospholipids, or both. Similarly, it is difficult to speculate whether our results would hold for every implementation of these techniques (e.g., with different solutions).

iii. Emulsion transfer results in too little cholesterol in vesicles.

The emulsion transfer method we used creates large shifts in lipid compositions of vesicle solutions made from five-component lipid mixtures (Fig. 2.3). The largest of these shifts is that the emulsion transfer method incorporated 80% less cholesterol than expected from the master stock solution. This result is consistent with previous reports of severe reduction in cholesterol for vesicle membranes made by emulsion techniques such as cDICE (< 1% of the expected cholesterol (46), double-layer cDICE (25-35% of the expected cholesterol (48)), and emulsion phase transfer (28-50% of the expected cholesterol (47)), as discussed in (46)). The problem likely arises because cholesterol lacks a large polar headgroup to drive it out of bulk oil, toward an interface with water. The problem can be mitigated, but not eliminated, by switching from heavy (46) to light mineral oil or by adding higher levels of cholesterol to the oil than the target level desired in membranes (47). Given that the choice of oil impacts cholesterol incorporation into vesicles, the exact values we measure apply only to one way of implementing the technique.

iv. Emulsion transfer exhibits large, chain-dependent shifts in PC-lipids.

The emulsion transfer method we used vastly skews the ratio of the PC-lipids for five-component lipid mixtures. Specifically, di(16:0)PC is over-represented by a factor of ~1.5 in the vesicle solution compared to the master stock solution (Fig. 2.3), an absolute increase from ~30% to ~45%. The effect is so large that nearly all loss of cholesterol in emulsion transfer vesicles appears to be counteracted by a gain in one of the phospholipids, di(16:0)PC. For comparison, the other PC-lipid, di(18:1)PC, decreases by only ~2 mol%. To our knowledge, shifts in phospholipid compositions this large have not previously been measured in emulsion transfer vesicles. Shifts in the relative amounts of PC-lipids in vesicle solutions made by other techniques (ITO electroformation, Pt wire electroformation, and gentle hydration) are minor. The largest of these is an increase of ~5 mol% for di(18:1)PC by ITO electroformation (Fig. 2.3A). Other shifts in PC-lipids are on the order of 2 mol%, consistent with the scatter from independent trials in Fig. 2.3B. Similarly, shifts in PE-lipid and PG-lipid are on the order of sample-to-sample variations (Fig. S2.11).

v. Binary vesicles show shifts in lipid ratios due to unsaturation and cholesterol content.

Two structural characteristics of PC lipids, their chain length and their unsaturation, could have caused di(16:0)PC to be grossly over-represented relative to di(18:1)PC in vesicles made by our emulsion transfer method. Likewise, these characteristics could have contributed to the small shifts in PC-lipids in vesicle solutions made by other techniques. To determine which characteristics cause major shifts in lipid ratios, we designed three sets of experiments using binary mixtures of lipids. The first set probes lipid unsaturation. The second probes lipid chain length. The third probes PC-lipids vs. sterol content. Vesicles made by gentle hydration required a small fraction of charged lipid (≤ 5 mol% di(18:1)PG).

The first set of binary experiments reveals that all methods except for emulsion transfer faithfully incorporate lipids from the stock solution (~50%:50% di(16:0)PC/di(16:1)PC) into vesicle solutions, within sample-to-sample variation.

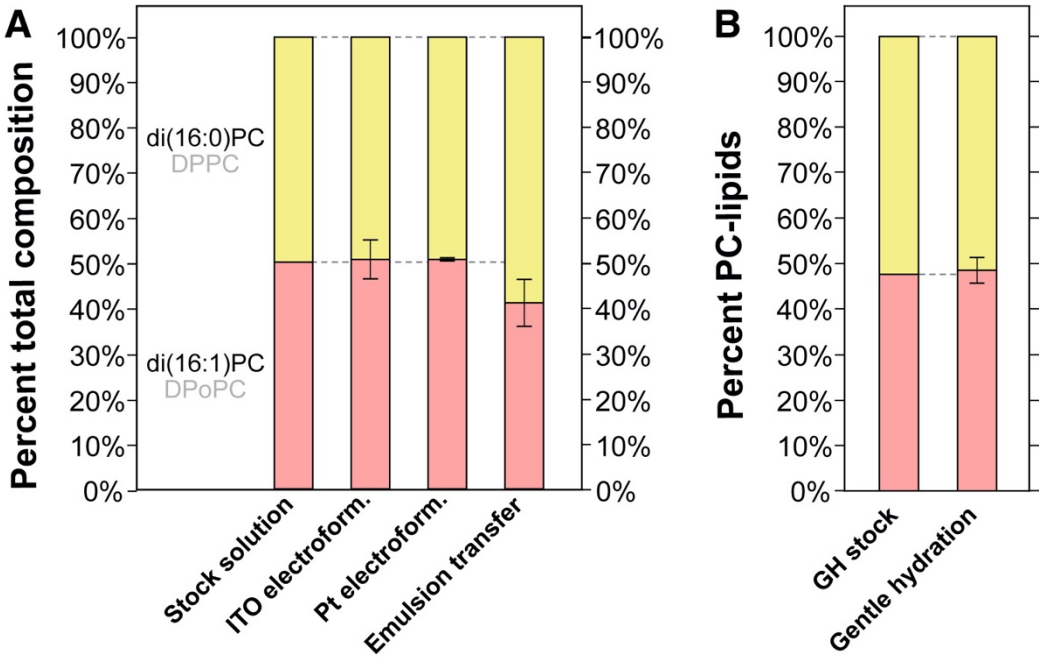

Figure 2.4. Percent of saturated and unsaturated lipids in binary vesicle solutions produced by different methods. A) Percent of di(16:0)PC and di(16:1)PC in a stock solution and in averages from three independent vesicle solutions of electroformation and emulsion transfer techniques made from the stock. Error bars above each section of the bar chart are standard deviations of the three independent experiments. Full data appear in Tables S2.2, S2.3, and S2.13. **B)** Percent of di(16:0)PC and di(16:1)PC in the gentle hydration (GH) stock solution and averages from three independent gentle hydration vesicle solutions. This stock also contained charged lipids (≤ 5 mol% di(18:1)PG, see Fig. S2.16A).

In contrast, saturated lipid is overrepresented in our emulsion technique, across two sets of experiments (Figs. 2.4 and S2.15). This overrepresentation of saturated lipid by a factor of ~1.2 cannot be due to known, favorable interactions between saturated lipids and cholesterol because the binary solution contains no cholesterol (69). Given that sample-to-sample lipid ratios in the five-component vesicle solutions in Fig. 2.3 were within ± 2 mol%, we expect ratios in the binary mixtures (which have higher overall percentages) to be within ~4 mol%, which generally holds true. Small sample sizes of $n = 3$ contribute to variations in uncertainties; uncertainties of ± 1 mol% are observed in Fig. S2.15A, and uncertainties of ± 5 mol% are observed in Fig. 2.4A, for the same lipid composition and method. Representative micrographs of vesicles appear in Fig. S2.12.

The second set of binary experiments investigates the chain length of unsaturated PC-lipids (di(16:1)PC and di(18:1)PC; Fig. 2.5). Two methods (ITO electroformation and gentle hydration) faithfully incorporate the same ratio of these lipids from the stock solution.

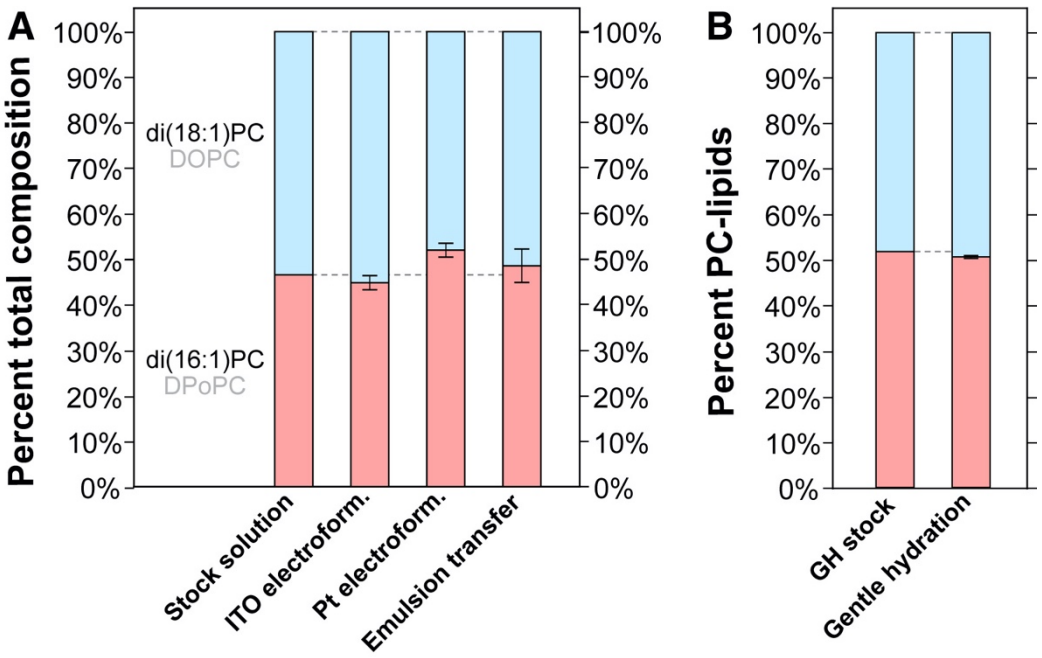

Figure 2.5. Percent of shorter and longer chained PC-lipids in binary vesicle solutions produced by different methods. A) Percent of di(16:1)PC and di(18:1)PC in a stock solution and averages from three independent vesicle solutions of electroformation and emulsion transfer techniques made from the stock. Error bars above each section of the bar chart are standard deviations of the three independent experiments. Full data appear in Tables S2.4, S2.5, and S2.14. **B)** Percent of di(16:1)PC and di(18:1)PC in the gentle hydration (GH) stock solution and averages from three independent gentle hydration vesicle solutions. This stock also contained charged lipids (≤ 5 mol% di(18:1)PG, see Fig. S2.16B).

Pt wire electroformation incorporates slightly more long-chain lipid (a shift of ~5 mol%). No conclusion can be reached from emulsion transfer experiments except that uncertainties are large, resulting in an apparent decrease of ~2 mol% in long-chain lipid in one set of experiments (Fig. 2.5), contradicted by an apparent increase of ~6 mol% in an independent set of experiments (Fig. S2.15), with overlapping uncertainties. The large uncertainty is consistent with a lower yield of vesicles for this binary mixture by our emulsion transfer method, compared to other methods. Representative micrographs of vesicles appear in Fig. S2.13.

The third set of binary experiments (Fig. 2.6) investigates the mole fraction of cholesterol with respect to a PC-lipid (di(18:1)PC). Shifts in the lipid ratios mirror the trends in the five-component vesicles in Fig. 2.3. For example, emulsion transfer again incorporates 80% less than the expected amount of cholesterol. Gentle hydration again incorporates 20% more than expected.

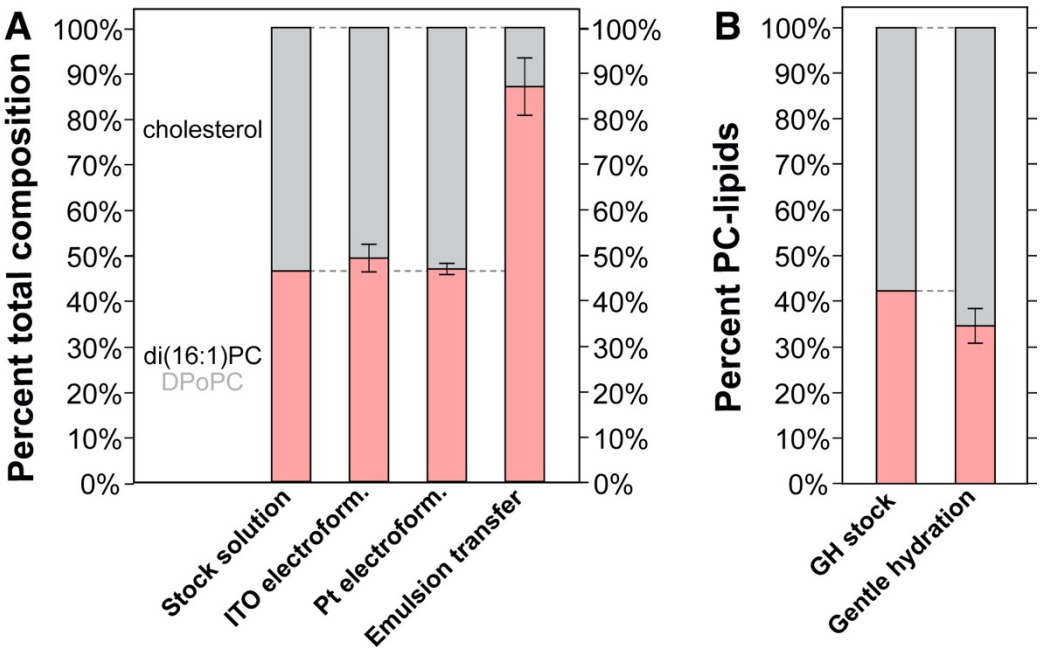

Figure 2.6. Percent of unsaturated PC-lipid and cholesterol in binary vesicle solutions produced by different methods. A) Percent of di(16:1)PC and cholesterol in a stock solution and averages from three independent vesicle solutions of electroformation and emulsion transfer techniques made from the stock. Error bars above each section of the bar chart are standard deviations of the three independent experiments. Full data appear in Tables S2.6, S2.7, S2.15, and S2.16. **B)** Percent of di(16:1)PC and cholesterol in the gentle hydration (GH) stock solution and averages from three independent gentle hydration vesicle solutions. This stock also contained charged lipids (≤ 5 mol% di(18:1)PG, see Fig. S2.16C).

This is surprising in light of recent results that find that cholesterol is, on average, slightly under-incorporated (about 10% less than expected) into vesicles of POPC (16:0/18:1PC) via a related gentle hydration technique (70). The remaining methods (ITO electroformation and Pt wire electroformation) again agree with the stock solution, within uncertainty. For all experiments, initial stock solutions were chosen to contain < 60 mol% cholesterol, below the maximum possible concentration of cholesterol in membranes (41, 44, 68). We chose to mix cholesterol with an unsaturated lipid because the mixture produced vesicles of high quality (Fig. S2.14), whereas the yield of vesicles comprised of cholesterol and saturated lipid (di(16:0)PC) were too low to accurately analyze.

vi. Extrusion of vesicles results in lower cholesterol fractions.

Some powerful techniques of assessing membrane phase behavior use giant vesicles whereas others (e.g., electron microscopy and neutron scattering (71–73) require ~100 nm vesicles, produced by extruding vesicles through polycarbonate filters. Here, we conducted a new series of experiments to compare ratios of lipids in solutions of giant vesicles generated by gentle hydration with ratios from the same solutions after extrusion. Corresponding micrographs are in Fig. S2.6.

We find systematic decreases in cholesterol due to extrusion (Fig. 2.7). In terms of absolute numbers, these shifts are not huge, a decrease of 5.0 ± 3.3 mol% cholesterol, where the uncertainty is the standard deviation for three independent experiments. In terms of the total percent of cholesterol, the shifts are significant; ~20% of cholesterol is lost upon extrusion of vesicles made by gentle hydration. This value falls in the middle of ranges previously reported: no loss of cholesterol was observed from some membranes (ternary mixtures of 2:1:3 PC-lipids/eggPC/cholesterol, binary mixtures of 33% cholesterol with di(18:1)PC or di(14:0)PC, or binary mixtures of 30/70, 40/60, or 50/50 cholesterol with 16:0/18:1PC), whereas a loss of ~1/3 to ~1/2 of cholesterol was observed from other membranes (for binary mixtures of 33% cholesterol with 16:0/18:1PC, di(16:0)PC, or di(20:4)PC (45, 70). In other words, no clear correlation seems to exist between lipid unsaturation and a loss of cholesterol from vesicles upon extrusion.

For any mixture of lipids, there is a potential for extruded vesicles to have compositions that differ from the stock solutions given that some common methods for gentle hydration of GUVs leave > 50% of all lipids behind in the reservoir, and extrusion can incur a further loss of ~20% of lipids (70, 74).

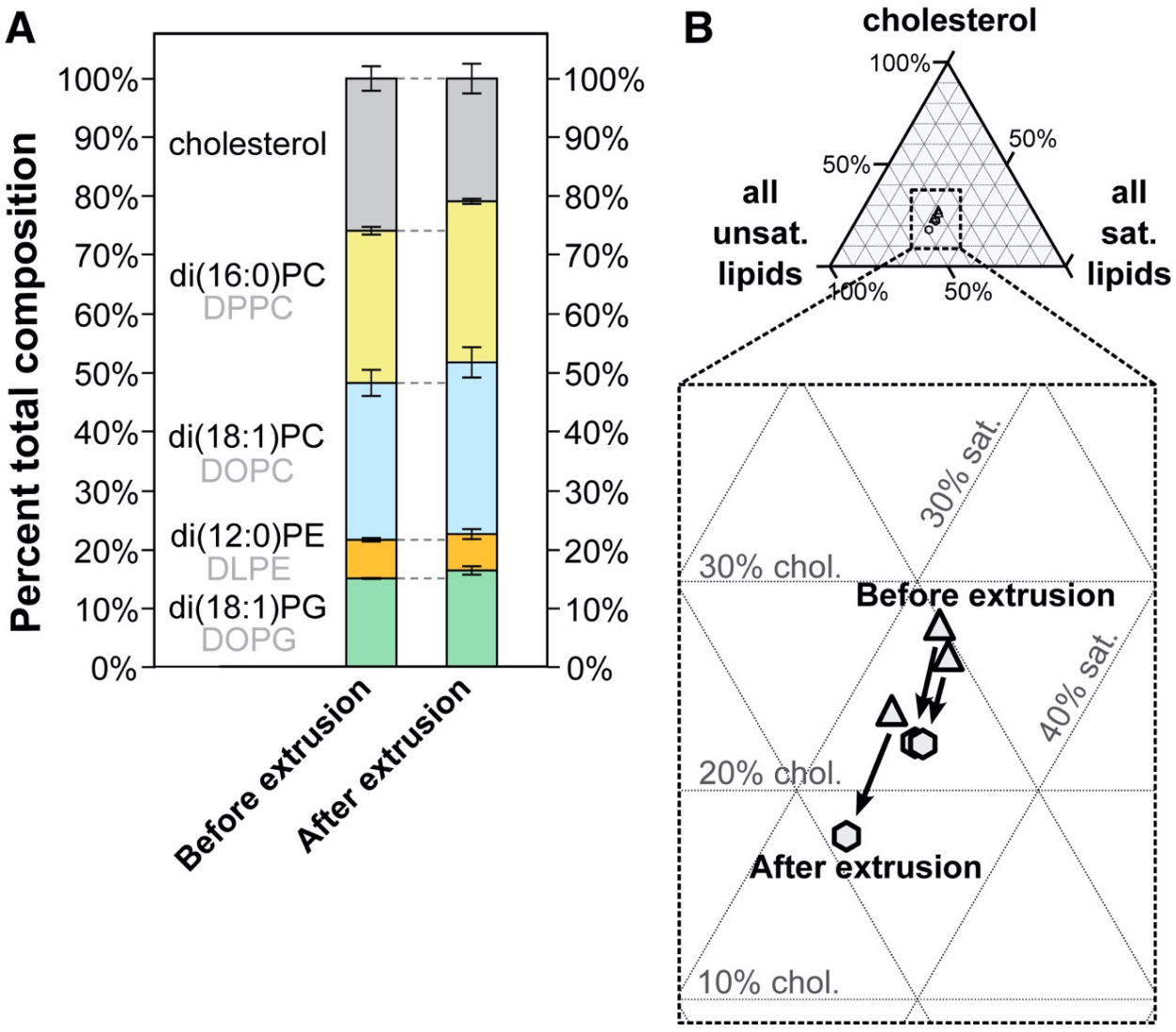

Figure 2.7. Extrusion of giant vesicles decreases their cholesterol content. A) Percentage of all five lipids in vesicle solutions made via gentle hydration, before and after extrusion through a 0.1 μM filter. Values are averages, and error bars above each section of the bar chart are standard deviations of three independent experiments. **B)** Mole fractions of each experiment plotted on a pseudo-ternary diagram, before and after extrusion. The three vertices correspond to cholesterol, the sum of the saturated lipids (di(16:0)PC and di(12:0)PE), and the sum of the unsaturated lipids (di(18:1)PC and di(18:1)PG). Full data appear in Tables S2.8, S2.17, and S2.18. These gentle hydration samples were prepared and measured separately from samples comparing the four other methods.

We find that the decrease in cholesterol upon extrusion is offset by smaller increases in PC-lipids (1.4 ± 0.7 mol% for di(16:0)PC, and 1.5 ± 0.8 mol% for di(18:1)PC, respectively). Shifts in PE- and PG-lipids are insignificant (0.4 ± 0.9 mol% for di(12:0)PE and 2.5 ± 3.4 mol% for di(18:1)PG). As before, one main conclusion is that experiments that report results at high precision (e.g., 1 mol%) will be sensitive to how vesicles are made and to sample-to-sample differences.

vii. Caveats.

Several experimental caveats arise. The first is that although sedimentation increases the concentration of vesicles in solutions, it does not completely eliminate aggregates. Another caveat is that the steps within each method of making vesicles can skew the ratio of lipids in membranes. Some variations on these methods have already been explored. For example, it was already known that varying the type of oil in emulsion transfer methods results in wide ranges of cholesterol content in vesicles (46–48, 75). Similarly, it was known that accurate membrane phase transitions (and presumably lipid compositions) relied on electroformation being performed at a temperature well above the highest melting temperature of any lipid in the sample using lipid films of sufficient thickness (7, 12).

However, many other variations on each method remain unexplored. For example, gentle hydration could have been conducted in salt solutions (rather than in sugar), or from lipid films deposited on surfaces of tracing paper (76) or polymer-coated substrates (77, 78) (rather than on bare glass). Similarly, gentle hydration of lipid films could have been achieved for different lengths of time using lipids in different ratios (70), followed by either shaking or vortexing (30) (rather than in a static solution) using different types of vortexers (70), and the subsequent multilamellar vesicles could have been made smaller through freeze/thaw cycles or sonication (rather than extrusion) (70, 71, 79). Details of each technique vary from laboratory to laboratory, and it is unclear how these details influence the ratio of lipids in membranes.

Similar caveats apply to the choice of stock solutions. Many lipid mixtures are relevant, and each may produce different shifts in lipid ratios, especially if interdependencies between lipids affect their incorporation into vesicles. These interdependencies will be challenging to assess when lipid stocks contain small fractions of some lipids (like the PE-and PG-lipids in our five-component

sample) because correspondingly small shifts in their absolute mole fractions will be observed, even if percent changes are high.

Although we found minor shifts in lipid fractions for most methods, it is worth bearing in mind that small shifts can result in big changes in membrane behavior. For example, if a membrane lies near a phase boundary, a small shift in its lipid composition can lead a previously uniform membrane to demix into coexisting phases, or a liquid membrane to turn into a solid phase. For researchers who are comparing vesicles made by different methods, a best practice is to choose a ratio of lipids that lies in the middle of the preferred phase region.

2.5 Conclusions.

In summary, the five methods we used to make vesicles result in a range of deviations in lipid ratio relative to five-component and binary stock solutions. Electroformation, whether on an ITO slide or on platinum wires, results in the smallest shifts (≤ 5 mol%). Researchers will find the magnitudes of these shifts to be either comfortingly small or alarmingly large, depending on how they design their experiments. For example, experiments that report concentrations incremented by only ~1 mol% will be highly sensitive to the choice of vesicle-making method and to sample-to-sample differences. On the other side of the spectrum, the largest shifts are observed with emulsion transfer. It was already known that emulsion transfer resulted in a wide range of low cholesterol fractions in vesicles (46–48, 75). In our experiments, ~80% less cholesterol was incorporated into vesicles than expected from the stock solution. A surprising result is that emulsion transfer also shifts the relative amount of saturated and unsaturated lipid; it incorporates more di(16:0)PC than expected relative to di(16:1)PC.

For the five-component stock, sample-to-sample variations for all methods were ~± 2 mol% for independent experiments. Again, researchers who rely on 1% precision will be sensitive to sample-to-sample variations, and others will find the reproducibility reassuring. As mole fractions increase for each lipid, some corresponding sample-to-sample variations increase concomitantly (as in binary vesicles made by emulsion transfer), whereas others remained low, on the order of ± 2 mol%.

The shifts in lipid compositions that we measured are context dependent. That context can include the types of lipids in the system (as explored in the binary mixtures in Figs. 2.4-2.6 and S2.15), the amount of lipid, the type of solvents, the temperature, and differences in experimental protocol. What should communities of researchers do when faced with so many potential variables? Of course, we should adhere to accepted best practices (e.g., electroforming with enough lipid and at high enough temperature) and we should report detailed descriptions of our methods. We can shift our mindset to think big rather than to think small. Armed with estimates of how lipid compositions might vary from lab to lab, we have a better sense of how to look for broad trends and new phenomena, and to celebrate when those trends are supported by other methods, even if the quantitative data vary subtly.

2.6 Acknowledgements.

We thank the staff at the UW Statistical Consulting Services for their expertise. Heidi M. J. Weakly was supported by the National Institute of General Medical Sciences of the National Institutes of Health under Award Number T32GM008268. This research was supported by National Science Foundation grant MCB-1925731 and MCB-2325819 to Sarah L. Keller and by National Institutes of Health grant R01HD092659 and R01 AI136979 to Libin Xu.

2.7 Supporting Materials.

i. Supporting Figures.

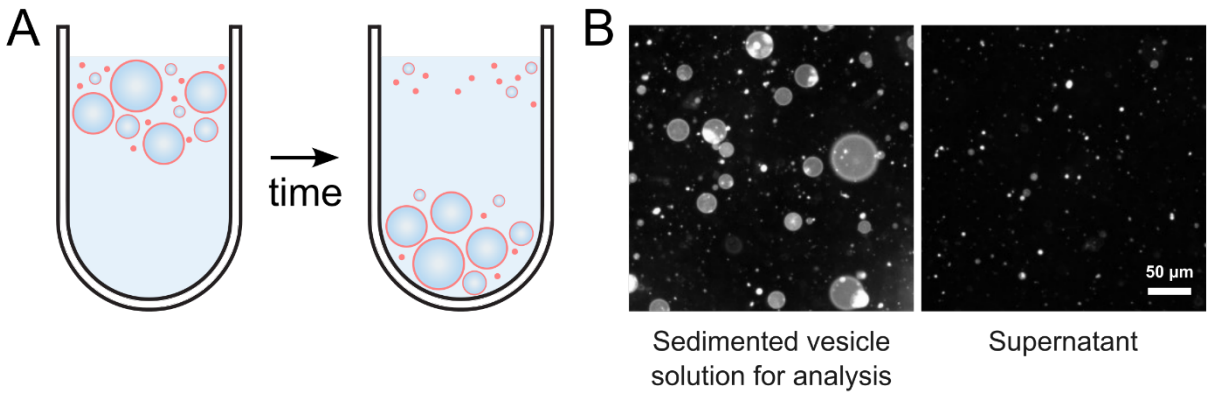

Figure S2.1. Sedimenting vesicles removes some lipid aggregates. A) Vesicles filled with a dense sucrose solution sink in an osmotically matched glucose solution. **B)** After sinking, large vesicles are observed only in the sedimented solution, and not in the supernatant. The sedimented solution still contains some lipid aggregates. The vesicles in these images were made by emulsion phase transfer. The low density of giant vesicles in the supernatant is representative of all techniques.

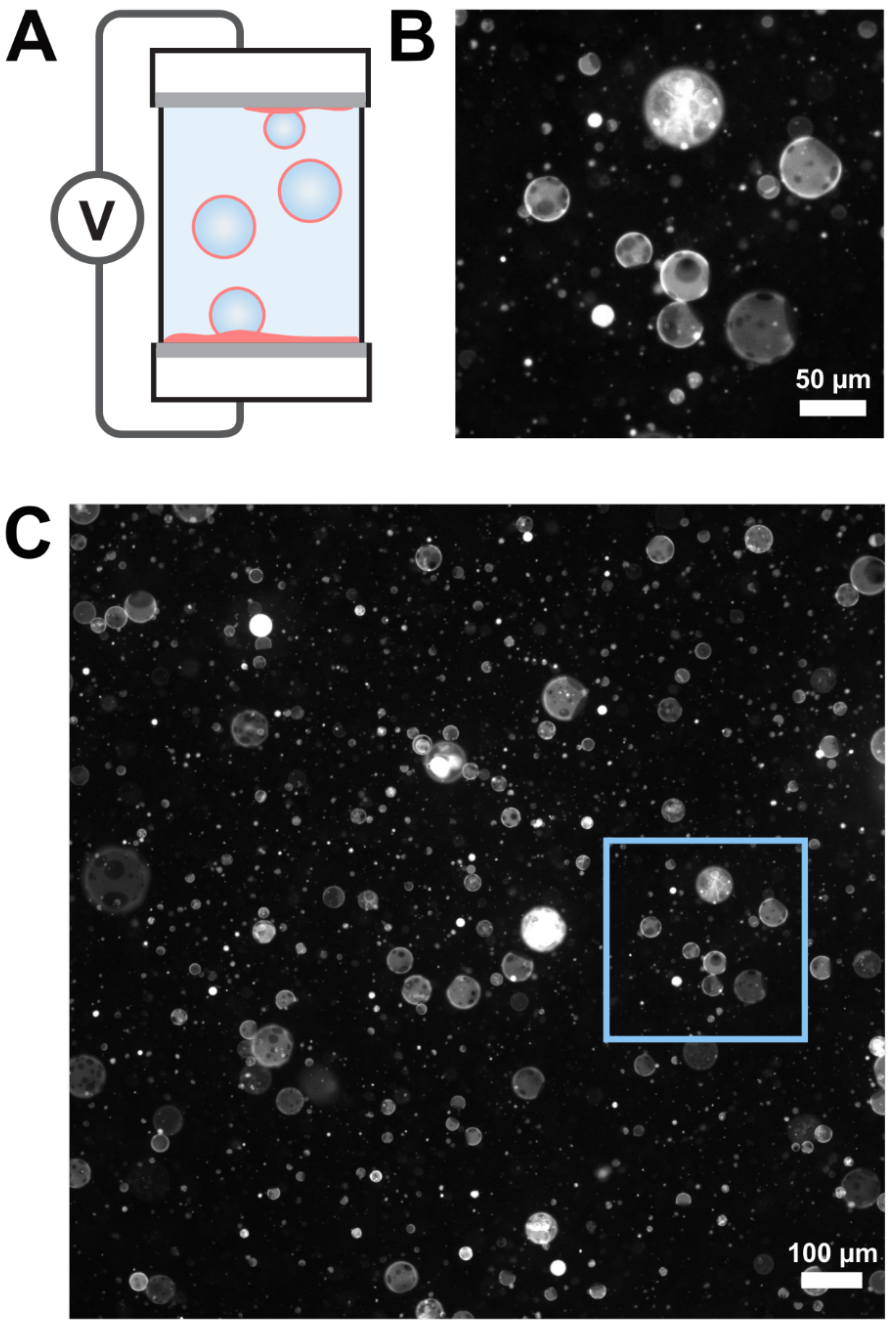

Figure S2.2. Representative fluorescence micrographs of vesicles made by electroformation on ITO-coated slides. A) Schematic of ITO electroformation. **B)** Close-up of vesicles in the blue box in panel C. **C)** Larger field of view of vesicles produced by electroformation on ITO slides. As expected, ITO electroformation produces the highest yield of giant, unilamellar vesicles (GUVs) of the four methods tested for producing these vesicles. Some multilamellar vesicles, some nested vesicles (large vesicles filled with smaller vesicles), and some bright, lipid aggregates are also produced.

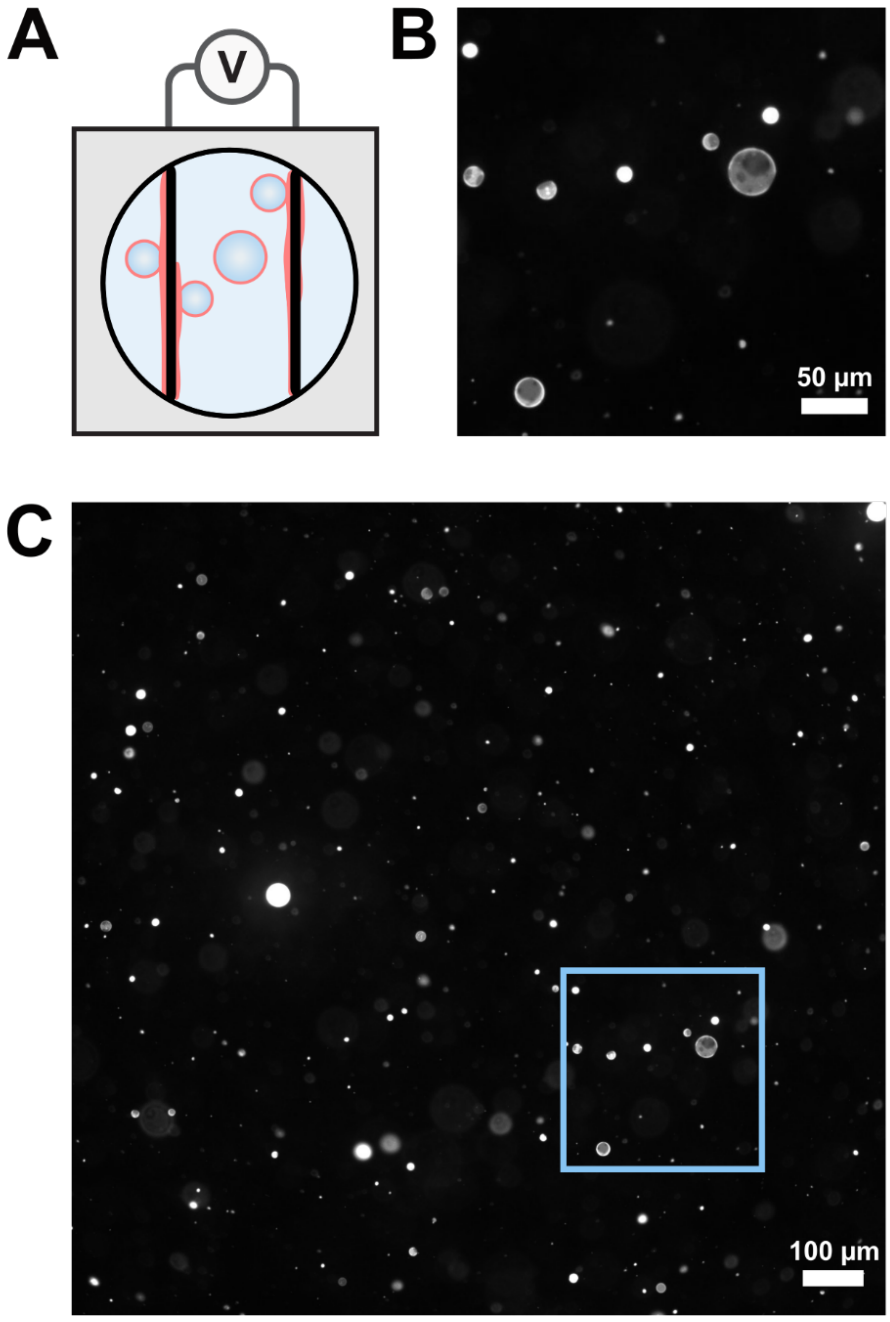

Figure S2.3. Representative fluorescence micrographs of vesicles made by electroformation on platinum wires. A) Schematic of Pt electroformation. **B)** Close-up of vesicles in the blue box in panel C. **C)** Larger field of view of vesicles produced by electroformation on Pt wires. The volume of stock solution used is low relative to the other methods and therefore produces a lower yield of vesicles at the same stock concentration.

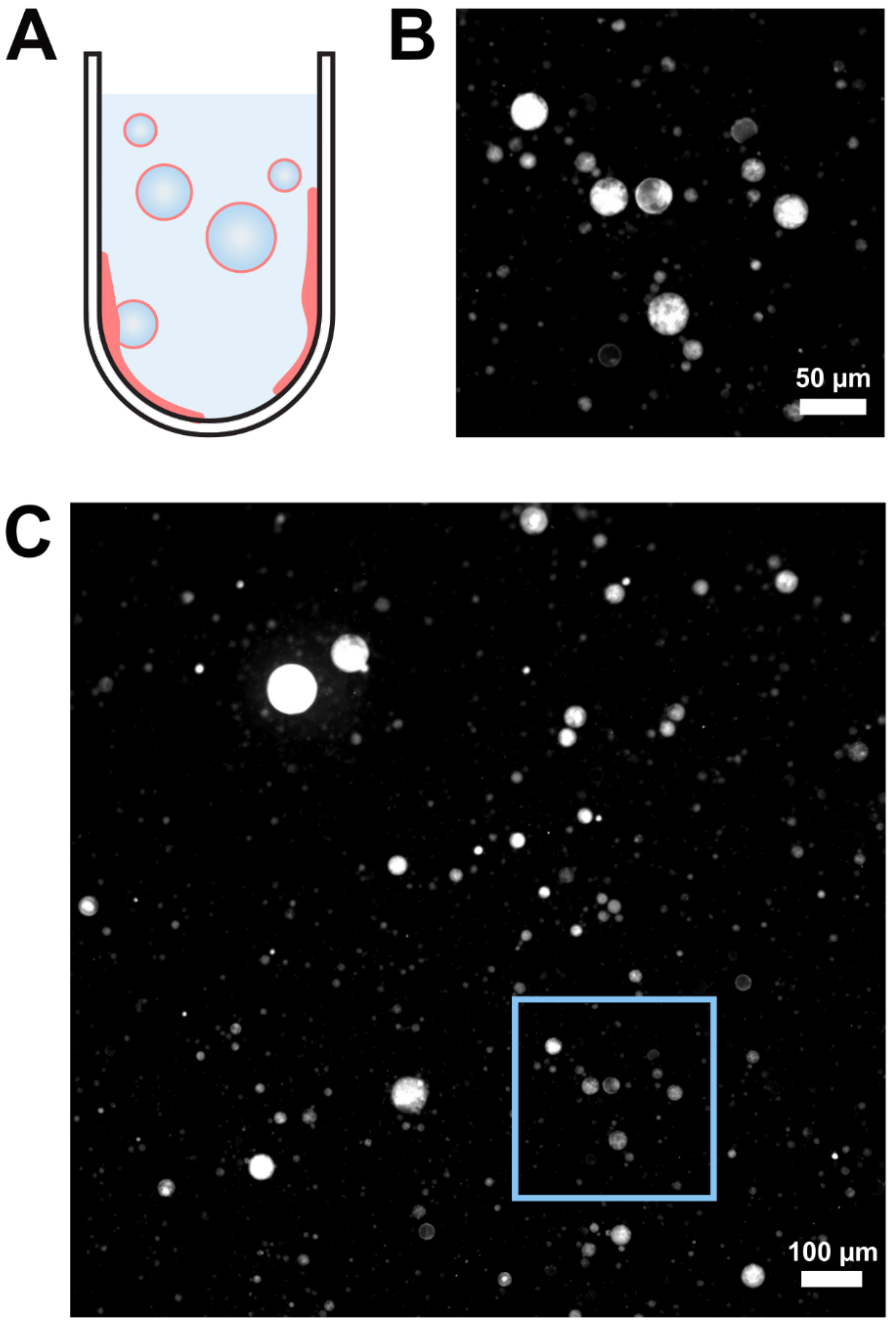

Figure S2.4. Representative fluorescence micrographs of vesicles made by gentle hydration for 24 h. A) Schematic of gentle hydration. **B)** Close-up of vesicles in the blue box in panel C. **C)** Larger field of view of vesicles produced by gentle hydration. As expected, the sample predominantly contains multilamellar vesicles and nested vesicles. When contrast is optimized for the bright, multi-layered vesicles, unilamellar vesicles in the same field of view can be too dim to be imaged.

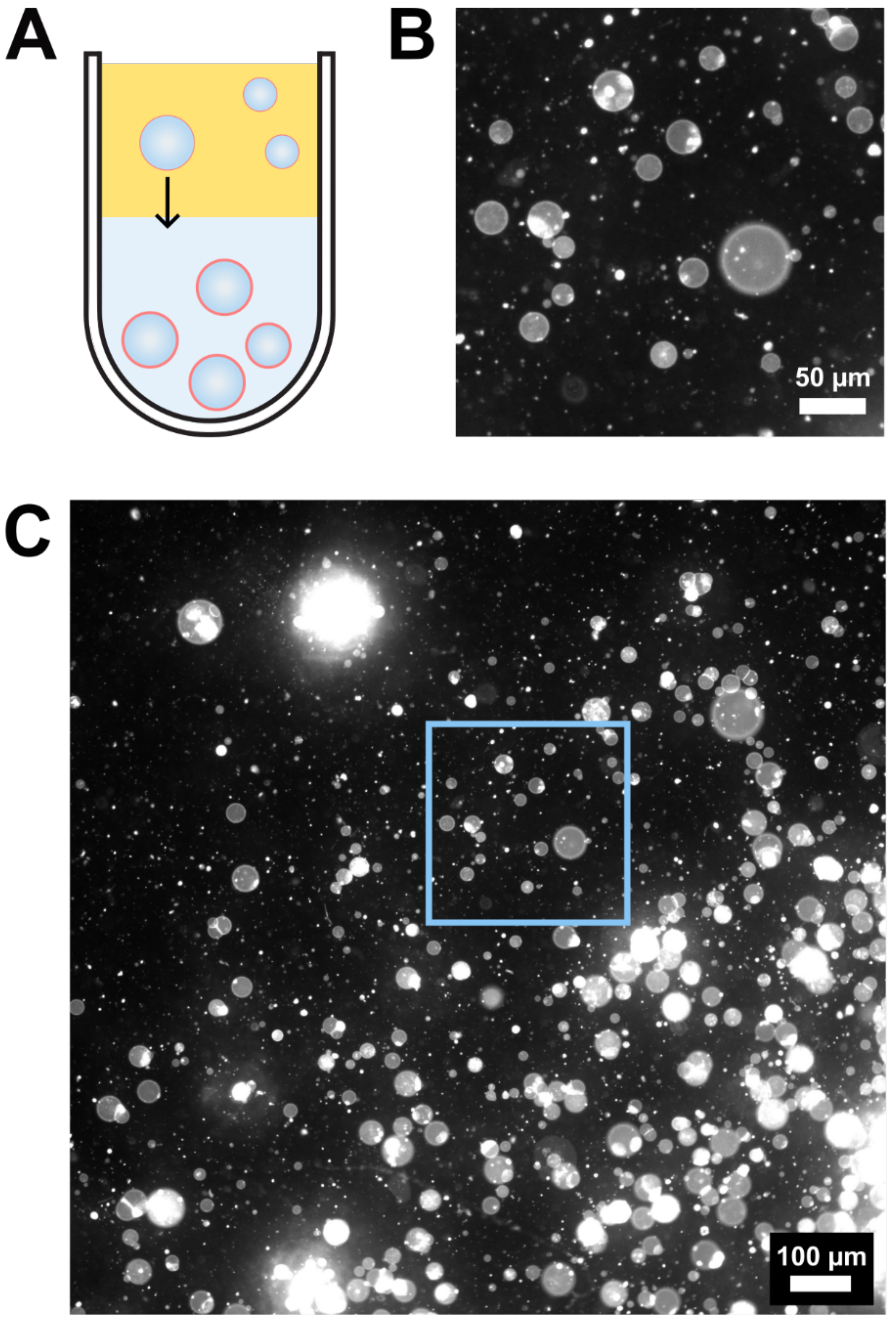

Figure S2.5. Representative fluorescence micrographs of vesicles made by emulsion phase transfer. A) Schematic of emulsion phase transfer. **B)** Close-up of vesicles in the blue box in panel C. **C)** Larger field of view of vesicles produced by emulsion phase transfer. The emulsion transfer method produces a high yield of giant unilamellar vesicles as well as defects including nested vesicles and lipid aggregates.

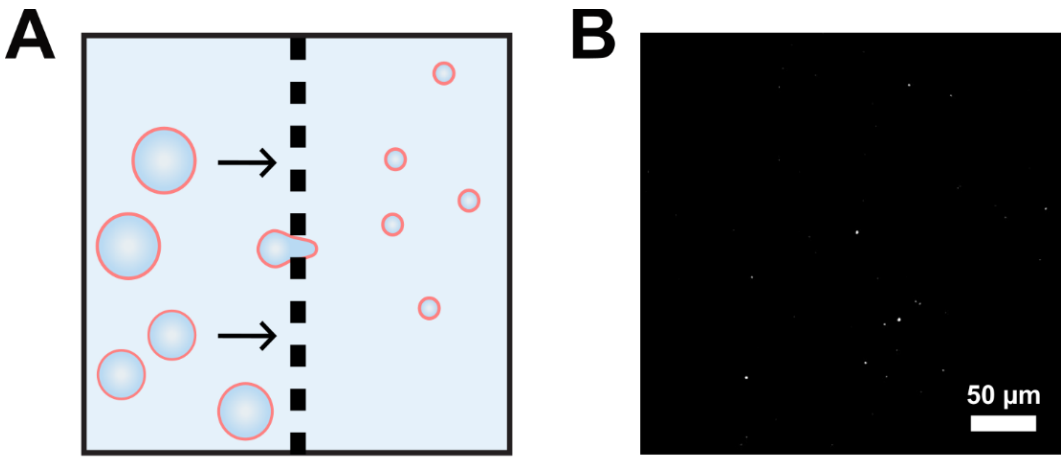

Figure S2.6. Vesicles after extrusion. A) Schematic of extrusion. **B)** Representative fluorescence micrograph of vesicles after extrusion through a filter with 100 nm diameter holes. As expected, most extruded vesicles are too small to be resolved with standard fluorescence microscopy techniques.

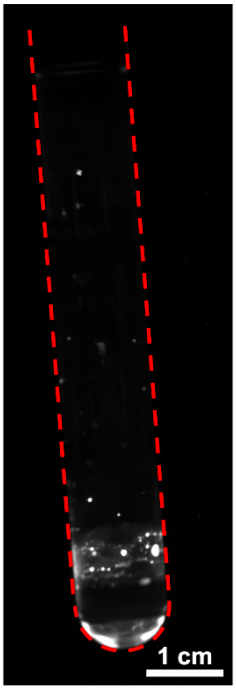

Figure S2.7. Residual lipid due to the gentle hydration technique, detected by fluorescence microscopy. Residual lipid left on the interior of a glass test tube is shown after a sample of vesicles made by gentle hydration was removed. A dashed red outline defines the edges of the test tube. The image was captured on an Amersham ImageQuant 800 (Cytiva) with a Cy3 (UV) filter.

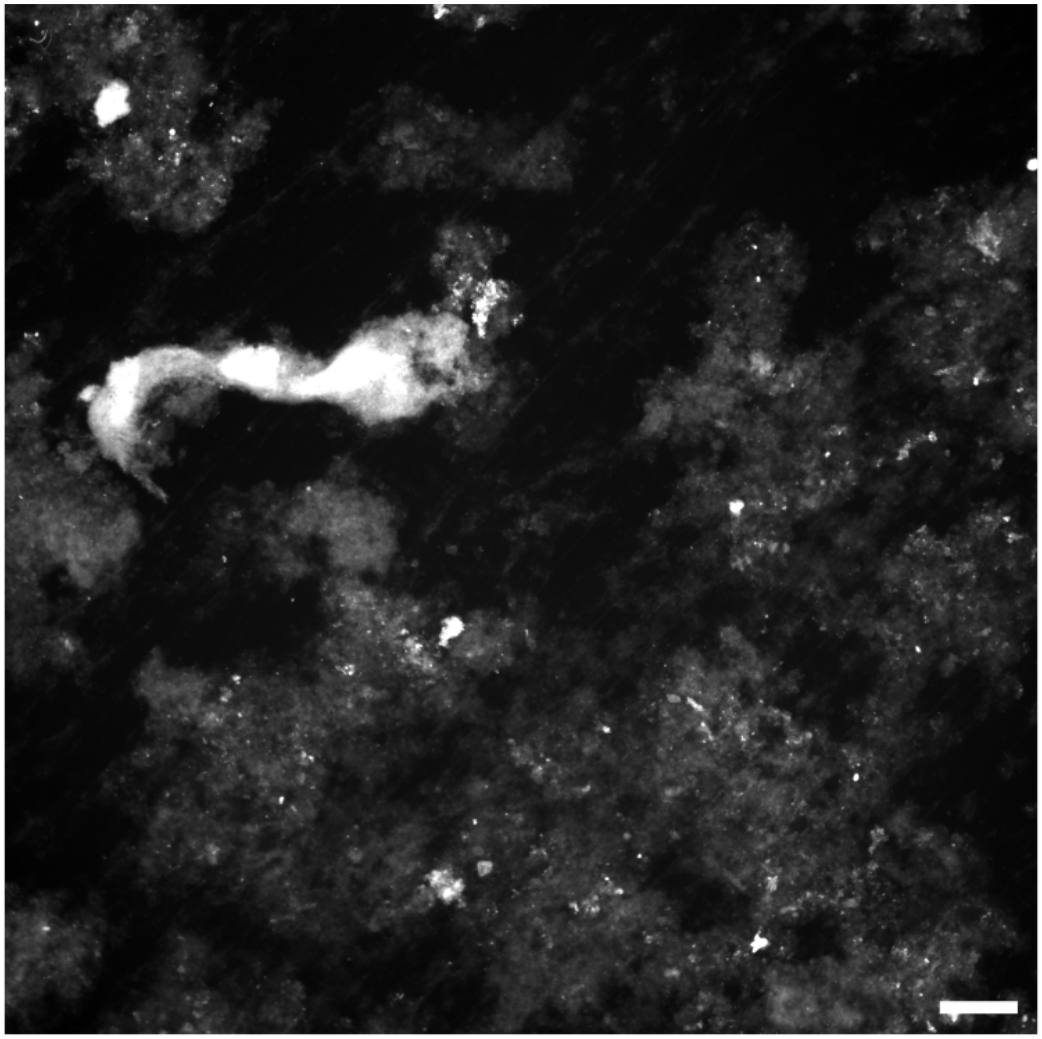

Figure S2.8. Residual lipid due to the ITO electroformation technique, detected by fluorescence microscopy. Residual lipid left on an ITO slide is shown after a sample of vesicles made by electroformation was removed. The image is representative of all experiments using electroformation on ITO slides. Scale bar: 500 μm.

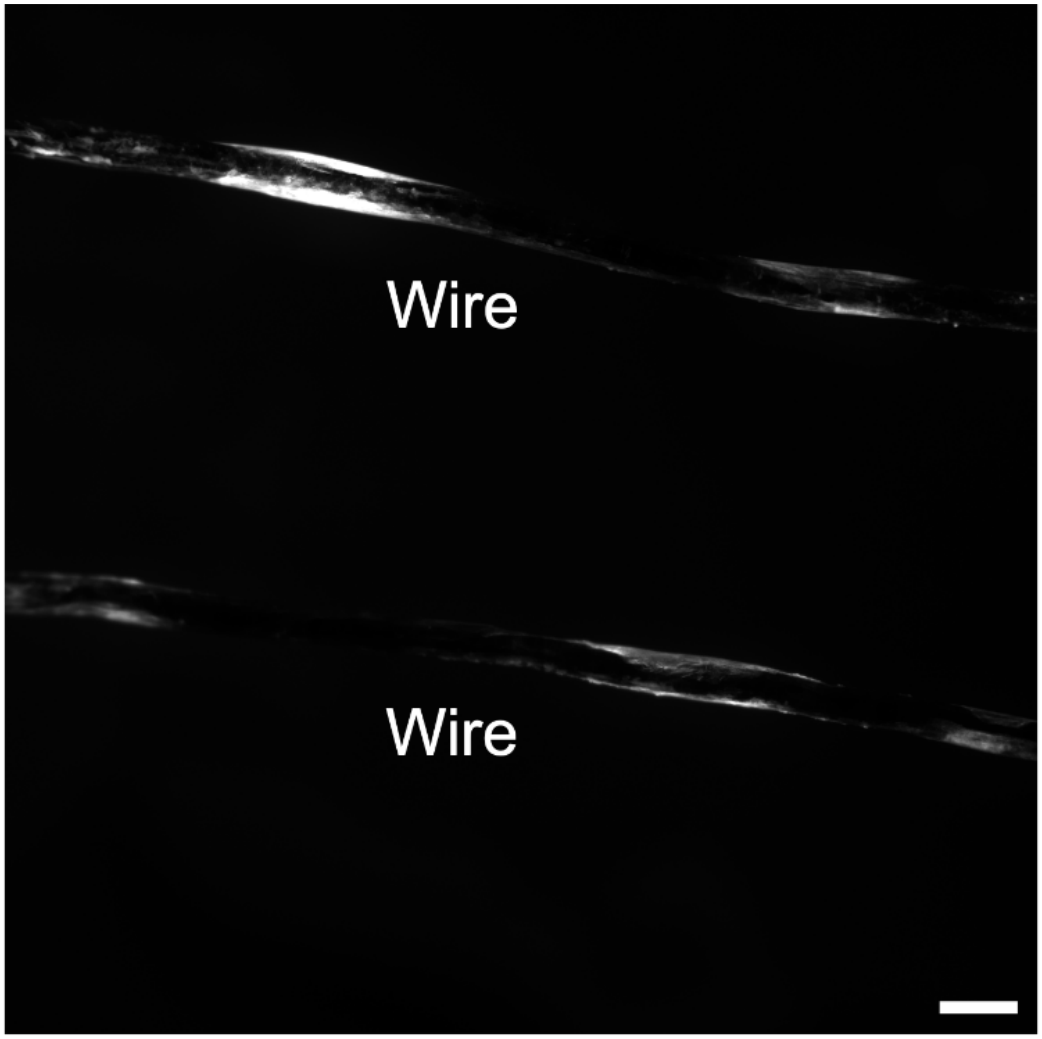

Figure S2.9. Residual lipid due to the Pt wire electroformation technique, detected by fluorescence microscopy. Residual lipid left on platinum wires is shown after a sample of vesicles made by electroformation was removed. The image is representative of all experiments using electroformation on Pt wires. Scale bar: 500μm.

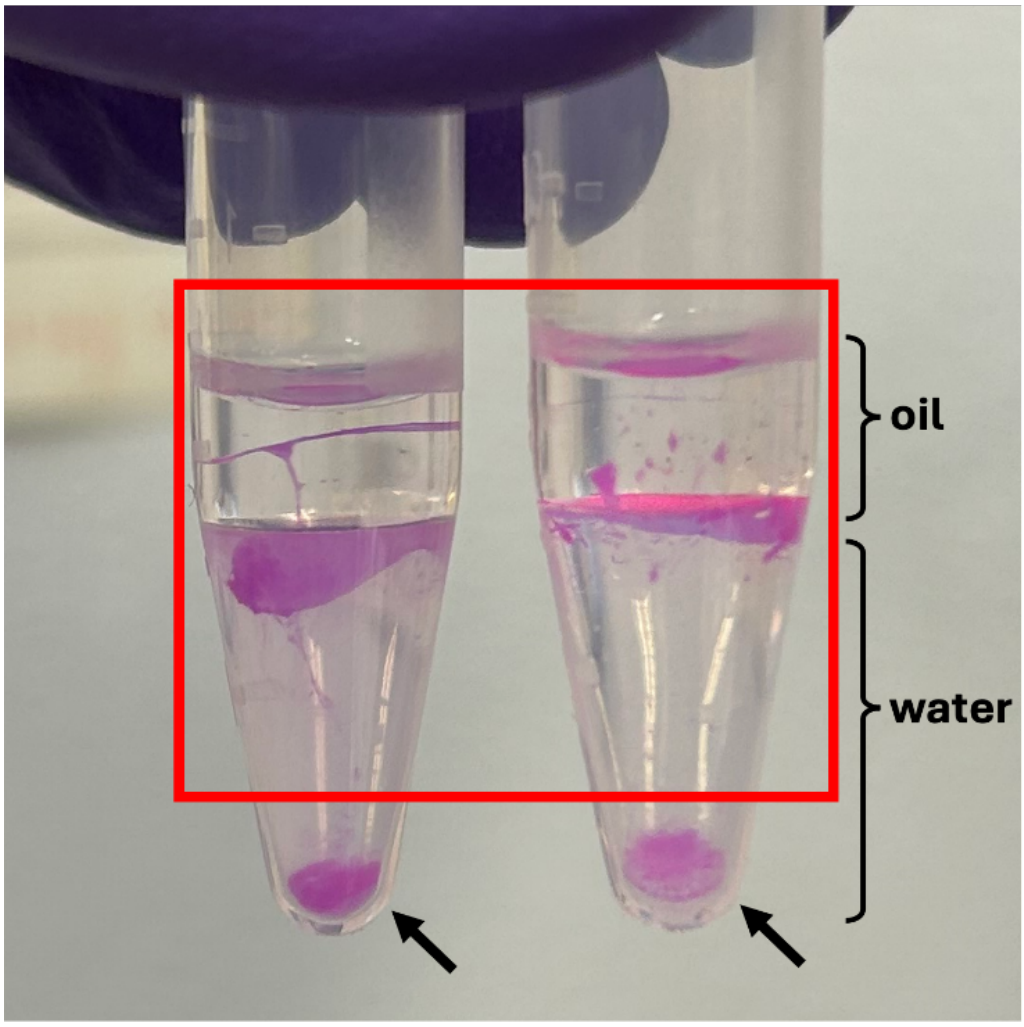

Figure S2.10. Residual lipid due to the emulsion transfer method, imaged in ambient light. Residual lipid left in oil and at the oil-water interface is shown after completing two emulsion transfer experiments. The images are representative of all experiments using emulsion transfer. The red box encloses the supernatant, which was removed before analysis by mass spectrometry. Most residual lipid is trapped at the interface between the water and oil. Black arrows indicate pellets of vesicles. These pellets were subsequently resuspended in 300 mM glucose solution, imaged, and analyzed as described in the methods.

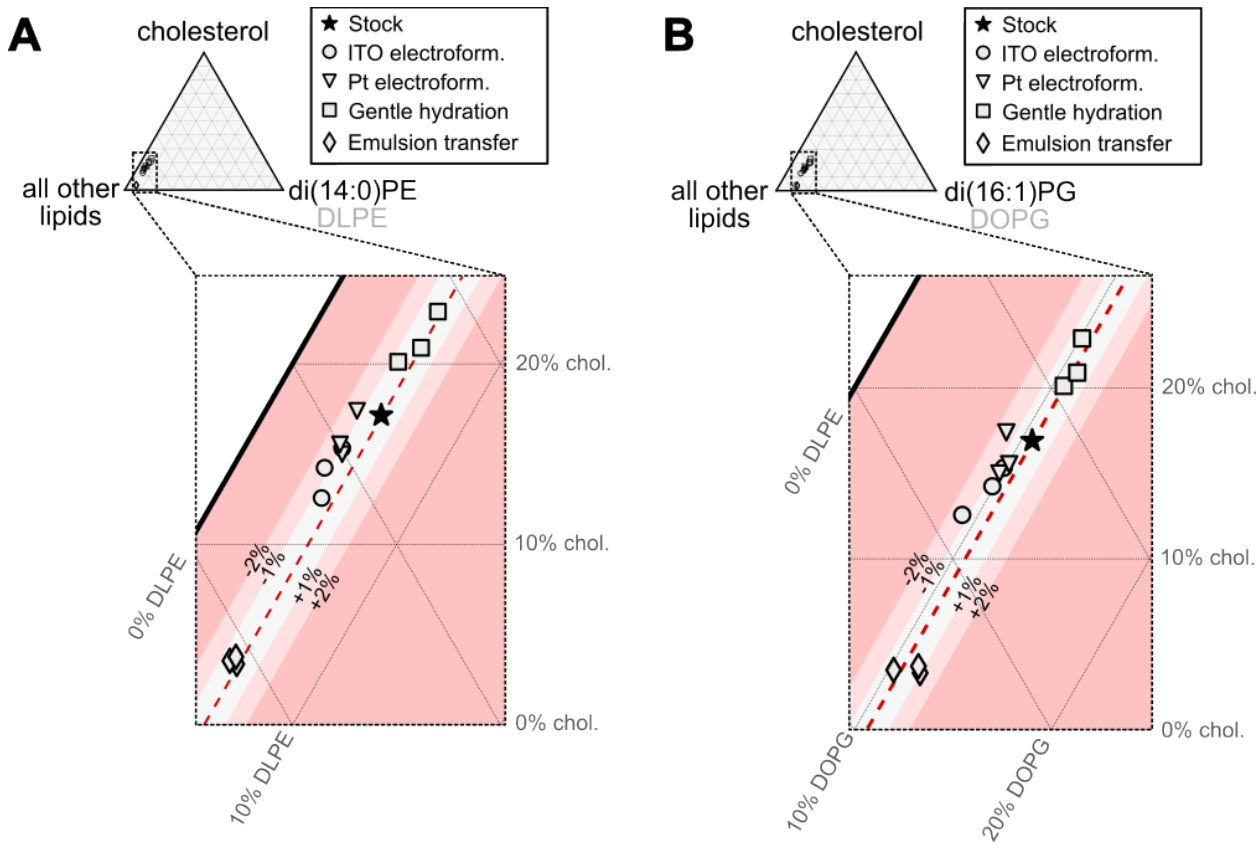

Figure S2.11. Lipid percentages in 5-component vesicle solutions produced by different methods, plotted as pseudo-ternary diagrams in which one vertex is di(12:0)PE (DLPE) or di(18:1)PG (DOPG). Vesicles were prepared by four methods: electroformation on ITO slides, electroformation on platinum wires, gentle hydration, and emulsion phase transfer. Three independent preparations and experiments were run for each method. **A)** Lipid percentages from each independent experiment are plotted on a pseudo-ternary diagram, where the three vertices represent di(12:0)PE, cholesterol, and the sum of all other lipids. **B)** Lipid percentages from each independent experiment are plotted on a pseudo-ternary diagram, where the three vertices represent di(18:1)PE, cholesterol, and the sum of all other lipids. In both panels, the lipid composition measured for the stock solution is shown as a star. Deviations from the master stock solution in increments of 1% and 2% of DLPE or DOPG are shown by shaded bands.

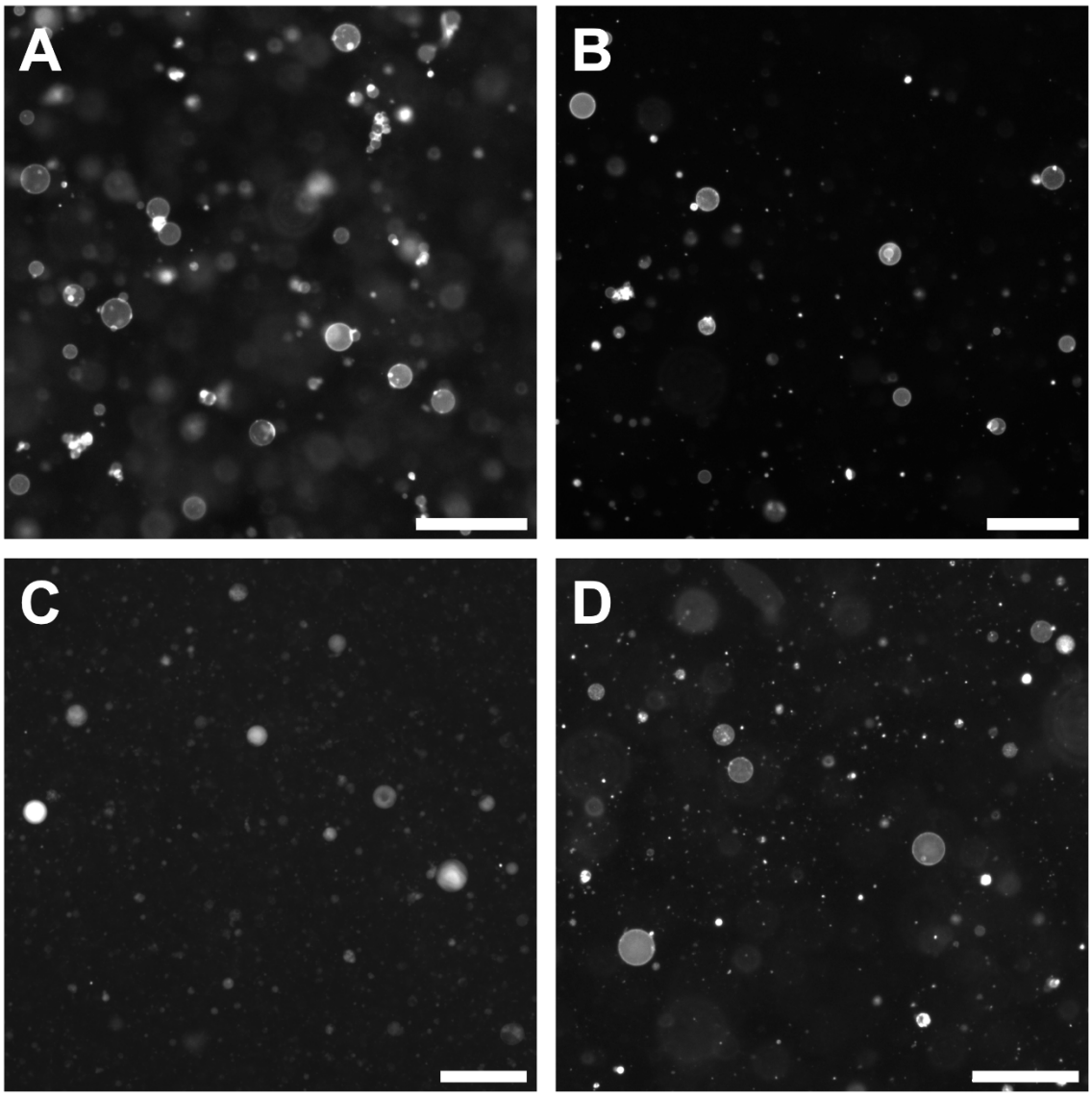

Figure S2.12. Representative fluorescence micrographs of solutions of vesicles comprised of binary mixtures of saturated lipid (di(16:0)PC) and unsaturated lipid (di(16:1)PC). Vesicles were formed by **A)** ITO electroformation, **B)** Pt wire electroformation, **C)** gentle hydration, and **D)** emulsion transfer. For this lipid composition, most giant unilamellar vesicles have some type of defect such as adhered vesicles, nested vesicles, or bright aggregates (Panels A, B, and D). Scale bars: 100 μm.

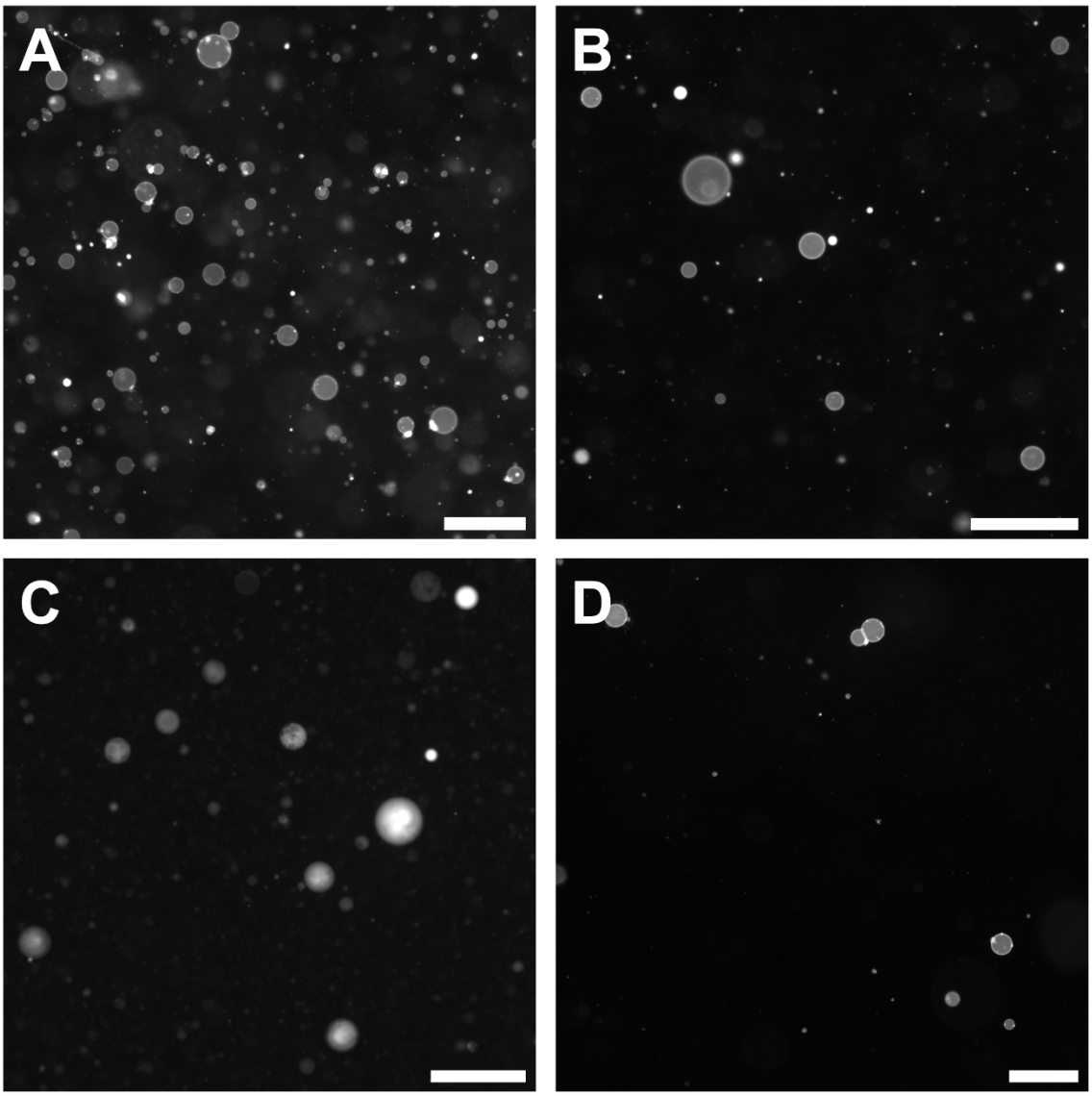

Figure S2.13. Representative fluorescence micrographs of solutions of vesicles comprised of binary mixtures of unsaturated lipids with shorter chains (di(16:1)PC and longer chains (di(18:1)PC). Vesicles were formed by **A)** ITO electroformation, **B)** Pt wire electroformation, **C)** gentle hydration, and **D)** emulsion transfer. For this mixture of lipids, emulsion transfer had lower vesicle yields compared to other techniques. Scale bars: 100 μm.

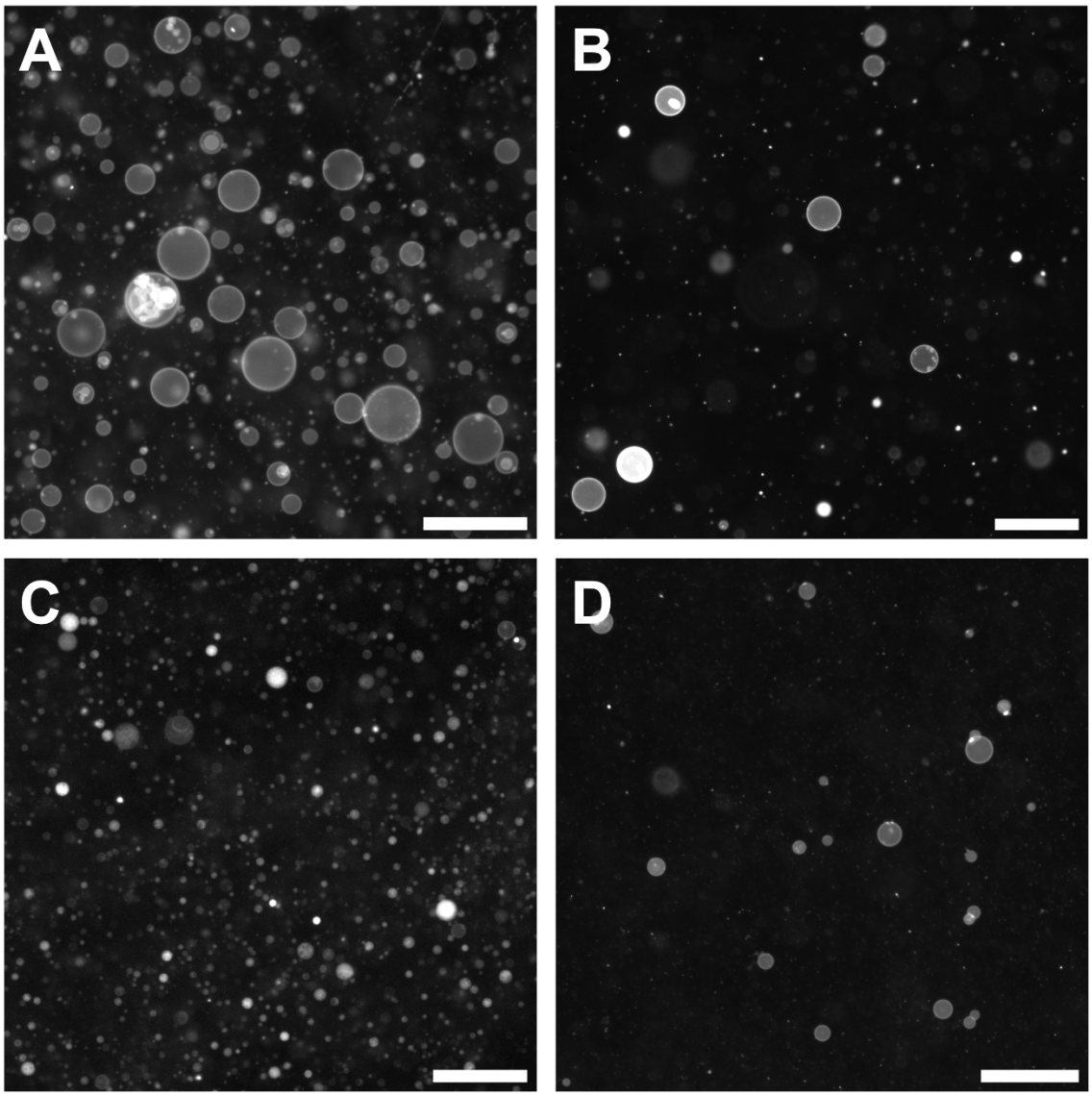

Figure S2.14. Representative fluorescence micrographs of solutions of vesicles comprised of binary mixtures of an unsaturated lipid (di(16:1)PC) and cholesterol. Vesicles were formed by **A)** ITO electroformation, **B)** Pt wire electroformation, **C)** gentle hydration, and **D)** emulsion transfer. For this mixture of lipids, gentle hydration yielded smaller vesicles compared to other techniques. Scale bars: 100 μm.

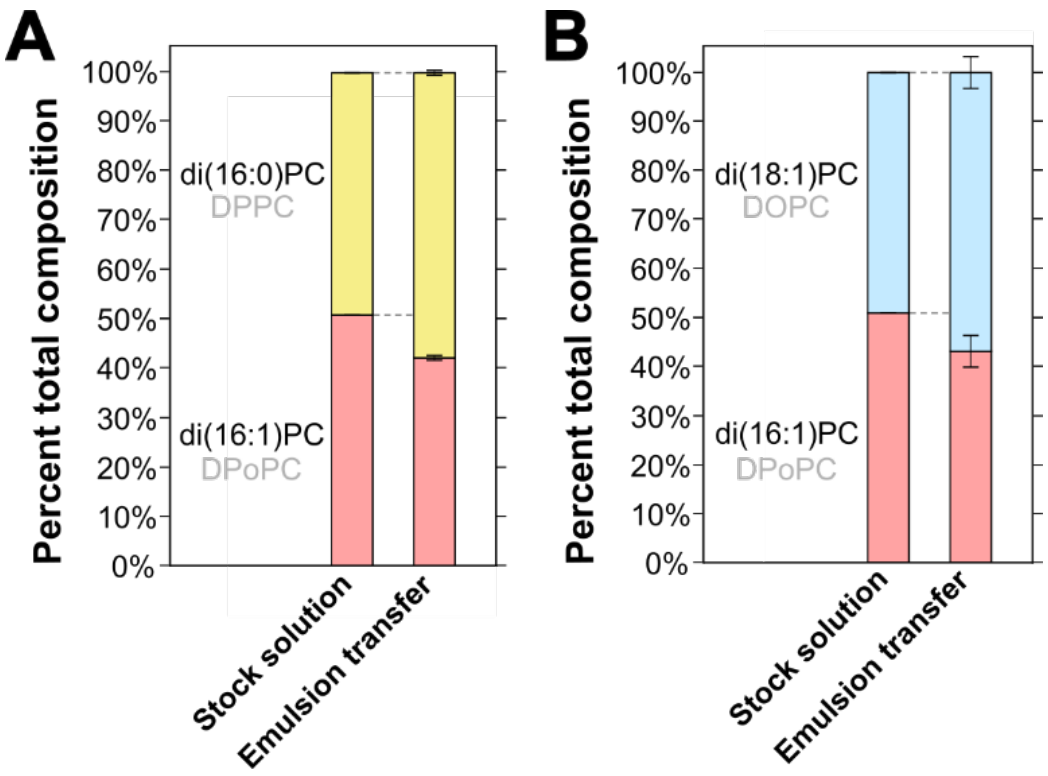

Figure S2.15. Saturated lipids and longer-chain lipids are over-represented in binary vesicle solutions made by emulsion transfer. A) Percent of a saturated PC-lipid (di(16:0)PC) and an unsaturated lipid (di(16:1)PC) in a stock solution and in vesicle solutions made by emulsion transfer from that stock. **B)** Percent of a longer-chain PC-lipid (di(18:1)PC) and a shorter-chain lipid (di(16:1)PC) in a stock solution and in vesicle solutions made by emulsion transfer from that stock. In both panels, values are averages of three independent experiments, error bars above each section of the bar chart are standard deviations, and all experiments are independent from the data in Figs. 2.4 and 2.5 of the main text, including the use of a different stock solution. For these triplicates, it was not necessary to concentrate them by a factor of 5 since abundances were sufficiently above the background. Full data appear in Tables S2.9, S2.10, S2.19 and S2.20.

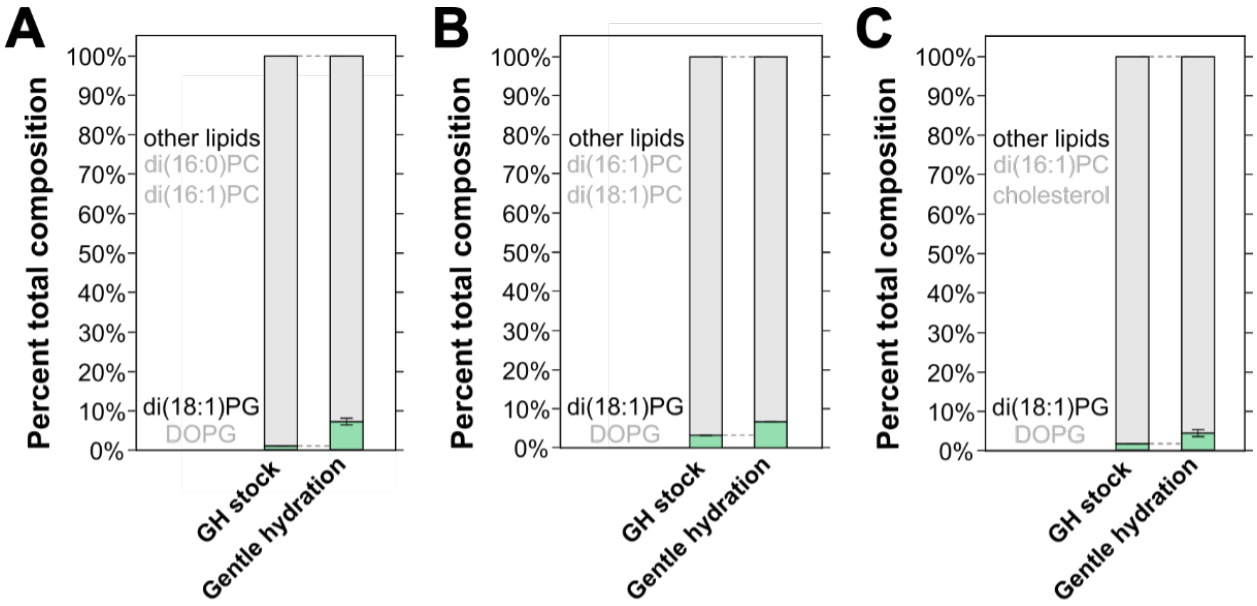

Figure S2.16. PG-lipids are over-represented in vesicle solutions made by gentle hydration from stock solutions initially containing < 5 mol% PG-lipid. In all three panels, the percent of di(18:1)PC lipids and the percent of other lipids are shown for a stock solution in chloroform (left bar of each panel) and for vesicle solutions made by gentle hydration from those stocks (right bar). Vesicle data are averages, and error bars above each section of the bar chart are standard deviations of three independent experiments. **A)** The other lipids are di(16:0)PC and di(16:1)PC. Full data appear in Tables S2.3 and S2.13. **B)** The other lipids are di(16:1)PC and di(18:1)PC. Full data appear in Tables S2.5 and S2.14. **C)** The other lipids are di(16:1)PC and cholesterol. Full data appear in tables S7, S15, and S16.

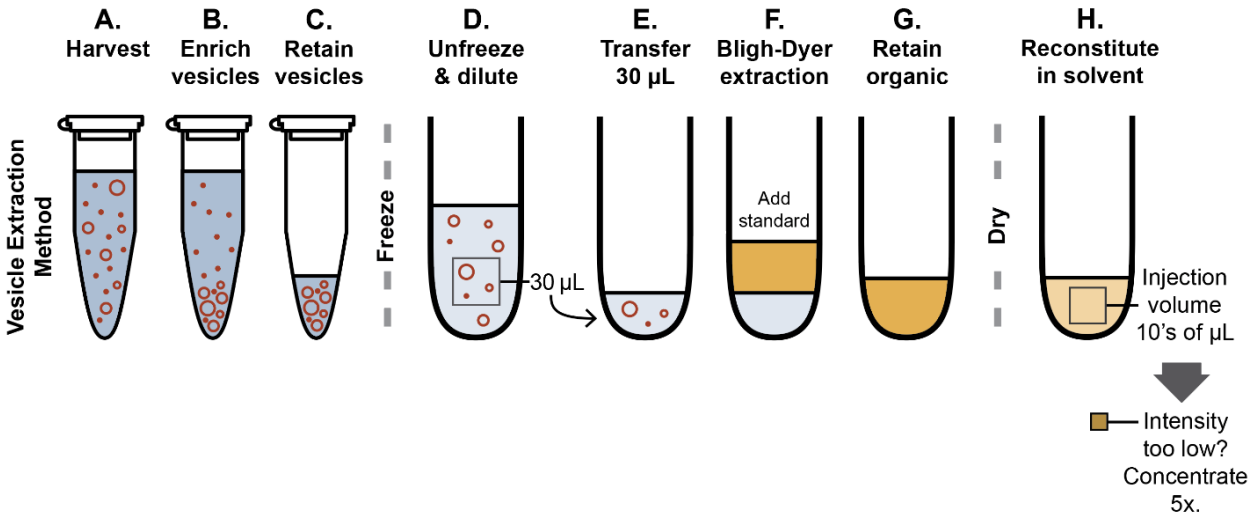

Figure S2.17. Extraction Procedure. A) Each vesicle method produces an aqueous solution containing vesicles and lipid aggregates. Concentrations and volumes of each solution may be different. **B)** A portion of each solution is enriched in sedimented vesicles. **C)** The portion of each solution enriched in vesicles is retained and frozen. The remainder is discarded. **D)** Batches of samples are unfrozen at the same time and diluted. The volume for dilution is calculated with an assumption that 10% of the stock lipids used to make vesicles in each experiment is retained in Step C and with a goal that the concentration of the least prevalent lipid is ~1 µM in Step G. **E)** An aliquot of 30 µL from each sample is transferred to new glassware. **F)** Lipid standards are added to each sample, and all lipids are extracted into an organic solvent. **G)** The organic phase is retained, and the aqueous phase is discarded. **F)** The lipids are dried and then reconstituted in 2:1 acetonitrile:methanol. Tens of microliters of this solution is injected into the HILIC-IM-MS apparatus. If the peak intensity of the least prevalent lipid is too low, the remaining solution is concentrated 5 times and the same volume of solution is injected into the HILIC-IM-MS apparatus.

ii. Supporting Tables.

		Percentage of total lipid				
Method	Sample	Cholesterol	di(16:0)PC (DPPC)	di(18:1)PC (DOPC)	di(12:0)PE (DLPE)	di(18:1)PG (DOPG)
Stock solution	Master stock with 5 lipids	17.0%	28.4%	38.3%	5.8%	10.4%
ITO electroform.	ITO 1	14.2%	28.0%	43.4%	4.4%	9.9%
	ITO 2	15.3%	28.1%	41.9%	4.7%	9.9%
	ITO 3	12.6%	29.5%	43.6%	5.1%	9.2%
Pt electroform.	Pt 1	17.4%	28.5%	40.7%	4.4%	9.0%
	Pt 2	15.0%	29.2%	41.1%	4.9%	9.9%
	Pt 3	15.5%	30.1%	39.7%	4.5%	10.1%
Gentle hydration	GH 1	22.9%	26.1%	35.3%	5.5%	10.1%
	GH 2	20.1%	27.1%	37.1%	5.0%	10.6%
	GH 3	20.9%	26.3%	36.2%	5.7%	10.9%
Emulsion transfer	ET 1	3.4%	44.0%	35.4%	5.7%	11.6%
	ET 2	3.5%	45.9%	35.1%	5.2%	10.2%
	ET 3	3.8%	42.1%	37.3%	5.4%	11.3%

Table S2.1. Lipid compositions of five-component vesicle solutions analyzed by mass spectrometry, expressed as percentages of total lipid. The abundance of each lipid is shown in Tables S2.11 and S2.12.

		Percentage of total lipid	
Method	Sample	di(16:0)PC	di(16:1)PC
Stock solution	Stock of saturated and unsaturated lipids in chloroform	49.8%	50.2%
ITO electroformation	ITO 1	46.9%	53.1%
	ITO 2	54.2%	45.8%
	ITO 3	46.6%	53.4%
Pt electrofromation	Pt 1	49.7%	50.3%
	Pt 2	49.0%	51.0%
	Pt 3	49.4%	50.6%
Emulsion transfer	ET 1	53.1%	46.9%
	ET 2	60.2%	39.8%
	ET 3	63.2%	36.8%

Table S2.2. Percentages of lipids in vesicle solutions made by ITO electroformation, Pt wire electroformation, and emulsion transfer from a binary mixture of a saturated PC-lipid and an unsaturated PC-lipid. The abundance of each lipid is shown in Table S2.13. Results from an independent set of emulsion transfer experiments are shown in Tables S2.9 and S2.19.

		Percentage of total lipid		
Method	Sample	di(16:0)PC	di(16:1)PC	di(18:1)PG
Stock solution	Stock of saturated, unsaturated, and charged lipids in chloroform	51.9%	47.2%	0.9%
Gentle hydration	GH 1	47.3%	46.4%	6.3%
	GH 2	45.8%	47.2%	6.9%
	GH 3	50.3%	41.7%	8.0%

Table S2.3. Percentages of lipids in vesicle solutions made by gentle hydration from a mixture of a saturated and an unsaturated PC-lipid, including a charged lipid (di(18:1)PG), which is necessary for vesicle formation by this method. The abundance of each lipid is shown in Table S2.13.

		Percentage of total lipid	
Method	Sample	di(16:1)PC	di(18:1)PC
Stock solution	Stock of lipids with different chain lengths in chloroform	53.4%	46.6%
ITO electroformation	ITO 1	56.2%	43.8%
	ITO 2	55.9%	44.1%
	ITO 3	53.4%	46.6%
Pt electrofromation	Pt 1	49.7%	50.3%
	Pt 2	47.8%	52.2%
	Pt 3	46.6%	53.4%
Emulsion transfer	ET 1	47.5%	52.5%
	ET 2	54.8%	45.2%
	ET 3	52.0%	48.0%

Table S2.4. Percentages of lipids in vesicle solutions made by ITO electroformation, Pt wire electroformation, and emulsion transfer from a binary mixture of a shorter-chain PC-lipid and a longer-chain PC-lipid. The abundance of each lipid is shown in Table S2.14. Results from an independent set of emulsion transfer experiments are shown in Tables S2.10 and S2.20.

		Percentage of total lipid		
Method	Sample	di(16:1)PC	di(18:1)PC	di(18:1)PG
Stock solution	Stock of lipids with different chain lengths and charged lipids in chloroform	50.2%	46.6%	3.2%
Gentle hydration	GH 1	47.7%	45.6%	6.7%
	GH 2	47.2%	46.1%	6.7%
	GH 3	47.1%	46.2%	6.7%

Table S2.5. Percentages of lipids in vesicle solutions made by gentle hydration from a mixture of a shorter-chain PC-lipid and a longer-chain PC-lipid, including a charged lipid (di(18:1)PG), which is necessary for vesicle formation by this method. The abundance of each lipid is shown in Table S2.14.

		Percentage of total lipid	
Method	Sample	di(16:1)PC	Cholesterol
Stock solution	Stock of a PC-lipid and cholesterol in chloroform	46.4%	53.6%
ITO electroformation	ITO 1	47.1%	52.9%
	ITO 2	52.7%	47.3%
	ITO 3	47.8%	52.2%
Pt electroformation	Pt 1	47.2%	52.8%
	Pt 2	47.8%	52.2%
	Pt 3	45.4%	54.6%
Emulsion transfer	ET 1	80.3%	19.7%
	ET 2	92.9%	7.1%
	ET 3	87.8%	12.2%

Table S2.6. Percentages of lipids in vesicle solutions made by ITO electroformation, Pt wire electroformation, and emulsion transfer from a binary mixture of an unsaturated PC-lipid and cholesterol. The abundance of each lipid is shown in Tables S2.15 and S2.16.

		Percentage of total lipid		
Method	Sample	di(16:1)PC	Cholesterol	di(18:1)PG
Stock solution	Stock of a PC-lipid, cholesterol, and a charged lipid in chloroform	41.6%	56.8%	1.6%
Gentle hydration	GH 1	29.8%	66.8%	3.4%
	GH 2	36.5%	58.4%	5.2%
	GH 3	33.0%	62.7%	4.3%

Table S2.7. Percentages of lipids in vesicle solutions made by gentle hydration from a mixture of an unsaturated PC-lipid and cholesterol, including a charged lipid (di(18:1)PG), which is necessary for vesicle formation by this method. The abundance of each lipid is shown in Tables S2.15 and S2.16.

		Percentage of total lipid				
Method	Sample	Cholesterol	di(16:0)PC (DPPC)	di(18:1)PC (DOPC)	di(12:0)PE (DLPE)	di(18:1)PG (DOPG)
Before extrusion	Experiment 1 - Before	23.6%	25.2%	29.2%	6.9%	15.0%
	Experiment 2 - Before	26.3%	26.5%	25.6%	6.5%	15.1%
	Experiment 3 - Before	27.7%	25.8%	25.2%	6.3%	14.9%
After extrusion	Experiment 1 - After	18.0%	27.9%	32.1%	5.2%	16.9%
	Experiment 2 - After	22.4%	27.3%	27.1%	6.7%	16.6%
	Experiment 3 - After	22.3%	27.0%	28.4%	6.7%	15.6%

Table S2.8. Lipid compositions analyzed by mass spectrometry and expressed as percentages of total lipid for vesicle solutions produced by gentle hydration ("before extrusion") and then extruded ("after extrusion"). For example, "Experiment 1 – After" was made from an aliquot of the solution from "Experiment 1 – Before". The abundance of each lipid is shown in Tables S2.17 and S2.18.

		Percentage of total lipid	
Method	Sample	di(16:0)PC	di(16:1)PC
Stock solution for lipid saturation experiments	Stock of saturated and unsaturated lipids in chloroform	49.1%	50.9%
Emulsion transfer (ET)	ET saturation 1	58.2%	41.8%
	ET saturation 2	58.0%	42.0%
	ET saturation 3	57.3%	42.7%

Table S2.9. Percentages of lipids in vesicle solutions made by emulsion transfer from an additional binary mixture of a saturated PC-lipid and an unsaturated PC-lipid. The abundance of each lipid is shown in Table S2.19. Data from an independent set of emulsion transfer experiments are shown in Tables S2.2 and S2.13.

		Percentage of total lipid	
Method	Sample	di(18:1)PC	di(16:1)PC
Stock solution for lipid length experiments	Stock of lipids with different chain lengths in chloroform	49.1%	50.9%
Emulsion transfer (ET)	ET length 1	58.8%	41.2%
	ET length 2	58.7%	41.3%
	ET length 3	53.1%	46.9%

Table S2.10. Percentages of lipids in vesicle solutions made by emulsion transfer from an additional binary mixture of a shorter-chain PC-lipid and a longer-chain PC-lipid. The abundance of each lipid is shown in Table S2.20. Data from an independent set of emulsion transfer experiments are shown in Tables S2.4 and S2.14.

Lipid	di(15:0)PC *Internal standard*	di(16:0)PC	di(18:1)PC	di(15:0)PE *Internal standard*	di(12:0)PE	di(15:0)PG *Internal standard*	di(18:1)PG
m/z	706.5	734.6	786.6	686.5	602.4	717.5	797.5
Retention time (minutes)	3.467	3.467	3.414	2.725	2.847	0.708	0.621
Calibrated retention time (minutes)	6.760	6.760	6.672	5.542	5.742	2.233	2.038
Collisional cross section ($Å^2$)	274.4	279.8	285.1	268.9	252.5	268.6	279.4
5-component stock solution	5617.5	17245.3	23270.3	4528.2	2853.3	4441.4	5016.5
ITO electroform. 1 abundance	6741.8	17442.6	27025.4	4434.9	1810.2	5385.0	4914.3
ITO electroform. 2 abundance	6857.4	24043.3	35779.5	4280.0	2523.2	5170.9	6393.5
ITO electroform. 3 abundance	7240.7	15652.1	23118.4	4920.6	1843.7	6871.4	4625.1
Pt electroform. 1 abundance	6881.0	22694.3	32436.7	4665.2	2379.2	5772.2	6026.1
Pt electroform. 2 abundance	6679.0	16801.5	23631.0	5039.4	2124.3	6748.9	5740.9
Pt electroform. 3 abundance	5342.4	14477.7	19085.5	4548.3	1847.1	5020.5	4557.4
Gentle hydration 1 abundance	7353.0	30264.4	40917.1	5487.3	4792.2	5907.4	9413.3
Gentle hydration 2 abundance	7682.1	23456.5	32112.9	6630.8	3748.8	5247.5	6246.9
Gentle hydration 3 abundance	7625.5	22749.8	31393.1	5379.8	3504.5	5017.3	6195.7
Emulsion transfer 1 abundance	8370.8	9579.3	7712.5	5534.3	816.3	6091.2	1843.4
Emulsion transfer 2 abundance	8068.4	11843.5	9051.1	5553.9	931.3	5927.0	1931.0
Emulsion transfer 3 abundance	7626.0	9787.1	8667.5	5246.7	867.2	5531.6	1910.8

Table S2.11. Phospholipid abundances of five-component vesicle solutions analyzed by mass spectrometry. Corresponding lipid percentages are in Table S2.1.

	d7-cholesterol *Internal standard*	Cholesterol	Relative Response Factor (RRF)
5-component stock solution	321. x 10^5	85.9 x 10^5	1.063
ITO electroformation 1	268. x 10^5	51.3 x 10^5	
ITO electroformation 2	276. x 10^5	76.7 x 10^5	
ITO electroformation 3	253. x 10^5	33.9 x 10^5	
Pt electroformation 1	284. x 10^5	83.3 x 10^5	
Pt electroformation 2	261. x 10^5	49.1 x 10^5	
Pt electroformation 3	262. x 10^5	53.3 x 10^5	
Gentle hydration 1	299. x 10^5	157. x 10^5	
Gentle hydration 2	271. x 10^5	89.3 x 10^5	
Gentle hydration 3	233. x 10^5	80.5 x 10^5	
Emulsion transfer 1	223. x 10^5	2.85 x 10^5	
Emulsion transfer 2	235. x 10^5	3.88 x 10^5	
Emulsion transfer 3	367. x 10^5	6.13 x 10^5	
CholesterolStandardMix 1	192. x 10^5	37.0 x 10^5	1.038
CholesterolStandardMix 2	195. x 10^5	37.5 x 10^5	1.040
CholesterolStandardMix 3	192. x 10^5	36.4 x 10^5	1.055
CholesterolStandardMix 4	174. x 10^5	33.1 x 10^5	1.051
CholesterolStandardMix 5	184. x 10^5	32.6 x 10^5	1.129

Table S2.12. Cholesterol abundances of five-component vesicle solutions analyzed by mass spectrometry. Corresponding phospholipid abundances are in Table S2.11. Corresponding lipid percentages are in Table S2.1. "CholesterolStandardMix" samples contained 1 μg/mL of d7-cholesterol and 0.2 μg/mL of unlabeled cholesterol and were used to calculate an RRF value (right column). For example, the RRF for CholesterolStandardMix1 is calculated: (0.2 μg/mL / 3,700,000) / (1 μg/mL / 19,200,000) = 1.038. The average RRF value 1.063 was used to calculate the cholesterol composition in all five-component experimental samples.

Lipid	di(15:0)PC *Internal standard*	di(16:0)PC	(16:0/18:1)PC *Internal standard*	di(16:1)PC	di(15:0)PG *Internal standard*	di(18:1)PG
m/z	706.5	734.6	760.6	730.5	717.5	797.5
Retention time (minutes)	3.541	3.523	3.478	3.495	0.953	0.838
Calibrated retention time (minutes)	6.789	6.761	6.685	6.713	2.233	2.038
Collisional cross section ($Å^2$)	240.8	249.6	248.3	241.8	238.5	247.0
Stock for lipid saturation tests	30860.0	43216.7	31604.8	44611.7		
ITO electroform. 1 abundance	24366.7	14971.9	24647.1	17159.7		
ITO electroform. 2 abundance	35109.7	48160.5	39166.9	45440.7		
ITO electroform. 3 abundance	33117.1	42203.3	29583.7	43222.0		
Pt. electroform. 1 abundance	33264.2	10641.9	35170.3	11384.6		
Pt. electroform. 2 abundance	33512.3	8938.4	36105.9	10028.2		
Pt. electroform. 3 abundance	27387.5	13675.6	28251.8	14440.8		
Emulsion transfer 1 abundance	20453.6	24519.6	21912.5	23201.6		
Emulsion transfer 2 abundance	28376.8	29801.8	35758.6	24827.5		
Emulsion transfer 3 abundance	28682.9	10546.0	29830.2	6389.1		
Gentle hydration stock solution for lipid saturation	24928.8	211952.6	28549.2	221074.0	50120.7	7402.7
Gentle hydration 1 abundance	22683.3	271061.2	24664.9	289244.2	37829.3	60299.3
Gentle hydration 2 abundance	19336.3	193665.6	22045.5	227491.3	26953.7	40829.7
Gentle hydration 3 abundance	24807.4	214717.1	31620.1	227134.8	35032.4	48250.1

Table S2.13. Phospholipid abundances in a stock solution and in vesicle solutions made by ITO electroformation, Pt wire electroformation, emulsion transfer, and gentle hydration from a binary mixture of a saturated PC-lipid and an unsaturated PC-lipid. Samples for gentle hydration included a charged lipid (di(18:1)PG), which is necessary for vesicle formation by this method. Corresponding lipid percentages are in Tables S2.2 and S2.3.

Lipid	(16:0/18:1)PC *Internal standard*	di(16:1)PC	di(18:1)PC	di(15:0)PG *Internal standard*	di(18:1)PG
m/z	760.6	730.5	786.6	717.5	797.5
Retention time (minutes)	3.478	3.495	3.460	0.953	0.838
Calibrated retention time (minutes)	6.685	6.713	6.655	2.233	2.038
Collisional cross section (Å^2)	248.3	241.8	253.6	238.5	247.0
Stock for lipid chain length tests	40517.6	51795.3	45140.3		
ITO electroform. 1 abundance	42931.2	40892.1	31852.8		
ITO electroform. 2 abundance	27139.4	51297.7	40433.5		
ITO electroform. 3 abundance	32141.3	24546.7	21443.9		
Pt. electroform. 1 abundance	31357.6	4782.7	4848.0		
Pt. electroform. 2 abundance	31208.7	15504.4	16947.8		
Pt. electroform. 3 abundance	29936.8	14025.6	16057.0		
Emulsion transfer 1 abundance	177920.3	5960.2	7214.3		
Emulsion transfer 2 abundance	164180.2	52330.3	46925.3		
Emulsion transfer 3 abundance	153561.4	15236.5	15315.4		
Gentle hydration stock solution for lipid chain length	33285.1	224719.0	208349.3	41982.4	18184.9
Gentle hydration 1 abundance	22137.7	314265.2	301021.1	31340.2	62579.6
Gentle hydration 2 abundance	24301.7	266692.5	260436.7	34032.5	53013.6
Gentle hydration 3 abundance	27693.0	241373.4	236986.2	35637.8	44135.2

Table S2.14. Phospholipid abundances in stock solutions and in vesicle solutions made by ITO electroformation, Pt wire electroformation, emulsion transfer, and gentle hydration from a mixture of a lipids with different chain lengths. Samples for gentle hydration included a charged lipid (di(18:1)PG), which is necessary for vesicle formation by this method. Corresponding lipid percentages are in Tables S2.4 and S2.5.

Lipid	(16:0)(18:1)PC *Internal standard*	di(16:1)PC	di(15:0)PG *Internal standard*	di(18:1)PG
m/z	760.6	730.5	717.5	797.5
Retention time (minutes)	3.478	3.495	0.953	0.838
Calibrated retention time (minutes)	6.685	6.713	2.233	2.038
Collisional cross section (Å^2)	248.3	241.8	238.5	247.0
Stock for PC-lipid vs. cholesterol	31657.8	46654.6		
ITO electroform. 1 abundance	30214.6	35616.8		
ITO electroform. 2 abundance	26795.1	54201.0		
ITO electroform. 3 abundance	36225.0	59824.3		
Pt. electroform. 1 abundance	32660.1	20906.6		
Pt. electroform. 2 abundance	34421.4	40375.1		
Pt. electroform. 3 abundance	33803.4	31500.6		
Emulsion transfer 1 abundance	162535.6	41325.6		
Emulsion transfer 2 abundance	152545.4	195281.5		
Emulsion transfer 3 abundance	159797.7	90395.7		
Gentle hydration stock for PC-lipid vs. cholesterol	33090.1	272405.7	47084.9	14735.5
Gentle hydration 1 abundance	23214.1	341451.9	32808.2	54979.6
Gentle hydration 2 abundance	24085.7	296331.5	30982.6	53893.9
Gentle hydration 3 abundance	26059.0	306777.7	30714.2	47246.0

Table S2.15. Phospholipid abundances in stock solutions and in vesicle solutions made by ITO electroformation, Pt wire electroformation, emulsion transfer, and gentle hydration from a mixture of a PC-lipid and cholesterol. Samples for gentle hydration included a charged lipid (di(18:1)PG), which is necessary for vesicle formation by this method. Corresponding cholesterol abundances are in Table S2.16. Corresponding lipid percentages are in Tables S2.6 and S2.7.

	d7-cholesterol *Internal standard*	Cholesterol	Relative Response Factor (RRF)
Stock for PC-lipid vs. cholesterol	71.91 x 10^5	13.64 x 10^5	0.7511
ITO electroformation 1	127.5 x 10^5	18.31 x 10^5	
ITO electroformation 2	116.1 x 10^5	23.90 x 10^5	
ITO electroformation 3	154.8 x 10^5	30.65 x 10^5	
Pt electroform 1	154.4 x 10^5	9.520 x 10^5	
Pt electroform 2	158.9 x 10^5	20.60 x 10^5	
Pt electroform 3	160.3 x 10^5	17.96 x 10^5	
Emulsion transfer 1	1019. x 10^5	9.249 x 10^5	0.8300
Emulsion transfer 2	308.5 x 10^5	4.048 x 10^5	
Emulsion transfer 3	18.63 x 10^5	0.2113 x 10^5	
Gentle hydration stock for PC-lipid vs. cholesterol	148.7 x 10^5	211.9 x 10^5	0.7511
Gentle hydration 1	169.4 x 10^5	701.6 x 10^5	
Gentle hydration 2	163.2 x 10^5	406.1 x 10^5	
Gentle hydration 3	160.1 x 10^5	454.3 x 10^5	
Cholesterol Standard Mix 1	223.1 x 10^5	32.97 x 10^5	0.7389
Cholesterol Standard Mix 2	224.1 x 10^5	32.89 x 10^5	0.7339
Cholesterol Standard Mix 3	221.1 x 10^5	32.76 x 10^5	0.7411
Cholesterol Standard Mix 4	230.0 x 10^5	34.46 x 10^5	0.7492
Cholesterol Standard Mix 5	225.5 x 10^5	34.06 x 10^5	0.7553
Cholesterol Standard Mix 6	224.7 x 10^5	34.70 x 10^5	0.7721
Cholesterol Standard Mix 7	231.6 x 10^5	35.56 x 10^5	0.7677
Cholesterol Standard Mix 8	237.2 x 10^5	35.49 x 10^5	0.7480
Cholesterol Standard Mix 9	240.5 x 10^5	36.25 x 10^5	0.7536
Cholesterol Standard Mix 10	347.6 x 10^5	57.44 x 10^5	0.8263
Cholesterol Standard Mix 11	342.1 x 10^5	57.29 x 10^5	0.8373
Cholesterol Standard Mix 12	335.9 x 10^5	55.55 x 10^5	0.8268
Cholesterol Standard Mix 13	331.1 x 10^5	54.95 x 10^5	0.8297

Table S2.16. Cholesterol abundances in stock solutions and in vesicle solutions made by ITO electroformation, Pt wire electroformation, emulsion transfer, and gentle hydration from a mixture of a PC-lipid and cholesterol. Corresponding phospholipid abundances are in Table S2.15. Corresponding lipid percentages are in Tables S2.6 and S2.7. "Cholesterol Standard Mix" samples contained 1 μg/mL of d7-cholesterol and 0.2 μg/mL of unlabeled cholesterol and were used to calculate an RRF value (right column). For example, the RRF for Cholesterol Standard Mix 1 is calculated: (0.2 μg/mL / 3297000) / (1 μg/mL / 22310000) = 0.7389. Cholesterol Standard Mix 1-9 were used to calculate an average RRF value 0.7511 which was used to calculate the cholesterol compositions for all binary PC-lipid vs. cholesterol experimental samples, excluding emulsion transfer. Cholesterol Standard Mix 10-13 were used to calculate an average RRF value 0.8300 which was used to calculate cholesterol compositions for binary PC-lipid vs. cholesterol samples produced only by emulsion transfer after they were concentrated by a factor of 5.

Lipid	di(15:0)PC *Internal standard*	di(16:0)PC	di(18:1)PC	di(15:0)PE *Internal standard*	di(12:0)PE	di(15:0)PG *Internal standard*	di(18:1)PG
m/z	706.5	734.6	786.6	664.5	580.4	717.5	797.5
Retention time (minutes)	3.312	3.312	3.225	2.570	2.692	0.674	0.553
Calibrated retention time (minutes)	5.445	5.445	5.459	5.560	5.541	2.233	2.020
Collisional cross section ($Å^2$)	239.9	249.9	254.0	232.0	216.8	239.8	248.4
Before extrusion 1 abundance	56822.3	84583.4	97994.1	85471.0	34719.6	36543.5	32416.2
Before extrusion 2 abundance	63191.0	113815.1	109639.1	101636.3	44984.7	39897.5	40816.1
Before extrusion 3 abundance	63430.2	159911.8	156115.9	95764.3	59014.5	30611.1	44526.0
After extrusion 1 abundance	54683.8	32544.4	37473.0	89296.3	9911.4	43706.7	15788.9
After extrusion 2 abundance	65041.1	65510.5	65082.1	96925.9	23877.9	37763.1	23185.0
After extrusion 3 abundance	50216.3	63415.0	66752.6	85189.5	26663.7	36801.5	26753.6

Table S2.17. Phospholipid abundances in vesicle solutions produced by gentle hydration ("before extrusion") and then extruded ("after extrusion"). For example, "After extrusion 1" was made from an aliquot of the solution from "Before extrusion 1". Corresponding lipid percentages are in Table S2.8.

Sample	d7-cholesterol*Internal standard*	Cholesterol	Relative Response Factor (RRF)
5-component stock solution	161.0 x 10^5	3879. x 10^5	0.8608
Before extrusion 1	170.1 x 10^5	42.56 x 10^5	
Before extrusion 2	169.5 x 10^5	54.41 x 10^5	
Before extrusion 3	165.1 x 10^5	80.23 x 10^5	
After extrusion 1	158.4 x 10^5	10.93 x 10^5	
After extrusion 2	166.2 x 10^5	24.68 x 10^5	
After extrusion 3	154.1 x 10^5	28.86 x 10^5	
CholesterolStandardMix 1	183.5 x 10^5	42.44 x 10^5	0.8650
CholesterolStandardMix 2	185.1 x 10^5	43.33 x 10^5	0.8545
CholesterolStandardMix 3	182.6 x 10^5	42.33 x 10^5	0.8628

Table S2.18. Cholesterol abundances in vesicle solutions produced by gentle hydration ("before extrusion") and then extruded ("after extrusion"). For example, "After extrusion 1" was made from an aliquot of the solution from "Before extrusion 1". Corresponding phospholipid abundances are in Table S2.17. Corresponding lipid percentages are in Table S2.8. "CholesterolStandardMix" samples contained 1 μg/mL of d7-cholesterol and 0.2 μg/mL of unlabeled cholesterol and were used to calculate an RRF value (right column). For example, the RRF for CholesterolStandardMix1 is calculated: (0.2 μg/mL / 4,244,000) / (1 μg/mL / 18,350,000) = 0.8650. The average RRF value 0.8608 was used to calculate the cholesterol composition in all five-component experimental samples.

Lipid	di(15:0)PC *Internal standard*	di(16:0)PC	(16:0/18:1)PC *Internal standard*	di(16:1)PC
m/z	706.5	734.6	760.6	730.5
Retention time (minutes)	3.312	3.312	3.259	3.414
Calibrated retention time (minutes)	5.445	5.445	5.453	5.429
Collisional cross section (Å2)	239.9	249.9	248.7	240.9
Emulsion transfer stock for lipid saturation tests	14259.5	490722.3	12208.1	434934.4
ET saturation 1 abundance	54941.2	45862.2	52621.1	31490.8
ET saturation 2 abundance	58862.0	21123.8	55943.2	14554.5
ET saturation 3 abundance	57614.3	39973.9	54335.7	28099.2

Table S2.19. Phospholipid abundances in vesicle solutions made for an additional emulsion transfer triplicate from a binary mixture of an unsaturated lipid and a saturated lipid. Corresponding lipid percentages are in Table S2.9. Data from an independent set of emulsion transfer experiments are shown in Tables S2.2 and S2.13.

Lipid	(16:0/18:1)PC *Internal standard*	di(16:1)PC	di(18:1)PC
m/z	760.6	730.5	786.6
Retention time (minutes)	3.259	3.414	3.225
Calibrated retention time (minutes)	5.453	5.429	5.459
Collisional cross section ($Å^2$)	248.7	240.9	254.0
Emulsion transfer stock for lipid chain length tests	8362.4	428416.6	412967.2
ET length 1 abundance	51197.1	13380.6	19090.4
ET length 2 abundance	53042.6	5718.8	8128.1
ET length 3 abundance	54721.9	10486.8	11892.0

Table S2.20. Phospholipid abundances in vesicle solutions made for an additional emulsion transfer triplicate from a binary mixture of lipids with different chain lengths. Corresponding lipid percentages are in Table S2.10. Data from an independent set of emulsion transfer experiments are shown in Tables S2.4 and S2.14.

Chapter 3

Micron-scale, liquid-liquid phase separation in ternary lipid membranes containing DPPE

*This chapter is adapted from a manuscript in preparation for submission to the *Biophysical Journal*. It was written in collaboration with Sasha Naomi, Angelique M. Madrigal, Catherine L. A. Chang, Caitlin E. Cornell, and Sarah L. Keller.

G. J. Goetz, S. Naomi, A. M. Madrigal, C. L. A. Chang, C. E. Cornell, S. L. Keller. 2025. Micron-scale, liquid-liquid phase separation in ternary lipid membranes containing DPPE. *Manuscript in preparation, January 5, 2025.*

3.1 Abstract.

Micron-scale, liquid-liquid phase separation occurs in membranes of living cells, with physiological consequences. To discover which lipids support phase separation and how they partition between phases, miscibility phase diagrams have been mapped for model membranes. Typically, model membranes are composed of ternary mixtures of a lipid with a high melting temperature, a lipid with a low melting temperature, and cholesterol. Most phospholipids in ternary mixtures have historically been chosen to favor stable membranes (phosphatidylcholines and sphingomyelins) or to add charge (phosphatidylglycerols and phosphatidylserines). A major class of phospholipids missing from experimental ternary diagrams has been the phosphatidylethanolamines (PEs). PE-lipids constitute up to 20 mol% of common biological membranes, where they influence protein function and facilitate membrane fusion. These biological effects are often attributed to PE's smaller headgroup, which leads to higher monolayer spontaneous curvatures and higher melting temperatures. Taken alone, the higher melting points of saturated PE-lipids imply that liquid-liquid phase separation should persist to higher temperatures in membranes containing PE-lipids. Here, we tested that hypothesis by substituting a saturated PE-lipid (DPPE) for its corresponding PC-lipid (DPPC) in two well-studied ternary

membranes (DOPC/DPPC/cholesterol and DiphyPC/DPPC/cholesterol). We used fluorescence microscopy to map full ternary phase diagrams for giant vesicles over a range of temperatures. Surprisingly, we found no micron-scale, liquid-liquid phase separation in vesicles of the first mixture (DOPC/DPPE/cholesterol), and only a small region of liquid-liquid phase separation in the second mixture (DiphyPC/DPPE/cholesterol). Instead, coexisting solid and liquid phases were widespread, with the solid phase enriched in DPPE. An unusual feature of these ternary membranes is that solid and liquid-ordered phases can be distinguished by fluorescence microscopy, so tie-line directions can be estimated throughout the phase diagram, and transition temperatures to the 3-phase region (containing a liquid-disordered phase, L_d, a liquid-ordered phase, L_o, and a solid phase, S) can be accurately measured.

3.2 Introduction.

Liquid-liquid phase separation of membranes is key to the function of some cells, which adjust their membrane compositions with respect to the phase transition (17, 18). Independent of whether membranes are derived from a cell with hundreds of lipids (5, 80, 81), or from minimal model systems with only two lipids (82), all membranes that demix into micron-scale liquid phases contain at least three moieties: lipid chains with high order, lipid chains with low order, and sterols (13, 56, 83).

To discover which types of lipids support liquid-liquid phase separation and how the lipids partition between the phases, researchers have mapped phase diagrams, typically of ternary mixtures of a lipid with saturated chains, a lipid with either unsaturated or methylated chains, and cholesterol (Fig. 3.1). When researchers are faced with the question of exactly which lipids to incorporate into ternary membranes, they often choose PC-lipids, which are widely, commercially available and produce stable membranes over broad experimental temperatures (57). Although researchers have made forays into producing ternary membranes containing other types of lipids (e.g., sphingomyelins (23, 24), ceramides (84, 85), and charged PS- or PG-lipids (21, 22)), mapping phase diagrams can be expensive, in both materials and time. As a result, there have been major gaps in the literature, for example in the lack of ternary membranes containing phosphatidylethanolamine (PE) lipids.

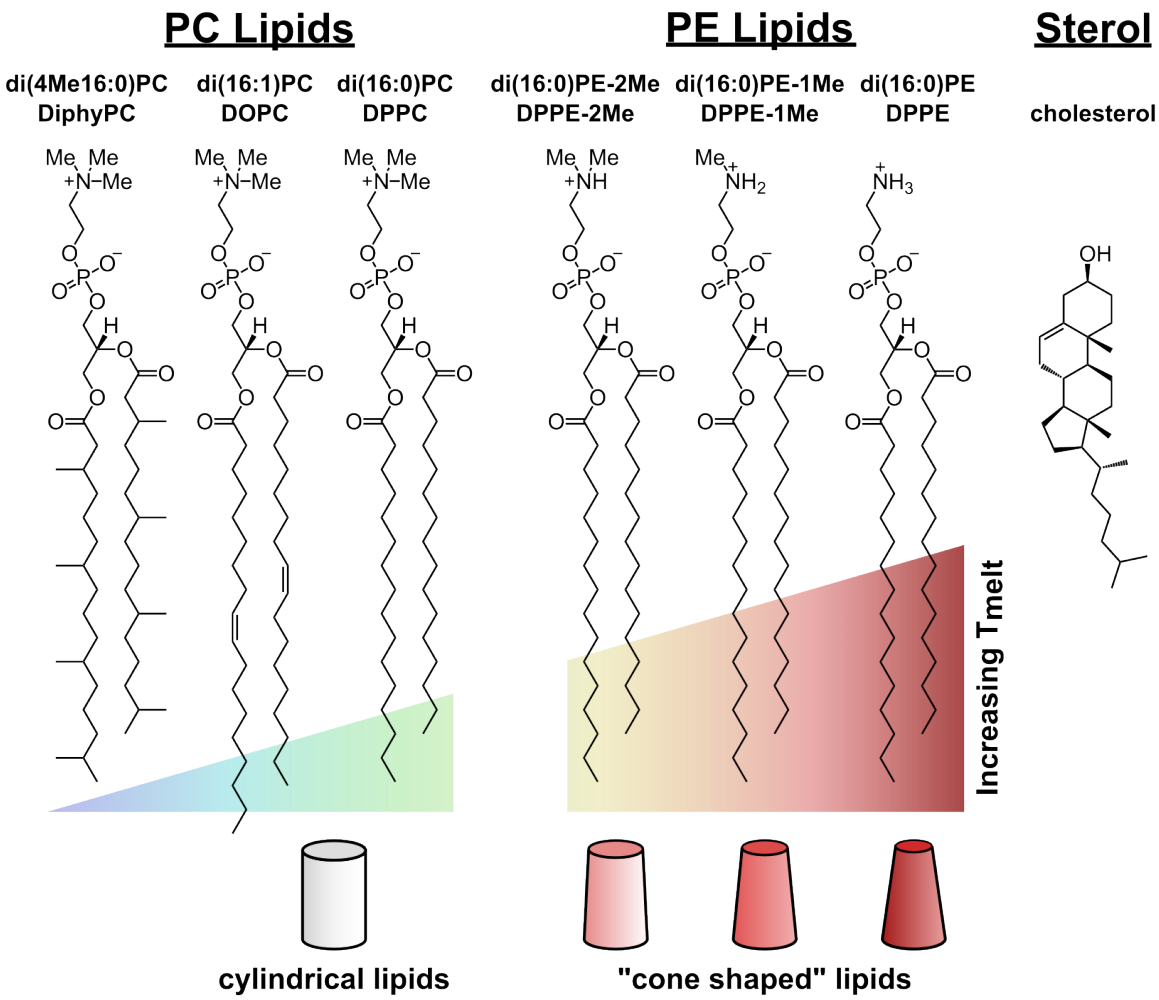

Figure 3.1. Structures of lipids. Vesicles were made from ternary mixtures of lipids with a high melting temperature (T_{melt}), a low melting temperature, and a sterol. Phospholipids are ordered from left to right by increasing T_{melt}. Headgroups of PC- and PE-lipids differ only by the number of methyl groups on the amine.

PE-lipids are distinguished by smaller headgroups than PC-lipids and by the potential to hydrogen bond with neighboring phosphates, both of which contribute to the cone shape of PE-lipids (2, 86).

There are several strong reasons to expand the known set of miscibility phase diagrams to include membranes with PE-lipids:

- First, some channels and proteins function and fold differently in membranes containing PE-lipids (e.g., (87–90), and others reviewed in (91)). Phase separation of membranes should concentrate PE-lipids in domains, locally enhancing the effect.

- Second, PE-lipids have higher chain order than corresponding PC-lipids, and they impart higher chain order in neighboring lipids (1). Higher chain order parameters hold whether they are assessed at equivalent absolute temperatures or at equivalent reduced temperatures (92). Higher chain order results in higher T_{melt} values: for di(16:0)PE, also known as DPPE, T_{melt} = 62.3 ± 5.0°C (25), whereas for di(16:0)PC, also known as DPPC, T_{melt} = 41.3 ± 1.8°C (57).
- Third, PE-lipids are common in biological membranes. They constitute ~10% of red blood cell membranes (5), ~8% of giant plasma membrane vesicles from zebrafish ZF4 cells (18), ~15% of total yeast membranes (93), and 10-20% of yeast vacuole membranes (80, 81).
- Fourth, the spontaneous curvature that cone-shaped lipids impart to each leaflet of a membrane (or to the whole of an asymmetric membrane) has biological implications beyond protein function. Curvature can influence membrane fusion (94) as well as the size and shape of phase-separated domains ((95), and reviewed in (96)). Likewise, high fractions of PE-lipids are associated with transitions from flat, lamellar sheets to curved, inverted hexagonal (H_{II}) and cubic phases (25, 97). The pressure dependence of the lamellar-H_{II} transition (98) explains why deep-sea creatures such as ctenophores undergo "tissue melting" at atmospheric pressure (99).
- Fifth, as more diverse lipids are incorporated into simulations (reviewed in (100)), data for complex membranes containing PE-lipids are needed as ground truth, particularly in the context of curvature stress of asymmetric membranes (101).

Here, we produce giant unilamellar vesicles (GUVs) composed of ternary mixtures of cholesterol, a PE-lipid with a high melting temperature (DPPE, or di(16:0)PE), and a PC-lipid with a low melting temperature (either DOPC/di(18:1)PC or DiphyPC/di(16:0-4Me)PC). We chose DPPE because it has been reported to form a lamellar phase at common experimental temperatures (25). Nevertheless, membranes with DPPE likely experience curvature frustration because DPPE transitions into an inverted hexagonal phase at 120°C (25) and a cubic phase may lie nearby (98, 102). In our experiments, we use fluorescence microscopy to identify coexisting phases in vesicle membranes, and we map their miscibility phase diagrams. We compare our

data with existing phase diagrams for membranes without PE-lipids, and we adjust the methylation of lipid headgroups to understand intermediate steps between the two extremes.

3.3 Materials and Methods.

i. Lipids.

1,2-dipalmitoyl-sn-glycero-3-phosphoethanolamine (DPPE or di(16:0)PE, T_{melt} = 62.3 ± 5.0°C, T_{hex} = 120.6 ± 3.6°C (25)), 1,2-dipalmitoyl-sn-glycero-3-phosphoethanolamine-N-methyl (DPPE-1Me or di(16:0)PE-1Me, T_{melt} = 57.6 ± 1.5°C (25)(26)), 1,2-dipalmitoyl-sn-glycero-3-phosphoethanolamine-N,N-dimethyl (DPPE-2Me or di(16:0)PE-2Me, T_{melt} = 43.2 ± 2.0°C (25)), 1,2-dipalmitoyl-sn-glycero-3-phosphocholine (DPPC or di(16:0)PC, T_{melt} = 41.3 ± 1.8°C (57)), 1,2-dioleoyl-sn-glycero-3-phosphocholine (DOPC or di(16:1)PC, T_{melt} = −18.3 ± 3.6°C (57)), 1,2-diphytanoyl-sn-glycero-3-phosphocholine (DiPhyPC or di(16:0-4Me)PC, T_{melt} = < −120°C (103)(37)), and a fluorescent dye, rhodamine-DPPE, were obtained from Avanti Polar Lipids (Alabaster, AL). Cholesterol was obtained from Sigma Aldrich (St. Louis, MO). All lipids were used without further purification. Cholesterol was mixed from powder in chloroform to a concentration of 10 mg/ml. DPPE, DPPE-1Me, and DPPE-2Me were mixed from powder in 9:1 chloroform/methanol to a concentration of 10 mg/ml. All other unlabeled lipids were supplied from Avanti in chloroform, and their nominal concentrations of 10 mg/ml were not verified. Lipid stocks were sealed with Teflon tape and parafilm and stored at −20°C.

ii. Electroformation.

Vesicles were made by electroformation (8). Two halves of a glass slide coated with indium-tin-oxide (ITO) (Delta Technologies, Loveland, CO) were heated on a heat block at 60°C, which is just below the boiling point of chloroform. A comparison of data from ITO-coated slides on a heat block at 75°C appears in Fig. S3.1. Stocks of phospholipids and cholesterol (with 0.8 mol% rhodamine-DPPE) in chloroform or chloroform/methanol were mixed to achieve a total of 0.25 mg total lipid and heated to 60°C for 15 min on the heat block. The lipid solutions were spread evenly across the slides with the side of a glass Pasteur pipette. As the solvent evaporated from the lipid layer, thin-film interference was visible by eye. The slide-halves were exposed to vacuum for ≥ 30 min to allow any remaining chloroform to evaporate. The two halves were assembled face-

to-face, separated by Teflon spacers of 0.3 mm thickness held in place with vacuum grease. The chamber was filled with 18 MΩ–cm water, sealed with vacuum grease, and attached to metal electrodes using binder clips. An AC voltage of 1.0 V at 10 Hz was applied across the electrodes for 1-2 h at 75°C while vesicles formed (60°C for DiphyPC/DPPC/cholesterol). This temperature was chosen to be well above the highest T_{melt} of any lipid used, to adequately incorporate all lipids into vesicles and to minimize uncertainty in transition temperatures (12). For vesicles containing DPPE, 60°C is not a sufficiently high electroformation temperature (Fig. S3.2). After electroformation, vesicles were transferred into an Eppendorf tube and typically imaged immediately (or within 2 h). From limited data on how lipid ratios in vesicles differ from ratios in stock solutions, we expect at least three of the lipids in our study (saturated PE-lipid, DOPC, and cholesterol) faithfully incorporate into electroformed vesicles (104).

iii. Vesicle Imaging.

Vesicle solutions were diluted to achieve roughly 100-200 vesicles per field of view (usually a 10:1 dilution) and placed between glass coverslips. Coverslip edges were coated with vacuum grease, a second coverslip was placed on top to seal the vesicle solution inside, and the coverslip assembly was placed on a layer of Omegatherm thermal paste (Omega Engineering, Norwalk, CT) on top of a Peltier temperature controller on a home-built microscope stage. Vesicles were imaged on a Nikon (Melville, NY) Eclipse ME600L upright epifluorescence microscope using a Hamamatsu (Bridgewater, NJ) C13440 camera. Contrast between phases in the membrane arises from preferential partitioning of the lipid dye into disordered phases. For every sample with coexisting phases, a representative image was selected for a field of view of vesicles at ~30°C (Figs. S3.4-3.6 and S3.9-3.11). Fiji (105) was used to crop the image to 300 x 300 pixels, to adjust brightness and contrast so that vesicle features were visible (gamma = 1), and to add scalebars.

iv. Transition Temperatures and Plotting.

Phase transition temperatures (T_{mix}, which denotes three possible transitions that result in an increase in the number of phases as temperature decreases: L→ L_o/L_d, L→ S/L, and S/L→ $S/L_o/L_d$) of membranes were first estimated, then measured. For estimates, an initial coverslip assembly was heated at ~1°C/min, and the approximate range of temperatures over which phase-separated domains disappeared was recorded. Temperature was then set 5-10°C above the estimated

transition. The initial coverslip assembly was discarded and replaced with a new one. Fields of vesicles (usually > 100 vesicles total) were imaged as temperature was decreased stepwise over a range of ≥ 12°C. At each step, temperature was allowed to equilibrate for ~1-2 min before images were collected. For each field image, the number of vesicles with phase-separated membranes and the number with uniform membranes were tabulated by hand. To calculate value of the transition temperature, T_{mix}, a non-linear least squares algorithm from the open-source Python library, SciPy (106), was used to fit a sigmoidal curve with the form

$$\%\ \text{Phase separated} = \text{Max} \,/\, \left(1 + e^{(-k(T - T_{mix}))}\right)$$

where Max is the maximum percent of vesicles that phase separate, k is the steepness of the curve, T_{mix} is the phase transition temperature located at the inflection point, and T is the temperature input variable. Plots of sigmoidal curves were generated using the open-source Python library, Matplotlib (107), and are shown in Figs. S3.13-3.18. Plots of ternary phase diagrams were generated using the open-source Python library, mpltern (108). All phase transition temperatures and errors are additionally recorded in Tables S3.1-3.8.

v. Measurement Errors.

Error was quantified in four ways: 1) For each sigmoidal curve, a 95% confidence interval (shown in Figs. S3.13-3.18) was calculated, which provides errors of the fit parameters. For T_{mix}, these fit errors are very small (< 0.5°C) and are recorded in Tables S3.1-S3.8. 2) For each sigmoidal curve, ½($|T_{90\%} - T_{10\%}|$) was calculated; this is half the range between temperatures at which 90% of vesicles and 10% of vesicles are phase separated (Figs. S3.13-3.18). These errors are recorded in Tables S3.1-3.8. 3) Three researchers tabulated numbers of phase-separated vesicles. To estimate the error that different researchers introduced, all of them tabulated the same four data sets in Fig. S3.19. The resulting values of T_{mix} were typically within ± 0.5°C. 4) Sample-to-sample variation was measured by standard deviations across three duplicate sample sets and nineteen triplicate sample sets, shown in bolded data in Tables S3.1-3.8. The average standard deviation across all duplicate and triplicate sample sets was 0.7 ± 0.6°C and ranged from 0.1°C to 2.8°C.

3.4 Results and Discussion.

i. Vesicles are stable over wide ranges of DPPE mole fractions.

Ternary lipid mixtures containing DPPE produce stable, giant vesicles over broad spans of temperature and mole fraction (Fig. 3.2). The solubility of cholesterol in PE-membranes is lower than in equivalent PC-membranes, so we maintained cholesterol fractions at ≤ 50 mol% to avoid exceeding cholesterol's solubility limit of 51 ± 3 mol% in DPPE membranes (41, 43).

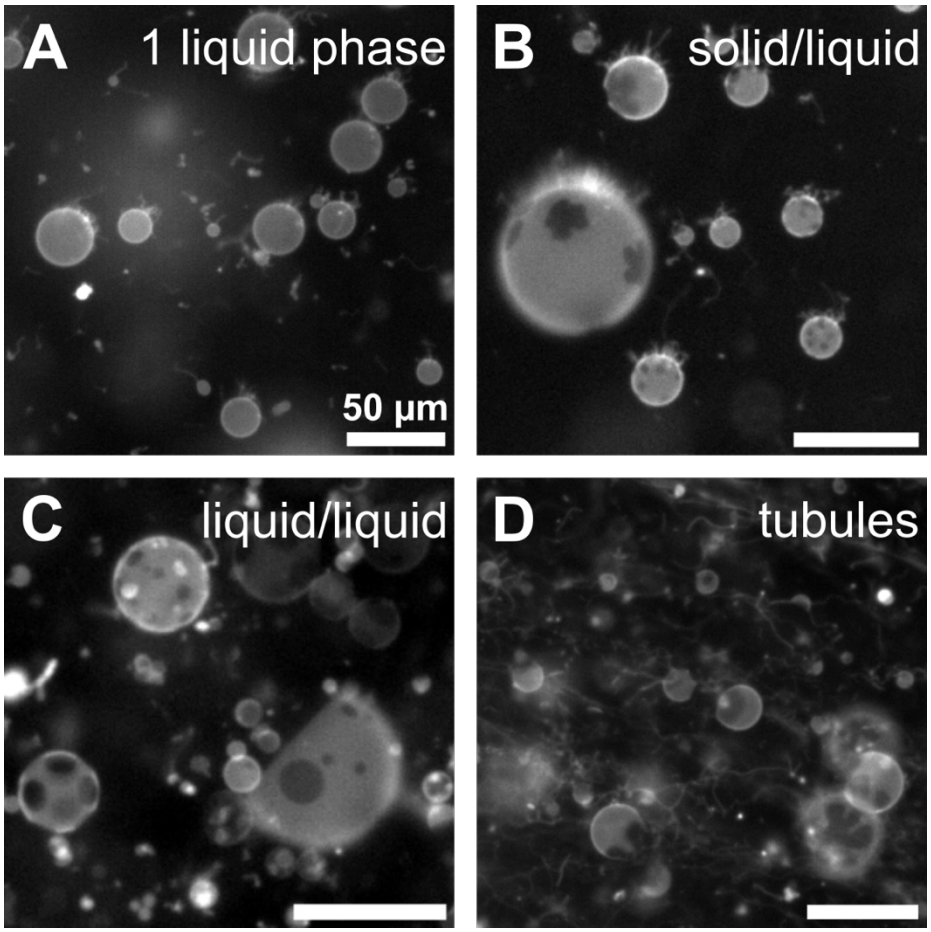

Figure 3.2. Lipid mixtures containing DPPE can form stable vesicles that phase separate, often with tubes. A) At high temperature (50°C), vesicle membranes of 20:50:30 DOPC/DPPE/cholesterol are in one liquid phase. **B)** At lower temperature (46°C), vesicles in the same sample phase separate into coexisting solid (dark) and liquid (bright) phases. Solid phases are characterized by noncircular domains that do not coalesce over time. **C)** Coexisting L_o and L_d liquid phases appear for some ratios of DiphyPC/DPPE/cholesterol, shown here for 30:40:30 at 45°C. Liquid phases are characterized by circular domains that merge in taut vesicles. **D)** Long tubules often emanate from vesicles containing DPPE, shown here for a ratio of 10:60:30 of DOPC/DPPE/cholesterol at 52°C.

Although DPPE's saturated chains make it less conical than unsaturated PE-lipids, challenges persist in forming ternary vesicles with DPPE. Nearly every vesicle we produced has high-curvature tubules (Fig. 3.2), and nearly every field of view contains a bright aggregate of lipids, unlike in corresponding samples with PC-lipids (14, 19). Moreover, when the combined mole fraction of DPPE and cholesterol exceeds 80-90 mol%, vesicle yields are too small for data collection. Although tubulation is not a necessary outcome of making vesicles with PE-lipids (109), tubulation is enhanced when temperature fluctuates near solid-liquid and liquid-liquid transitions (109, 110), and inclusion of cholesterol can reduce the temperature of the lamellar-H_{II} transition by 20°C (86).

ii. Replacing DPPC with DPPE eradicates liquid-liquid coexistence in ternary membranes.

Ternary membranes containing DPPE differ starkly from membranes containing the corresponding PC-lipid. In Fig. 3.3, liquid-liquid coexistence is obliterated across the entire phase diagram of DOPC/DPPE/cholesterol (Fig. 3.3B), whereas it persists across broad ranges of temperature and lipid composition in vesicles of corresponding PC-lipids (Fig. 3.3C) (14, 111).

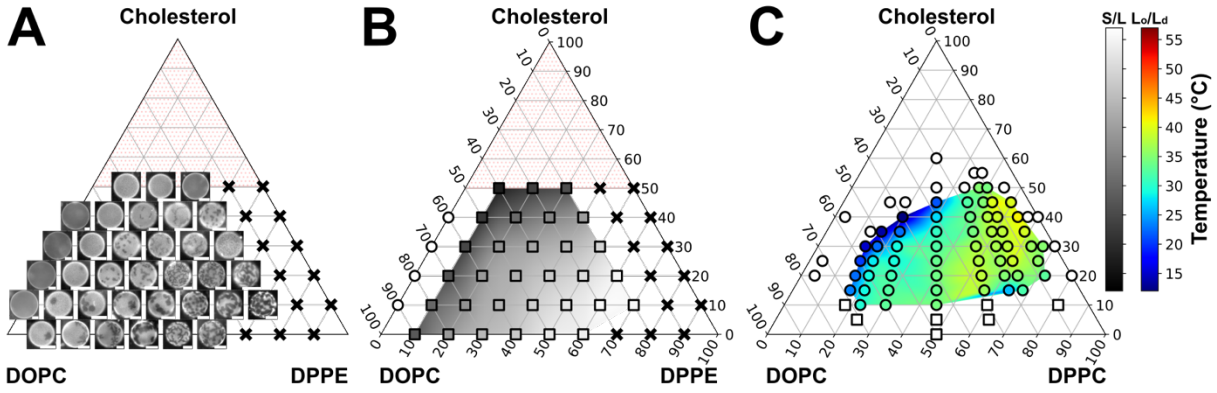

Figure 3.3. Vesicles of DOPC/DPPE/cholesterol exhibit coexisting solid and liquid phases (rather than coexisting liquid phases). A) Representative images at 30°C of vesicles of DOPC/DPPE/cholesterol. Solid phases are dark, and liquid phases are bright. Scale bars: 20 μm. Black X's mark compositions for which vesicle yields were too small to measure transition temperatures. Cholesterol mole fractions above 50% were avoided (red stipple) because they likely exceed maximum cholesterol levels that can incorporate in membranes with PE-lipids (41). Wider fields of view are in Fig. S3.4-3.6. **B)** Transition temperatures in vesicles of DOPC/DPPE/cholesterol, from one liquid phase at high temperature to coexisting solid and liquid phases at lower temperatures (filled squares). Unfilled circles indicate that only one liquid phase was observed. Errors in T_{mix} are shown in Fig. S3.3. Sigmoidal curves used to calculate T_{mix} are in Fig. S3.13-S3.15. All values are recorded in Table S3.1. **C)** Transition temperatures in vesicles of DOPC/DPPC/cholesterol, from one liquid phase at high temperature to either coexisting L_o and L_d phases (filled circles) or coexisting solid and liquid phases (squares), reproduced from (14).

In place of liquid-liquid coexistence, solid-liquid coexistence is observed (Fig. 3.3B). The area fraction of dark, noncircular, solid domains in vesicles monotonically increases as the mole fraction of DPPE increases (toward the bottom right vertex in the small images in Fig. 3.3A and in the large fields of view in Figs. S3.4-3.6). This observation is in line with the expectation that solid phases are enriched in lipids with high T_{melt}. Transition temperatures along the binary DOPC/DPPE axis follow the same trend as values reported for vesicles made by gentle hydration at 70.0°C (112), but consistently at least 2°C higher, even at low fractions of DPPE. This shift is not expected because DOPC and a similar PE-lipid (DLPE; di(12:0)PE) incorporate equally well in vesicles made by electroformation and by gentle hydration (104).

The lack of liquid-liquid phase separation in Fig. 3.3A is surprising because DPPE's melting temperature (T_{melt} = 62.3 ± 5.0°C (25)) is close to the melting temperature of DAPC (di(20:0)PC, T_{melt} = 65.3 ± 1.5°C (57)), and yet coexisting liquid phases persist in equivalent ternary membranes with DAPC (14). Increasing the T_{melt} of PC-lipids or sphingomyelins in ternary mixtures tends to simply increase liquid-liquid transition temperatures (14, 20, 23) rather than suppress liquid-liquid coexistence. Instead, Fig. 3.3A is reminiscent of ternary phase diagrams in which palmitoyl-ceramide (PCer) is the high melting temperature lipid (85). This is surprising because PCer is structurally very different from DPPE: PCer has no polar headgroup at all, which gives it an extraordinarily high melting temperature of 90.0°C (113).

We hypothesized that replacing the low-T_{melt} lipid of DOPC with DiphyPC (also known as di(16:0-4Me)PC) might produce liquid-liquid phase separation in membranes containing DPPE (Fig. 3.4). The methylated chains of DiphyPC give it a very low T_{melt} of < −120°C (103). Even though DiphyPC is typically associated with robust liquid-liquid phase separation over broad composition ranges (19, 82), in vesicles containing DPPE, coexisting liquid phases appear over only a small island of mole ratios near the center of the phase diagram (Fig. 3.4B). Liquid phases are characterized by round domains (Fig. 3.2C). In taut vesicles, these domains diffuse, collide, and coalesce until only one domain of each phase remains. The liquid ordered (L_o) phase is identified as being enriched in high-T_{melt} lipids and as excluding the dye relative to the liquid disordered (L_d) phase, as in Fig. S3.8.

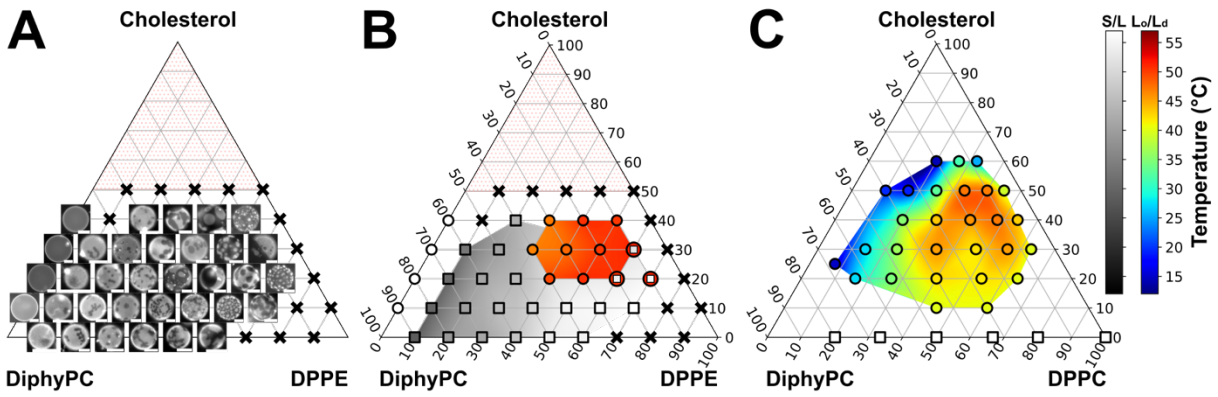

Figure 3.4. Vesicles of DiPhyPC/DPPE/cholesterol exhibit coexisting liquid phases and coexisting solid and liquid phases. A) Representative images at 30°C of vesicles of DiphyPC/DPPE/cholesterol. Dark, noncircular domains are solid. L_d domains are bright with respect to both L_o and solid domains. Scale bars: 20 µm. Black X's mark compositions for which vesicle yields were too small to measure transition temperatures. Cholesterol mole fractions above 50% were avoided (red stipple) because they likely exceed maximum cholesterol levels that can incorporate in membranes with PE-lipids (41). Wider fields of view are in Figs. S3.9-3.11. **B)** Transition temperatures in vesicles of DiphyPC/DPPE/cholesterol, from one liquid phase at high temperature to either coexisting solid and liquid phases (filled squares) or coexisting L_o and L_d phases (filled circles). Unfilled circles indicate that only one liquid phase was observed. At three lipid ratios (10:60:30, 10:70:20, and 20:60:20 DiphyPC/DPPE/cholesterol), vesicle membranes were in one liquid phase at high temperature, coexisting solid and liquid phases at an intermediate temperature, and three coexisting phases (L_o, L_d, and S) at a lower temperature. Errors in T_{mix} are shown in Fig. S3.7. Sigmoidal curves used to calculate T_{mix} values are in Figs. S3.16-3.18. All values are recorded in Tables S3.2 and S3.3. **C)** Transition temperatures in vesicles of DiphyPC/DPPC/cholesterol, from one liquid phase at high temperature to either coexisting L_o and L_d phases (filled circles) or coexisting solid and liquid phases (squares), reproduced from (19).

When coexisting solid and liquid phases are observed, the area fraction of solid phase increases with DPPE mole fraction, indicating the solid is enriched in DPPE (Fig. 3.4A, and large fields of view in Figs. S3.9-3.11).

iii. Replacing DPPC with DPPE makes Lo and solid phases distinguishable by fluorescence microscopy. An unexpected advantage of incorporating DPPE into ternary membranes is that Lo and solid phases become distinguishable by fluorescence microscopy, and subsequent transitions into the 3-phase region (Lo, Ld, and S) are clearly visible (Fig. 3.5). Previously, 3-phase coexistence has been observed by fluorescence microscopy for only a few combinations of dyes, lipids, and solutions (e.g., (114, 115)). As a result, identification of 3-phase regions by fluorescence microscopy has required observation of changes in domain shapes (20) or in the inability of domains to diffuse and coarsen quickly (19).

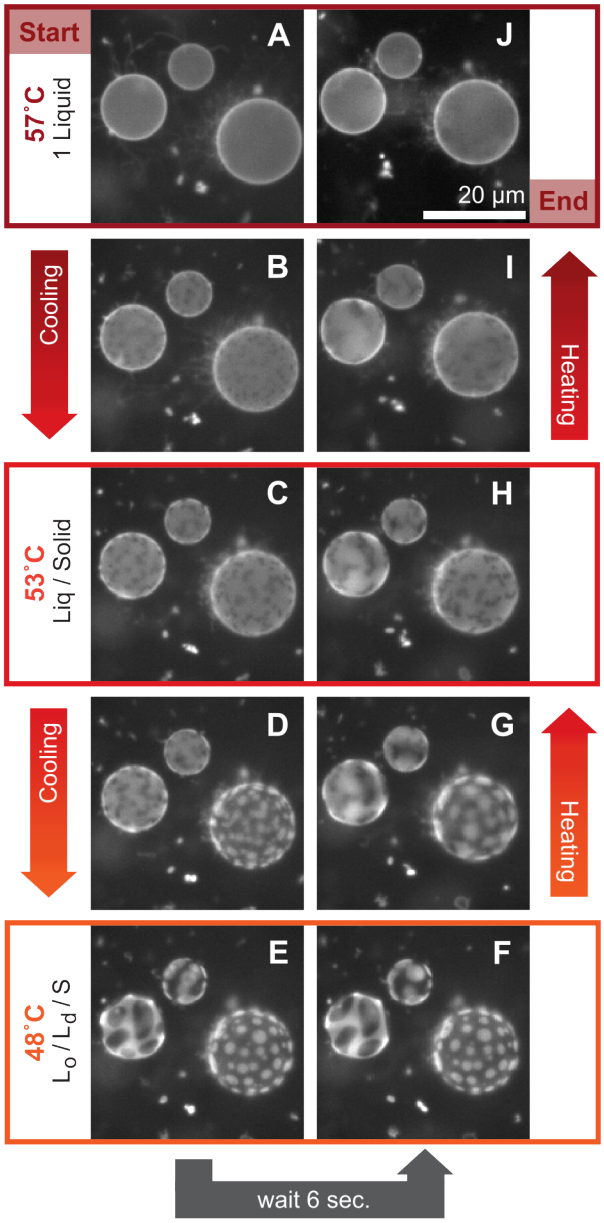

Figure 3.5. Liquid-liquid phase separation occurs at lower temperature than solid-liquid separation in 10:70:20 DiPhyPC/DPPE/cholesterol membranes. A) Vesicle membranes are in one liquid phase at high temperature. **B)** Solid domains nucleate at ~56°C. **C)** Domains of dark, noncircular, solid phase coexist with a bright, liquid phase. **D)** At ~52°C, the liquid phase begins demixing into L_o and L_d phases. The L_o phase is identified by an intermediate fluorescence level between the dark solid and bright L_d phases. **E)** At ~48°C, micron-scale regions of three fluorescence levels are observed, corresponding to solid, L_o, and L_d phases. Solid phases are usually wet by L_o domains. **E-F)** With time, domains diffuse, and liquid domains can merge. **F-J)** Phase transitions are reversible with temperature. Images correspond to Video S3.1; timepoints for images A–J are 0, 16, 31, 40, 48, 54, 70, 76, 96 and 119 sec, respectively. The transitions occur in the same order in vesicles of 10:60:30 and 20:60:20 DiphyPC/DPPE/cholesterol, with additional videos provided (Videos S3.2 and S3.3).

Without the ability to distinguish L_o and solid phases, alternative spectroscopic techniques (20, 111, 116) or atomic force microscopy (115, 117) must be deployed to conclusively identify the 3-phase region.

Figure 3.5 shows an example of a liquid phase at a high temperature (57°C) demixing into coexisting liquid and solid phases at a lower temperature (53°C). As temperature decreases further (48°C), three fluorescence levels are visible, a bright L_d phase, a gray L_o phase, and a dark solid phase. In many cases, as in Fig. 3.5, solid domains constrain the motion of the liquid domains. Additional images of vesicles with 3-phase coexistence are shown in Fig. S3.12.

Viewed in the 3-dimensional space of a ternary phase diagram, the volume in which all three phases (L_o, L_d, and S) coexist is most easily imagined as an irregular triangular pyramid, with its tip pointing up toward high temperatures. In traditional ternary membranes with PC-lipids (e.g., DOPC/DPPC/cholesterol), the pyramid is shaped like a shard lying on its side, with two long edges defined by long tie-lines between the L_d phase and the other phases (116). In contrast, in the DiphyPC/DPPE/cholesterol phase diagram in Fig. 3.4B, the pyramid must be more compact because the L_o/L_d coexistence region is smaller. The face of the pyramid that touches the L_o/S coexistence region must have a shallow slope because transitions as in Fig. 3.5 (from a 2-phase, L_o/S region to a 3-phase, L_o/L_d/S region) occur over lipid compositions that span at least 10 mol%.

Because L_o and S phases are distinguishable by fluorescence microscopy, we can learn more about how the substitution of DPPE for DPPC results in a phase diagram with primarily solid-liquid coexistence (Fig. 3.4), as opposed to a diagram with only liquid-liquid coexistence (DiphyPC/DPPC/cholesterol, (19)). The change from DPPE to DPPC involves the addition of only three methyl groups to the lipid headgroup. In Fig. 3.6, we add these methyl groups one-by-one for three lipid ratios. The largest change occurs upon addition of the first methyl group, whereupon temperatures of the 2-phase (S/L) and 3-phase (L_o/L_d/S) transitions become nearly indistinguishable (Fig. 3.6).

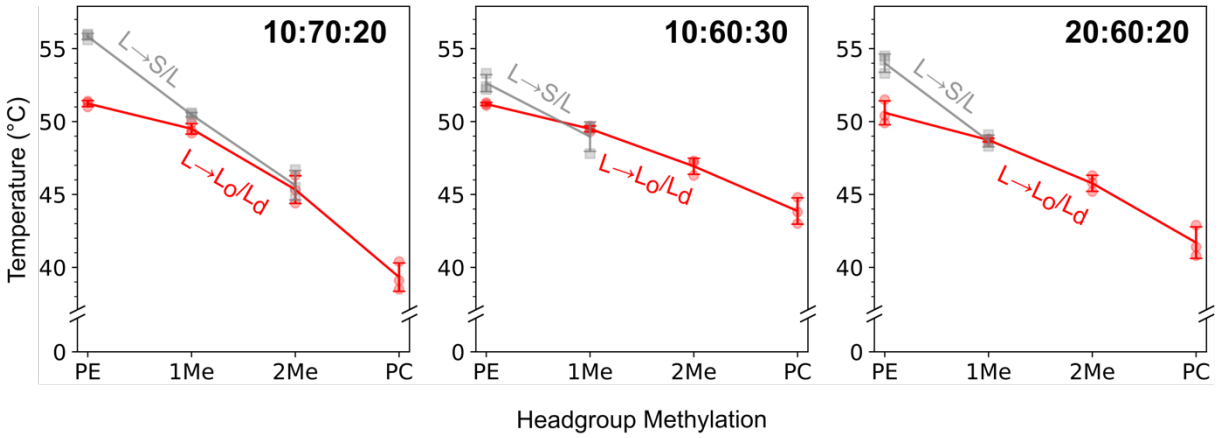

Figure 3.6. Methylation of DPPE headgroup eradicates solid-liquid coexistence at high temperatures. As temperature is decreased in vesicles of 10:70:20, 10:60:30, and 20:60:20 DiphyPC/DPPE/cholesterol (denoted "PE" on each x-axis) transitions are observed from one liquid phase at high temperature, to coexisting solid and liquid phases, and then to three phases (L_o, L_d, and S). For the three mixtures, DPPE was replaced by singly- ("1Me), doubly- ("2Me"), or triply-methylated ("PC") versions of the molecule. Gray squares show temperatures at which coexisting solid and liquid phases appear, and red circles show temperatures at which both L_o and L_d phases appear, for three independent measurements. Error bars are standard deviations of the triplicate measurements. Lines through triplicate averages are to guide the eye and are not fits to a model. Corresponding data are tabulated in Tables S3.2-3.8.

Of course, many PE-lipids beyond DPPE are relevant and interesting. One strong outcome of our research would be to facilitate future investigations of liquid-liquid phase separation in membranes containing other PE-lipids. Of high interest would be PE-lipids with unsaturated chains and with vinyl linkages to the chains (plasmalogens), both of which are prevalent in biological membranes and have been the subject of molecular dynamics simulations (5, 80, 99, 118–121).

3.5 Conclusions.

In this manuscript, we substituted a PE-lipid (DPPE) for a PC-lipid (DPPC) in ternary lipid membranes. Changes to the molecular structure are small: the two lipids differ by only three methyl groups. However, changes to the miscibility phase diagrams of ternary membranes containing the lipids are large. Liquid-liquid phase separation is entirely absent from the phase diagram of vesicles of DOPC/DPPE/cholesterol, and only a small island of liquid-liquid phase separation appears in the phase diagram of vesicles of DiphyPC/DPPE/cholesterol. Inside that island, membranes of a small set of compositions begin first in a liquid phase at high temperature, then

separate into coexisting solid and liquid phases as temperature is decreased, and then undergo a transition into a three-phase region after decreasing the temperature further. This three-phase region contains coexisting liquid-ordered, liquid-disordered, and solid phases, all of which are distinguishable by fluorescence microscopy. In most other cases, transitions into the three-phase region are difficult to observe by microscopy, due to solid phases nucleating within liquid-ordered phases and/or due to poor contrast of fluorophores between liquid-ordered and solid phases. Ideally, our investigation of ternary membranes containing DPPE will serve as a starting point for other researchers to map the phase behavior of membranes containing other PE-lipids, especially the unsaturated PEs or plasmalogens prevalent in biological membranes.

3.6 Acknowledgements.

This research was supported by National Science Foundation grant MCB-1925731 and MCB-2325819 to SLK. The authors thank Bob Weng for preliminary experiments.

3.7 Supporting Material.

i. Supporting Video Descriptions.

Video S3.1
Timelapse video of membrane phase transitions for vesicles composed of 10:70:20 DiphyPC/DPPE/cholesterol. Temperature is first ramped from high to low. Solid domains nucleate at ~56°C. Domains of dark, noncircular, solid phase coexist with a bright, liquid phase. At ~52°C, the liquid phase begins demixing into L_o and L_d phases. The L_o phase is identified by an intermediate fluorescence level between the dark solid and bright L_d phases. At ~48°C, micron-scale regions of three fluorescence levels are observed, corresponding to solid, L_o, and L_d phases. Liquid domains can diffuse around and merge over time but may be constrained by the solid phase. Solid phases are usually wet by L_o domains. Temperature is ramped back up to 52°C, and then to 56°C, showing that the phase transitions are reversible. Video corresponds to images shown in Fig. 3.5 of the main text.

Video S3.2

Timelapse video of membrane phase transitions for vesicles composed of 10:60:30 DiphyPC/DPPC/cholesterol. Temperature is first ramped from high to low. Solid domains nucleate at ~53°C. Domains of dark, noncircular, solid phase coexist with a bright, liquid phase. At ~51°C, the liquid phase begins demixing into L_o and L_d phases. The L_o phase is identified by an intermediate fluorescence level between the dark solid and bright L_d phases. At ~50°C, micron-scale regions of three fluorescence levels are observed, corresponding to solid, L_o, and L_d phases. Liquid domains can diffuse around and merge over time but may be constrained by the solid phase. Solid phases are usually wet by L_o domains. Temperature is ramped back up to 52°C, and then to 56°C, showing that the phase transitions are reversible.

Video S3.3

Timelapse video of membrane phase transitions for vesicles composed of 20:60:20 DiphyPC/DPPC/cholesterol. Temperature is first ramped from high to low. Solid domains nucleate at ~54°C. Domains of dark, noncircular, solid phase coexist with a bright, liquid phase. At ~51°C, the liquid phase begins demixing into L_o and L_d phases. The L_o phase is identified by an intermediate fluorescence level between the dark solid and bright L_d phases. At ~50°C, micron-scale regions of three fluorescence levels are observed, corresponding to solid, L_o, and L_d phases. Liquid domains can diffuse around and merge over time but may be constrained by the solid phase. Solid phases are usually wet by L_o domains. Temperature is ramped back up to 54°C, and then to 58°C, showing that the phase transitions are reversible.

ii. Supporting Figures.

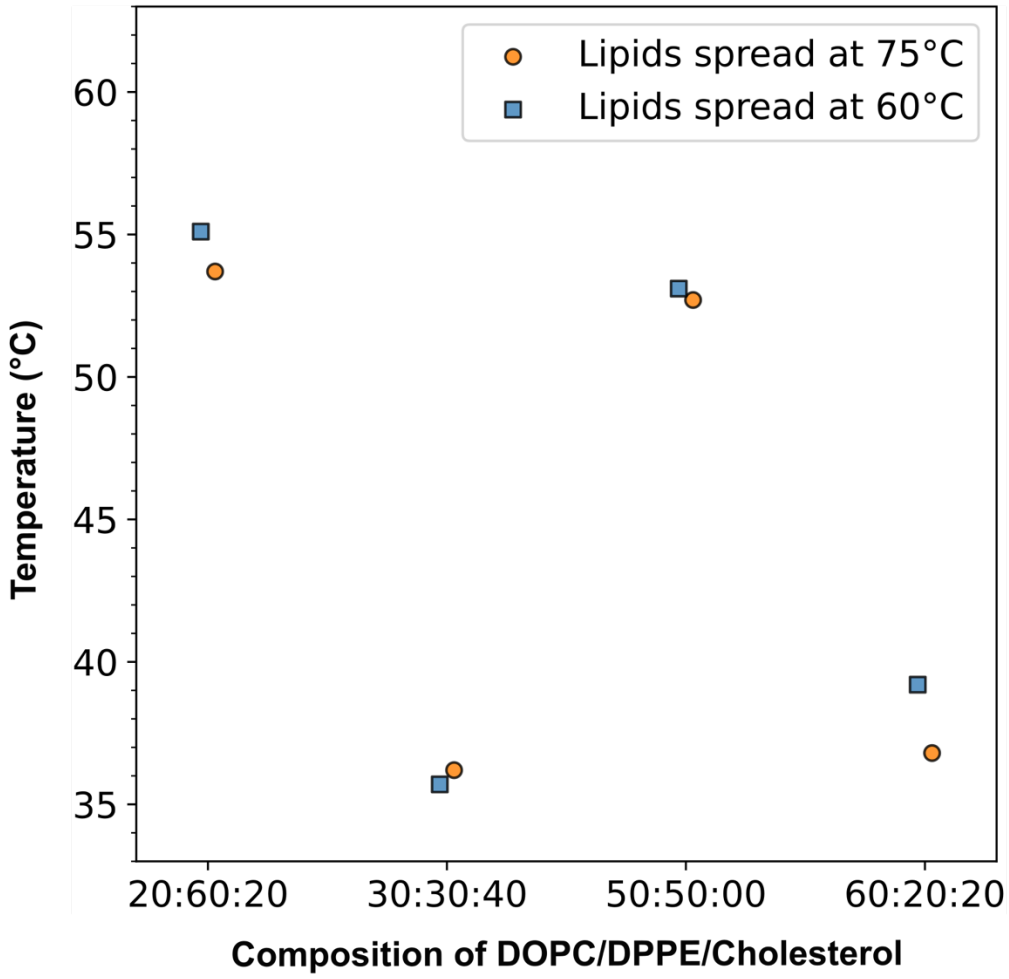

Figure S3.1. Lipid films spread on slides at 60°C or 75°C (and then electroformed at 75°C) produce vesicles with similar T_{mix} values. In all experiments in the main text, vesicles were electroformed at 75°C. This temperature was chosen to be well above the T_{melt} of DPPE, which is 62.3 ± 5.0°C (25). Ideally, to prepare lipid films for electroformation, they should have been spread on indium-tin-oxide slides at the same high temperature. However, it is technically difficult to do so, given that chloroform boils at 61°C. Therefore, we assessed if spreading the films at 60°C, a temperature just below chloroform's boiling point, affected the miscibility phase transition temperature of subsequently electroformed vesicles. We would expect bigger effects for mixtures with higher mole fractions of DPPE, which are the first three mixtures in the plot. For these mixtures, differences between T_{mix} of vesicles made from films spread at 60°C and 75°C are inconsequential, and justify our decision to spread all films at 60°C. We were perplexed but not concerned by the larger difference in T_{mix} for the mixture with 20% DPPE (the rightmost mixture in the plot). For all four samples, the average difference in T_{melt} between samples spread at 60°C and 75°C is ± 1.2°C (range 0.4°C to 2.4°C). For comparison, sample-to-sample variations are ± 0.1 to ± 1.3°C (range 0.1°C to 2.8°C).

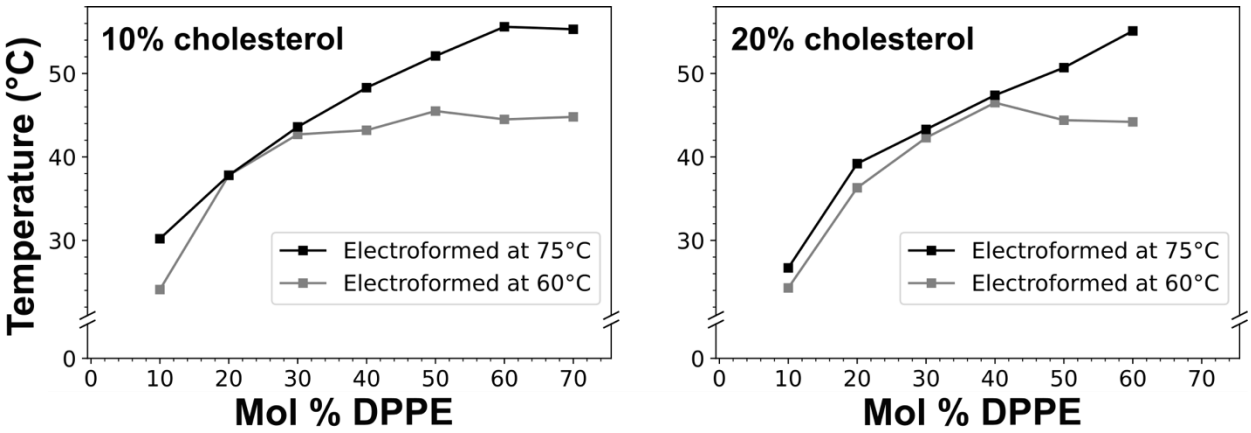

Figure S3.2. DOPC/DPPE/cholesterol vesicles electroformed at 60°C (below the T_{melt} for DPPE) exhibit lower T_{mix} values than vesicles electroformed at 75°C, especially at higher DPPE mole fractions. In all experiments in the main text, vesicles were electroformed at 75°C, well above T_{melt} for DPPE (62.3 ± 5.0°C (25)). To illustrate the importance electroforming above T_{melt}, several ternary lipid mixtures composed of DOPC/DPPE/cholesterol were electroformed at 60°C, a temperature commonly used for electroforming vesicles containing PC-lipids such as POPC, DOPC, and DPPC. At higher DPPE compositions, the measured Tmix value is as much as ~10°C lower for samples electroformed at 60°C than at 75°C. These results imply that insufficient DPPE is incorporated into vesicles at 60°C and are consistent with (12).

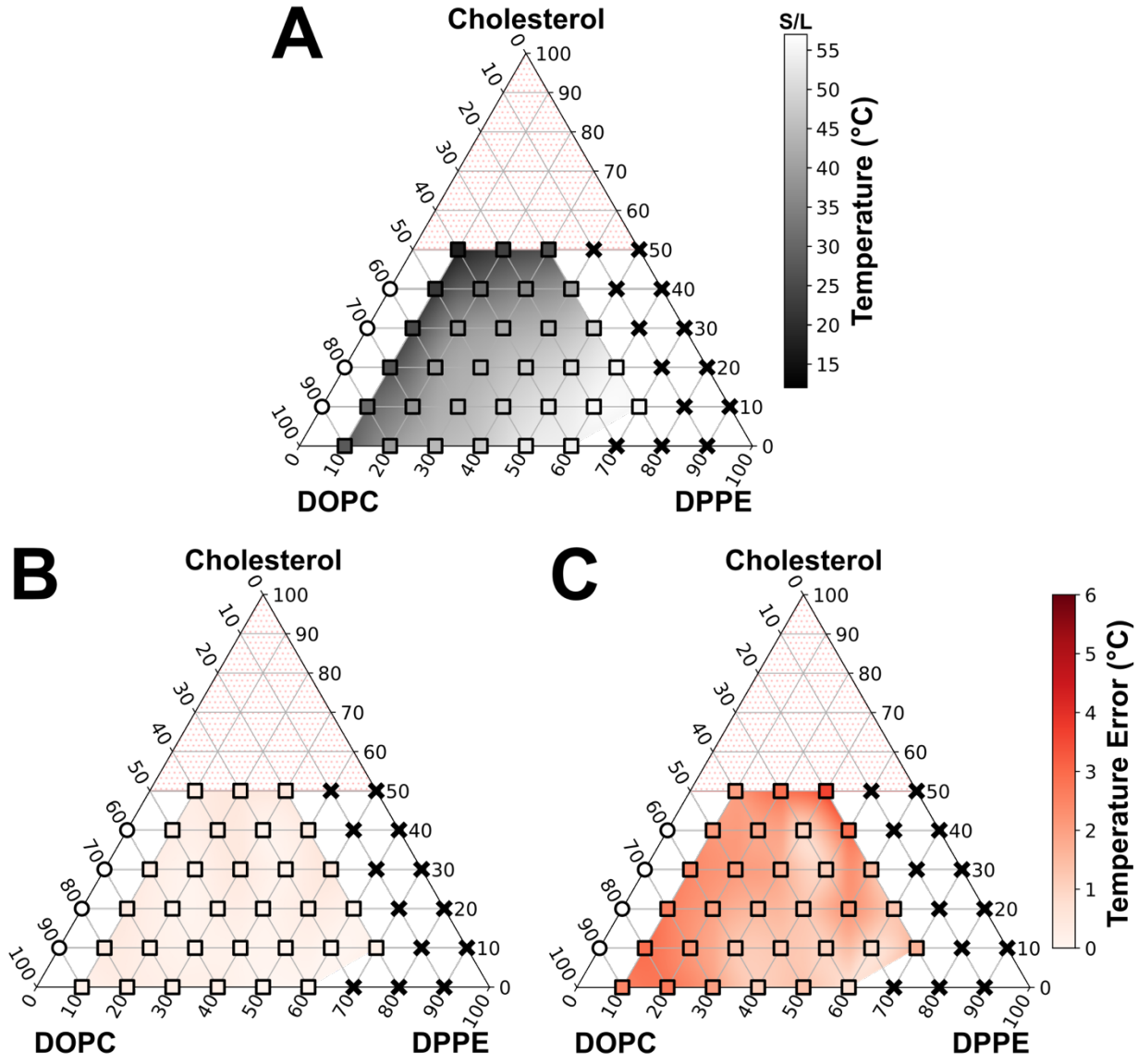

Figure S3.3. Two methods of assessing error from single measurements of T_{mix} for vesicles of DOPC/DPPE/Cholesterol. A) Temperatures of phase transitions from one liquid at high temperature to coexisting solid and liquid phases at lower temperatures, from Fig. 3.3B. **B)** Error in the T_{mix} fit parameter calculated from 95% confidence intervals of the sigmoidal fits (Figs. S3.13-3.15), centered at $T = T_{mix}$. This method yields very small errors in T_{mix} (< 0.5°C), indicating the sigmoidal fits are good. However, the errors do not give information about the breadth of the transition. **C)** Error in T_{mix} calculated as $\frac{1}{2}(|T_{90\%} - T_{10\%}|)$, which is half the difference between the temperature at which 90% of vesicles are phase separated and that at which 10% are phase separated. Errors calculated by this method give more information about sample preparation and the shape of the phase boundary. Smaller errors reflect more uniformity in vesicle-to-vesicle composition and/or more constant transition temperatures from composition to composition. In the absence of independent measurements to measure standard deviations, this method can provide a useful way to assess experimental error. Corresponding data are tabulated in Table S3.1.

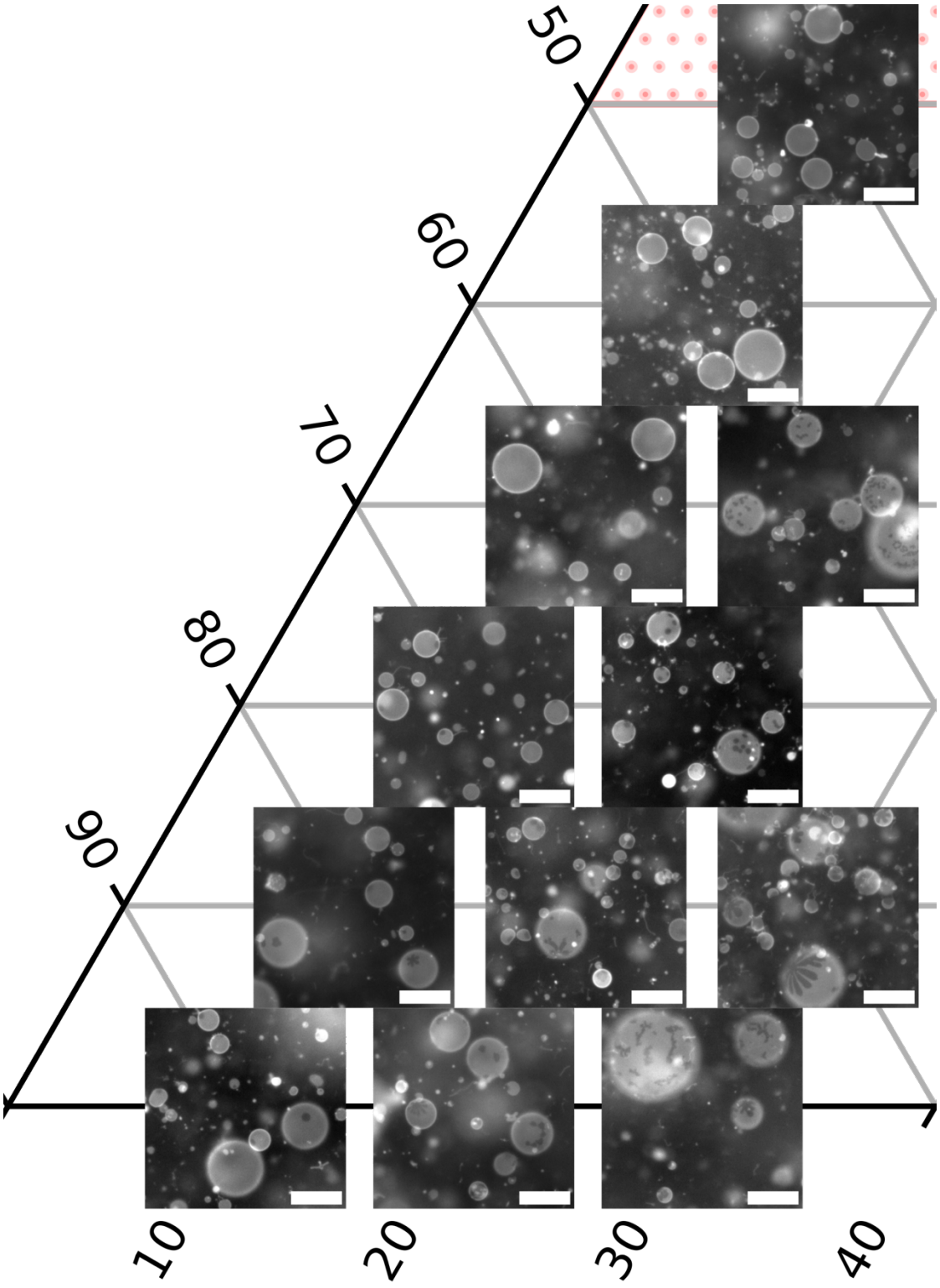

Figure S3.4. Representative fields of view at 30°C for vesicles made of DOPC/DPPE/cholesterol, covering the left third of the phase diagram in Figure 3.3B of the main text. The vertex at the left represents 100% DOPC, and high cholesterol is toward the top. Scalebars are 50 μm.

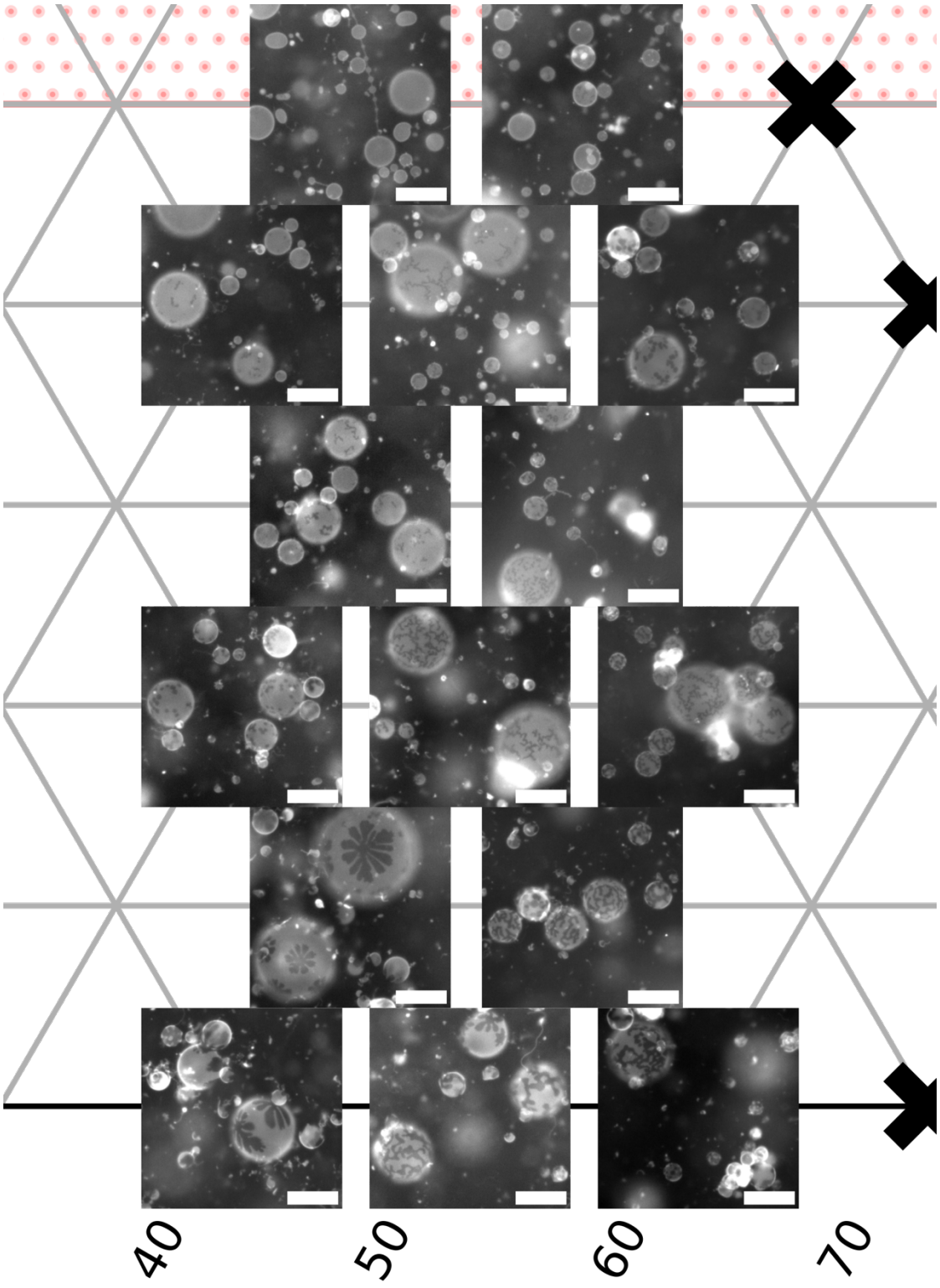

Figure S3.5. Representative fields of view at 30°C for vesicles made of DOPC/DPPE/cholesterol, covering the middle third of the phase diagram in Figure 3.3B of the main text. High DOPC fractions are on the left, high DPPE fractions on the right, and high cholesterol toward the top. Scalebars are 50 μm.

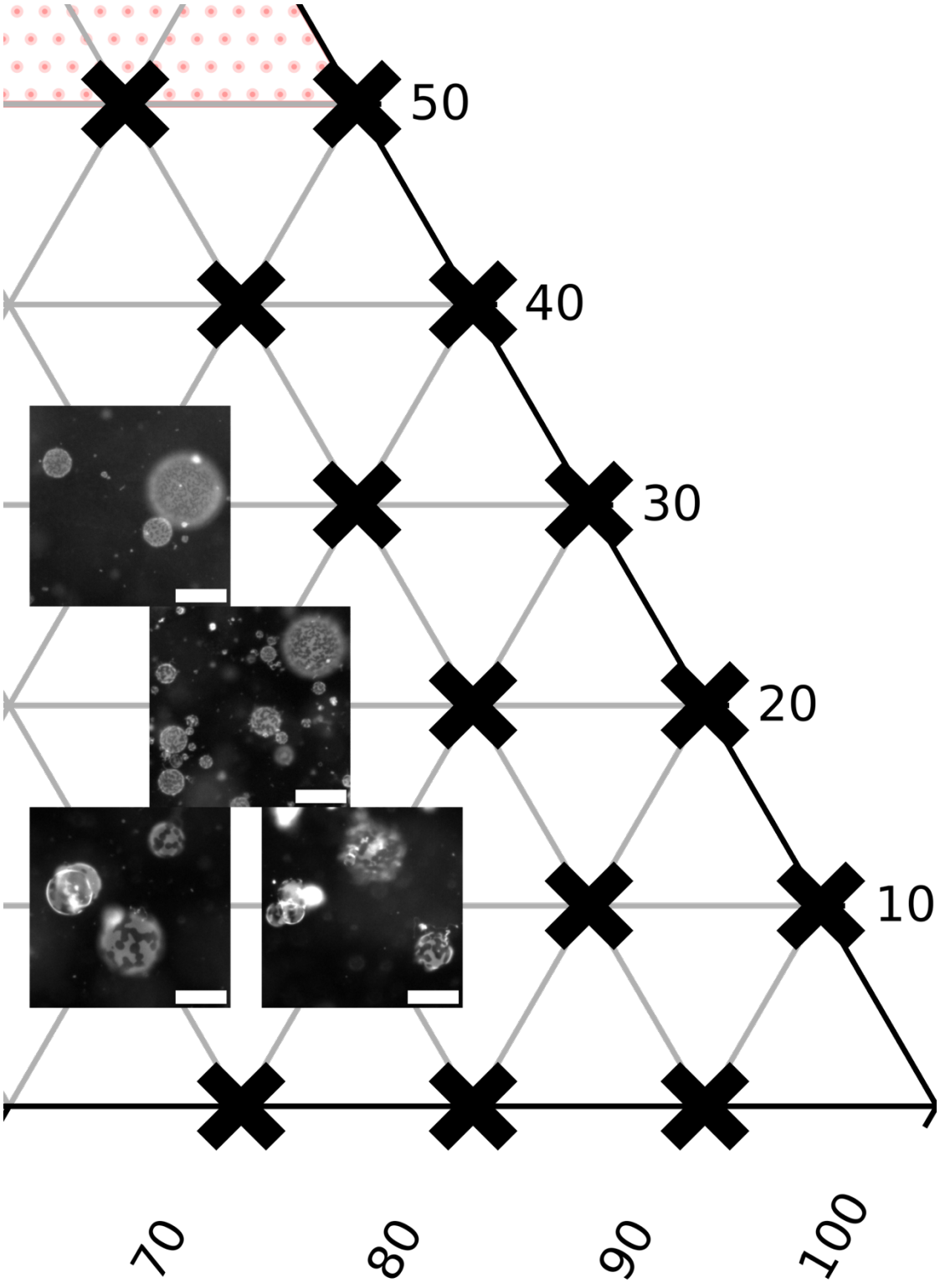

Figure S3.6. Representative fields of view at 30°C for vesicles made of DOPC/DPPE/cholesterol, covering the right third of the phase diagram in Figure 3.3B of the main text. The vertex at the right represents 100% DPPE, and high cholesterol is toward the top. Scalebars are 50 μm.

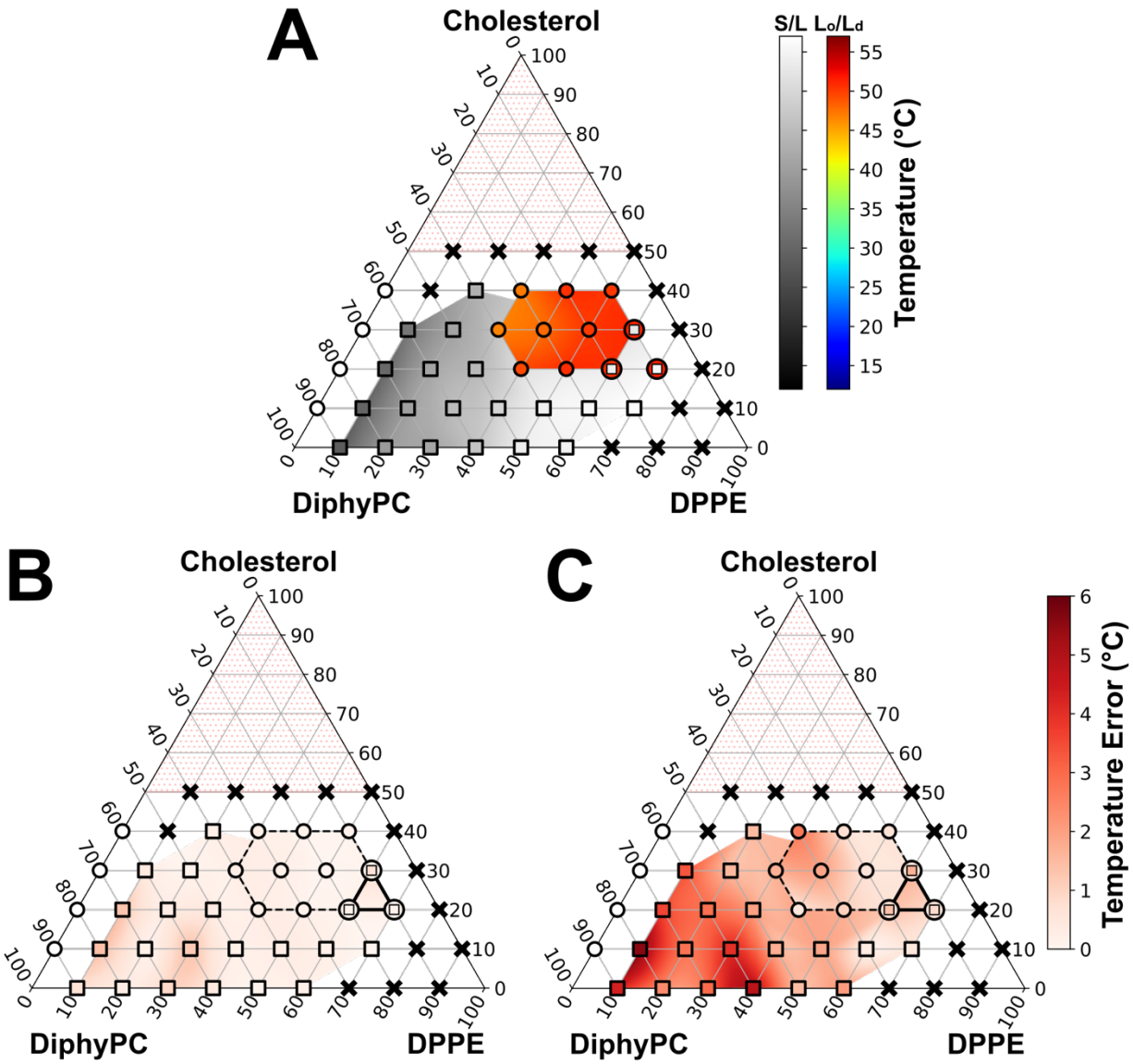

Figure S3.7. Two methods of assessing error from single measurements of T_{mix} for vesicles of DiphyPC/DPPE/Cholesterol. A) Temperatures of phase transitions from one liquid to coexisting solid and liquid phases (squares) or to coexisting Lo and Ld phases (circles), from Fig. 3.4B. **B)** Error in the T_{mix} fit parameter calculated from 95% confidence intervals of the sigmoidal fits (Figs. S3.16-3.18), centered at $T = T_{mix}$. This method yields very small errors in T_{mix} (typically < 0.5°C), indicating good sigmoidal fits. However, the errors do not give information about the breadth of the transition. Compositions for which the transition is from one liquid phase to coexisting Lo and Ld phases are bounded by a dotted black line. Compositions for which we could clearly observe a transition into a three-phase region are bounded by a solid black line. **C)** Error in T_{mix} calculated as $\frac{1}{2}(|T_{90\%} - T_{10\%}|)$, which is half the difference between the temperature at which 90% of vesicles are phase separated and that at which 10% are phase separated. Errors calculated by this method give more information about sample preparation and the shape of the phase boundary. Smaller errors reflect more uniformity in vesicle-to-vesicle composition and/or more constant transition temperatures from composition to composition. In the absence of independent measurements to measure standard deviations, this method can provide a useful way to assess experimental error. Corresponding data are tabulated in Tables S3.2 and S3.3.

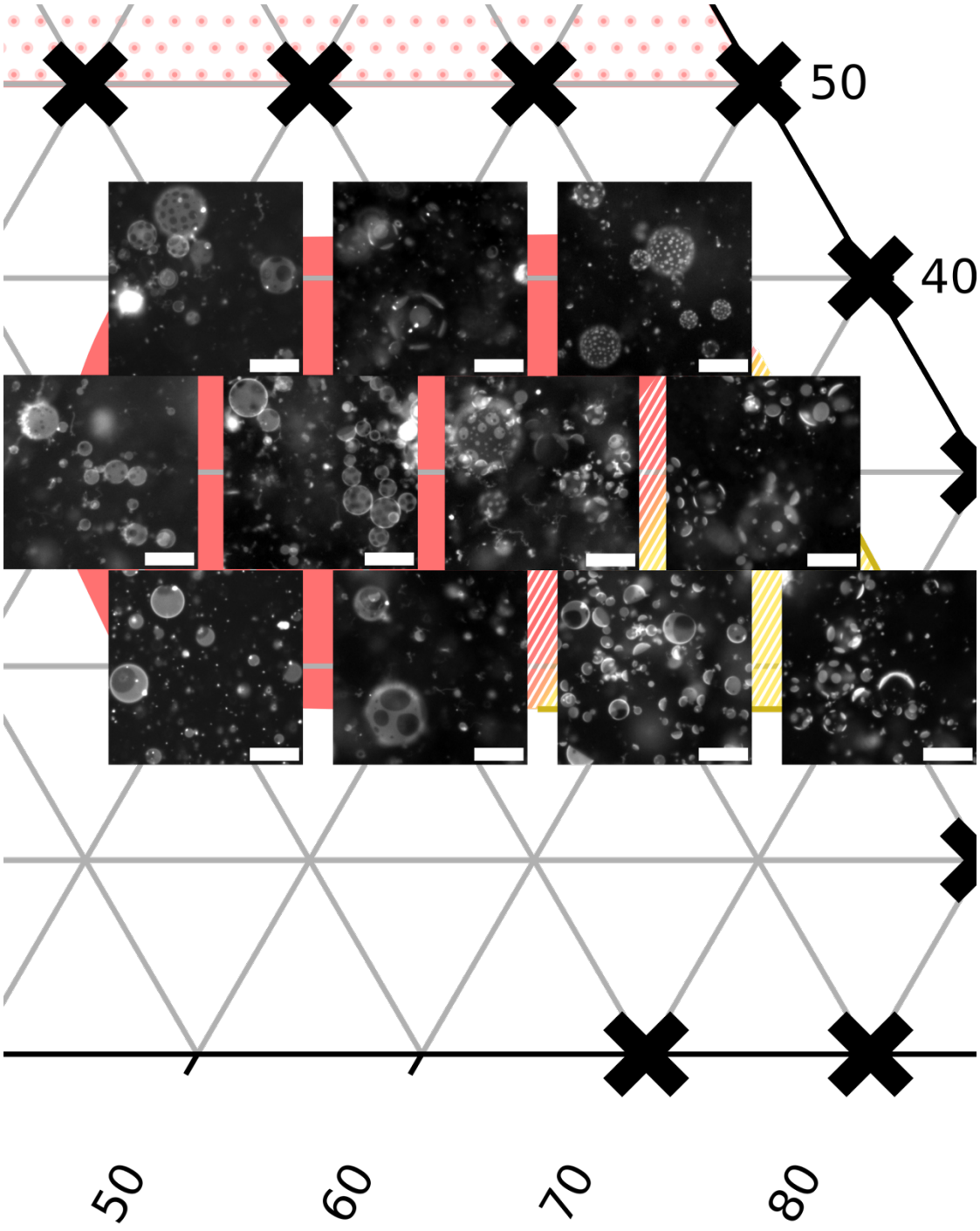

Figure S3.8. Representative fields of view for vesicles of DiphyPC/DPPE/cholesterol in the liquid-liquid coexistence region in Figure 3.4B in the main text. Vesicle images were collected between 46-47°C. The region with a red background approximates the L_o/L_d region at this temperature, and the region with a yellow background approximates the 3-phase triangle. Because data were taken in increments of 10 mol%, the fade from red to yellow represents uncertainty in the location of the left edge of the 3-phase triangle. Scalebars are 50 μm.

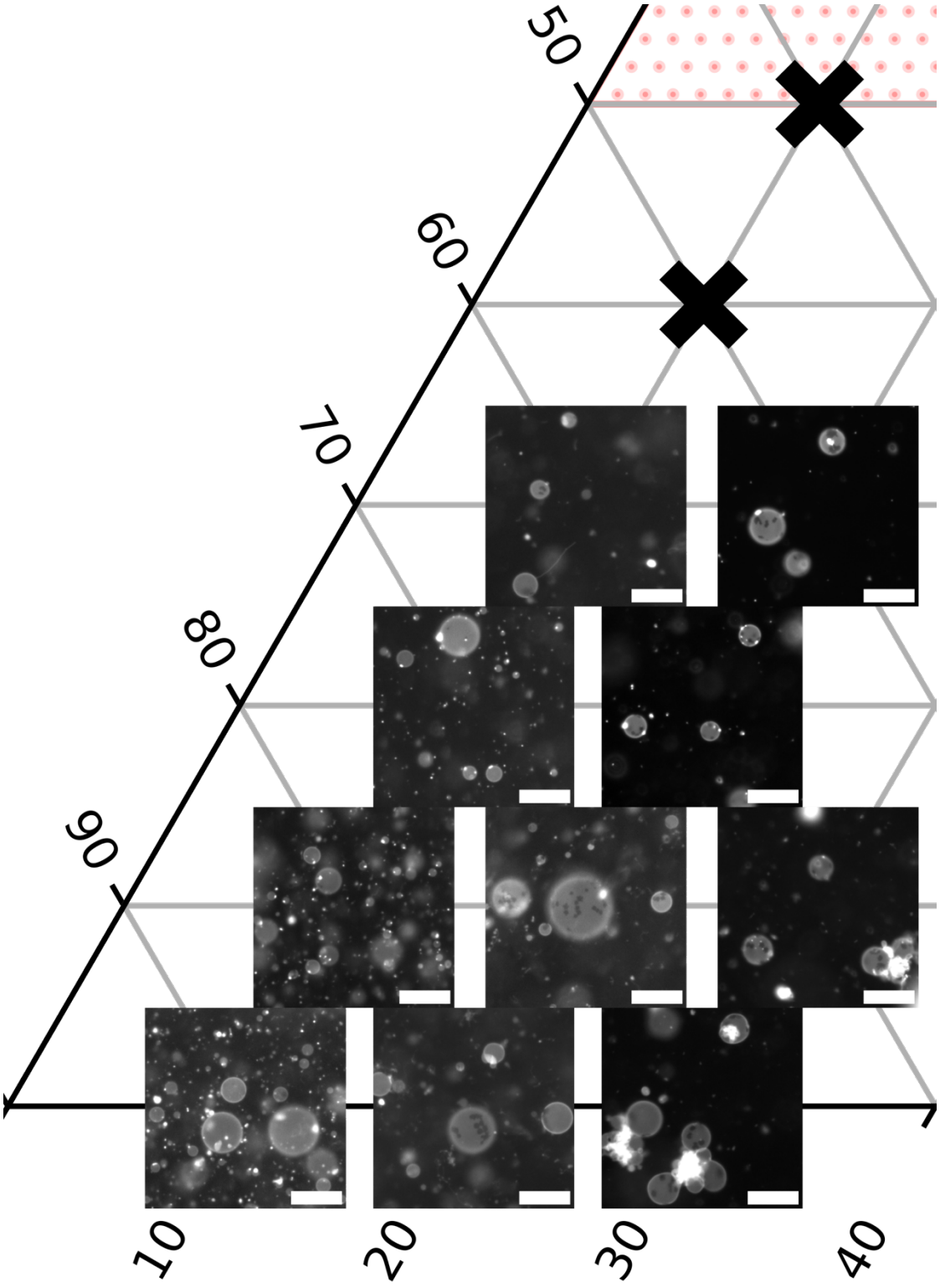

Figure S3.9. Representative fields of view at 30°C for vesicles made of DiphyPC/DPPE/cholesterol, covering the left third of the phase diagram in Figure 3.4B of the main text. The vertex at the left represents 100% DiphyPC. High cholesterol is toward the top. Scalebars are 50 μm.

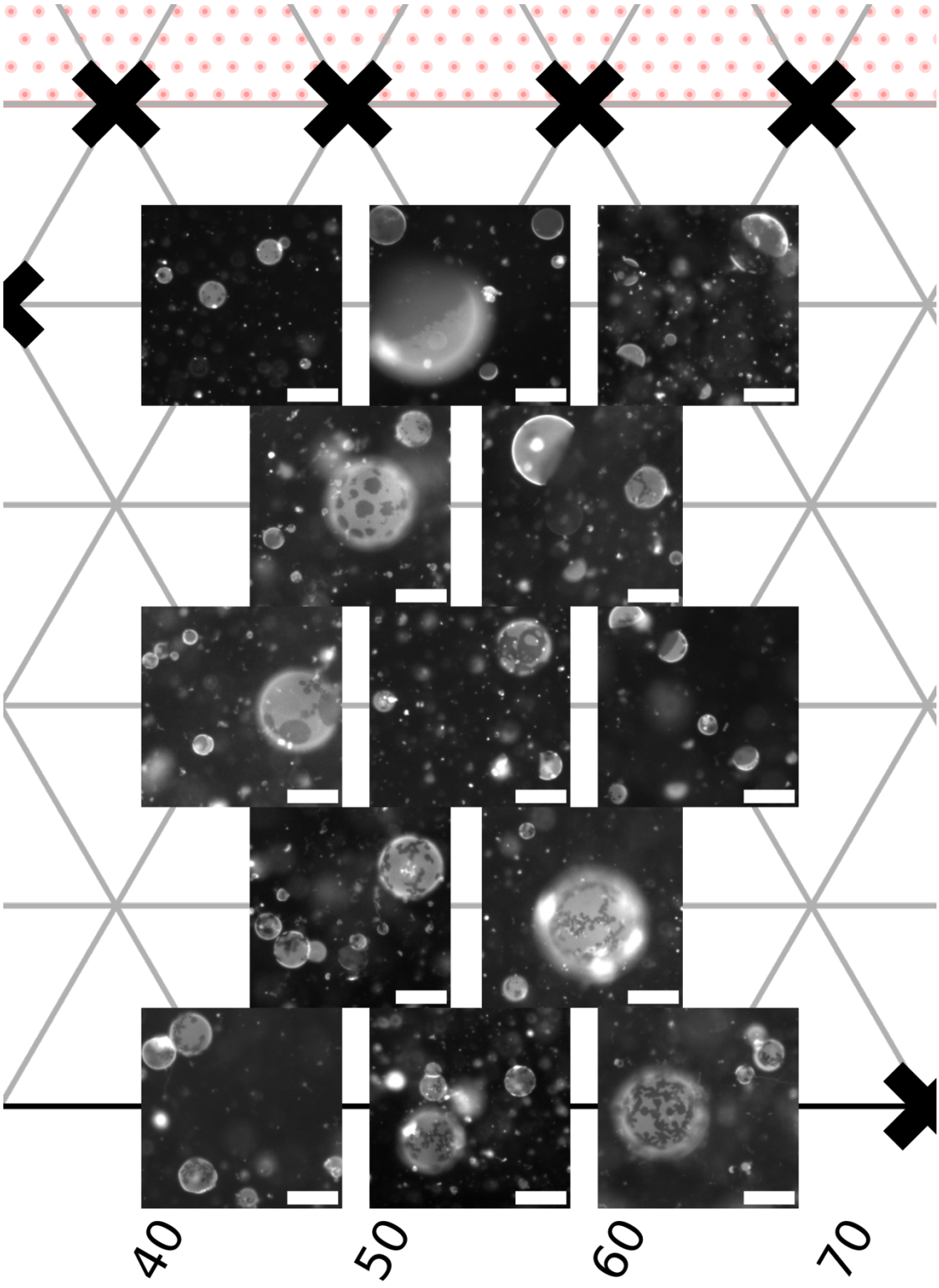

Figure S3.10. Representative fields of view at 30°C for vesicles made of DiphyPC/DPPE/cholesterol, covering the middle third of the phase diagram in Figure 3.4B of the main text. High DiphyPC fractions are on the left, high DPPE fractions on the right, and high cholesterol toward the top. Scalebars are 50 μm.

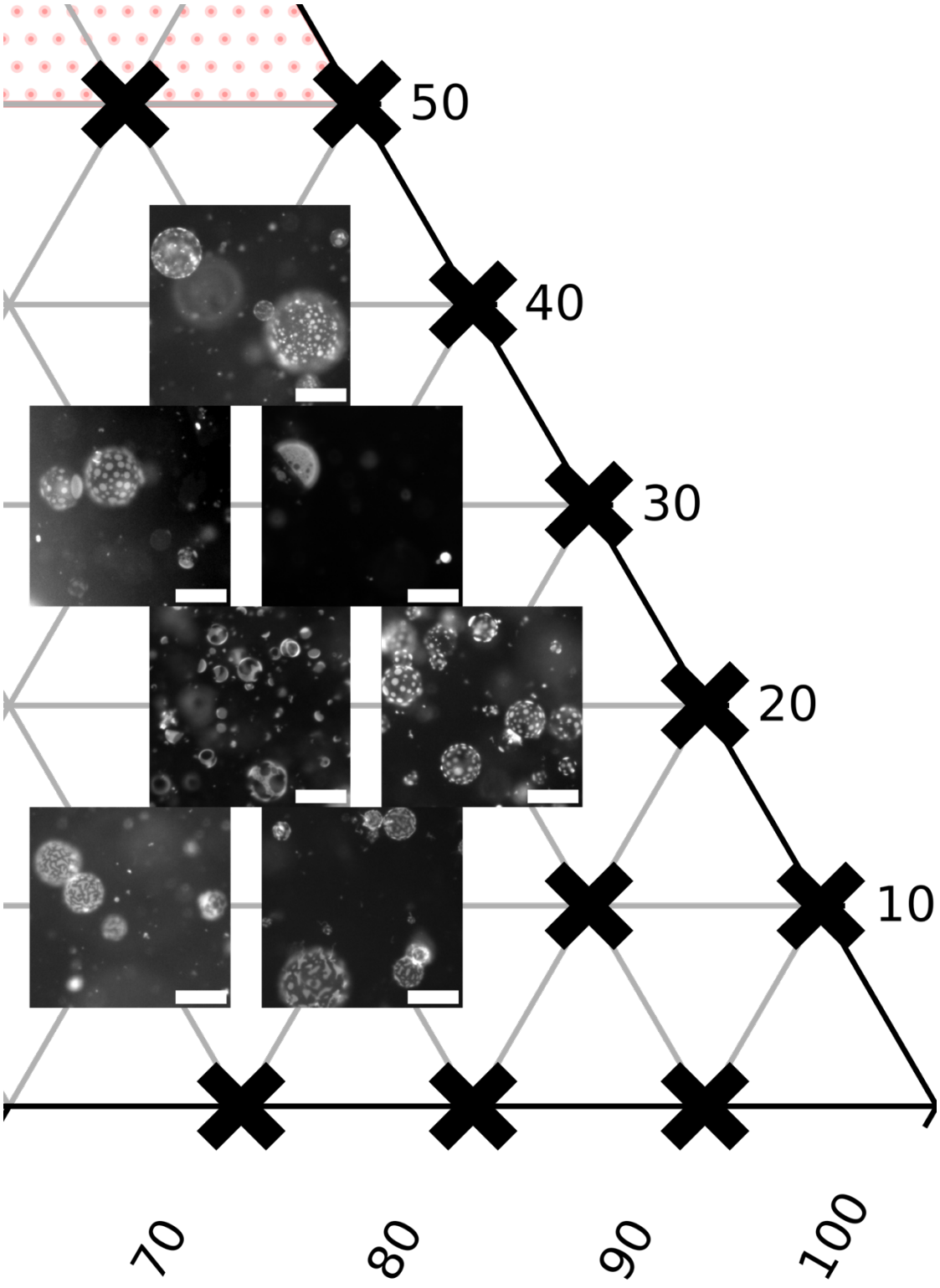

Figure S3.11. Representative fields of view at 30°C for vesicles made of DiphyPC/DPPE/cholesterol, covering the right third of the phase diagram in Figure 3.4B of the main text. The vertex at the right represents 100% DPPE, and high cholesterol is toward the top. Scalebars are 50 μm.

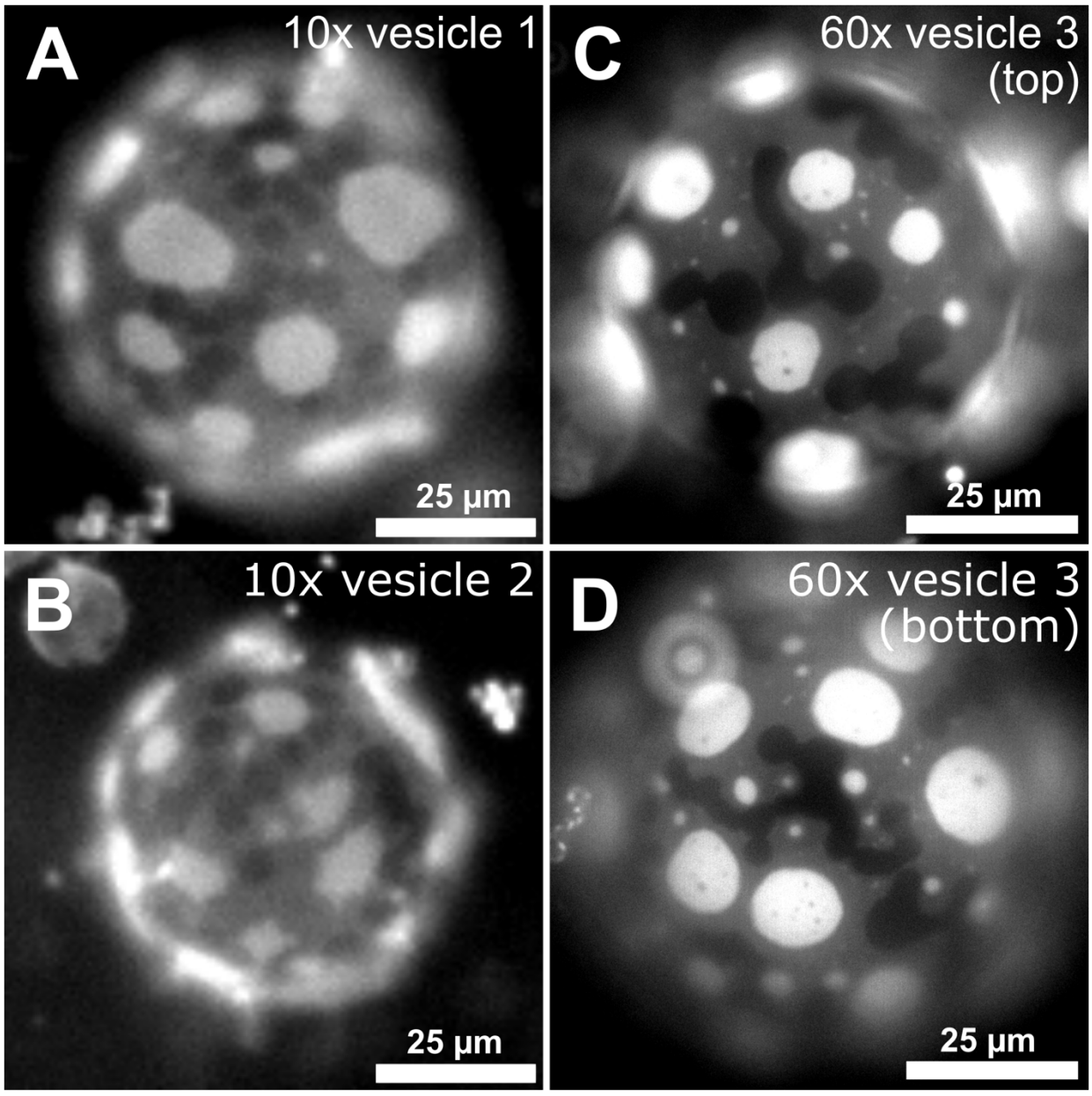

Figure S3.12. Images of vesicles composed of 10:70:20 DiphyPC/DPPE/cholesterol with three fluorescence intensities due to 3-phase coexistence of L_d-phase domains (bright), a L_o-phase domains (middle gray), and solid-phase domains (dark). In all cases, vesicles are close to a transition temperature in which vesicles with S/L coexistence were cooled into a region of S/L_d/L_o coexistence. Shapes of the L_d domains are not static; they are typically noncircular due to low line tension, but they can also be noncircular due to constraints imposed by neighboring solid domains. **A-B)** Images of two different vesicles, collected with a 10x objective. **C-D)** Images of the top and bottom hemispheres of a single vesicle exhibiting three distinct fluorescence levels for coexisting L_o, L_d, and solid phases. As would be expected, images collected with a 60x objective are at higher resolution than those collected with a 10x objective, and it is easier to distinguish the three phases.

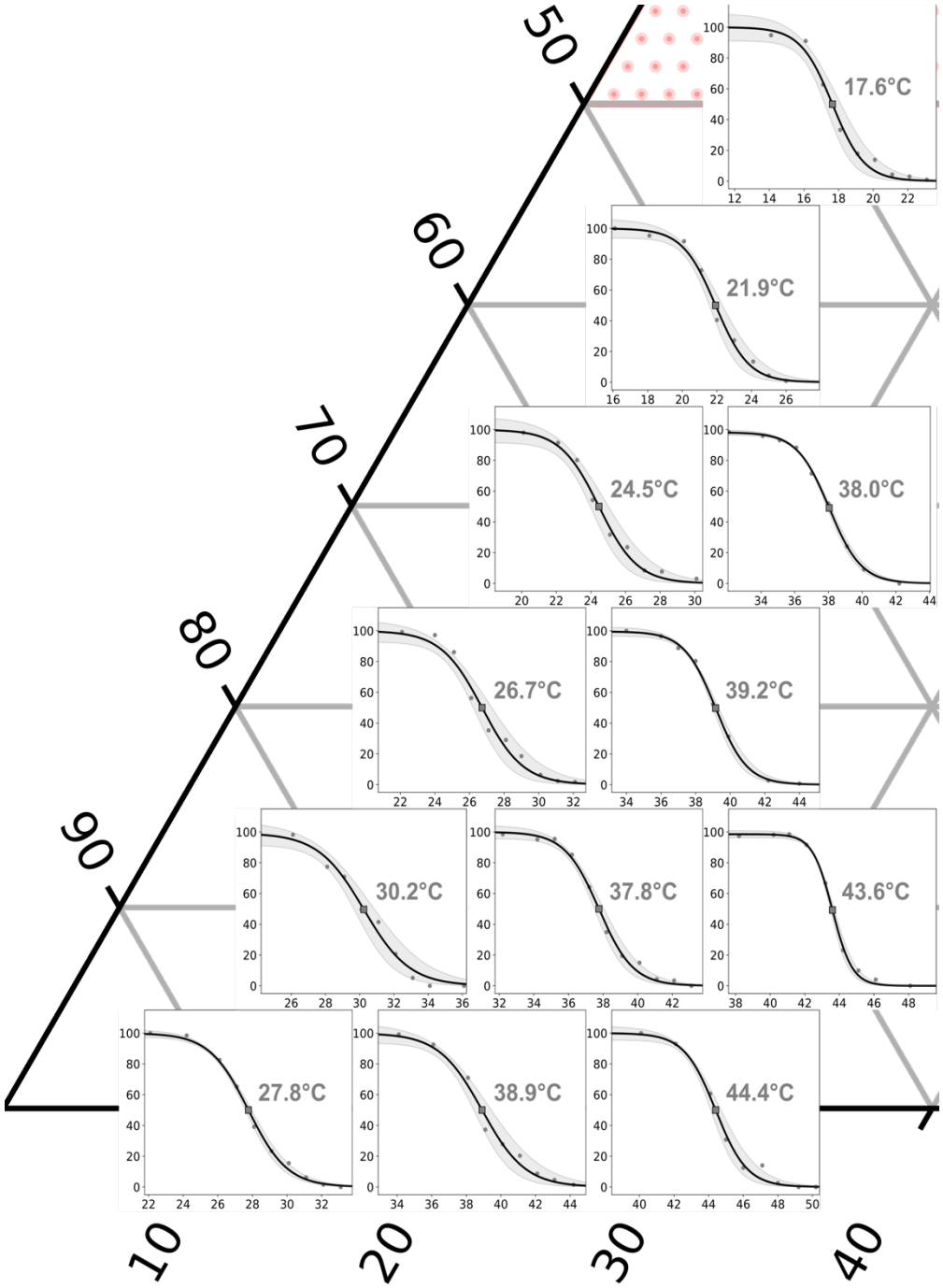

Figure S13. Sigmoidal fits with 95% confidence intervals (gray bands) for T_{mix} for vesicles of DOPC/DPPE/cholesterol, covering the left third of the phase diagram in Figure 3.3B of the main text. The vertex at the left represents 100% DOPC, and high cholesterol is toward the top. X-axes show temperatures (°C), y-axes show percent of phase-separated vesicles. Transition temperatures shown in gray font are transitions from one liquid phase at a high temperature to coexisting solid and liquid phases at a lower temperature.

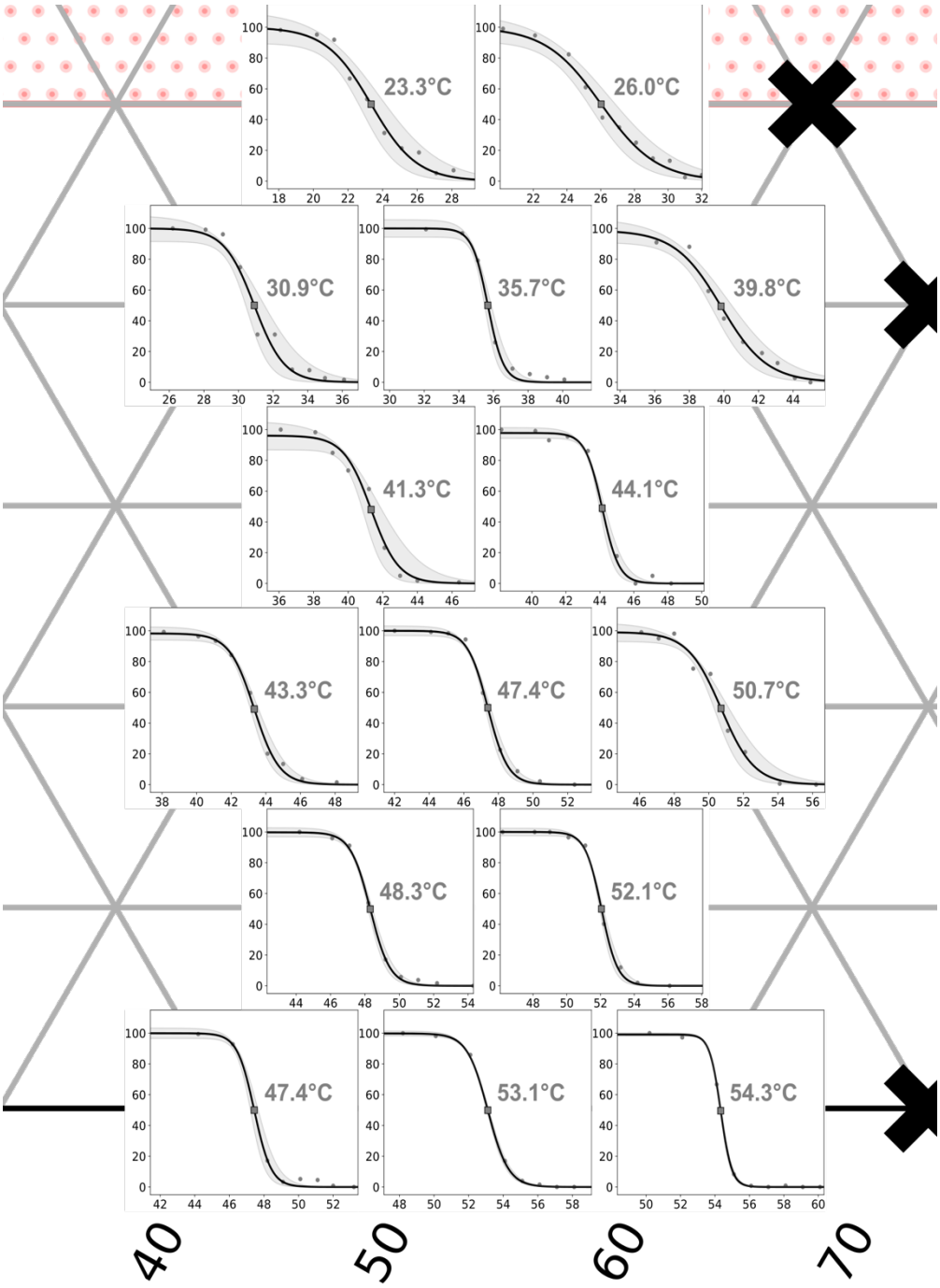

Figure S3.14. Sigmoidal fits with 95% confidence intervals (gray bands) for vesicles of DOPC/DPPE/cholesterol, covering the middle third of the phase diagram in Figure 3.3B of the main text. High DOPC fractions are on the left, high DPPE fractions on the right, and high cholesterol toward the top. X-axes show temperatures (°C), y-axes show percent of phase-separated vesicles. Transition temperatures shown in gray font are transitions from one liquid phase at a high temperature to coexisting solid and liquid phases at a lower temperature.

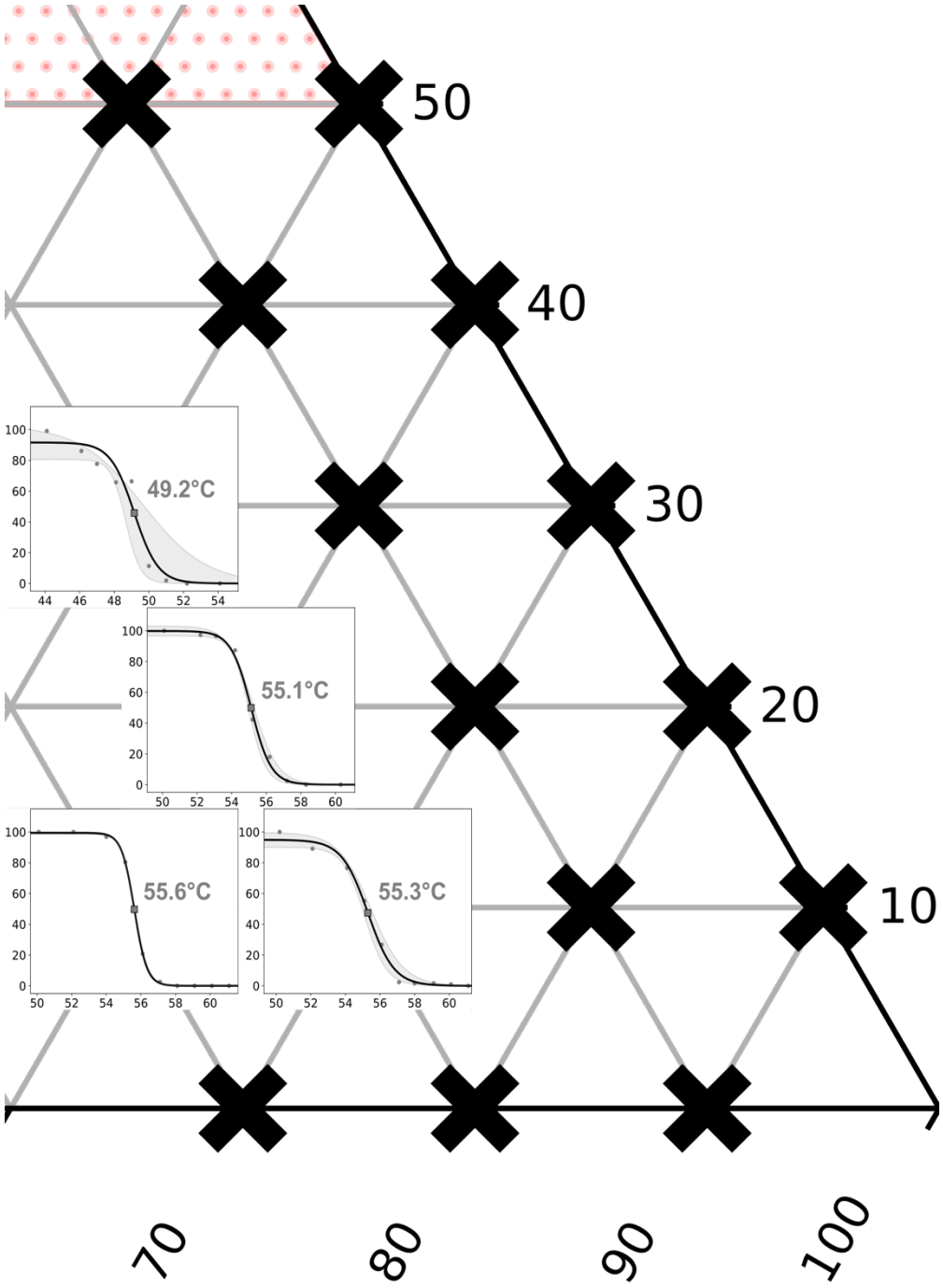

Figure S3.15. Sigmoidal fits with 95% confidence intervals (gray bands) for vesicles of DOPC/DPPE/cholesterol, covering the right third of the phase diagram in Figure 3.3B of the main text. The vertex at the right represents 100% DPPE, and high cholesterol is toward the top. X-axes show temperatures (°C), y-axes show percent of phase-separated vesicles. Transition temperatures shown in gray font are transitions from one liquid phase at a high temperature to coexisting solid and liquid phases at a lower temperature.

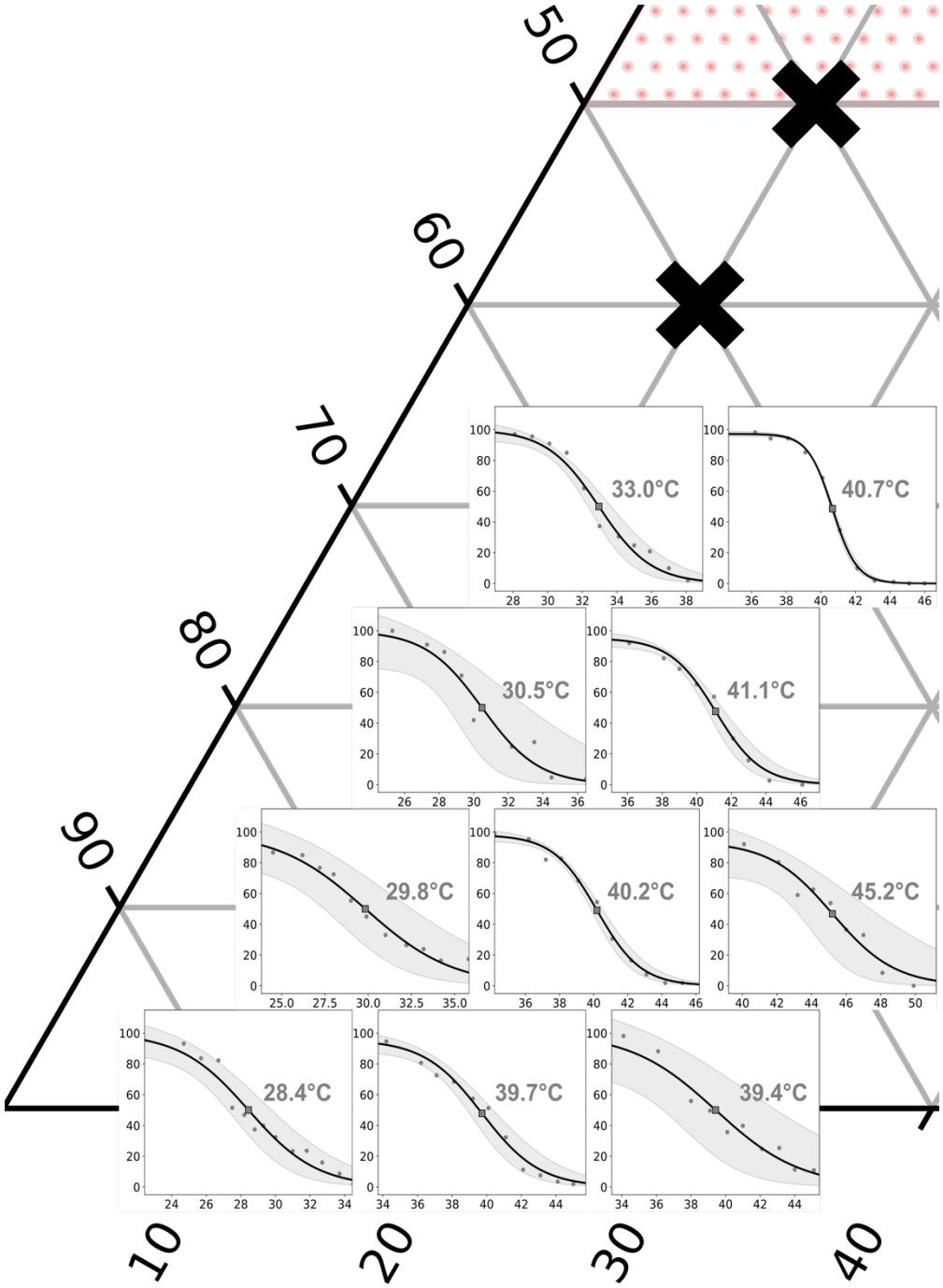

Figure S3.16. Sigmoidal fits with 95% confidence intervals (gray bands) for vesicles of DiphyPC/DPPE/cholesterol, covering the left third of the phase diagram in Figure 3.4B of the main text. The vertex at the left represents 100% DiphyPC, and high cholesterol is toward the top. X-axes show temperatures (°C), y-axes show percent of phase-separated vesicles. Transition temperatures shown in gray font are transitions from one liquid phase at a high temperature to coexisting solid and liquid phases at a lower temperature.

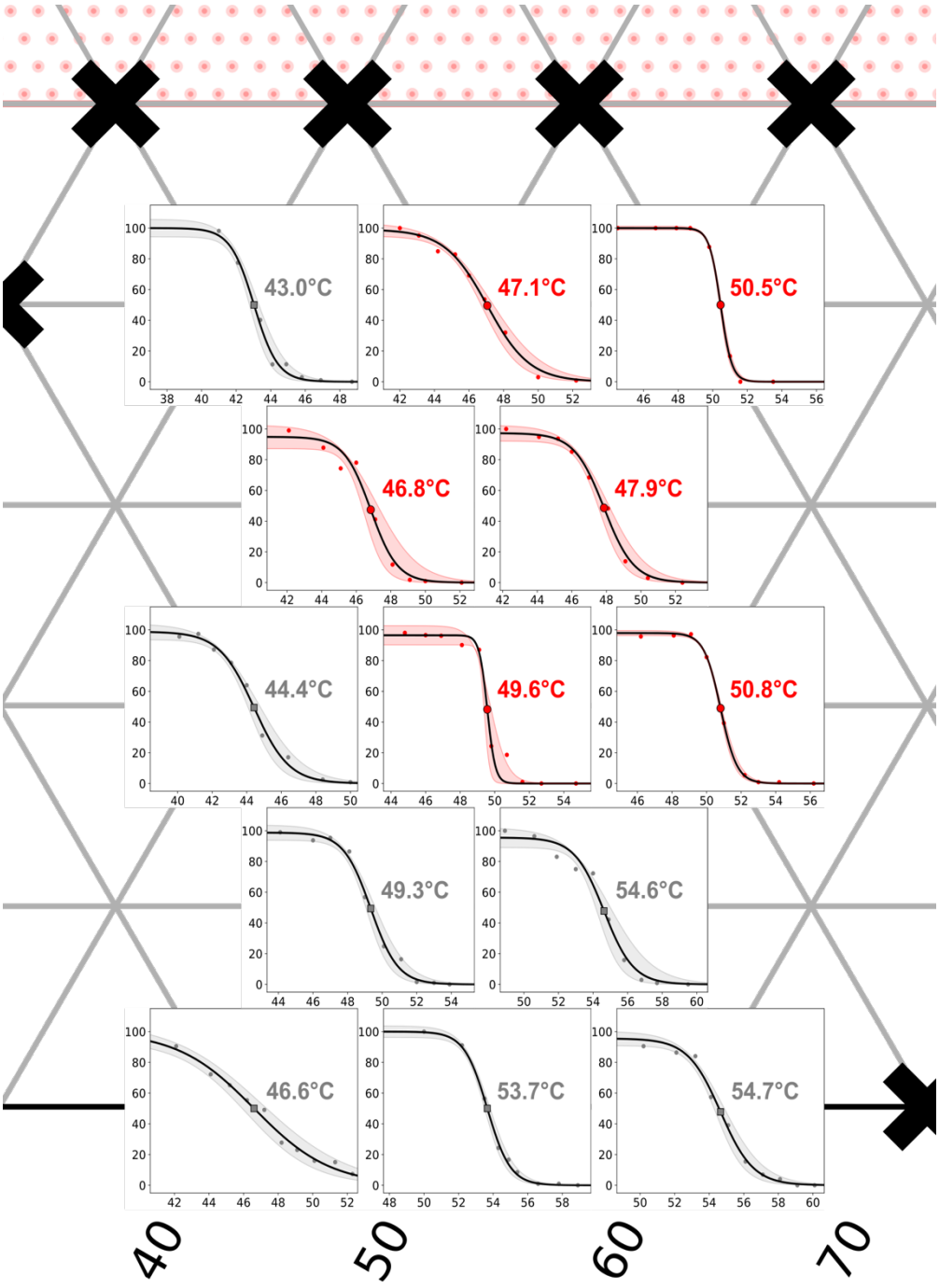

Figure S3.17. Sigmoidal fits with 95% confidence intervals (red and gray bands) for vesicles of DiphyPC/DPPE/cholesterol, covering the middle third of the phase diagram in Figure 3.4B of the main text. High DiphyPC fractions are on the left, high DPPE fractions on the right, and high cholesterol toward the top. X-axes show temperatures (°C), y-axes show percent of phase-separated vesicles. Transition temperatures shown in gray font are transitions from one liquid phase at a high temperature to coexisting solid and liquid phases at a lower temperature. Transition temperatures shown in red font are transitions in which coexisting L_o and L_d phases appear as temperature decreases.

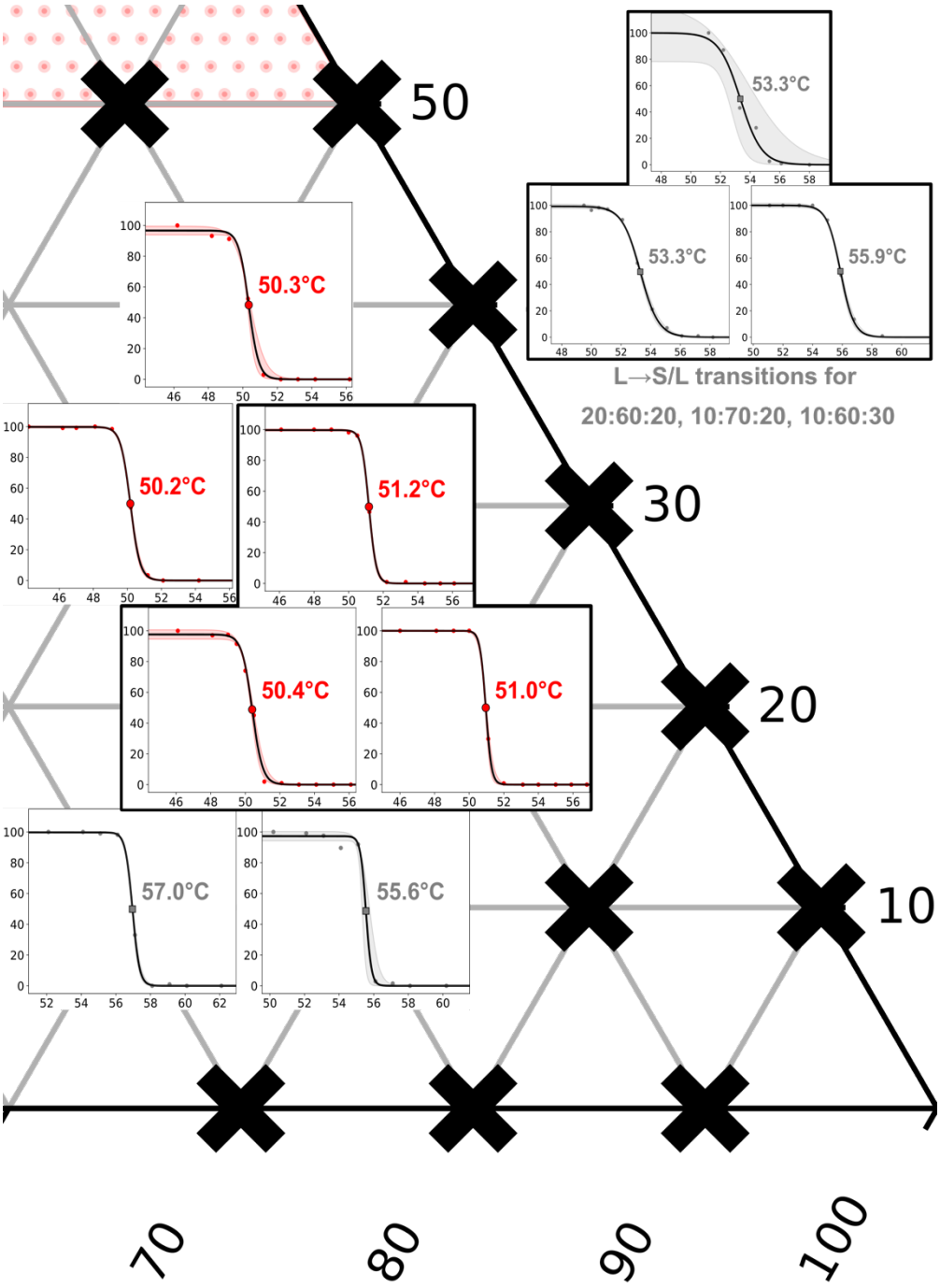

Figure S3.18. Sigmoidal fits with 95% confidence intervals (red and gray bands) for vesicles of DiphyPC/DPPE/cholesterol, covering the right third of the phase diagram as in Figure 3.4B of the main text. The vertex at the right represents 100% DPPE, and high cholesterol is toward the top. X-axes show temperatures (°C), y-axes show percent of phase-separated vesicles. Transition temperatures shown in gray font are transitions from one liquid phase at a high temperature to coexisting solid and liquid phases at a lower temperature. Transition temperatures shown in red font are transitions in which coexisting L_o and L_d phases appear as temperature decreases.

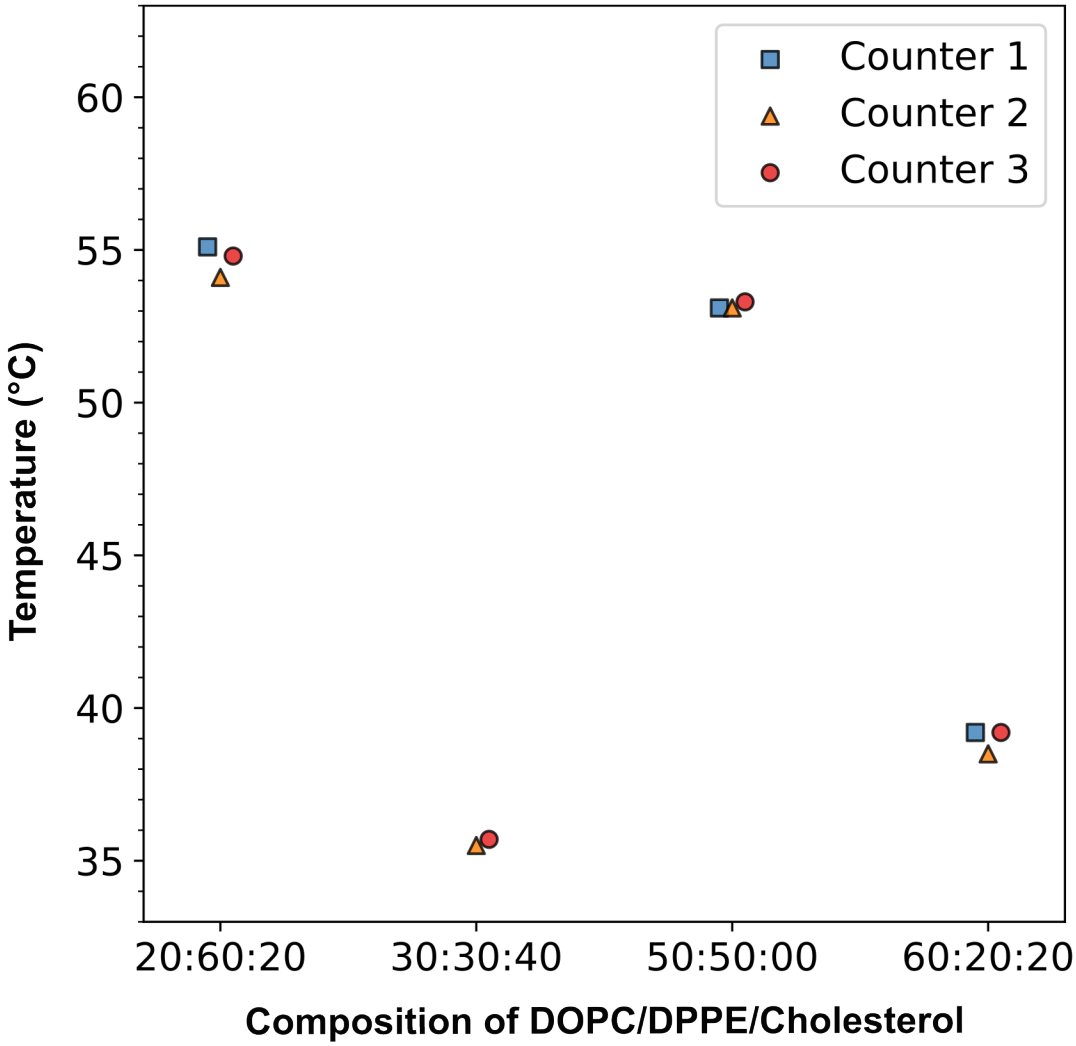

Figure S3.19. Values of T_{mix} are independent of which researcher analyzed the data. In this manuscript, three different researchers tabulated numbers of phase-separated vesicles from fields of view as in Figs. S3.4-3.6 and S3.9-3.11. To estimate the error that this introduced, all three researchers (represented by the square, triangle, and circle for Counters 1, 2, and 3) tabulated data from the same fields of view for vesicles made from the four compositions shown on the x-axis. In each case, the analyzed values of T_{mix} typically differed by ± 0.5°C or less. For comparison, sample-to-sample variations are on the order of ± 0.1 to ± 1.3°C (range 0.1°C to 2.8°C).

iii. Supporting Tables.

DOPC (mol%)	DPPE (mol%)	Chol (mol%)	L→S/L T_{mix} (°C)	Error in T_{mix} fit parameter (°C)	½(|$T_{90\%} - T_{10\%}$|) (°C)
90	10	00	27.8	0.1	2.5
80	20	00	38.9	0.3	2.7
80	10	10	30.2	0.4	2.9
70	30	00	44.4	0.2	2.0
70	20	10	37.8	0.2	2.2
70	10	20	26.7	0.4	2.6
60	40	00	47.4	0.2	1.1
60	30	10	43.6	0.1	1.3
60	20	20	39.2	0.1	2.0
60	10	30	24.5	0.3	2.4
50	50	00	53.1	0.0	1.3
50	40	10	48.3	0.1	1.3
50	30	20	43.3	0.2	1.6
50	20	30	38.0	0.1	2.1
50	10	40	21.9	0.3	2.1
40	60	00	54.3	0.0	0.7
40	50	10	52.1	0.1	1.1
40	40	20	47.4	0.1	1.3
40	30	30	41.3	0.4	1.7
40	20	40	30.9	0.4	1.9
40	10	50	17.6	0.3	2.0
30	60	10	55.6	0.0	0.8
30	50	20	50.7	0.3	2.1
30	40	30	44.1	0.1	1.1
30	30	40	35.7	0.1	1.0
30	20	50	23.3	0.5	2.9
20	70	10	55.3	0.2	1.7
20	60	20	55.1	0.1	1.3
20	50	30	49.2	0.5	1.5
20	40	40	39.8	0.4	2.9
20	30	50	26.0	0.5	3.6

Table S3.1. Data for transition temperatures (T_{mix}) from one liquid phase at high temperature to coexisting solid and liquid phases at low temperature (L→S/L) for vesicles composed of varying ratios of DOPC/DPPE/cholesterol.

DiphyPC (mol%)	DPPE (mol%)	Chol (mol%)	L→S/L T_{mix} (°C)	Error in Tmix fit parameter (°C)	½(|$T_{90\%} - T_{10\%}$|) (°C)
90	10	00	28.4	0.7	2.5
80	**20**	**00**	**39.7**	**0.5**	**2.7**
80	**20**	**00**	**38.6**	**0.1**	**2.9**
80	10	10	29.8	1.4	2.0
70	**30**	**00**	**43.4**	**0.0**	**2.2**
70	**30**	**00**	**39.4**	**1.7**	**2.6**
70	20	10	40.2	0.2	1.1
70	10	20	30.5	1.3	1.3
60	40	00	46.6	0.4	2.0
60	30	10	45.2	1.2	2.4
60	20	20	41.1	0.3	1.3
60	10	30	33.0	0.4	1.3
50	50	00	53.7	0.1	1.6
50	40	10	49.3	0.2	2.1
50	**30**	**20**	**44.5**	**0.3**	**2.1**
50	**30**	**20**	**44.4**	**0.2**	**0.7**
50	20	30	40.7	0.1	1.1
40	60	00	54.7	0.2	1.3
40	50	10	54.6	0.3	1.7
40	20	40	43.0	0.2	1.9
30	60	10	55.6	0.2	2.0
20	70	10	57.0	0.0	0.8
20	**60**	**20**	**54.5**	**0.1**	**0.9**
20	**60**	**20**	**53.3**	**0.1**	**1.3**
20	**60**	**20**	**54.2**	**0.3**	**1.8**
10	**70**	**20**	**55.6**	**0.0**	**0.7**
10	**70**	**20**	**55.9**	**0.1**	**1.0**
10	**70**	**20**	**56.0**	**0.2**	**0.8**
10	**60**	**30**	**52.4**	**0.4**	**1.9**
10	**60**	**30**	**52.2**	**1.2**	**1.5**
10	**60**	**30**	**53.3**	**0.6**	**1.6**

Table S3.2. Data for transition temperatures (T_{mix}) from one liquid phase at high temperature to coexisting solid and liquid phases at low temperature (L→S/L) for vesicles composed of varying ratios of DiphyPC/DPPE/cholesterol. Rows in bold font indicate repeated samples from duplicate or triplicate independent experiments.

DiphyPC (mol%)	DPPE (mol%)	Chol (mol%)	L→ L_o/L_d T_{mix} (°C)	Error in Tmix fit parameter (°C)	½(|$T_{90\%} - T_{10\%}$|) (°C)
40	40	20	49.6	0.2	2.5
40	30	30	46.8	0.3	2.7
30	50	20	50.8	0.1	2.9
30	40	30	47.9	0.2	2.0
30	30	40	47.1	0.2	2.2
20	**60**	**20**	**49.9**	**0.1**	**2.6**
20	**60**	**20**	**50.4**	**0.1**	**1.1**
20	**60**	**20**	**51.5**	**0.2**	**1.3**
20	50	30	50.2	0.0	2.0
20	40	40	50.5	0.1	2.4
10	**70**	**20**	**51.3**	**0.0**	**1.3**
10	**70**	**20**	**51.0**	**0.0**	**1.3**
10	**70**	**20**	**51.4**	**0.1**	**1.6**
10	**60**	**30**	**51.1**	**0.2**	**2.1**
10	**60**	**30**	**51.2**	**0.0**	**2.1**
10	**60**	**30**	**51.3**	**0.0**	**0.7**
10	50	40	50.3	0.1	1.1

Table S3.3. Data for transition temperatures (T_{mix}) for vesicles with a liquid phase (and perhaps a solid phase) at high temperatures, and coexisting L_o and L_d phases at lower temperatures (L→ L_o/L_d), for vesicles composed of varying ratios of DiphyPC/DPPE/cholesterol. Rows in bold font indicate repeated samples from duplicate or triplicate independent experiments.

DiphyPC (mol%)	DPPE-1Me (mol%)	Chol (mol%)	L→S/L T_{mix} (°C)	Error in Tmix fit parameter (°C)	½(|$T_{90\%} - T_{10\%}$|) (°C)
20	**60**	**20**	**48.3**	**0.2**	**1.0**
20	**60**	**20**	**49.1**	**0.2**	**0.6**
20	**60**	**20**	**48.6**	**0.4**	**1.5**
10	**70**	**20**	**50.3**	**0.5**	**1.4**
10	**70**	**20**	**50.6**	**0.0**	**0.7**
10	**70**	**20**	**50.5**	**0.1**	**0.9**
10	**60**	**30**	**49.5**	*	**0.1**
10	**60**	**30**	**49.6**	**0.1**	**0.4**
10	**60**	**30**	**47.8**	*	**2.1**

Table S3.4. Data for transition temperatures (T_{mix}) from one liquid phase at high temperature to coexisting solid and liquid phases at low temperature (L→S/L) for vesicles composed of varying ratios of DiphyPC/DPPE-1Me/cholesterol. Rows in bold font indicate repeated samples from duplicate or triplicate independent experiments. Star symbols (*) indicate T_{mix} fit parameter values that were non-physical due to the proximity of the transition to the 3-phase region at temperatures just below the L→S/L T_{mix}. The temperature range to observe S/L coexistence narrows with increasing headgroup methylation and increasing DOPC composition.

DiphyPC (mol%)	DPPE-1Me (mol%)	Chol (mol%)	L→ L_o/L_d T_{mix} (°C)	Error in Tmix fit parameter (°C)	½(|$T_{90\%} - T_{10\%}$|) (°C)
20	**60**	**20**	**48.8**	**0.1**	**0.4**
20	**60**	**20**	**48.8**	**0.1**	**0.5**
20	**60**	**20**	**48.6**	**0.0**	**0.4**
10	**70**	**20**	**49.4**	**0.0**	**0.2**
10	**70**	**20**	**49.2**	**0.0**	**0.4**
10	**70**	**20**	**49.9**	**0.1**	**0.6**
10	**60**	**30**	**49.5**	**0.0**	**0.3**
10	**60**	**30**	**49.3**	**0.0**	**0.3**
10	**60**	**30**	**49.7**	**0.0**	**0.3**

Table S3.5. Data for transition temperatures (T_{mix}) for vesicles with a liquid phase (and perhaps a solid phase) at high temperatures, and coexisting L_o and L_d phases at lower temperatures (L→ L_o/L_d), for vesicles composed of varying ratios of DiphyPC/DPPE-1Me/cholesterol. Rows in bold font indicate repeated samples from duplicate or triplicate independent experiments.

DiphyPC (mol%)	DPPE-2Me (mol%)	Chol (mol%)	T_{mix} (°C)	Error in Tmix fit parameter (°C)	½(|$T_{90\%} - T_{10\%}$|) (°C)
10	**70**	**20**	**46.7**	**0.1**	**0.5**
10	**70**	**20**	**44.7**	**0.1**	**0.5**
10	**70**	**20**	**45.5**	**0.1**	**0.6**

Table S3.6. Data for transition temperatures (T_{mix}) from one liquid phase at high temperature to coexisting solid and liquid phases at low temperature (L→S/L) for vesicles composed of varying ratios of DiphyPC/DPPE-2Me/cholesterol. Rows in bold font indicate repeated samples from duplicate or triplicate independent experiments.

DiphyPC (mol%)	DPPE-2Me (mol%)	Chol (mol%)	L→ L_o/L_d T_{mix} (°C)	Error in Tmix fit parameter (°C)	½(|$T_{90\%} - T_{10\%}$|) (°C)
20	**60**	**20**	**45.8**	**0.0**	**0.6**
20	**60**	**20**	**45.2**	**0.1**	**0.8**
20	**60**	**20**	**46.3**	**0.0**	**0.4**
10	**70**	**20**	**44.4**	**0.1**	**0.7**
10	**70**	**20**	**46.3**	**0.1**	**0.3**
10	**70**	**20**	**45.3**	**0.0**	**0.6**
10	**60**	**30**	**47.2**	**0.0**	**1.1**
10	**60**	**30**	**47.3**	**0.1**	**0.3**
10	**60**	**30**	**46.3**	**0.1**	**0.9**

Table S3.7. Data for transition temperatures (T_{mix}) for vesicles with a liquid phase (and perhaps a solid phase) at high temperatures, and coexisting L_o and L_d phases at lower temperatures (L→ L_o/L_d), for vesicles composed of varying ratios of DiphyPC/DPPE-2Me/cholesterol. Rows in bold font indicate repeated samples from duplicate or triplicate independent experiments.

DiphyPC (mol%)	DPPC (mol%)	Chol (mol%)	L→ L_o/L_d T_{mix} (°C)	Error in Tmix fit parameter (°C)	½(|$T_{90\%} - T_{10\%}$|) (°C)
20	**60**	**20**	**41.4**	**0.4**	**2.0**
20	**60**	**20**	**42.9**	**0.3**	**2.3**
20	**60**	**20**	**40.8**	**0.3**	**2.4**
10	**70**	**20**	**40.4**	**0.2**	**1.1**
10	**70**	**20**	**38.5**	**0.4**	**2.5**
10	**70**	**20**	**39.1**	**0.2**	**2.1**
10	**60**	**30**	**43.0**	**0.2**	**2.2**
10	**60**	**30**	**43.8**	**0.3**	**1.9**
10	**60**	**30**	**44.8**	**0.1**	**1.8**

Table S3.8. Data for transition temperatures (T_{mix}) for vesicles with a liquid phase (and perhaps a solid phase) at high temperatures, and coexisting L_o and L_d phases at lower temperatures (L→ L_o/L_d), for vesicles composed of varying ratios of DiphyPC/DPPC/cholesterol. Rows in bold font indicate repeated samples from duplicate or triplicate independent experiments.

Chapter 4

Ripples at edges of blooming lilies and torn plastic sheets

*This chapter was first published in the *Biophysical Journal* in 2022. It was written in collaboration with Thomas Portet, Zachary R. Cohen, Nicole Panek, Peter N. Holmes, Sean A. Stephens, Tamas Varga, and Sarah L. Keller.

Portet, T., Z. R. Cohen, G. J. Goetz, N. Panek, P. N. Holmes, S. A. Stephens, T. Varga, S. L. Keller. 2024. Ripples at Edges of Blooming Lilies and Torn Plastic Sheets. *Biophys. J.* 121:2389-2397.

4.1 Abstract.

Ripples arise at edges of petals of blooming *Lilium casablanca* flowers and at edges of torn plastic sheets. In both systems, ripples are a consequence of excess length along the edge of a sheet. Through the use of time-lapse videos of blooming lilies and published images of torn plastic sheets, we find that ripples in both systems are well-described by the scaling relationship $a \propto \sqrt{w(L-w)}$, where a is amplitude, w is wavelength, and L is arc length. A phenomenological relationship previously reported for self-similar ripple patterns, namely $\langle a \rangle \propto \langle w \rangle$, can be recovered by assuming that buckling stress is constant. Excess length along petal edges can also influence their overall Gaussian curvature, such that petals invert from a cup shape to a saddle shape upon blooming. Previous simulations of these shape changes have assumed that petal thickness decreases at least quadratically. Here, we evaluate tomograms of several varieties of lily buds and find that this assumption is valid along the short axis of the buds, but not the long axis. A challenge of employing traditional tomography methods to measure petal thickness is that the sample is destroyed; a single bud cannot be followed through the entire blooming process. To address this challenge, we provide proof of principle that the non-destructive, label-free method of X-ray

tomography produces high-contrast three-dimensional scans on time scales short enough to follow lily blooming.

4.2 Introduction.

Morphological changes in flowers elegantly connect the abstract beauty of mathematics and the tangible beauty of nature. Two recent studies inspired our current investigation of lilies. In the first, the authors applied a growth hormone to the edge of flat plant leaves to create ripples (26). In the second, the authors combined surgical manipulations of *L. casablanca* lilies, numerical simulations, and exact calculations to argue that lily blooming is driven primarily by edge growth (27). In this mechanism, growth along edges of lily tepals (colloquially termed petals) is enhanced with respect to tepal faces, such that excess length accumulates along edges. Blooming of lilies from closed buds to six-pointed stars (Fig. 4.1) entails curvature reversal of tepals from cup shapes to saddle shapes and may be accompanied by the emergence of ripples at the edges of the tepals.

Flowers that exhibit ripples along their edges, whether lily tepals or daffodil trumpets, do not necessarily genetically encode rippling beyond driving a generalized edge growth that results in blooming (26, 122). Ripples are observed in a wide class of systems that accommodate excess length along an edge. Simulations of elastic ribbons with high rates of edge growth result in rippled morphologies (123). Similarly, polymer disks that undergo nonuniform swelling can buckle at their rippled edges, as can annular thin strips undergoing nonuniform stresses (124–128). In more quotidian examples, knitters create ripples by inserting stitches at edges, and ripples form at the new edges of a torn plastic sheet (26, 28, 122, 129, 130).

Here, our central goal is to quantitatively explain the shape of ripples in sheets undergoing edge growth. When rippling is the result of buckling, a simple scaling law arises that relates a ripple's amplitude a, wavelength w, and arc length L. The exact form of the scaling relationship depends on whether stress is constant. We test which form of scaling applies to single ripples at edges of lily tepals (which we might expect to have nonuniform stresses) and torn plastic sheets (which we might expect to be uniform at long length scales, but perhaps not at short ones).

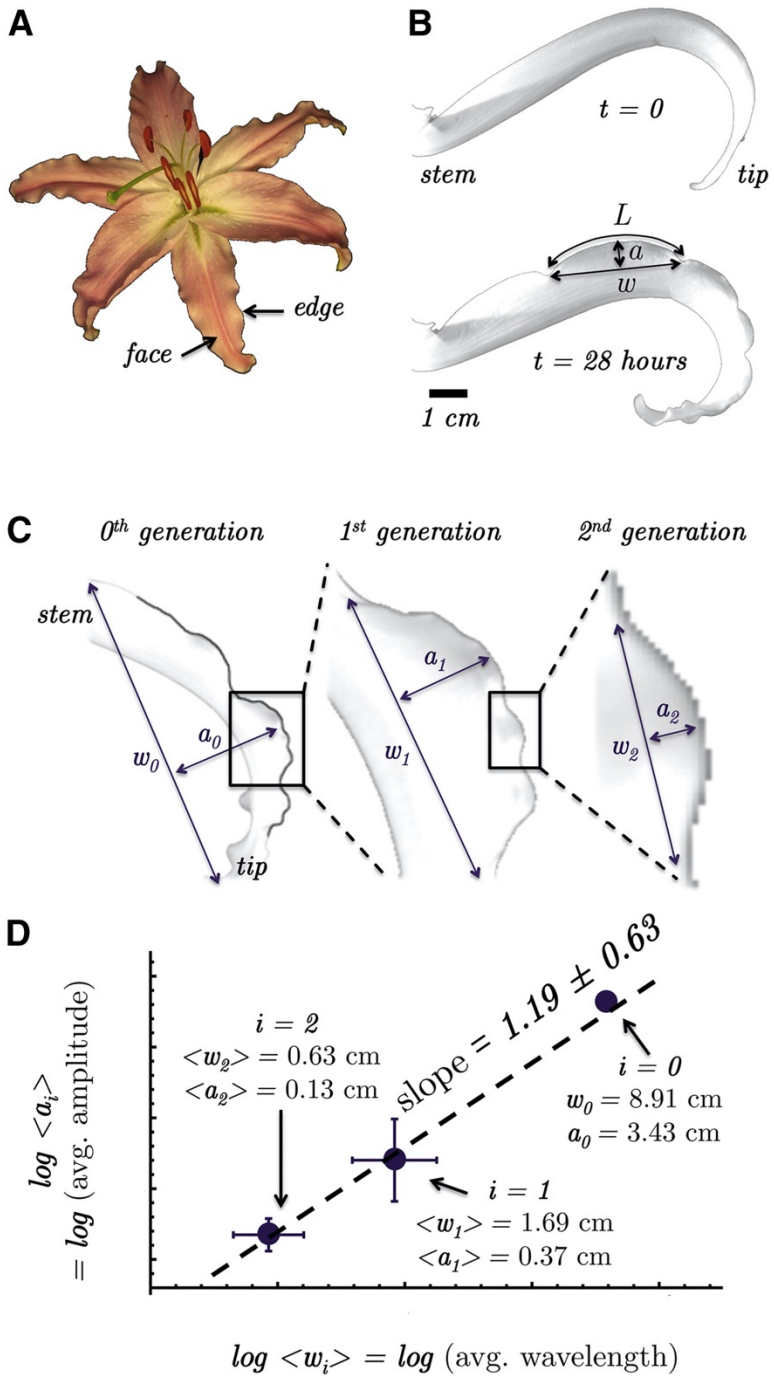

Figure 4.1. Self-similar ripples in lilies. A) Top view of an open stargazer lily with three inner and three outer tepals. **B)** Side view of an outer tepal of *Lilium casablanca* before (*top*) and after (*bottom*) edge rippling, with amplitude a, wavelength w, and arc length L. **C)** Examples of an amplitude a_i and wavelength w_i for ripples for each generation i. The leftmost image is outlined in black. **D)** Log-log plot of average final ripple amplitude $\langle a\_i \rangle$ versus average final wavelength $\langle w\_i \rangle$ for each generation i. Fig. 4.2 labels all of the ripples analyzed in **D**. Error bars are standard deviations, and numbers of measurements are $N_0 = \sim 1, N_1 = \sim 5, N_2 = \sim 6$. Lily sizes limit observable length scales to one order of magnitude.

Overall, our data support a view that biology and physics work in tandem to create lily tepals with delicate ripples along their edges: genes regulate the rate of edge growth, and buckling within each tepal converts this growth into wavy edges (131).

Our second goal is to image lily buds, for two reasons. To enable future calculations of curvature reversal in tepals from realistic starting configurations, we use surgical tomography to record 3-dimensional shapes of closed buds of several lily varieties. To enable future imaging of the full 3-dimensional shape changes of a single lily, we establish that label-free X-ray tomography collects high-contrast scans on time scales an order of magnitude shorter than blooming. Each of these methods presents an advantage: surgical tomography is broadly accessible, and X-ray computed tomography is less destructive.

One could ask whether ripples confer an evolutionary advantage to lilies. Michael Pollan argues in *The Botany of Desire* that genetic expression in many plants is influenced by the aesthetic and culinary tastes of humans. Evolution in plants records both natural history and human history. Pollan writes how a tulip with "petals attenuated like sabers, contains detailed instructions on how to best catch the eye not of a bee but of an Ottoman Turk; it has something to tell us about that age's idea of beauty" (132). Judging from how common it is to find rippled lilies in Seattle's gardens, which lie far from the flowers' ancestral homes in Asia, it appears that lilies have successfully harnessed edge growth and buckling in an evolutionary strategy that has motivated humans to feed them, propagate them, and extend their range.

4.3 Materials and Methods.

i. Videos and Measurement Uncertainty.

Videos were collected of lilies blooming and rippling. *L. casablanca* and *L. stargazer* varieties, which are Division VII oriental hybrids, were trimmed so only one outer tepal remained, as in Fig. S4.1. The remaining tepal was imaged from the side at constant illumination of 60 $\mu mol/m^2 s$ and 20°C in a time-lapse chamber previously described by Stewart Lilley et al. (133). Image capture started a few hours after blooming commenced (before rippling) and stopped when ripples became static. Measurement uncertainties for a, w, and L are equivalent and on the order of $\pm$ 0.05

cm. Uncertainties arise mainly because tepal edges deviate from the camera's focal plane due to flower motion or shape changes. Smaller uncertainties arise from image analysis, which combines manual detection of ripple zeniths and nadirs with automated edge detection by ImageJ (https://imagej.nih.gov/ij).

ii. Tomography of Closed Lily Buds.

Closed buds of lilies (oriental hybrids and tiger lilies, *L. lancifolium* were loosely wrapped in Teflon tape and held with the tip downward on a cylindrical pedestal. A circular rim on the pedestal protruded 1.8 ± 0.2 mm (for *L. speciosum* (*var. alba*)) or ~3 mm (for other lilies) above the center. Buds were sectioned by clamping a tomography blade in a vice-grip and using the pedestal rim as a guide along which the blade slid to cut the bud. After each slice was cut, the cross section of the remaining bud was imaged using a standard digital camera (PowerShot SD1100 IS; Canon, Melville, NY) or, for *L. speciosum* (*var. alba*) a cell phone (iPhone 7, Apple, Cupertino, CA).

iii. Image Analysis of Tomograms.

In each photograph of lily slices, areas of outer tepals and an H-shaped scale bar were traced by hand in Photoshop (Adobe, San Jose, CA) to produce binarized images. The scale bar was converted from pixels to mm using functions from the scikit-image library (134). Specifically, "skeletonize", "label", and "regionprops_table" were used to identify, isolate, and measure the length of the scale bar. The three outer tepals were then identified within the binarized image, and each tepal image was cropped and placed into its own file using the scikit-image function library. Images of all slices of each tepal were then grouped in ordered sets corresponding to the original position of the slice within the bud. Each binarized tepal image was then skeletonized, and tepal thicknesses were measured along a line perpendicular to the skeleton (Fig. S4.2). The length of the semi-minor axis, b, of each tepal was defined to be the maximum distance between points on the skeleton and defined to be at $x = 0$. The length of the semi-major axis, c, was defined to be the distance between $x = 0$ and the tip of the tepal. The authors have made all original Python code available by public license at https://github.com/nicolepanek/2021_LilyProject.

iv. X-ray Microtomography.

X-ray computed tomography was conducted at the Environmental Molecular Sciences Laboratory at the Pacific Northwest National Laboratory in Richland, WA. Each lily was mounted and kept hydrated in a rotating chuck that held a tube filled with water. The X-ray power settings were 85 kV and 250 μA. Lilies were translated vertically to image sequential slices, in 0.886 mm steps for a lily bud and 1.1 mm steps for a lily bloom. Individual radiographs were collected with 708 ms exposure times, and 4 frames were recorded per projection, for a total of 3142 projections. Lilies were rotated during the scans to capture 3-dimensional data. The image voxel size for the lily bud was 0.0439 mm and 0.0536 mm for the lily bloom. Each scan was completed in approximately 4 h. Although exposure to X-rays eventually damages plant tissue, the technique is considered nondestructive.

v. Alternative Derivation of Eq. 4.2.

We consider the simple case of a first-generation ripple that has no second-generation ripples superimposed on it. We model the ripple's edge as a planar curve for which each point has coordinates $(x, f(x))$, where x ∈ $[-w/2, w/2]$ because the ripple's wavelength is w. We assume the ripple is symmetric and pinned at the edges, which means that the function f is smooth, is even, and satisfies boundary conditions of f$(w/2)$ = f$(-w/2)$ = 0 and f(0) = a. The arc length L of the curve is, by definition, L = ∫ _{$-w/2$}^{$w/2$}√{1 + f^′ ⊢(x⊣)^2}dx, which is simplified via a Taylor expansion to L ≈ $w + (1/2)\int_{-w/2}^{w/2} f'(\mathrm{x})^2\, d$x for a smooth function f. Because the function f is even, its expansion does not contain odd powers and is, to second-order, f(x) ≈ $a + f''(0)x^2/2$. Using a difference quotient approximation, the second derivative at the origin is $f''(0) \approx -\epsilon(a/w^2)$, with dimensionless factor ϵ. Direct integration of f'^2 yields a ∝ $\sqrt{w(L-w)}$, which is Eq. 4.2. If arc length were directly proportional to wavelength, as in a small-angle approximation for ripples of small amplitude, then insertion of L ∝ w (where L > w) in Eq. 4.2 would yield a ∝ w. In practice, L is difficult to measure in a rippled edge that has additional generations of ripples superimposed on it.

4.4 Results and Discussion.

i. Rippling.

Ripples in lily tepals appear singly or in multiple generations. Fig. 4.1C shows a large, first-generation ripple decorated with smaller, second-generation ripples. These patterns are reminiscent of self-similar ripples at edges of torn plastic sheets. Sharon et al. (28) have related the amplitudes, a, and wavelengths, w, for five generations of superimposed ripples in plastic sheets, spanning two orders of magnitude, by

$$a \propto w\,. \tag{4.1}$$

However, when we attempted to apply Eq. 4.1 to ripples in lily tepals, we found a poor fit. The fit improved only after averaging all amplitudes and wavelengths within each generation (Fig. 4.1C-D). Even after averaging, the uncertainty was large; the slope of $\log\langle w\rangle$ versus $\log\langle a\rangle$ is 1.19 with a 90% confidence interval of ± 0.63.

The reason that averaging over many ripples leads to a better fit of a $\propto w$ lies in the equations that describe buckling in thin sheets. The amplitude of a buckled beam scales as a $\propto w\sqrt{strain}$. This equation has previously been applied to sheets under tensile strain (135) and attached to compliant supports (136). The definition of $\mathrm{strain} = (L - w)/\mathrm{w}$ yields

$$a \propto \sqrt{w(L-w)}\,. \tag{4.2}$$

Another way to derive Eq. 4.2 is to introduce a function $\mathrm{f}(x)$ that describes the height at every point on a ripple (see the Materials and Methods). The ripple begins at $\mathrm{x} = -\mathrm{w}/2$ (with zero height), rises to an amplitude a at $\mathrm{x} = 0$, and returns to a height of zero at $\mathrm{x} = \mathrm{w}/2$. The only assumptions that need to be imposed are that the function is smooth and symmetric. By taking a second-order Taylor expansion of the function, we find that a $\propto \sqrt{w(L-w)}$.

When strain is constant, Eq. 4.2 simplifies to $a \propto w$. However, strain is not constant in lilies. Strain due to growth at the edges of *L. casablanca* tepals increases linearly in the direction of the long axis, more than doubling from ~0.2 at the tepal base to ~0.5 near the tip, with large standard deviations, on the order of ± 0.1 (27). Therefore, for individual ripples in lily tepals, we expect $a \propto \sqrt{w(L-w)}$ to provide a better fit than $a \propto w$.

To test Eq. 4.2, we collected videos of lilies blooming and rippling. We used *L. casablanca* specimens because buds are large (~10 cm), are widely available, and bloom over the course of approximately 1 day (137). We focused on single ripples, which we define as having no higher-order generation ripples superimposed upon them. Single ripples minimize ambiguity in how to define a and w. Fig. 4.2 shows frames of single, first-generation ripples at edges of tepals. A movie corresponding to Fig. 4.1B appears in the supporting material (Video S4.1).

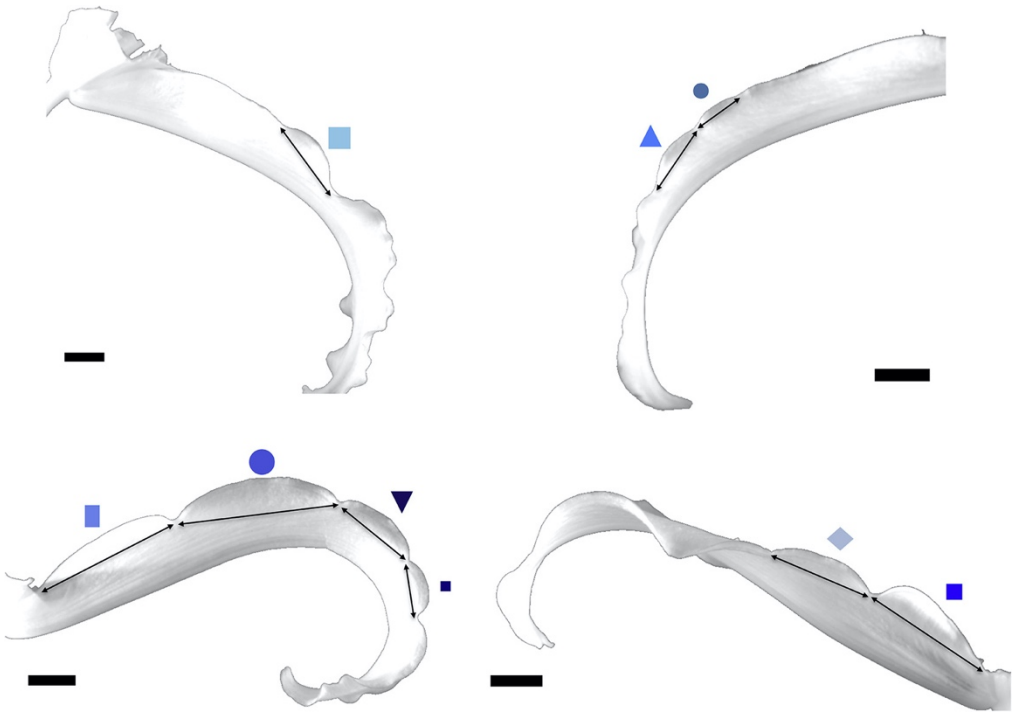

Figure 4.2. Photograph with symbols marking all simple, first-generation lily tepal ripples that were evaluated. Ripples were evaluated if they were smooth (i.e., without smaller, second-generation ripples) and if their white edges were imaged against a dark background rather than against another part of the white tepal, which made them straightforward to track automatically. Symbols for each ripple correspond to multiple data points through time in Figs. 4.3, 4.4, S4.3, and S4.4. In all cases, tepal stems are toward the figure edges. Scale bars are 1 cm.

Ripples appear at higher densities near the tips of tepals than at their stems (Fig. 4.2), consistent with greater edge growth near the tip.

As lilies bloomed, we tracked each ripple's amplitude, wavelength, and arc length over time (Video S4.1). Ripple amplitudes and arc lengths increase over time (Figs. 4.3A and S4.4).

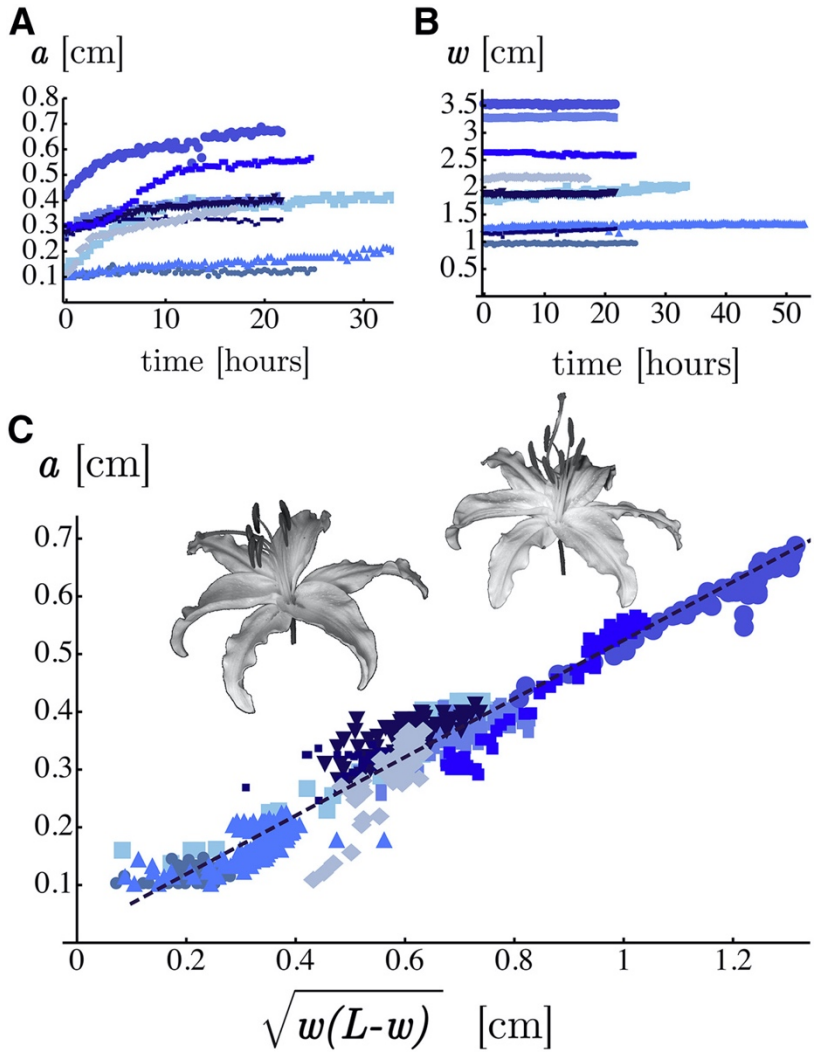

Figure 4.3. Relationships between amplitude a, wavelength w, and arc length L for nine first-generation ripples in lily tepals. Fig. 4.2 contains images of all ripples analyzed for this figure. Each ripple is identified by a different symbol and generates many data points as the ripple changes shape over time. **A)** Amplitude increases with time (as does arc length, see large-format graphs in Fig. S4.4). **B)** In contrast, wavelength w remains approximately constant over time. **C)** Within uncertainty, all data collapse onto a straight line when plotted as a $\propto \sqrt{w(L-w)}$. For clarity, this figure displays data for only single ripples with no superimposed higher generation ripples, excludes ripples with amplitudes ≤ 0.1 cm, and does not show experimental uncertainties. Full data sets with experimental uncertainties appear in Fig. S4.3.

In contrast, wavelengths are approximately constant over time (Fig. 4.3B), making boundary conditions of $a = 0$ at $x = \pm w/2$ straightforward to implement. We find that ripple amplitude a, wavelength w, and arc length L are related by Eq. 4.2 for single ripples in tepals of *L. casablanca* (Fig. 4.3C).

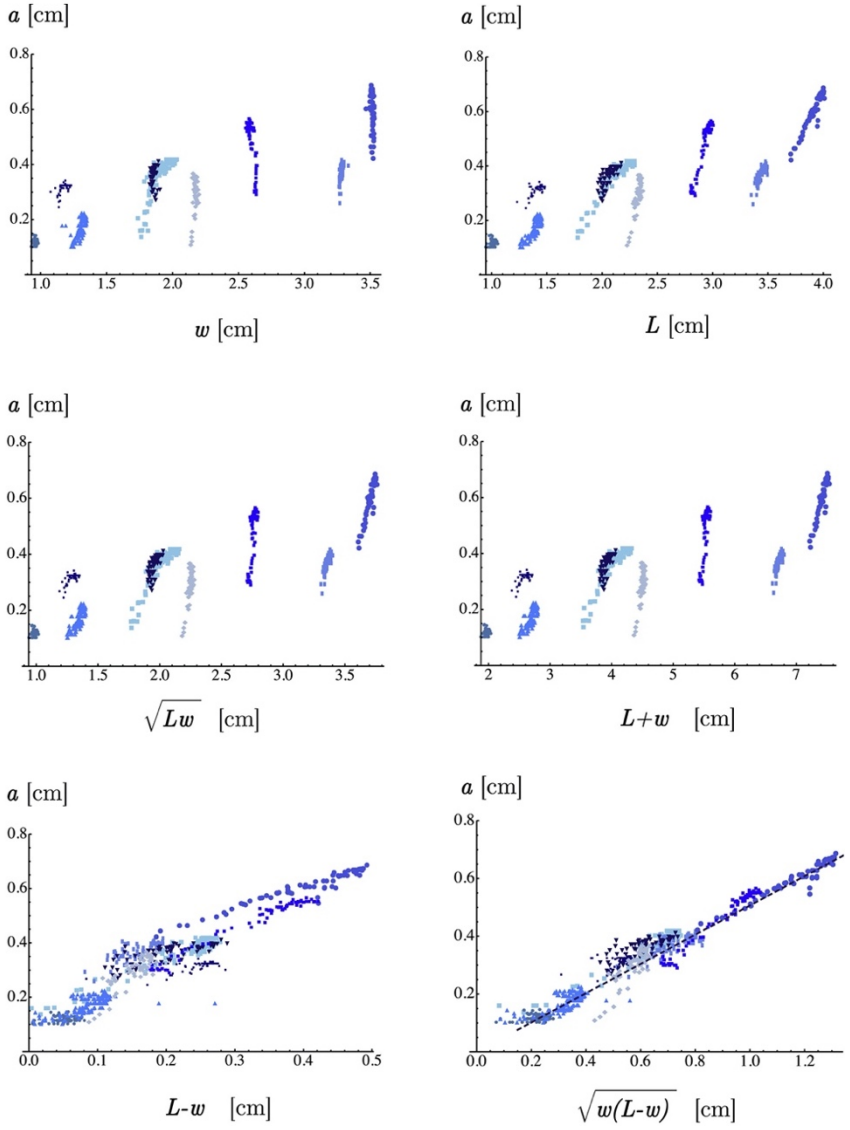

Figure 4.4. Examples of scaling relationships. Data from time-lapse movies of the tepals in Fig. 4.2 are plotted in six simple relationships between a and d, where d is a distance constructed from various manipulations of w and L. For example, the top left panel shows a vs. w, the same relationship in Eq. 4.1. The next three plots yield similarly poor correlation between a and d, where $d = L$ (**top right**), $d = \sqrt{Lw}$ (**middle left**), and $L + w$ (**middle right**). A better collapse of the data onto a line is found for a vs. $L - w$ (**bottom left**). The best collapse is found for a versus $\sqrt{w(L-w)}$, the equation for buckling in Eq. 4.2 (**bottom right**).

All other scaling relationships fail in which amplitude a is proportional to a simple expression with units of length, namely w, L, $\sqrt{Lw}$, L + w, or L − w (Fig. 4.4). For clarity, Fig. 4.3 displays data for only single ripples, excludes ripples with amplitudes ≤ 0.1 cm, and does not show experimental uncertainties. Full data sets with experimental uncertainties appear in Fig. S4.3.

For any sheet with edge growth, whether a lily tepal or a plastic film, determining whether the relationship a $\propto w$ fits ripple shapes as well as the relationship a $\propto \sqrt{w(L-w)}$ does is a means of assessing the length scale of inhomogeneities. The plastic sheet of Sharon et al. (28) was presumably uniform before it was torn. As it ripped, inhomogeneities may have arisen, which would be most evident in ripples of the same length scale. To test for these inhomogeneities, we analyzed raw images of fifth-generation single ripples from Sharon (28), as in Figs. S4.5-4.6.

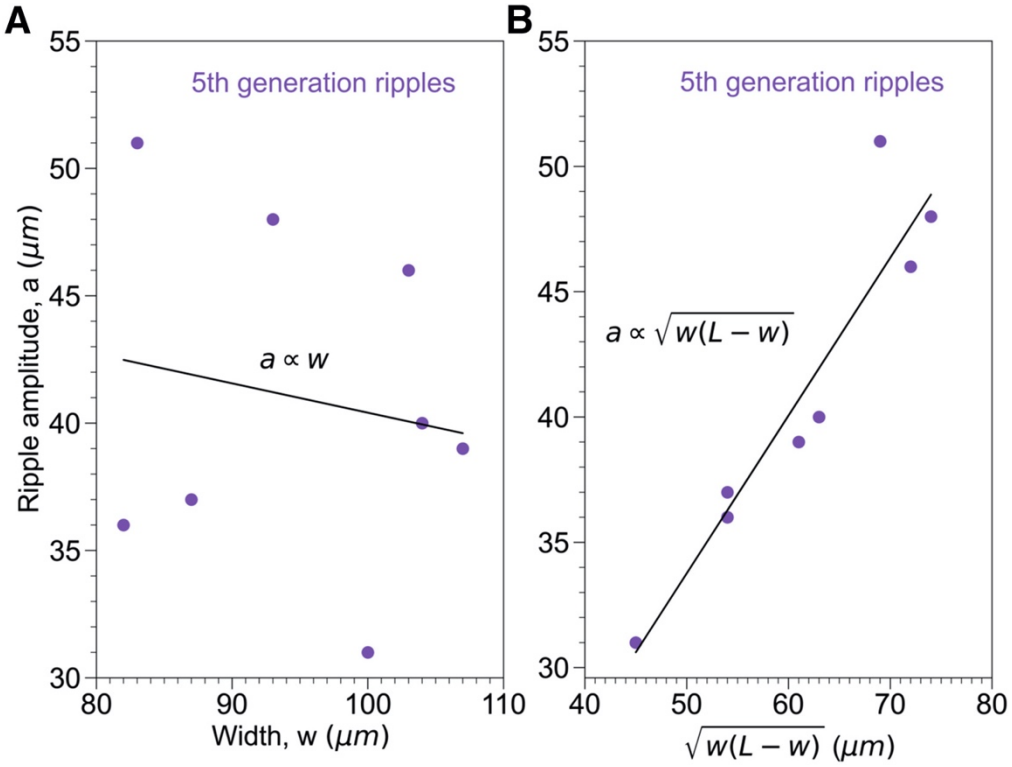

Figure 4.5. Tests of relationships between amplitude *a*, wavelength *w*, and arc length *L* for single ripples in plastic sheets. The sketch at the center represents single, 5th-generation ripples (N = 8) in a plastic sheet viewed from the edge (adapted from (28) as in Figs. S4.5 and S4.6). **A)** The shapes of these ripples are fit poorly by a line of a $\propto w$ (slope = – 0.12, confidence interval = ± 0.27). **B)** The same ripple shapes are fit well by a $\propto \sqrt{w(L-w)}$, (slope = 0.63, confidence interval = ± 0.095.

These small ripples have wavelengths on the order of 100 μm and are not fit by a $\propto w$. (Fig. 4.5A, slope of – 0.12 ± 0.27). We expected that larger ripples would be insensitive to inhomogeneities, and found a better, but still only approximate agreement with a $\propto w$, even at length scales larger than 1 mm (Fig. 4.6A, slope = 1.1 ± 0.037).

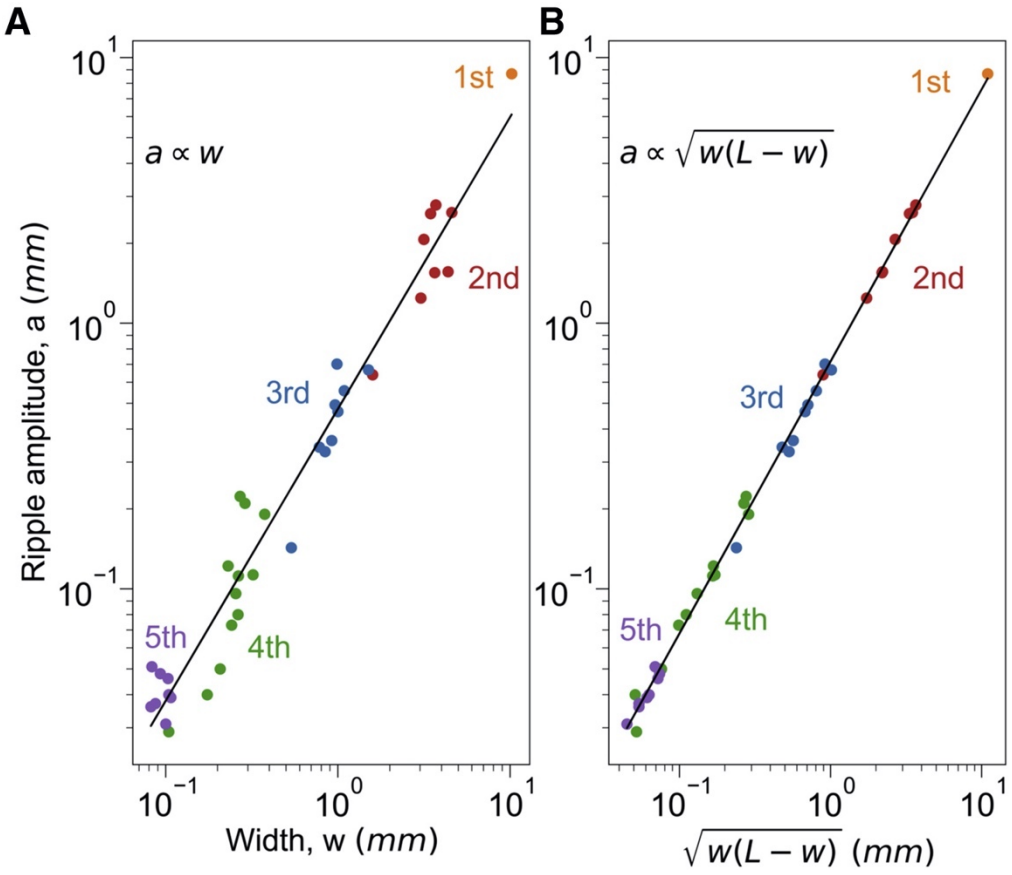

Figure 4.6. Tests of relationships between amplitude *a*, wavelength *w*, and arc length *L* for five generations of ripples in torn plastic sheets from original data in (28). Each point represents an individual ripple (rather than an average), and colors correspond to successive generations of ripples in Fig. S4.6. **A)** The data fall roughly along a line when plotted as a $\propto w$ (on a log-log plot), with a slope of 1.1 and a confidence interval of ± 0.037. **B)** The same data collapse more fully onto a line when plotted as a $\propto \sqrt{w(L-w)}$ (on a log-log plot) with a slope of 1.0 and a confidence interval of ± 0.0083.

In other words, strain was not constant while the sheet was torn, either at the sub-millimeter length scales of 5th generation ripples (where local inhomogeneities might be expected) or in larger ripples approaching ~10 mm (where strains might be expected to average out). Sharon et al. (28) reported a closer fit, which likely arose because their data were binned and averaged. In contrast,

the relationship a $\propto \sqrt{w(L-w)}$ from Eq. 4.2 holds for all five generations of ripples in torn plastic sheets (Fig. 4.6B, slope = 1.0 ± 0.0083), including the smallest ripples (Fig. 4.5B, slope = 0.63 ± 0.095). The excellent fit to Eq. 4.2 indicates that the second-order Taylor expansion used in the derivation Eq. 4.2 is sufficient.

A separate question is how the shape descriptors of ripples evolve over time. In rippled two-dimensional sheets, preferential wavelengths emerge from a competition between stretching and bending: the former favors short wavelengths, and the latter favors longer ones (135). As a tepal edge grows, small, first-generation ripples appear at sites separated by a distance w that presumably arises from minimization of the stretching and bending energies. Our data in Fig. S4.4 show that w remains approximately constant, implying that the tepal's elastic modulus does not change significantly over time. As a tepal edge grows, the arc length L of ripples increases. The tepal reacts to the excess edge length by buckling, so ripple amplitude a also grows with time, where a scales as $\sqrt{w(L-w)}$.

Rippling is largely independent of the original (pre-rippled) length of the tepal, which is consistent with the notion that ripples arise from local strains. In Videos S4.2-4.4, in the Supporting materials, ripples appear roughly synchronously in outer tepals that are 67%, 75%, and 100% of their original length. In some blooms (Videos S4.2 and S4.3), ripples arise when all tepals are in cup shapes, whereas in others (Video S4.4), rippling begins only after larger shape changes. Rare exceptions occur; Fig. S4.8 shows a bloom in which ripples in the shortest tepal have smaller amplitudes than ripples in longer tepals. Similar differences in amplitudes occasionally occur when all tepals are the same length.

ii. Blooming.

Whereas *L. casablanca* lilies are characterized by ripples at tepal edges, *L. lancifolium*, tiger lilies, are not (Fig. 4.7). In both varieties, blooming entails a reversal of curvature as the tepals progress from cup to saddle shapes. In a model by Liang and Mahadevan (27), edge growth drives this curvature reversal. The model assumes that the tepal is initially an elliptical cup with a lenticular cross-section of thickness, t, that decreases at least quadratically along both the long and short axes of the tepal such that $t = t_0(1 - x^n/c^n - y^n/b^n)$, where t_0 is the maximum thickness, c is the

semi-major axis of the elliptical cup, b is the semi-minor axis, and $n \geq 2$. The assumption that tepal thickness varies at least quadratically renders tepal edges free of forces and torques (27).

Here, we tested the model's assumption by collecting tomograms of buds from several lily varieties and measuring tepal thickness (Fig. 4.7 and Videos S4.5-4.8). The lily tepals vary in their overall size, their aspect ratio, and their final curvatures after blooming.

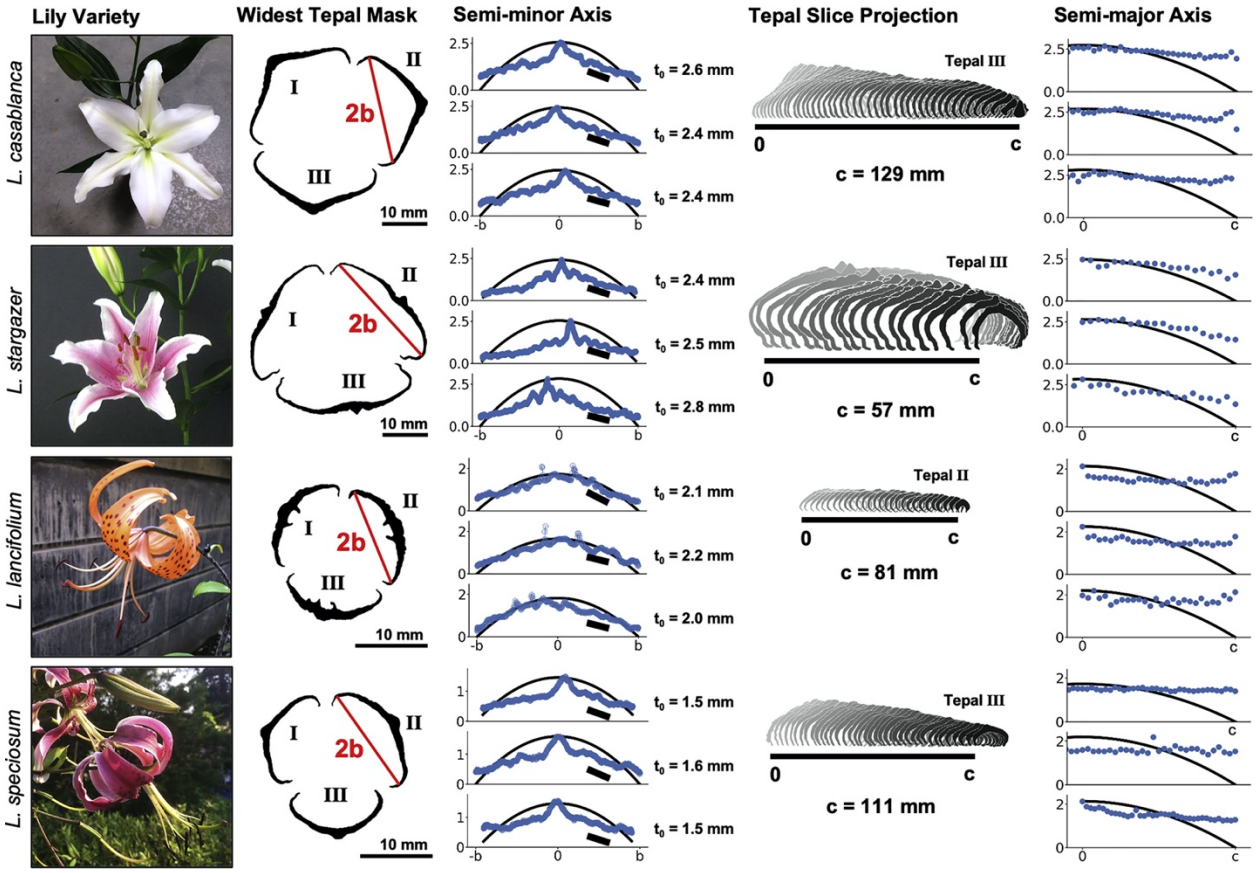

Figure 4.7. Shapes of lily buds. Column 1: Photos of blooms of four lily varieties. **Column 2:** Binarized masks of slices through the three outer tepals at $x = 0$ for each variety. The red line shows the semi-minor axis (from $y = -b$ to $+b$) of tepal II. A set of 24 slices for *L. Lancifolium* is shown in Fig. S4.7. **Column 3:** Thicknesses in millimeters (y-axis) of one tepal are plotted against their corresponding location on the semi-minor axis (x-axis). The profiles show a central peak with thickness t_0 due to the woody spine. Thicknesses typically decrease at least as fast as $t = t_0(1 - y^2/b^2)$ (thin black curve). Short black lines show the slope over an intermediate distance between the woody spine and the edge. **Column 4:** Projection of slice masks for one of the three outer tepals of each variety. The mask at $x = 0$ is at the left, and the mask at $x = c$ is at the right. Movies through the stack of slice masks are in the supporting material. **Column 5:** Tepal thicknesses at $y = 0$ are roughly constant or decrease slowly along the semi-major axis (from $x = 0$ to $+c$). The y-axis is in millimeters.

For some varieties, each tepal in a bud is well approximated by an elliptical cup. However, for others, tepal edges double back toward the center such that thickness is double-valued in y and nonzero at $y = \pm b$. If we truncate tepals before they double back, we find that tepal thickness generally decays at least as fast as $t = t_0(1 - y^2/b^2)$ in the semi-minor direction (Fig. 4.7). However, thickness is constant or only slowly decreases in the semi-major direction. Both of these results are related to the thick, woody spine at $y = 0$. The center of the spine has a roughly uniform thickness along the semi-major direction. Away from the spine, tepal thickness decreases roughly linearly with y for all lily varieties. Although the spine's uniform thickness means that the model's assumptions do not entirely represent the biological system, the result does not have any bearing on whether edge growth is the primary driver of curvature reversal in tepals. To enhance the realism of future simulations, we have compiled a set of tomogram slices for a *L. lancifolium* bud in Fig. S4.7, and we have assembled all slices of the projections in Fig. 4.7 in movies in the supporting material.

Tepal shapes in Fig. 4.7 were found by hand-sectioning lily buds. This process is straightforward and could be easily adapted for citizen science projects. However, it is time-consuming and destroys the sample so that a single bud cannot be followed through the blooming process. Moreover, after a lily has begun to bloom, it is too fragile to hand-section; the flower would have to be immobilized in resin and sectioned in a microtome. A related approach for quantifying the shape and edge growth of a tepal after a lily has begun to bloom is to cut thin strips from the edge of a ripple. When disconnected from the larger sheet, strips of this type curl into a flat annulus. Given physical values that characterize individual strips, numerical minimizations of the strip's energy result in rippled solutions (126, 127). However, cutting strips also destroys the sample.

To overcome these challenges, we tested the feasibility of an alternative, non-destructive technique. Fig. 4.8 shows a label-free X-ray computed tomogram of a lily bud and reconstructed bloom. These images (as well as Fig. S4.9 and Video S4.9 in the Supporting Materials) demonstrate strong contrast in X-ray absorption between the lily tissue and the surrounding air. In some images, individual cells are resolvable, which could be used to discover if the biological mechanism of edge growth involves changes in cell size, cell shape and/or cell number.

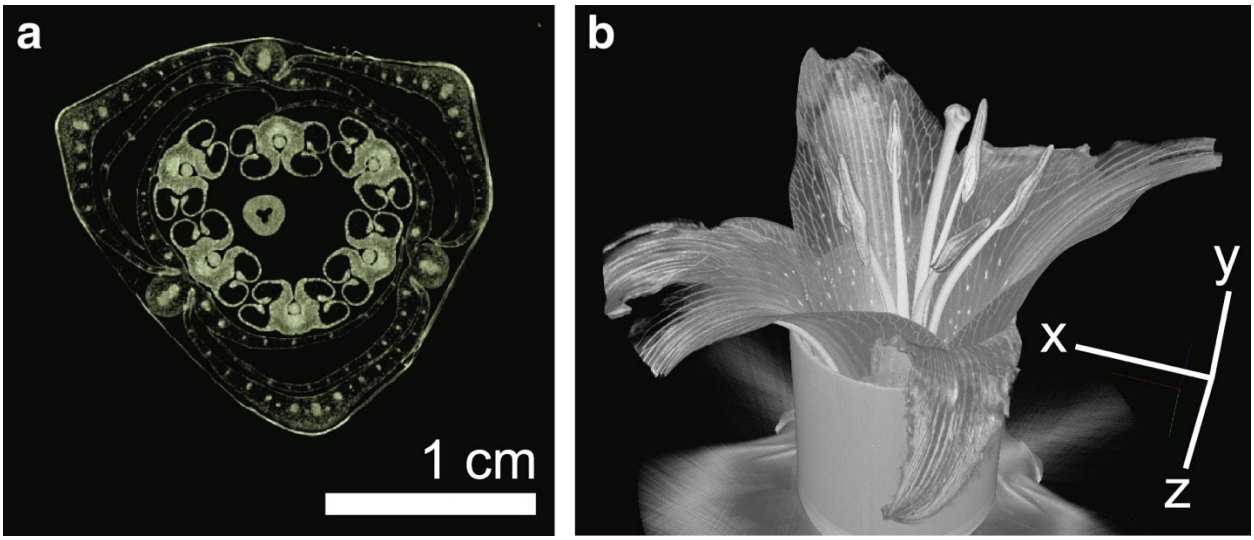

Figure 4.8. X-ray tomogram and reconstruction. A) Slice from an X-ray tomogram of a lily (oriental hybrid). Visible structural elements include, from the outside to the center: the three outer tepals, the three inner tepals, six anthers, and the style. **B)** 3-dimensional reconstruction of a lily bloom of the same variety. The tilt of the reconstruction is shown by the axes.

Higher contrast and shorter acquisition times might be achievable if a contrast agent (e.g., iodine) were added to the aqueous solution that hydrates the lily stems. Here, acquisition times were on the order of hours. Computed X-ray tomography has previously been used to image delicate biological structures of air-water interfaces in lungs (138).

4.5 Conclusions.

Our results fit within a framework that edge growth can lead to ripples and the resulting "length scales could be set by elasticity and geometry rather than by explicit genetic encoding" (122). No constraints are set on the method by which a lily tepal achieves edge growth; any biological mechanism is allowed. Here, we find that the amplitude, wavelength, and arc length of ripples are excellently fit by the equation of a buckling beam, a $\propto \sqrt{w(L-w)}$. An alternative equation of a $\propto w$, does a poor job of fitting ripples in lilies (which could be expected) and across all length scales of torn plastic sheets (which was not expected). Because ripples occur at the edges of many types of leaves and petals (26), assessment of whether ripples are well described by a $\propto w$ is a widely applicable method of determining if nonuniform stresses act in these biological materials.

Edge growth is not the only possible mechanism of blooming. Historically, lily blooming has also been attributed to enhanced expansion of cells on the adaxial (interior) face of tepals with respect to cells on the abaxial (exterior) face. Bieleski et al. assert that any differential expansion of this type must play a minor role because it follows (rather than precedes) the onset of blooming (139). Changes in the angle and curvature of the midrib—the tepal's woody spine—also contribute to blooming (27, 139). In this manuscript, we have shown that X-ray tomography can be used in a nondestructive and label-free manner to image lilies on time scales of hours, which is commensurate with time scales for budding. In the future, X-ray tomography could be used to assess relative sizes, shapes, and growth rates of cells throughout the tepal.

This manuscript has focused on edge growth in lilies, which is only one example of how biology and physics complement each other to influence plant shape. Some flower types are subject to directional growth, as in *Antirrhinum* (snapdragon) (140), and cell-shape anisotropy, as in *Aquilegia* (columbine) (141). Moreover, rippling can be influenced by external forces. The magnitude of water flow around long kelp leaves influences whether growing blades adopt flat or rippled morphologies, and pushing on the blade's edge can alter the wavelength and amplitude of ripples (142). Similarly, in lotus leaves, the wavelength of edge ripples and the overall leaf shape are influenced by whether the leaves rest on a water surface or not (143). Our results and these prior studies illustrate ways that biological morphologies could be recapitulated in biomimetic systems and tuned by physical factors.

4.6 Acknowledgements.

We thank Jennifer Nemhauser and her group for access to and assistance with time-lapse imaging. We thank Julie Graber for the loan of a time-lapse camera. Lilies were from local florists or the kind gifts of Dianne Carlson, Marie Davis, Elizabeth Harasek, and Beth Hammermeister. We thank L. Mahadevan for his engaging seminar that inspired this study, and we thank Jonathan Litz and Ido Levin for their critiques of our manuscript. We are grateful for correspondence with Harry Swinney, Michael Marder, Benoit Roman, and especially Eran Sharon for his assessment that we "are probably right" that data in Fig. 4.1A of (28) were averaged, with error bars of standard deviations. We thank every one of our anonymous reviewers for outstandingly constructive

feedback, especially for suggesting the alternate derivation below Eq. 4.4.2. Sarah L. Keller thanks the Whitely Center at UW's Friday Harbor Laboratories for a writing retreat. This research was funded by NSF MCB-0744852 and MCB-1925731 to the Keller Lab. Thomas Portet was funded by the Raymond and Beverly Sackler Foundation and the Fondation Bettencourt Schueller. X-ray tomography was performed at EMSL, a DOE Office of Science User Facility sponsored by the Biological and Environmental Research program, through rapid access proposal 47680 coordinated with Mark E. Bowden.

4.7 Supporting Materials.

i. Supporting Video Descriptions.

Video S4.1
A video of rippling of the tepal displayed in Fig. 4.1B of the main text. Each ripple edge is highlighted in a different color. Arrows indicate wavelengths and amplitudes. Each frame corresponds to 20 minutes.

Video S4.2
Shape changes in three outer tepals of a *L. stargazer* bud during blooming. The bud is imaged from the front and in two reflections, as in the schematic in Fig. S4.8. The three inner tepals were excised, and the three outer tepals were cut to 67%, 75%, or 100% (not cut) of their original lengths. The value of 67% corresponds to a length at which tepals typically remain in cup shapes throughout blooming. The time between frames is 10 min (6 frames per hour), and the total movie length corresponds to 47.5 hours. Variations in lighting are due to diurnal cycles.

Video S4.3
Shape changes in three outer tepals of a *L. stargazer* bud during blooming. The bud is imaged from the front and in two reflections, as in the schematic in Fig. S4.8. The three inner tepals were excised, and the three outer tepals were cut to 67%, 75%, or 100% (not cut) of their original lengths. The value of 67% corresponds to a length at which tepals typically remain in cup shapes throughout blooming. The time between frames is 10 min (6 frames per hour), and the total movie length corresponds to 21.5 hours. Variations in lighting are due to diurnal cycles.

Video S4.4
Shape changes in three outer tepals of a white lily bud (oriental hybrid) during blooming. The bud is imaged from the front and in two reflections, as in the schematic in Fig. S4.8. The three inner tepals were excised, and the three outer tepals were cut to 67%, 75%, or 100% (not cut) of their original lengths. The value of 67% corresponds to a length at which tepals typically remain in cup shapes throughout blooming. The time between frames is 10 min (6 frames per hour), and the total movie length corresponds to 37 hours. Variations in lighting are due to diurnal cycles.

Video S4.5
A video progressing through a stack of tomogram slices (and back again) for one lily tepal that corresponds to the *L. casablanca* projection in Column 3 of Fig. 4.7 of the main text.

Video S4.6
A video progressing through a stack of tomogram slices (and back again) for one lily tepal that corresponds to the *L. stargazer* projection in Column 3 of Fig. 4.7 of the main text.

Video S4.7
A video progressing through a stack of tomogram slices (and back again) for one lily tepal that corresponds to the *L. lanciforum* projection in Column 3 of Fig. 4.7 of the main text.

Video S4.8
A video progressing through a stack of tomogram slices (and back again) for one lily tepal that corresponds to the *L. speciosum* projection in Column 3 of Fig. 4.7 of the main text.

Video S4.9
A video of a stack of X-ray tomogram slices corresponding to the bud in Fig. 4.8A of the main text.

ii. Supporting Figures.

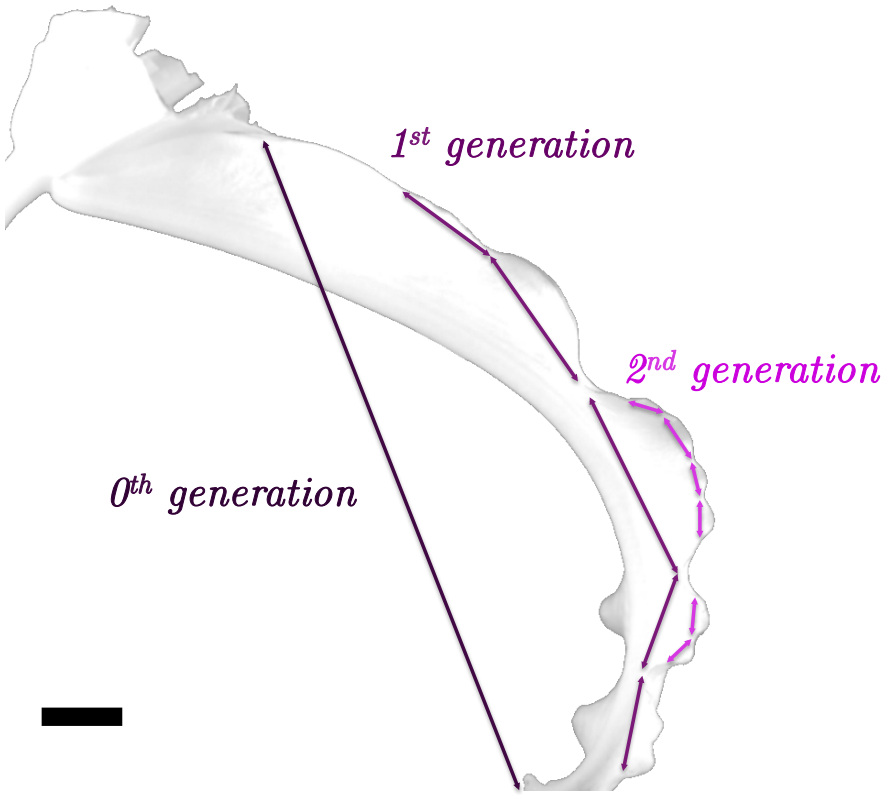

Figure S4.1. Index of ripples analyzed in Fig. 4.1. Photograph of *L. Casablanca* tepal ripples of generation 0, 1 and 2 used to plot $\log(a)$ vs. $\log(w)$ in Fig. 4.1 of the main text. In the image, the stem of the lily is at the left, bases of five excised tepals are at the top, and the tip of the single remaining tepal is at the bottom. Scale bar: 1 cm.

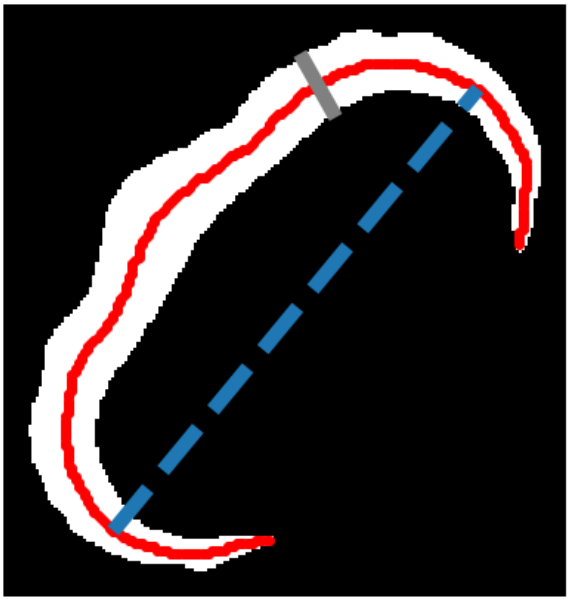

Figure S4.2. Thickness and semi-minor axis in a single tepal slice. Binarized images for each slice of each lily tepal (white area) were skeletonized (red curve). A series of tepal thicknesses (short grey line) were measured perpendicular to the skeletonized curve. Within each slice, the maximum distance between points on the skeleton was found (blue dashed line). The slice containing the largest of these distances, sets three parameters. First, the semi-minor axis, b, is half the length of the dashed line. Second, t_0 is the largest value of the thickness. Third, the slice lies at $x = 0$, one end of the semi-major axis of length c.

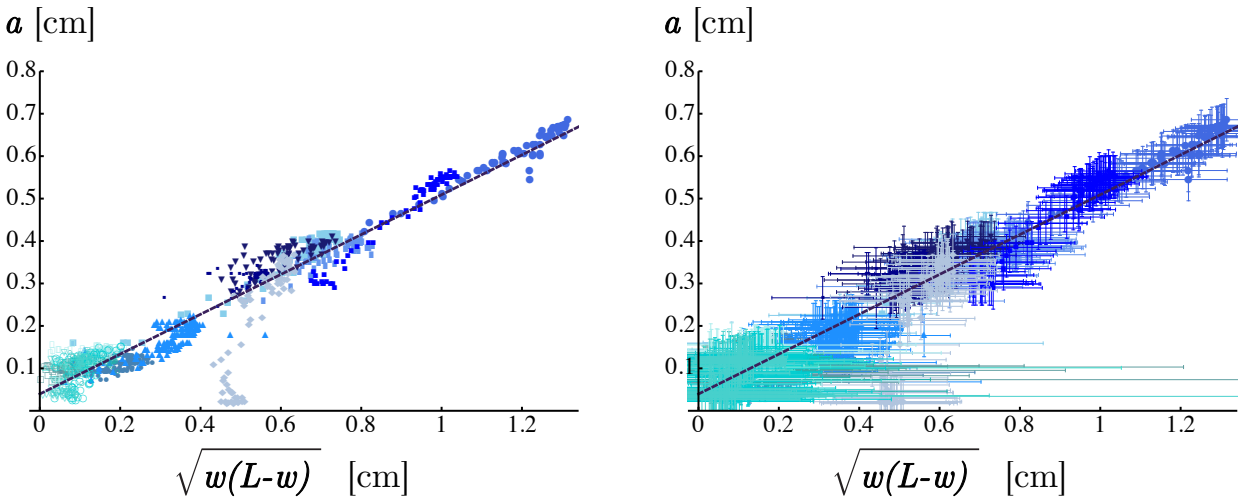

Figure S4.3. Data for smaller ripples through time. Data in Fig. 4.3C of the main text were restricted to ripples with amplitudes greater than 0.1 cm, well above the detection limit. This cutoff excludes second-generation ripples and small, first-generation ripples. The corresponding figures above include all simple ripples analyzed, including those with amplitudes smaller than 0.1 cm. The left panel shows that data for all six of the second-generation ripples are consistent with the scaling relationship a $\propto \sqrt{w(L-w)}$, even though the amplitudes of small ripples approach the measurement uncertainties. In the right panel, the same data are reproduced with uncertainties of ± 0.05 cm for each measured length (amplitude a, wavelength w, and arc length L).

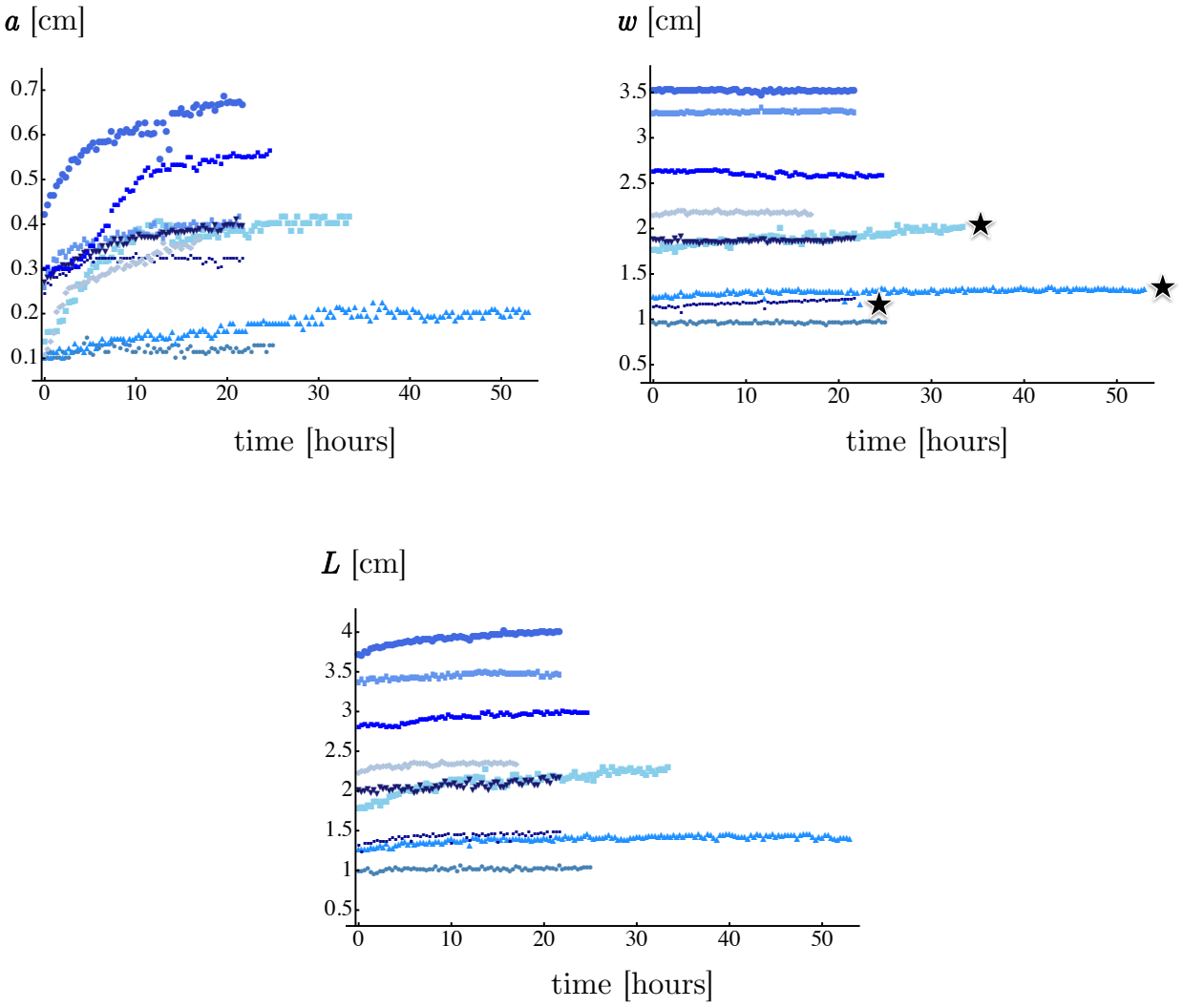

Figure S4.4. Evolution of shape descriptors. The scaling analysis presented in main text is restricted to simple, first generation ripples whose amplitudes are greater than 0.1 cm, well above our detection limit. (Data for smaller ripples are included in Fig. S4.3.) The figure above shows the evolution of three shape descriptors (amplitude a, wavelength w, and arc length L) throughout time for all simple ripples in Fig. 4.2 of the main text. We define "simple" to mean that no smaller ripples are superimposed on the ripple that is analyzed. For example, first generation ripples were analyzed only if they contained no second-generation ripples, and when second generation ripples were analyzed, the underlying first-generation ripples were not analyzed. The top left panel shows that amplitudes increase with time, and then plateau. The top right panel (and Video S4.1) shows that wavelengths are approximately constant in time. The slight increase in *w* through time in the three traces marked with stars (out of nine) is an artifact due to gradual rotation of one of the tepals toward the camera during imaging. The bottom panel shows that for all ripples, arc length L increases, and then plateaus.

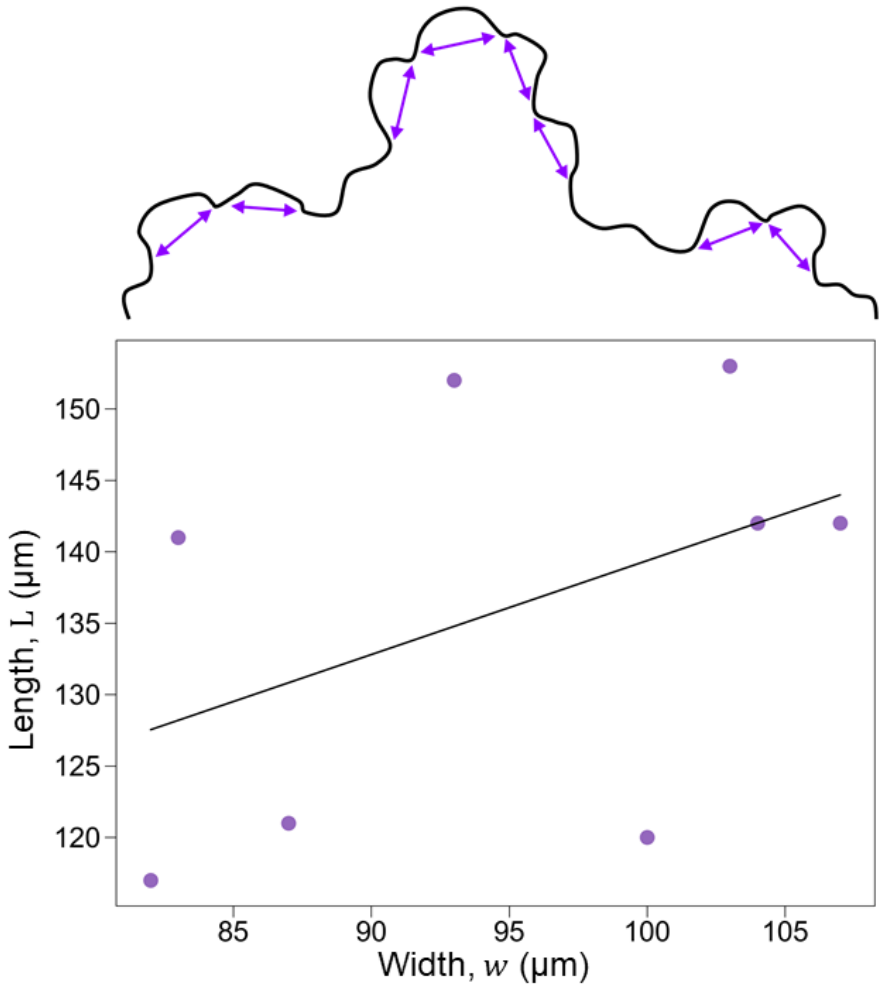

Figure S4.5. Data from torn plastic sheets. For eight "simple" ripples in images of torn plastic sheets in Sharon et al. (28), the arc length L is plotted as a function of the wavelength w. The data poorly fit a straight line with a slope of 0.66 and a confidence interval of ± 0.53. Additional data for these ripples appear in Fig. 4.5 of the main text. To aid the reader, a black curve is shown that roughly reproduces the fifth-generation ripples in Fig. 1 found in Sharon et al (28).

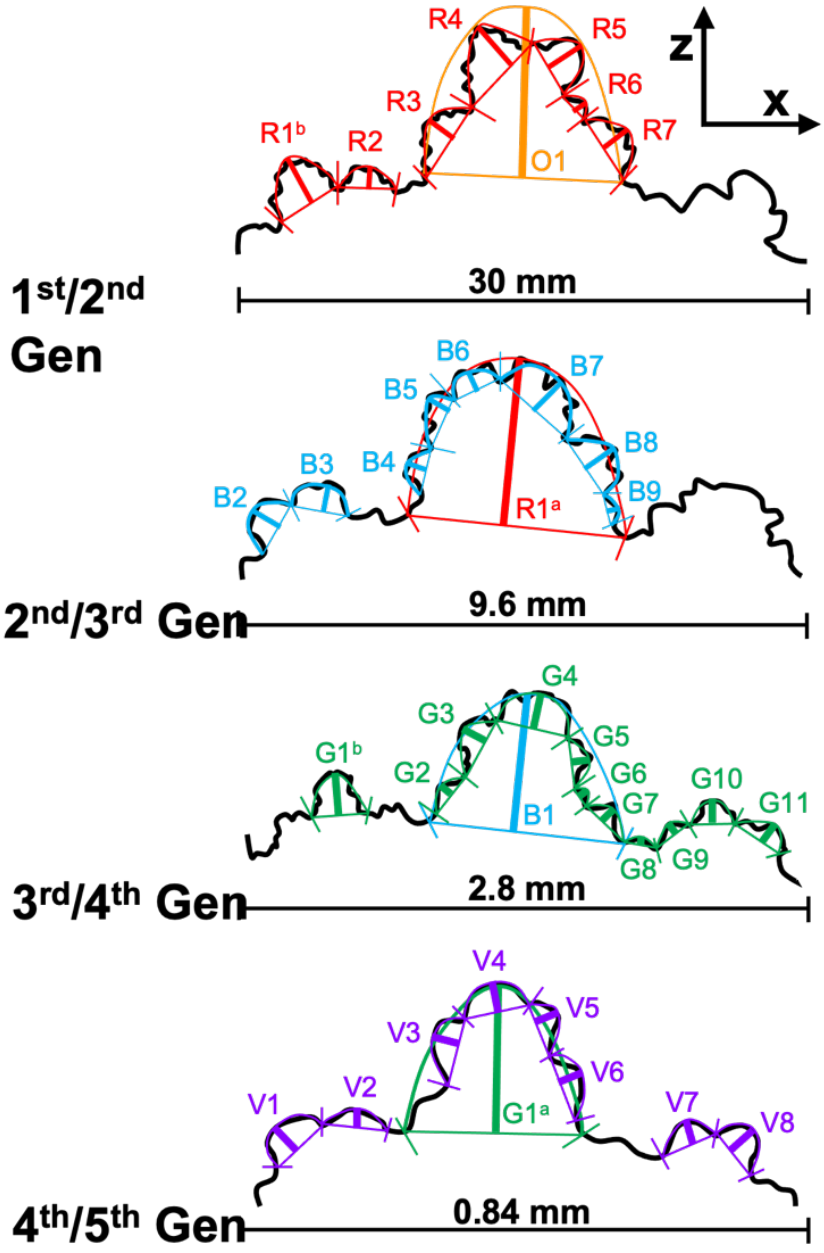

Figure S4.6. Index of ripples from multiple generations of torn plastic sheets. Generations of ripples are indexed from images of torn plastic sheets in Sharon et al. (28). The generations are indexed as orange (O, 1st generation), red (R, 2nd), blue (B, 3rd), green (G, 4th), and violet (V, 5th) for clarity. Because the shape and boundaries of a ripple are ambiguous when additional ripples are superimposed on it, colored lines show the amplitude and wavelength measured for each ripple, and curves show the arc length for each ripple. Within ImageJ (105), the amplitude a, wavelength w, and arc length L were found using the Segmented Line tool. A spline fit was applied for arc length measurements. To aid the reader, black curves are shown that roughly reproduce the ripples in Fig. 1 by Sharon et al. (28).

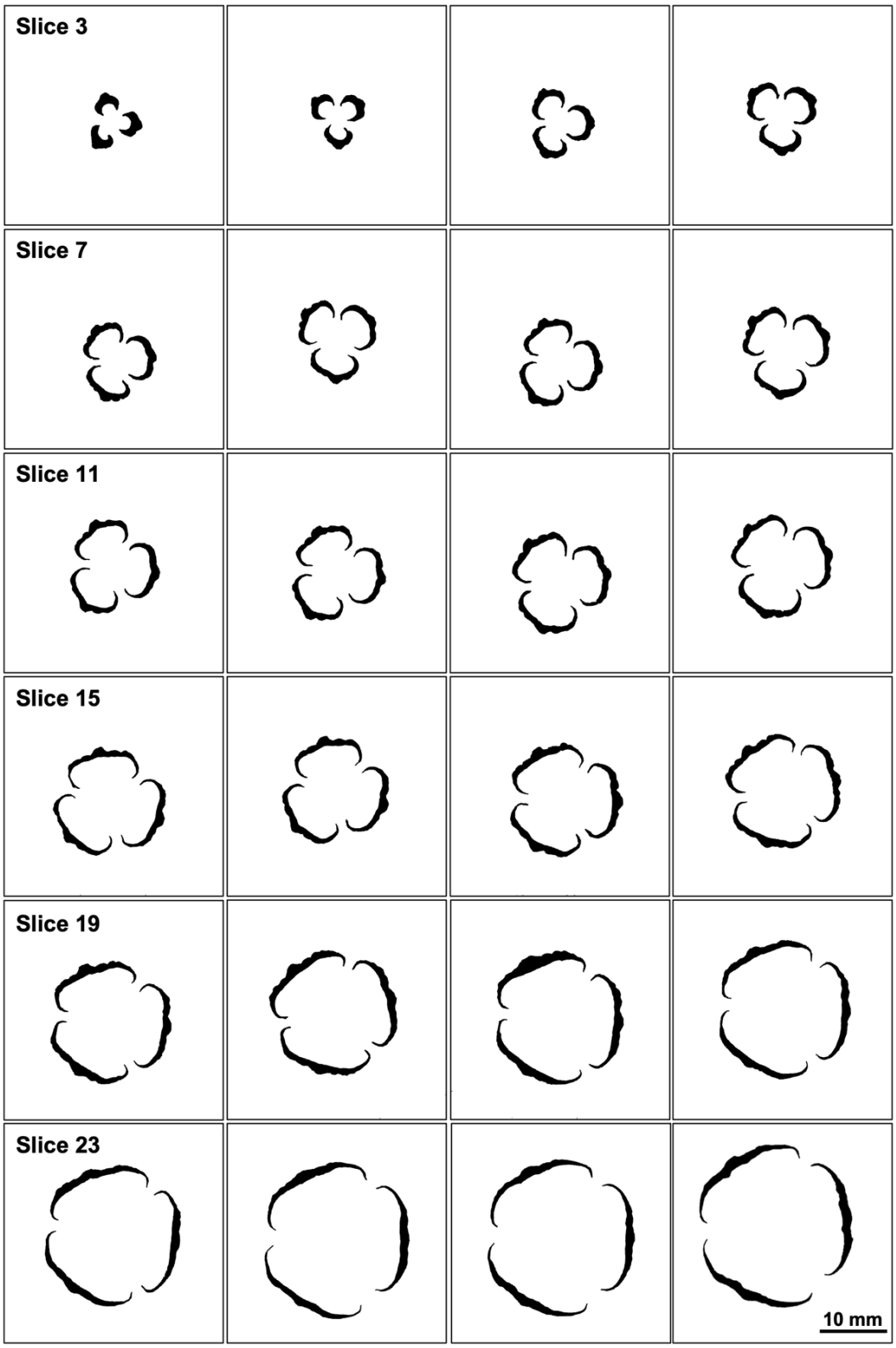

Figure S4.7. Binarized images of slices of a *L. lancifolium* (tiger lily) bud. The slices were used to generate the images in Column 4 of Fig. 4.7 of the main text.

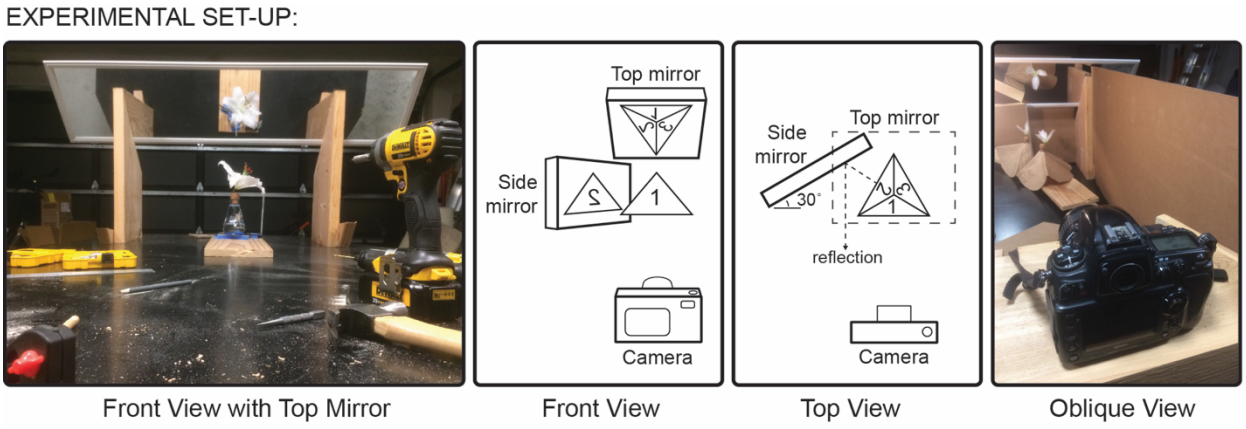

Figure S4.8. Experimental set-up and final frames corresponding to Videos S4.2-4.4. (**Top**) Front, top, and oblique views of the camera and mirrors. In the schematic, the lily is represented as a triangular pyramid with top faces labeled "1", "2", and "3". The three inner tepals of the lily bud were excised and the stem was placed in an Erlenmeyer flask filled with water. A side mirror at 30˚ and a top mirror at 45˚ reflected additional views to the camera. (**Bottom**) Final images from Videos S4.2-4.4. A rare exception is shown at the right, in which ripples in the shortest tepal have smaller amplitudes than ripples in longer tepals. Similar differences in ripple amplitudes occasionally occur when all tepals are the same length.

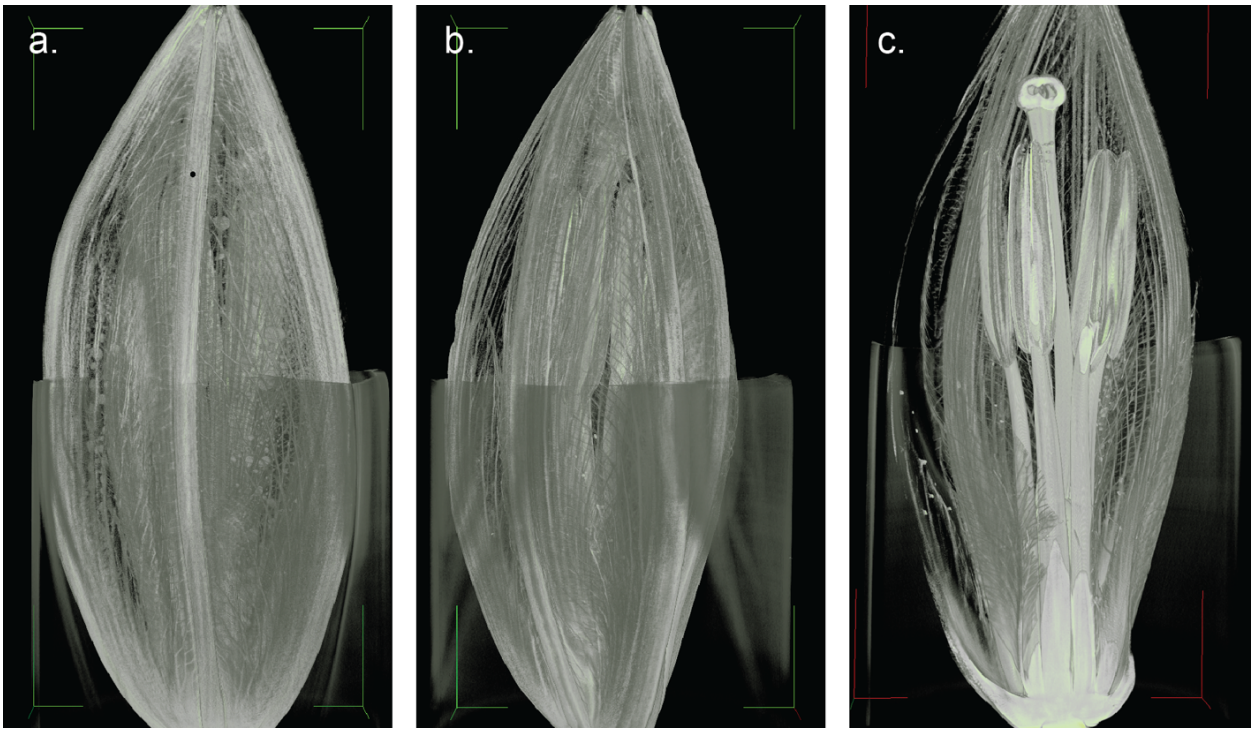

Figure S4.9. Side views from X-ray tomograms of a lily bud. (**a-b**) Two side views and (**c**) a cut-away view of a lily bud (oriental variety). The container that held the bud upright is faintly visible in the lower half of all three images.

Chapter 5

Conclusion

In this document, I have discussed several techniques used to measure the biophysical properties of lipid membranes and lily flowers. For each, complex biophysical behavior can be broken down into building blocks, whether liquid-liquid phase separation in membranes or rippling and blooming in lilies. Experimentally measuring the biophysical properties of lipid membranes often precedes relevant theory, whereas experiments on rippling and blooming in lilies were directly motivated by previous simulations.

In Chapter 2, we confronted a widely held assumption that the composition of a lipid stock solution generally matches the composition of the membranes produced by that lipid stock. By using a five-component mixture containing major classes of lipids, and binary mixtures of saturated and unsaturated PC-lipids and cholesterol, we confirmed this assumption to be sound (barring a few caveats). Researchers will be reassured that two membrane compositions will be distinguishable if they vary lipid composition by 2 mol% or more. In contrast, compositional increments smaller than 2 mol% will likely be indistinguishable from sample-to-sample variation. Our results can serve as an initial point of confidence that our membrane compositions align with our intention, and an encouragement for future work to characterize the impacts of additional or more specialized techniques on lipid incorporation into membranes.

We expect that our newly mapped phase diagrams for vesicle compositions that replace DPPC with DPPE are at the forefront of new theory and simulation. In Chapter 3, we made three surprising discoveries: 1) Liquid-liquid phase separation is eradicated completely and replaced by solid-liquid coexistence in vesicles made of DOPC, DPPE, and cholesterol, 2) liquid-liquid phase separation is severely limited in vesicles made of DiphyPC, DPPE, and cholesterol, and 3) solid and liquid-ordered phases are distinguishable by fluorescence microscopy in membranes containing DPPE. As a result, it is possible to observe solid-liquid phase separation at high temperature, followed by a transition to a three-phase region with coexisting solid, liquid-ordered,

and liquid-disordered phases at a lower temperature. The newly mapped phase diagrams can serve as building blocks, aiding in the understanding of the effects PE-lipids have on organization within biological membranes.

In Chapter 4, we shifted our focus to a more macrobiological system: lily flowers. We explored several techniques for acquiring biophysical measurements of lilies, including surgical tomography, X-ray tomography, and image analyses of ripple evolution in timelapse videos and lily tepal thicknesses in photographs. We successfully applied a scaling law for ripples in plastic sheets to ripples in lilies and improved upon it by applying the scaling law for a buckling beam, where stresses are not held constant. Furthermore, our thickness measurements indicated that models of lily petals as thin, lenticular shells can be made more accurate in the future by considering the thick, woody spine along the longitudinal axis of the lily tepal. Finally, given that surgical tomography of lily buds is destructive, we a proof of principle that X-ray tomography can be used as an alternative method to measure structural features in plants, even allowing measurement of lily buds as they bloom and ripple in real time.

References

1. Cullis, P.R., M.J. Hope, and C.P.S. Tilcock. 1986. Lipid polymorphism and the roles of lipids in membranes. *Chem. Phys. Lipids*. 40:127–144.

2. Pitman, M.C., F. Suits, K. Gawrisch, and S.E. Feller. 2005. Molecular dynamics investigation of dynamical properties of phosphatidylethanolamine lipid bilayers. *J. Chem. Phys.* 122:244715.

3. Korlach, J., P. Schwille, W.W. Webb, and G.W. Feigenson. 1999. Characterization of lipid bilayer phases by confocal microscopy and fluorescence correlation spectroscopy. *Proc. Natl. Acad. Sci. USA*. 96:8461–8466.

4. Macháň, R., and M. Hof. 2010. Lipid diffusion in planar membranes investigated by fluorescence correlation spectroscopy. *BBA - Biomembr.* 1798:1377–1391.

5. Lorent, J.H., K.R. Levental, L. Ganesan, G. Rivera-Longsworth, E. Sezgin, M. Doktorova, E. Lyman, and I. Levental. 2020. Plasma membranes are asymmetric in lipid unsaturation, packing and protein shape. *Nat. Chem. Biol.* 16:644–652.

6. Akashi, K., H. Miyata, H. Itoh, and K. Kinosita. 1996. Preparation of giant liposomes in physiological conditions and their characterization under an optical microscope. *Biophys. J.* 71:3242–3250.

7. Dimitrov, D.S., and M.I. Angelova. 1988. Lipid swelling and liposome formation mediated by electric fields. *Bioelectrochem. Bioenerg.* 19:323–336.

8. Veatch, S.L. 2007. Electro-formation and fluorescence microscopy of giant vesicles with coexisting liquid phases. *Methods Mol. Biol.* 398:59–72.

9. Pautot, S., B.J. Frisken, and D.A. Weitz. 2003. Production of Unilamellar Vesicles Using an Inverted Emulsion. *Langmuir*. 19:2870–2879.

10. Singer, S.J., and G.L. Nicolson. 1972. The Fluid Mosaic Model of the Structure of Cell Membranes. *Science*. 175:720–731.

11. Simons, K., and E. Ikonen. 1997. Functional rafts in cell membranes. *Nature*. 387:569–572.

12. Veatch, S.L., and S.L. Keller. 2005. Seeing spots: Complex phase behavior in simple membranes. *BBA - Mol. Cell Res.* 1746:172–185.

13. Veatch, S.L., and S.L. Keller. 2002. Organization in Lipid Membranes Containing Cholesterol. *Phys. Rev. Lett.* 89:268101.

14. Veatch, S.L., and S.L. Keller. 2003. Separation of Liquid Phases in Giant Vesicles of Ternary Mixtures of Phospholipids and Cholesterol. *Biophys. J.* 85:3074–3083.

15. Toulmay, A., and W.A. Prinz. 2013. Direct imaging reveals stable, micrometer-scale lipid domains that segregate proteins in live cells. *J. Cell Biol.* 202:35–44.

16. Wang, C.-W., Y.-H. Miao, and Y.-S. Chang. 2014. A sterol-enriched vacuolar microdomain mediates stationary phase lipophagy in budding yeast. *J. Cell Biol.* 206:357–366.

17. Leveille, C.L., C.E. Cornell, A.J. Merz, and S.L. Keller. 2022. Yeast cells actively tune their membranes to phase separate at temperatures that scale with growth temperatures. *Proc. Natl. Acad. Sci. USA*. 119:e2116007119.

18. Burns, M., K. Wisser, J. Wu, I. Levental, and S.L. Veatch. 2017. Miscibility Transition Temperature Scales with Growth Temperature in a Zebrafish Cell Line. *Biophys. J.* 113:1212–1222.

19. Veatch, S.L., K. Gawrisch, and S.L. Keller. 2006. Closed-Loop Miscibility Gap and Quantitative Tie-Lines in Ternary Membranes Containing Diphytanoyl PC. *Biophys. J.* 90:4428–4436.

20. Zhao, J., J. Wu, F.A. Heberle, T.T. Mills, P. Klawitter, G. Huang, G. Costanza, and G.W. Feigenson. 2007. Phase studies of model biomembranes: Complex behavior of DSPC/DOPC/Cholesterol. *BBA - Biomembr.* 1768:2764–2776.

21. Blosser, M.C., J.B. Starr, C.W. Turtle, J. Ashcraft, and S.L. Keller. 2013. Minimal Effect of Lipid Charge on Membrane Miscibility Phase Behavior in Three Ternary Systems. *Biophys. J.* 104:2629–2638.

22. Vequi-Suplicy, C.C., K.A. Riske, R.L. Knorr, and R. Dimova. 2010. Vesicles with charged domains. *BBA - Biomembr.* 1798:1338–1347.

23. Veatch, S.L., and S.L. Keller. 2005. Miscibility Phase Diagrams of Giant Vesicles Containing Sphingomyelin. *Phys. Rev. Lett.* 94:148101.

24. Ionova, I.V., V.A. Livshits, and D. Marsh. 2012. Phase Diagram of Ternary Cholesterol/Palmitoylsphingomyelin/Palmitoyloleoyl-Phosphatidylcholine Mixtures: Spin-Label EPR Study of Lipid-Raft Formation. *Biophys. J.* 102:1856–1865.

25. Koynova, R., and M. Caffrey. 1994. Phases and phase transitions of the hydrated phosphatidylethanolamines. *Chem. Phys. Lipids*. 69:1–34.

26. Sharon, E., M. Marder, and H.L. Swinney. 2004. Leaves, Flowers and Garbage Bags: Making Waves. *Am. Sci.* 92:254–261.

27. Liang, H., and L. Mahadevan. 2011. Growth, geometry, and mechanics of a blooming lily. *Proc. Natl. Acad. Sci. USA*. 108:5516–5521.

28. Sharon, E., B. Roman, M. Marder, G.-S. Shin, and H.L. Swinney. 2002. Buckling cascades in free sheets. *Nature*. 419:579.

29. Dimova, R., and C. Marques. 2019. The Giant Vesicle Book. CRC Press, Taylor & Francis Group.

30. Olson, F., C.A. Hunt, F.C. Szoka, W.J. Vail, and D. Papahadjopoulos. 1979. Preparation of liposomes of defined size distribution by extrusion through polycarbonate membranes. *BBA - Biomembr.* 557:9–23.

31. Sugiura, S., T. Kuroiwa, T. Kagota, M. Nakajima, S. Sato, S. Mukataka, P. Walde, and S. Ichikawa. 2008. Novel Method for Obtaining Homogeneous Giant Vesicles from a Monodisperse Water-in-Oil Emulsion Prepared with a Microfluidic Device. *Langmuir*. 24:4581–4588.

32. Zhu, T.F., and J.W. Szostak. 2009. Preparation of Large Monodisperse Vesicles. *PLoS One*. 4:e5009.

33. Angelova, M.I. 1988. Lipid Swelling and Liposome Formation in Electric Fields. Ph.D. Thesis.

34. Ghellab, S.E., Q. Li, T. Fuhs, H. Bi, and X. Han. 2017. Electroformation of double vesicles using an amplitude modulated electric field. *Colloids Surf. B Biointerfaces*. 160:697–703.

35. Ip, T., Q. Li, N. Brooks, and Y. Elani. 2021. Manufacture of Multilayered Artificial Cell Membranes through Sequential Bilayer Deposition on Emulsion Templates. *Chembiochem*. 22:2275–2281.

36. Pautot, S., B.J. Frisken, and D.A. Weitz. 2003. Engineering asymmetric vesicles. *Proc. Natl. Acad. Sci. USA*. 100:10718–10721.

37. Elani, Y., S. Purushothaman, P.J. Booth, J.M. Seddon, N.J. Brooks, R.V. Law, and O. Ces. 2015. Measurements of the effect of membrane asymmetry on the mechanical properties of lipid bilayers. *Chem. Commun.* 51:6976–6979.

38. Doktorova, M., F.A. Heberle, B. Eicher, R.F. Standaert, J. Katsaras, E. London, G. Pabst, and D. Marquardt. 2018. Preparation of asymmetric phospholipid vesicles: The next generation of cell membrane models. *Nat. Protoc.* 13:2086–2101.

39. Dominak, L.M., and C.D. Keating. 2007. Polymer Encapsulation within Giant Lipid Vesicles. *Langmuir*. 23:7148–7154.

40. Abkarian, M., E. Loiseau, and G. Massiera. 2011. Continuous droplet interface crossing encapsulation (cDICE) for high throughput monodisperse vesicle design. *Soft Matter*. 7:4610–4614.

41. Huang, J., J.T. Buboltz, and G.W. Feigenson. 1999. Maximum solubility of cholesterol in phosphatidylcholine and phosphatidylethanolamine bilayers. *BBA - Biomembr.* 1417:89–100.

42. Epand, R.M., D.W. Hughes, B.G. Sayer, N. Borochov, D. Bach, and E. Wachtel. 2003. Novel properties of cholesterol-dioleoylphosphatidylcholine mixtures. *Biochim. Biophys. Acta*. 1616:196–208.

43. Shaikh, S.R., V. Cherezov, M. Caffrey, S.P. Soni, D. LoCascio, W. Stillwell, and S.R. Wassall. 2006. Molecular Organization of Cholesterol in Unsaturated Phosphatidylethanolamines: X-ray Diffraction and Solid State 2H NMR Reveal Differences with Phosphatidylcholines. *J. Am. Chem. Soc.* 128:5375–5383.

44. Stevens, M.M., A.R. Honerkamp-Smith, and S.L. Keller. 2010. Solubility Limits of Cholesterol, Lanosterol, Ergosterol, Stigmasterol, and β-Sitosterol in Electroformed Lipid Vesicles. *Soft Matter*. 6:5882–5890.

45. Ibarguren, M., A. Alonso, B.G. Tenchov, and F.M. Goñi. 2010. Quantitation of cholesterol incorporation into extruded lipid bilayers. *BBA - Biomembr.* 1798:1735–1738.

46. Blosser, M.C., B.G. Horst, and S.L. Keller. 2016. cDICE method produces giant lipid vesicles under physiological conditions of charged lipids and ionic solutions. *Soft Matter*. 12:7364–7371.

47. Karamdad, K., J. W. Hindley, G. Bolognesi, M. S. Friddin, R. V. Law, N. J. Brooks, O. Ces, and Y. Elani. 2018. Engineering thermoresponsive phase separated vesicles formed via emulsion phase transfer as a content-release platform. *Chem. Sci.* 9:4851–4858.

48. Dürre, K., and A. R. Bausch. 2019. Formation of phase separated vesicles by double layer cDICE. *Soft Matter*. 15:9676–9681.

49. Gambhir, A., G. Hangyás-Mihályné, I. Zaitseva, D.S. Cafiso, J. Wang, D. Murray, S.N. Pentyala, S.O. Smith, and S. McLaughlin. 2004. Electrostatic Sequestration of PIP2 on Phospholipid Membranes by Basic/Aromatic Regions of Proteins. *Biophys. J.* 86:2188–2207.

50. Grusky, D.S., A. Bhattacharya, and S.G. Boxer. 2023. Secondary Ion Mass Spectrometry of Single Giant Unilamellar Vesicles Reveals Compositional Variability. *J. Am. Chem. Soc.* 145:27521–27530.

51. van der Veen, J.N., J.P. Kennelly, S. Wan, J.E. Vance, D.E. Vance, and R.L. Jacobs. 2017. The critical role of phosphatidylcholine and phosphatidylethanolamine metabolism in health and disease. *BBA - Biomembr.* 1859:1558–1572.

52. Brennan, P.J., and H. Nikaido. 1995. The Envelope of Mycobacteria. *Annu. Rev. Biochem.* 64:29–63.

53. Marsh, D. 2013. Handbook of Lipid Bilayers. 2nd ed. Boca Raton: CRC Press.

54. Verkleij, A.J., R.F.A. Zwaal, B. Roelofsen, P. Comfurius, D. Kastelijn, and L.L.M. van Deenen. 1973. The asymmetric distribution of phospholipids in the human red cell membrane. A combined study using phospholipases and freeze-etch electron microscopy. *BBA - Biomembr.* 323:178–193.

55. Yang, S.-T., A.J.B. Kreutzberger, J. Lee, V. Kiessling, and L.K. Tamm. 2016. The role of cholesterol in membrane fusion. *Chem. Phys. Lipids*. 199:136–143.

56. Dietrich, C., L.A. Bagatolli, Z.N. Volovyk, N.L. Thompson, M. Levi, K. Jacobson, and E. Gratton. 2001. Lipid Rafts Reconstituted in Model Membranes. *Biophys. J.* 80:1417–1428.

57. Koynova, R., and M. Caffrey. 1998. Phases and phase transitions of the phosphatidylcholines. *BBA - Rev. Biomembr.* 1376:91–145.

58. John R. Silvius and R. N. McElhaney. 1979. Effects of Phospholipid Acyl Chain Structure on Thermodynamic Phase Properties. 2: Phosphatidylcholines with Unsaturated or Cyclopropane Acyl Chains. *Chem. Phys. Lipids*. 25:125–134.

59. Findlay, E.J., and P.G. Barton. 1978. Phase behavior of synthetic phosphatidylglycerols and binary mixtures with phosphatidylcholines in the presence and absence of calcium ions. *Biochem.* 17:2400–2405.

60. Witkowska, A., L. Jablonski, and R. Jahn. 2018. A convenient protocol for generating giant unilamellar vesicles containing SNARE proteins using electroformation. *Sci. Rep.* 8:9422.

61. Moga, A., N. Yandrapalli, R. Dimova, and T. Robinson. 2019. Optimization of the Inverted Emulsion Method for High-Yield Production of Biomimetic Giant Unilamellar Vesicles. *Chembiochem*. 20:2674–2682.

62. Bligh, E.G., and W.J. Dyer. 1959. A rapid method of total lipid extraction and purification. *Can. J. Biochem. Physiol.* 37:911–917.

63. Hines, K.M., J.C. May, J.A. McLean, and L. Xu. 2016. Evaluation of Collision Cross Section Calibrants for Structural Analysis of Lipids by Traveling Wave Ion Mobility-Mass Spectrometry. *Anal. Chem.* 88:7329–7336.

64. Hines, K.M., J. Herron, and L. Xu. 2017. Assessment of altered lipid homeostasis by HILIC-ion mobility-mass spectrometry-based lipidomics. *J. Lipid. Res.* 58:809–819.

65. Li, A., K.M. Hines, and L. Xu. 2020. Lipidomics by HILIC-Ion Mobility-Mass Spectrometry. *Methods Mol. Biol.* 2084:119–132.

66. Ross, D.H., J.H. Cho, R. Zhang, K.M. Hines, and L. Xu. 2020. LiPydomics: A Python Package for Comprehensive Prediction of Lipid Collision Cross Sections and Retention Times and Analysis of Ion Mobility-Mass Spectrometry-Based Lipidomics Data. *Anal. Chem.* 92:14967–14975.

67. Herron, J., K.M. Hines, and L. Xu. 2018. Assessment of altered cholesterol homeostasis by xenobiotics using ultra-high performance liquid chromatography-tandem mass spectrometry. *Curr. Protoc. Toxicol.* 78:e65.

68. Garg, S., F. Castro-Roman, L. Porcar, P. Butler, P.J. Bautista, N. Krzyzanowski, and U. Perez-Salas. 2014. Cholesterol solubility limit in lipid membranes probed by small angle neutron scattering and MD simulations. *Soft Matter*. 10:9313–9317.

69. Shaw, T.R., K.C. Wisser, T.A. Schaffner, A.D. Gaffney, B.B. Machta, and S.L. Veatch. 2023. Chemical potential measurements constrain models of cholesterol-phosphatidylcholine interactions. *Biophys. J.* 122:1105–1117.

70. Kim, E., O. Graceffa, R. Broweleit, A. Ladha, A. Boies, and R.J. Rawle. 2024. Lipid loss and compositional change during preparation of liposomes by common biophysical methods. 2024.05.30.596670.

71. Cornell, C.E., A. Mileant, N. Thakkar, K.K. Lee, and S.L. Keller. 2020. Direct imaging of liquid domains in membranes by cryo-electron tomography. *Proc. Natl. Acad. Sci. USA*. 117:19713–19719.

72. Heberle, F.A., M. Doktorova, H.L. Scott, A.D. Skinkle, M.N. Waxham, and I. Levental. 2020. Direct label-free imaging of nanodomains in biomimetic and biological membranes by cryogenic electron microscopy. *Proc. Natl. Acad. Sci. USA*. 117:19943–19952.

73. Heberle, F.A., M. Doktorova, S.L. Goh, R.F. Standaert, J. Katsaras, and G.W. Feigenson. 2013. Hybrid and Nonhybrid Lipids Exert Common Effects on Membrane Raft Size and Morphology. *J. Am. Chem. Soc.* 135:14932–14935.

74. Cooper, A., and A.B. Subramaniam. 2024. Ultrahigh yields of giant vesicles obtained through mesophase evolution and breakup. 2024.06.03.597257.

75. Morita, M., H. Onoe, M. Yanagisawa, H. Ito, M. Ichikawa, K. Fujiwara, H. Saito, and M. Takinoue. 2015. Droplet-Shooting and Size-Filtration (DSSF) Method for Synthesis of Cell-Sized Liposomes with Controlled Lipid Compositions. *Chembiochem*. 16:2029–2035.

76. Pazzi, J., and A.B. Subramaniam. 2020. Nanoscale Curvature Promotes High Yield Spontaneous Formation of Cell-Mimetic Giant Vesicles on Nanocellulose Paper. *ACS Appl. Mater. Interfaces*. 12:56549–56561.

77. Horger, K.S., D.J. Estes, R. Capone, and M. Mayer. 2009. Films of Agarose Enable Rapid Formation of Giant Liposomes in Solutions of Physiologic Ionic Strength. *J. Am. Chem. Soc.* 131:1810–1819.

78. Weinberger, A., F.-C. Tsai, G.H. Koenderink, T.F. Schmidt, R. Itri, W. Meier, T. Schmatko, A. Schröder, and C. Marques. 2013. Gel-Assisted Formation of Giant Unilamellar Vesicles. *Biophys. J.* 105:154–164.

79. MacDonald, R.C., R.I. MacDonald, B.Ph.M. Menco, K. Takeshita, N.K. Subbarao, and L. Hu. 1991. Small-volume extrusion apparatus for preparation of large, unilamellar vesicles. *BBA - Biomembr.* 1061:297–303.

80. Reinhard, J., C.L. Leveille, C.E. Cornell, A.J. Merz, C. Klose, R. Ernst, and S.L. Keller. 2023. Remodeling of yeast vacuole membrane lipidomes from the log (one phase) to stationary stage (two phases). *Biophys. J.* 122:1043–1057.

81. Kim, H., and I. Budin. 2024. Intracellular sphingolipid sorting drives membrane phase separation in the yeast vacuole. *J. Biol. Chem.* 300:105496.

82. Wilson, K.J., H.Q. Nguyen, J. Gervay-Hague, and S.L. Keller. 2024. Sterol–lipids enable large-scale, liquid–liquid phase separation in bilayer membranes of only two components. *Proc. Natl. Acad. Sci. USA*. 121:e2401241121.

83. Samsonov, A.V., I. Mihalyov, and F.S. Cohen. 2001. Characterization of Cholesterol-Sphingomyelin Domains and Their Dynamics in Bilayer Membranes. *Biophys. J.* 81:1486–1500.

84. Lin, W.-C., C.D. Blanchette, and M.L. Longo. 2007. Fluid-Phase Chain Unsaturation Controlling Domain Microstructure and Phase in Ternary Lipid Bilayers Containing GalCer and Cholesterol. *Biophys. J.* 92:2831–2841.

85. Castro, B.M., L.C. Silva, A. Fedorov, R.F.M. de Almeida, and M. Prieto. 2009. Cholesterol-rich Fluid Membranes Solubilize Ceramide Domains: Implications for the Structure and Dynamics of Mammalian Intracellular and Plasma Membranes. *J. Biol. Chem.* 284:22978–22987.

86. Suits, F., M.C. Pitman, and S.E. Feller. 2005. Molecular dynamics investigation of the structural properties of phosphatidylethanolamine lipid bilayers. *J. Chem. Phys.* 122:244714.

87. Keller, S.L., S.M. Bezrukov, S.M. Gruner, M.W. Tate, I. Vodyanoy, and V.A. Parsegian. 1993. Probability of alamethicin conductance states varies with nonlamellar tendency of bilayer phospholipids. *Biophys. J.* 65:23–27.

88. Brown, M.F. 1994. Modulation of rhodopsin function by properties of the membrane bilayer. *Chem. Phys. Lipids*. 73:159–180.

89. Bogdanov, M., and W. Dowhan. 1998. Phospholipid-assisted protein folding: phosphatidylethanolamine is required at a late step of the conformational maturation of the polytopic membrane protein lactose permease. *EMBO J.* 17:5255–5264.

90. Wikström, M., A.A. Kelly, A. Georgiev, H.M. Eriksson, M.R. Klement, M. Bogdanov, W. Dowhan, and Å. Wieslander. 2009. Lipid-engineered *Escherichia coli* Membranes Reveal Critical Lipid Headgroup Size for Protein Function. *J. Biol. Chem.* 284:954–965.

91. Andersen, O.S., and R.E. Koeppe 2nd. 2007. Bilayer Thickness and Membrane Protein Function: An Energetic Perspective. *Annu. Rev. Biophys.* 36:107–130.

92. Davies, M.A., W. Hubner, A. Blume, and R. Mendelsohn. 1992. Acyl chain conformational ordering in 1,2 dipalmitoylphosphatidylethanolamine. Integration of FT-IR and 2H NMR results. *Biophys. J.* 63:1059–1062.

93. Klose, C., M.A. Surma, M.J. Gerl, F. Meyenhofer, A. Shevchenko, and K. Simons. 2012. Flexibility of a Eukaryotic Lipidome – Insights from Yeast Lipidomics. *PLoS ONE*. 7:e35063.

94. Siegel, D.P. 1993. Energetics of intermediates in membrane fusion: comparison of stalk and inverted micellar intermediate mechanisms. *Biophys. J.* 65:2124–2140.

95. Allender, D.W., and M. Schick. 2023. On the force between "rafts." *Eur. Phys. J. E*. 46:85.

96. Cornell, C.E., A.D. Skinkle, S. He, I. Levental, K.R. Levental, and S.L. Keller. 2018. Tuning Length Scales of Small Domains in Cell-Derived Membranes and Synthetic Model Membranes. *Biophys. J.* 115:690–701.

97. Shyamsunder, E., S.M. Gruner, M.W. Tate, D.C. Turner, P.T.C. So, and C.P.S. Tilcock. 1988. Observation of inverted cubic phase in hydrated dioleoylphosphatidylethanolamine membranes. *Biochem.* 27:2332–2336.

98. So, P.T.C., S.M. Gruner, and S. Erramilli. 1993. Pressure-induced topological phase transitions in membranes. *Phys. Rev. Lett.* 70:3455–3458.

99. Winnikoff, J.R., D. Milshteyn, S.J. Vargas-Urbano, M.A. Pedraza-Joya, A.M. Armando, O. Quehenberger, A. Sodt, R.E. Gillilan, E.A. Dennis, E. Lyman, S.H.D. Haddock, and I. Budin. 2024. Homeocurvature adaptation of phospholipids to pressure in deep-sea invertebrates. *Science*. 384:1482–1488.

100. Marrink, S.J., V. Corradi, P.C.T. Souza, H.I. Ingólfsson, D.P. Tieleman, and M.S.P. Sansom. 2019. Computational Modeling of Realistic Cell Membranes. *Chem. Rev.* 119:6184–6226.

101. Hossein, A., and M. Deserno. 2020. Spontaneous Curvature, Differential Stress, and Bending Modulus of Asymmetric Lipid Membranes. *Biophys. J.* 118:624–642.

102. Keller, S.L., S.M. Gruner, and K. Gawrisch. 1996. Small concentrations of alamethicin induce a cubic phase in bulk phosphatidylethanolamine mixtures. *BBA - Biomembr.* 1278:241–246.

103. Lindsey, H., N.O. Petersen, and S.I. Chan. 1979. Physicochemical characterization of 1,2-diphytanoyl-*sn*-glycero-3-phosphocholine in model membrane systems. *BBA - Biomembr.* 555:147–167.

104. Weakly, H.M.J., K.J. Wilson, G.J. Goetz, E.L. Pruitt, A. Li, L. Xu, and S.L. Keller. 2024. Several common methods of making vesicles (except an emulsion method) capture intended lipid ratios. *Biophys. J.* 123:3452–3462.

105. Schindelin, J., I. Arganda-Carreras, E. Frise, V. Kaynig, M. Longair, T. Pietzsch, S. Preibisch, C. Rueden, S. Saalfeld, B. Schmid, J.-Y. Tinevez, D.J. White, V. Hartenstein, K. Eliceiri, P. Tomancak, and A. Cardona. 2012. Fiji: an open-source platform for biological-image analysis. *Nat. Methods*. 9:676–682.

106. Virtanen, P., R. Gommers, T.E. Oliphant, M. Haberland, T. Reddy, D. Cournapeau, E. Burovski, P. Peterson, W. Weckesser, J. Bright, S.J. van der Walt, M. Brett, J. Wilson, K.J. Millman, N. Mayorov, A.R.J. Nelson, E. Jones, R. Kern, E. Larson, C.J. Carey, İ. Polat, Y. Feng, E.W. Moore, J. VanderPlas, D. Laxalde, J. Perktold, R. Cimrman, I. Henriksen, E.A. Quintero, C.R. Harris, A.M. Archibald, A.H. Ribeiro, F. Pedregosa, and P. van Mulbregt. 2020. SciPy 1.0: fundamental algorithms for scientific computing in Python. *Nat. Methods*. 17:261–272.

107. Hunter, J.D. 2007. Matplotlib: A 2D Graphics Environment. *Comput. Sci. Eng.* 9:90–95.

108. Ikeda, Y. 2023. yuzie007/mpltern: 1.0.2. *Zenodo*.

109. Sakuma, Y., T. Taniguchi, T. Kawakatsu, and M. Imai. 2013. Tubular Membrane Formation of Binary Giant Unilamellar Vesicles Composed of Cylinder and Inverse-Cone-Shaped Lipids. *Biophys. J.* 105:2074–2081.

110. Talbot, E.L., J. Kotar, L.D. Michele, and P. Cicuta. 2019. Directed tubule growth from giant unilamellar vesicles in a thermal gradient. *Soft Matter*. 15:1676–1683.

111. Davis, J.H., J.J. Clair, and J. Juhasz. 2009. Phase Equilibria in DOPC/DPPC-d62/Cholesterol Mixtures. *Biophys. J.* 96:521–539.

112. Sakuma, Y., M. Imai, M. Yanagisawa, and S. Komura. 2008. Adhesion of binary giant vesicles containing negative spontaneous curvature lipids induced by phase separation. *Eur. Phys. J. E*. 25:403–413.

113. Shah, J., J.M. Atienza, R.I. Duclos, A.V. Rawlings, Z. Dong, and G.G. Shipley. 1995. Structural and thermotropic properties of synthetic C16:0 (palmitoyl) ceramide: effect of hydration. *J. Lipid Res.* 36:1936–1944.

114. Pataraia, S., Y. Liu, R. Lipowsky, and R. Dimova. 2014. Effect of cytochrome c on the phase behavior of charged multicomponent lipid membranes. *BBA - Biomembr.* 1838:2036–2045.

115. Balleza, D., A. Mescola, N. Marín–Medina, G. Ragazzini, M. Pieruccini, P. Facci, and A. Alessandrini. 2019. Complex Phase Behavior of GUVs Containing Different Sphingomyelins. *Biophys. J.* 116:503–517.

116. Veatch, S.L., O. Soubias, S.L. Keller, and K. Gawrisch. 2007. Critical fluctuations in domain-forming lipid mixtures. *Proc. Natl. Acad. Sci. USA*. 104:17650–17655.

117. Aufderhorst-Roberts, A., U. Chandra, and S.D. Connell. 2017. Three-Phase Coexistence in Lipid Membranes. *Biophys. J.* 112:313–324.

118. Rog, T., and A. Koivuniemi. 2016. The biophysical properties of ethanolamine plasmalogens revealed by atomistic molecular dynamics simulations. *BBA - Biomembr.* 1858:97–103.

119. Ferraro, M., M. Masetti, M. Recanatini, A. Cavalli, and G. Bottegoni. 2015. Modeling lipid raft domains containing a mono-unsaturated phosphatidylethanolamine species. *RSC Adv.* 5:37102–37111.

120. West, A., V. Zoni, W.E.Jr. Teague, A.N. Leonard, S. Vanni, K. Gawrisch, S. Tristram-Nagle, J.N. Sachs, and J.B. Klauda. 2020. How Do Ethanolamine Plasmalogens Contribute to Order and Structure of Neurological Membranes? *J. Phys. Chem. B*. 124:828–839.

121. Girard, M., and T. Bereau. 2023. Induced asymmetries in membranes. *Biophys. J.* 122:2092–2098.

122. Sharon, E., B. Roman, and H.L. Swinney. 2007. Geometrically driven wrinkling observed in free plastic sheets and leaves. *Phys. Rev. E*. 75:046211.

123. Liang, H., and L. Mahadevan. 2009. The shape of a long leaf. *Proc. Natl. Acad. Sci. USA*. 106:22049–22054.

124. Kim, J., J.A. Hanna, M. Byun, C.D. Santangelo, and R.C. Hayward. 2012. Designing Responsive Buckled Surfaces by Halftone Gel Lithography. *Science*. 335:1201–1205.

125. Davidovitch, B., R.D. Schroll, D. Vella, M. Adda-Bedia, and E.A. Cerda. 2011. Prototypical model for tensional wrinkling in thin sheets. *Proc. Natl. Acad. Sci. USA*. 108:18227–18232.

126. Audoly, B., and A. Boudaoud. 2002. 'Ruban à godets': an elastic model for ripples in plant leaves. *Compt. Rendus Mec.* 330:831–836.

127. Marder, M., E. Sharon, S. Smith, and B. Roman. 2003. Theory of edges of leaves. *EPL*. 62:498.

128. Huang, C., Z. Wang, D. Quinn, S. Suresh, and K.J. Hsia. 2018. Differential growth and shape formation in plant organs. *Proc. Natl. Acad. Sci. USA*. 115:12359–12364.

129. Daniels, K.E., and M.W. Elting. 2020. Knitting Ripples. *Patterns*. 1:100034.

130. Audoly, B., and A. Boudaoud. 2003. Self-Similar Structures near Boundaries in Strained Systems. *Phys. Rev. Lett.* 91:086105.

131. Nath, U., B.C.W. Crawford, R. Carpenter, and E. Coen. 2003. Genetic Control of Surface Curvature. *Science*. 299:1404–1407.

132. Pollan, M. 2002. The botany of desire: A plant's-eye view of the world. Random House.

133. Lilley, J.L.S., C.W. Gee, I. Sairanen, K. Ljung, and J.L. Nemhauser. 2012. An Endogenous Carbon-Sensing Pathway Triggers Increased Auxin Flux and Hypocotyl Elongation. *Plant Physiol.* 160:2261–2270.

134. Walt, S. van der, J.L. Schönberger, J. Nunez-Iglesias, F. Boulogne, J.D. Warner, N. Yager, E. Gouillart, and T. Yu. 2014. scikit-image: image processing in Python. *PeerJ*. 2:e453.

135. Cerda, E., and L. Mahadevan. 2003. Geometry and Physics of Wrinkling. *Phys. Rev. Lett.* 90:074302.

136. Jiang, H., D.-Y. Khang, J. Song, Y. Sun, Y. Huang, and J.A. Rogers. 2007. Finite deformation mechanics in buckled thin films on compliant supports. *Proc. Natl. Acad. Sci. USA*. 104:15607–15612.

137. Bieleski, R., J. Elgar, J. Heyes, and A. Woolf. 2000. Flower Opening in Asiatic Lily is a Rapid Process Controlled by Dark-light Cycling. *Ann. Bot.* 86:1169–1174.

138. Ritman, E.L. 2004. Micro-Computed Tomography—Current Status and Developments. *Annu. Rev. Biomed. Eng.* 6:185–208.

139. Bieleski, R., J. Elgar, and J. Heyes. 2000. Mechanical Aspects of Rapid Flower Opening in Asiatic Lily. *Ann. Bot.* 86:1175–1183.

140. Rolland-Lagan, A.-G., J.A. Bangham, and E. Coen. 2003. Growth dynamics underlying petal shape and asymmetry. *Nature*. 422:161–163.

141. Puzey, J.R., S.J. Gerbode, S.A. Hodges, E.M. Kramer, and L. Mahadevan. 2012. Evolution of spur-length diversity in Aquilegia petals is achieved solely through cell-shape anisotropy. *Proc. R. Soc. B. Biol. Sci.* 279:1640–1645.

142. Koehl, M.A.R., W.K. Silk, H. Liang, and L. Mahadevan. 2008. How kelp produce blade shapes suited to different flow regimes: A new wrinkle. *Integr. Comp. Biol.* 48:834–851.

143. Xu, F., C. Fu, and Y. Yang. 2020. Water Affects Morphogenesis of Growing Aquatic Plant Leaves. *Phys. Rev. Lett.* 124:038003.

Appendix A

Detailed Electroformation Procedure

*The following electroformation procedure is adapted from a living document that is continually updated by members of the Keller Lab when improvements are made. I have added improvements and adjustments based on my own experience electroforming vesicles.

Preparing lipid mixtures and ITO-coated resistive slides.

1. Lipids, cholesterol, and lipid dyes are kept in the freezer at −4°C. Prior to preparing lipid samples, take out the required lipid stocks and allow them to sit at room temperature for ~15 minutes, or until no condensation remains on the outside of the vial and cap.
    - While stored in the freezer:
        i. Saturated lipids are good "forever" (~a decade).
        ii. Unsaturated lipids are good for about 1-2 years.
    - It is best practice to use fresh lipid stocks when collecting data for publication.
2. Set a heat block to 60°C. This will be used later to heat the lipid mixture.
3. Partially fill a glass scintillation vial with chloroform ($CHCl_3$) to use as a stock while preparing the lipid mixture. Use another glass scintillation vial (waste vial) for organic waste (lipids and $CHCl_3$).
4. For every set of vesicles, obtain a small, borosilicate glass test tube (10x75mm size). Label the tube(s) accordingly.
5. Rinse a glass Hamilton 10 μL syringe with $CHCl_3$. Use a Pasteur pipet to rinse the outside of the needle (roughly ¾ from the base of the syringe down to the tip) three or more times. Then, clean the interior of the syringe by transferring 10 μL of $CHCl_3$ into the waste vial 10 times.
6. Rinse the 10x75mm test tube(s) with a small amount of $CHCl_3$ and vortex for five seconds, 3-5 times. While vortexing, the $CHCl_3$ should reach close to the top of the tube(s).

7. Pour out the $CHCl_3$ used to rinse the tube(s) into the waste vial and allow the tubes to dry upside down on a rack.
8. Using the rinsed, Hamilton 10 µL syringe, sequentially add the desired volume from each lipid stock to the dry tube(s). Repeat step 5 above before switching to a new lipid stock to prevent contamination. Add any dye last, and then clean the interior of the syringe up to an additional 10 times as in step 5, ensuring no dye is visible in the syringe. Allow the syringe to dry for 10 or more minutes before storing.
    - I find it easiest to carefully insert the syringe so that the tip is only 1-2 cm from the bottom of the tube(s) to ensure that all lipid is transferred to the bottom.
    - A smooth and swift depression of the plunger will usually expel all the lipid solution. If a drop remains on the tip, gently transfer it to the inner side of the glass tube just above the lipid solution, taking care to note the location to avoid reusing it when dispensing the next lipid.
9. Gently add $CHCl_3$ to the top of the lipid tube(s) to wash any lipid on the inside glass walls into the bulk solution at the bottom. Use enough $CHCl_3$ to raise the volume a few millimeters above the curved portion of the bottom of the tube(s).
    - The total volume of solution should allow for ~15 min of evaporation on the heat block and provide enough solution to create two nickel- to quarter-sized pools of lipid solution that will each be spread into a lipid film. This volume can be adjusted based on the researcher's preference.
    - If there is too much volume, excess can be blown off under a gentle stream of nitrogen (N_2) gas.
10. Place the lipid tube(s) in the preheated heat block for about 15 min.
    - This generally brings the temperature of the lipids above their T_{melt}, which is believed to help improve vesicle composition homogeneity. In my experiments with DPPE, which melts higher than 60°C, I ran tests using the heat block at 60°C and 75°C and found no major difference in measured transition temperatures or vesicle quality. However, $CHCl_3$ evaporates at ~61°C, so it cannot be heated beyond that and remain in the liquid state at ambient conditions. An alternative solvent with a higher T_{melt} could be considered, though care must be taken to ensure no additional effects are introduced by the solvent.

11. While the lipid tubes are heating, wrap the lipid stock vials in Teflon tape and parafilm clockwise around the seal of the cap and the vial to aid in tightening it.
    - I like to leave a small corner of the wrapped parafilm smoothed over on the top of the cap to make it easy to reopen for the next experiment.
    - Important note: ensure the shiny, Teflon side of the cap septum for the lipid stock vials are facing down before closing. Exposure to plasticizers will contaminate the lipid stocks over time.
12. Obtain as many 25x75x1.1 mm, 70-100 Ω ITO-coated (indium tin oxide) glass slides as lipid tubes. Use a multimeter to measure the resistive, ITO-coated side. Use a glass cutter and guide (we use pre-marked Plexiglass squares) to score the non-resistive side in half widthwise. Line up the scored edge just over the edge of a firm surface (Plexiglass square if available). With a quick motion akin to a karate chop, hit the end of the overhanging ITO slide to cleanly break it in half along the scored edge (this takes some practice).
    - For clarity, label the non-resistive side with permanent marker. An underline or dot beneath the label makes it easier to determine whether the ITO-coated side is facing up for labels that may be symmetrical, otherwise they will appear mirrored.
13. Clean the resistive sides of the ITO slides by soaking a Kim Wipe (lint-free paper) with ethanol and gently swiping from one end to the other a few times. Watch the ethanol fully evaporate and ensure no specks remain on the surface.
    - Kim Wipe particles or tiny glass shards that remain on the ITO surface may inhibit smooth spreading of the lipid film. Try to avoid these if possible.
    - I like to additionally blow a strong stream of N_2 gas through a 1 mL micropipette tip over the ITO slide surface to remove any potential remaining debris.
14. Set the ITO-coated slides, resistive side up, on the preheated heat block for ~2 min to bring them to the same temperature of the lipid solutions. Additionally, separate 10x75 mm glass tubes with a Pasteur pipet set inside (tip facing down) should placed in the heat block to preheat them for transferring lipid solution to the ITO slides (one required for each sample).
15. Set aside two Teflon strips that are 0.3 mm thick for each vesicle sample (different thicknesses will require adjustments to electroformation parameters). Wet a Kim Wipe with ethanol and wipe the Teflon strips.

Spreading lipid films from lipid mixtures in chloroform.

16. Visually inspect the ITO slides again to ensure they are clean and resistive side up.
17. Using a preheated Pasteur pipet, pull up roughly half of the lipid solution. This should fill the pipet roughly to the curved portion of the glass connecting the neck and body of the pipet. Deposit a nickel- to quarter-sized drop of lipid solution onto the heated ITO slide.
    - Transfer the lipid solution as quickly as possible to the ITO slide on the heat block to minimize cooling. I leave one edge of the ITO slide very slightly off the heat block so I can easily pick it up after dispensing the lipid.
18. Quickly pick up the ITO slide, keeping it level, and place the neck of the Pasteur pipet flush with the surface of the ITO slide. Quickly and evenly move the pipet across the surface of the ITO slide, moving through the droplet of lipid solution to spread it over the surface. It should feel like the pipet neck is "gliding" over the surface.
    - Examples of lipid films are shown in Fig. A.1.

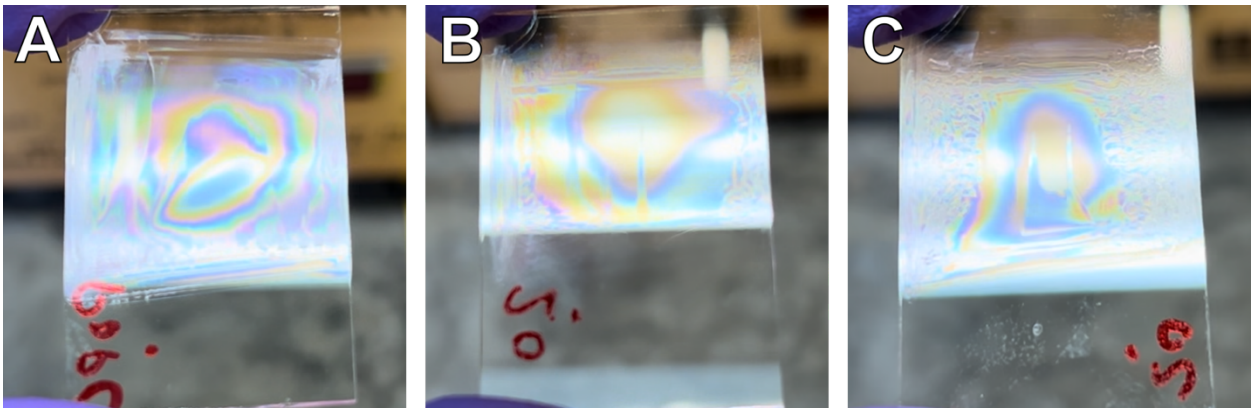

Figure A.1. Examples of lipid films. A) A good lipid film for a 100% POPC mixture. Note the smooth, thin film interference pattern. These generally result in good quality vesicle samples with high yields. **B-C)** A good lipid film in **B** and an acceptable lipid film in **C** are shown for a lipid composition containing DiphyPC and DPPE. Again, note the smooth, thin film interference pattern as in **A**, save for a streak imperfection at the center for **B**. The sides of the film in **C** are not of high quality. Although vesicles are often still produced with lipid films similar to **C**, they tend not to be as reliable for quality and quantity of vesicles produced.

    - Try to move the pipet at a constant rate.
    - For larger amounts of solvent, spread at a slightly slower rate to allow for more evaporation. Smaller amounts of solvent require faster spreading.

- Leave enough room on the cut edges of the ITO slide to attach metal rails.
- This is the most technical portion of the procedure, requiring a good deal of dexterity and practice to get correct. Practicing with chloroform alone and then with multiple sets of POPC samples are great ways to improve execution of this step.

19. Repeat step 18 for the second ITO slide of the sample using the remaining half of the lipid solution.
20. Repeat steps 18 and 19 for all other samples. I usually limit it to 2 samples at a time to optimize efficiency and quality.

Assembling the electroformation chamber ("ITO sandwich").

21. Carefully run a thin line of vacuum grease along the long edges of both ITO slides on the resistive side with the lipid film, leaving the cut side free of grease for attachment to the metal rails.
    - Use as little grease as possible: too much will squeeze out of the sides as the chamber is compressed and may affect the lipid films.
22. Use forceps to grab the two Teflon strips by the end. Lay each down gently on the strip of grease on each side of one of the ITO slides. Press each Teflon strip down to adhere it to the grease and use the forceps to carefully align the strips with the edges and corner of the slide.
23. Complete the electroformation chamber/sandwich by placing the greased ITO slide without Teflon strips grease-side down on the strips of the other slide so that edges are offset. Attach binder clips on each edge to secure the ITO slide-Teflon strip-ITO slide sandwich.
    - A diagram of the assembled electroformation chamber/sandwich is shown in Fig. A.2 on the next page.
24. Place the assembled electroformation chamber in a covered (dark, to protect fluorescent dye if present) vacuum chamber, pull a vacuum for 5 min, and then turn the vacuum off. Leave them in the vacuum for a minimum of 30 min to evaporate off remaining $CHCl_3$.
    - In a well-sealed vacuum chamber, films can be left overnight if desired. If left for extended periods of time, ensure the vacuum is maintained until ready to proceed.

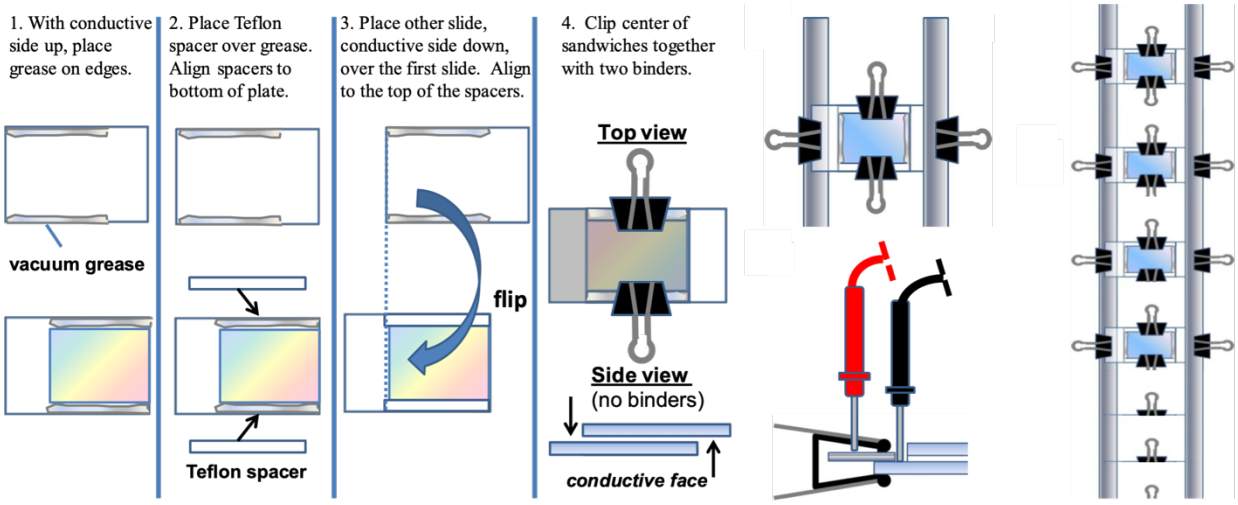

Figure A.2. Diagram of electroformation chamber assembled with ITO slides, vacuum grease, and Teflon strips. Step 1 shows where to place vacuum grease. Step 2 shows placement of the Teflon strips. Step 3 details assembly of the electroformation chamber. Step 4 shows securing with binder clips and an alternate view of the orientation of the ITO slides. Pictures at the right depict how to secure the electroformation chamber to metal rails, measure the quality of the contact to the metal rails using a multimeter (resistance should be between 80-200 Ω, around 100 Ω is best), and run multiple samples in parallel. Generally, no more than two samples in parallel works best. Diagram produced by Joan Bleecker.

Hydrating the lipid films and electroformation.

25. Obtain ultrapure water (18.0 MΩ–cm).
26. Seal one end of the electroformation chamber/sandwich with vacuum grease. Thoroughly clean excess grease off of ITO slide overhang using a Kim Wipe folded in fourths, soaked in ethanol.
    - The easiest and cleanest way to do this to collect a column of grease along the neck of a Pasteur pipet, roughly ¾ the length of the electroformation chamber opening. Then, carefully align the pipet to the opening, make contact with the lower ITO slide and begin spinning the neck in place, as if rolling towards the opening. This will collect a section of grease between the neck of the pipet and the opening that can easily be pushed to fill the gap by sliding the neck towards the opening.
    - Continually fold the Kim Wipe as the ITO slide overhang is cleaned to prevent tracking grease over the previously cleaned areas.

27. Remove the electroformation chamber/sandwich from the vacuum chamber after releasing the vacuum. Using a Pasteur pipet, carefully dispense ultrapure water down the middle of the remaining opening of the electroformation chamber. The water should hit the bottom, and smoothly fill up the entire chamber.
    - Others have suggested dispensing water along the inside edge of the electroformation chamber along the Teflon strip. In my experience, this has been more prone to air bubbles than dispensing the water down the middle.
    - If air bubbles form, the following solutions can be tried:
        i. Tap the chamber gently on the benchtop.
        ii. Angle the chamber so the bubble floats to the top.
        iii. Use skinny tweezers to guide it up to the surface.
        iv. When sealing the sandwich, the grease can be pushed in far enough such that it displaces the bubble, forcing it to the surface.
28. Seal the electroformation chamber/sandwich by running vacuum grease along the remaining ungreased gap. Start by filling grease at one side and working towards the other. This will help prevent air bubbles from getting trapped inside. Clean the overhang of the ITO slide with a Kim Wipe and ethanol as described in step 26.
    - Similar to step 26, I collect a column of grease on the Pasteur pipet. However, to fill from one side to the other, I angle the pipet at a ~30° angle and roll towards the opening while slowly dragging the pipet towards the other side, as the gap is sequentially filled with a few millimeters in depth of grease.
29. Clean two conductive metal rails with a Kim Wipe and ethanol.
    - Over time, metal rail surfaces can oxidize and degrade. I have found that using a coarse grit sand paper followed by a fine grit sand paper can help remove an imperfect coating and reveal a fresh layer of metal beneath, drastically improving the vesicle quality and yield. A picture of freshly sanded metal rails can be found in Fig. A.3.

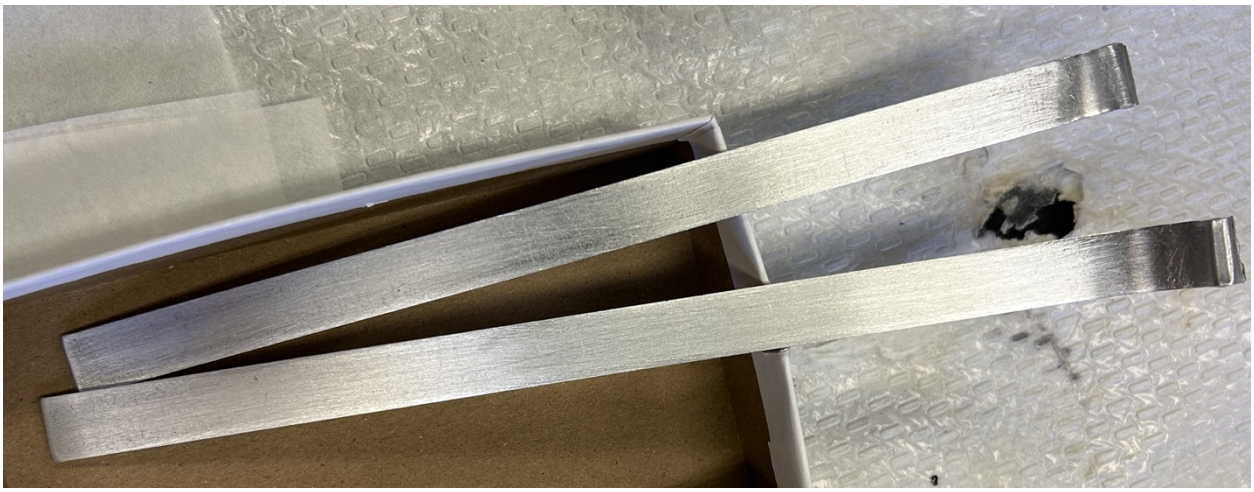

Figure A.3. Freshly sanded metal rails used for electroformation of vesicles. Sanding metal rails can remove an oxidized or deteriorated coating on the rails, revealing fresh metal beneath. Before sanding these rails, vesicle samples were regularly failing. After sanding, vesicle samples were of a much better quality, yield, and could be reliably reproduced. Additionally, resistances when measuring from a rail to the ITO-coated surface dropped by ~30-50 Ω compared to before the rails were sanded.

30. Firmly secure the overhanging ITO slide resistive sides of the electroformation chamber to metal rails with strong binder clips. The strength of the clips is required to maintain good contact between the rails and the ITO slides for good conductivity.
    - One overhanging ITO slide will be above the rail while the other overhanging ITO slide will be below the rail. See Fig. A.2 for diagrams of the set up.
31. Test the connections with a multimeter by touching one lead to the ITO surface and the other lead to the rail in contact with the same ITO surface. The resistance should read between 80-200 Ω, but around 100 Ω or lower seems to work best.
32. Place the electroformation chamber/sandwich and rail setup in a container to secure it (I prefer to use an old cardboard box that the ITO slides are shipped in).
33. Connect the power supply to the ends of the rails. Check the connection by measuring the voltage and frequency on the rails. It should be set to ~1.0 V (AC mode) peak-to-peak with a frequency of 10 Hz.
34. Place the electroformation chamber in an oven set to 60°C (or 10°C higher than the highest T_{melt} in your sample) for 1-2 h, taking care to arrange wires while shutting the oven door.
35. Remove the vesicles by gently cracking open the ITO slides over a microcentrifuge tube.
36. Dilute and prepare your sample for microscopy or further experiment as needed.

Appendix B

Code

[Python Code 1] Plotting a sigmoid to measure transition temperature.

The following packages are required to run this code:

countourpy 1.1.0
cycler 0.11.0
et-xmlfile 1.1.0
fonttools 4.42.0
kiwisolver 1.4.4
matplotlib 3.7.2
numpy 1.25.2
openpyxl 3.1.2
packaging 23.1
pandas 2.2.0
Pillow 10.0.0
pyparsing 3.0.9
python-dateutil 2.8.2
pytz 2024.1
scipy 1.11.2
six 1.16.0
tzdata 2023.4

```
### BEGIN CODE DOCUMENT FOR SIGMOID PLOTS ###

import os
import numpy as np
import csv
import matplotlib.pyplot as plt
import pandas as pd
from scipy.optimize import curve_fit


### CUSTOM FUNCTIONS

def sigmoid(x, L, x0, k):
    y = L / (1 + np.exp(-k * (x - x0)))
    return y


def sigmoid_inverse(y, L, x0, k):
    x = np.log(L / (y) - 1) / -k + x0
    return x


# Function to generate placeholder data to test code
```

```
def generate_testdata():
    x = np.linspace(10, 50, 21)                # 10°C to 50°C is a typical
temperature range
    y = sigmoid(x, -1, 30, 0.5, 1)
    rng = np.random.default_rng()
    x_noise = 1.0 * rng.normal(size=x.size)    # Create noise
    y_noise = 0.1 * rng.normal(size=x.size)
    xdata = x + x_noise                        # Add noise
    ydata = y + y_noise

    return xdata, ydata


def normalize(data):
    normed_data = (data - np.min(data)) / (np.max(data) - np.min(data))        #
Normalize data set to 1.0

    return normed_data


def get_csv_list():

    # Note

    csv_list = []

    with os.scandir() as it:
        for entry in it:
            if not entry.name.startswith('.') and entry.is_file():
                file = str(entry.name)
                if '.csv' in file:

                    csv_list.append(file)

    return csv_list


def get_csvdata(pathname):
    temperatures = []
    separated_count = []
    mixed_count = []

    with open(pathname) as csvfile:
        reader = csv.DictReader(csvfile)
        for row in reader:
            for label, data in row.items():
                if label == 'Temperature':
                    temperatures.append(np.round(float(data), 1))
```

```
                if label == 'Phase-separated':
                    separated_count.append(int(data))
                if label == 'Mixed':
                    mixed_count.append(int(data))

    xdata = np.array(temperatures)
    ydata = 100 * (np.array(separated_count) / (np.array(separated_count)+
np.array(mixed_count)))

    return xdata, ydata


def plot_sigmoids(xdata, ydata, popt, perr, color, scattersize, alpha):
    x = np.linspace(np.floor(popt[1] - 7), np.ceil(popt[1] + 7), 1001)

    popt_pos = popt + 2*perr       # 2 sigma, or 95% confidence

    popt_neg = popt - 2*perr       # 2 sigma, or 95% confidence


    sigmoid_pos = sigmoid(x, *popt_pos)
    sigmoid_neg = sigmoid(x, *popt_neg)

    plt.plot(x, sigmoid(x, *popt), color='black', linewidth=3)
    plt.scatter(xdata, ydata, color=color, s=scattersize)

    plt.plot(x, sigmoid_pos, color=color, alpha=alpha)
    plt.plot(x, sigmoid_neg, color=color, alpha=alpha)
    plt.fill_between(x, sigmoid_neg, sigmoid_pos, color=color, alpha=alpha - 0.05)

    return


def plot_Tmix(Tmix, popt, perr, color, marker='s', mfc='gray', mec='black',
markersize=10, ecolor='black', y_offset=56):
    popt_pos = popt + 2*perr       # 2 sigma, or 95% confidence
    popt_neg = popt - 2*perr       # 2 sigma, or 95% confidence

    # Plot Errorbars on Tmix point (multiply xerr x and y by *0 and set capsize and
capthick to 0 to omit bars)
    plt.errorbar(Tmix, 0.5*popt[0], xerr=[[abs(Tmix - popt_pos[1])*0], [abs(Tmix -
popt_neg[1])*0]],
             marker=marker, mfc=mfc, mec=mec, markersize=markersize,
             ecolor=ecolor, capsize=0, capthick=0, zorder=2)

    # Plot Tmix and 95% confidence error for Tmix paramter
    """plt.annotate('Tmix = ' + str(np.round(Tmix, 1)) + ' +/- ' + str(np.round(Tmix -
popt_neg[1], 1)) + '°C', ((Tmix + popt_pos[1])/2, y_offset),
```

```
            color=color, fontfamily='arial', fontweight='bold', font.size=24)"""

    # Plot Tmix ONLY
    plt.annotate(str(np.round(Tmix, 1)) + '°C', ((Tmix + 1 + popt_pos[1])/2,
y_offset),
            color=color, fontfamily='arial', fontweight='bold', fontsize=36)

    return



### BEGIN MAIN.PY ###

# Generate data to fit sigmoid, normalize ydata
#xtest, ytest = generate_testdata()
#ytest = normalize(ytest)


### SET COLOR LIST AND FONT SIZE
colors = ['gray', 'Blue', 'Green', 'Orange', 'Purple']
font_size = 24

lowTmelt_Lipid = "diphypc"

# Data Output Sets for pandas df for use in ternary diagram and SI data tables
lowTmeltCompList = []
highTmeltCompList = []
cholCompList = []
tmixList = []
errorFitList = []
tmixSpread1090List = []
upper10BoundList = []
lower90BoundList = []

csv_list = get_csv_list()


# LOOP THROUGH ALL CSV DATA FILES IN WORKING DIRECTORY, PLOT SIGMOIDS, SAVE FIGURES

for csvFile in csv_list:


    xdatas = []
    ydatas = []

    xdata1, ydata1 = get_csvdata(csvFile)
```

```
    p0_1 = [max(ydata1), np.median(xdata1), -1]
    print('p0_1 Guess: ', p0_1)

    # Fit a sigmoid curve to xdata and ydata, given inital parameters guess, p0
    popt1, pcov1 = curve_fit(sigmoid, xdata1, ydata1, p0_1, bounds=([0, 0, -np.inf],
[100, 100, np.inf]), check_finite=True, full_output=False)

    # Calculate the 1 sigma error from the covariance matrix
    perr1 = np.sqrt(np.diag(pcov1))

    # Extract optimized Tmix parameter
    Tmix1 = popt1[1]

    #Calculate Upper 10% PS and Lower 90% PS Temperatures
    upperTbound10ps = abs(Tmix1 - sigmoid_inverse(popt1[0]*0.1, *popt1))
    lowerTbound90ps = abs(Tmix1 - sigmoid_inverse(popt1[0]*0.9, *popt1))

    #Run custom plot_sigmoids function (see above) to plot the optimized sigmoid and
corresponding data
    plot_sigmoids(xdata1, ydata1, popt1, perr1, colors[0], scattersize=32, alpha=0.2)

    #Run custom plot_Tmix function (see above) to plot Tmix value on the sigmoid graph
    plot_Tmix(Tmix1, popt1, perr1, color=colors[0])

    #Set X-axis and Y-axis bounds
    plt.xlim((Tmix1 - 6), (Tmix1 + 6))
    plt.ylim(-5, 115)

    #Set tick size
    plt.tick_params(axis='both', which='major', labelsize=18)

    #Set the figure size
    fig = plt.gcf()     # Grabs current size of the figure
    fig.set_size_inches(6, 5)

    #Set the figure name and save it at 300 DPI
    figName = csvFile.removesuffix('.csv') + '_' + 'Tmix' + str(np.round(Tmix1,
decimals=1))
    fig.savefig(figName + '.svg', format='svg', bbox_inches='tight', pad_inches=0,
dpi=300)



### END CODE DOCUMENT FOR SIGMOID PLOTS ###
```

[Code 2] Plotting a ternary plot.

The following packages are required to run this code:

contourpy 1.2.0	cycler 0.12.1
fonttools 4.47.2	kiwisolver 1.4.5
matplotlib 3.8.2	mpltern 1.0.2
numpy 1.26.3	packaging 23.2
pillow 10.2.0	pyparsing 3.1.1
python-dateutil 2.8.2	six 1.16.0
scipy 1.12.0	

```
### BEGIN CODE DOCUMENT FOR TERNARY PLOTS ###

import csv
import numpy as np
import matplotlib as mpl
import matplotlib.pyplot as plt
from matplotlib.ticker import MultipleLocator
from scipy.interpolate import griddata
import mpltern


### SET HIGH AND LOW TMELT LIPIDS (COLUMNS IN .CSV FILE SHOULD EXACTLY MATCH)
lowTmeltLipid = 'diphypc'
highTmeltLipid = 'dppe'


### SET COLORMAPS FOR PHASE REGIONS (KEY: cmap1=main data set, cmap2=secondary data
set, cmap3=third data set)
cmap1 = "gray"
cmap2 = "jet"
cmap3 = "gray"


### SET MAX/MIN TEMP VALUES FOR CMAP

minTemp = 12        # 12°C for Tmix plots in PE paper, 0°C for Error ternary plots
maxTemp = 57        # 57°C for Tmix plots in PE paper, 6°C for Error ternary plots


### CUSTOM FUNCTIONS
```

```
def get_csvdata(pathname):

    dopc = []
    dppe = []
    chol = []
    tmix = []

    with open(pathname) as csvfile:
        reader = csv.DictReader(csvfile)
        for row in reader:
            for label, data in row.items():
                if label == lowTmeltLipid:
                    dopc.append(float(data))
                if label == highTmeltLipid:
                    dppe.append(float(data))
                if label == 'chol':
                    chol.append(float(data))
                if label == 'tmix':             # 'tmix' for tmix data; also
'1090bound (+/-)' or 'tmixError' for errors
                    tmix.append(float(data))

    return dopc, dppe, chol, tmix


# Function to assign a colormap to a temperature range
def tmix_to_colormap(tmix, cmap_name, minTemp, maxTemp):

    cmap = mpl.colormaps[cmap_name]

    # Scale tmix values using minT and maxT to between 0 and 1

    tmix_scaled = []


    for i, value in enumerate(tmix):
        tmix_scaled.append((tmix[i] - minTemp) / (maxTemp - minTemp))

    # Set the scaled tmix values to colors in cmap

    tmix_colors = cmap(tmix_scaled)


    return tmix_colors


# Function to interpolate Tmix using the griddata() function from SciPy
def interpolate_tmix(lowTlipid, highTlipid, tmix, scale=10, method='cubic'):
```

```
    ### INTERPOLATE DATA FOR SMOOTH SHADING AND GENERATE chol_interp,
lowTlipid_interp, highTlipid_interp, and tmix_interp DATA

    points = np.column_stack((lowTlipid, highTlipid))

    size_x = max(lowTlipid) - min(lowTlipid)
    size_y = max(highTlipid) - min(highTlipid)


    x = np.linspace(min(lowTlipid), max(lowTlipid), int(np.round(size_x * 10, 0)))
    y = np.linspace(min(highTlipid), max(highTlipid), int(np.round(size_y * 10, 0)))


    lowTlipid_grid, highTlipid_grid = np.meshgrid(x, y)    # 2D grid for interpolation

    # Interpolate tmix data using griddata function
    tmix_grid = griddata(points, tmix, (lowTlipid_grid, highTlipid_grid), method)

    chol_grid = (100 * np.ones(np.shape(lowTlipid_grid))) - lowTlipid_grid -
highTlipid_grid

    # Flatten the data into one dimension
    lowTlipid_interp = lowTlipid_grid.flatten()
    highTlipid_interp = highTlipid_grid.flatten()
    chol_interp = chol_grid.flatten()
    tmix_interp = tmix_grid.flatten()

    # Remove NaNs
    NaNs = np.isnan(tmix_interp)

    lowTlipid_interp_noNaNs = lowTlipid_interp[~NaNs]
    highTlipid_interp_noNaNs = highTlipid_interp[~NaNs]
    chol_interp_noNaNs = chol_interp[~NaNs]
    tmix_interp_noNaNs = tmix_interp[~NaNs]


    return lowTlipid_interp_noNaNs, highTlipid_interp_noNaNs, chol_interp_noNaNs,
tmix_interp_noNaNs



### BEGIN MAIN.PY ###

# Set the pathname for your CSV data file
pathname1 = "[CSV file name].csv"

# Read CSV data from pathname into variables
x1, y1, z1, T1 = get_csvdata(pathname1)
```

```
# Set pathnames for additional CSV data files if plotting more than 1 region
# (code likely needs to be modified for custom use)
pathname2 = "TmixFINALallLiquid_dataDiphy_forTernary.csv"
pathname3 = "TmixFINAL3phaseSolid_dataDiphy_forTernary.csv"
pathname4 = "Tmix_data_dopc_veatch2003.csv"
pathname5 = "Tmix_data_diphypc_veatch2006.csv"
pathname6 = "TmixFINALallSolid_dataDOPC.csv"


# Read CSV data from pathname into variables for pathame 2 and 3, code not set up for
4, 5, and 6
x2, y2, z2, T2 = get_csvdata(pathname2)
x3, y3, z3, T3 = get_csvdata(pathname3)


### MAP TMIX VALUES TO COLORMAPS FOR DATA POINT COLORS

tmix_colors = tmix_to_colormap(T1, cmap1, minTemp, maxTemp)
tmix2_colors = tmix_to_colormap(T2, cmap2, minTemp, maxTemp)
tmix3_colors = tmix_to_colormap(T3, cmap1, minTemp, maxTemp)


### INTERPOLATE TMIX DATA FOR PROPER COLORMAPPING IN TRIPCOLOR

lowTlipid_interp, highTlipid_interp, chol_interp, tmix_interp = interpolate_tmix(x1,
y1, T1)

lowTlipid2_interp, highTlipid2_interp, chol2_interp, tmix2_interp =
interpolate_tmix(x2, y2, T2)

lowTlipid3_interp, highTlipid3_interp, chol3_interp, tmix3_interp =
interpolate_tmix(x3, y3, T3)


### SET UP FIGURE ###

fig = plt.figure(figsize=(6,6))

ax = fig.add_subplot(1, 1, 1, projection='ternary', ternary_sum=100.0)


ax = plt.subplot(projection="ternary", ternary_sum=100.0)

ax.taxis.set_major_locator(MultipleLocator(10))
ax.laxis.set_major_locator(MultipleLocator(10))
ax.raxis.set_major_locator(MultipleLocator(10))
```

```
ax.tick_params(labelsize=14)


### PLOT PHASE DIAGRAM

# NON-INTERPOLATED DATA
#cs1 = ax.tripcolor(z1, x1, y1, T1, shading='gouraud', vmin=minTemp, vmax=maxTemp,
cmap='jet', rasterized=True, zorder=1)

# INTERPOLATED DATA
cs1 = ax.tripcolor(chol_interp, lowTlipid_interp, highTlipid_interp, tmix_interp,
shading='gouraud', vmin=minTemp, vmax=maxTemp, cmap=cmap1, rasterized=True, zorder=1)

cs2 = ax.tripcolor(chol2_interp, lowTlipid2_interp, highTlipid2_interp, tmix2_interp,
shading='gouraud', vmin=minTemp, vmax=maxTemp, cmap=cmap2, rasterized=True, zorder=1)
cs3 = ax.tripcolor(chol3_interp, lowTlipid3_interp, highTlipid3_interp, tmix3_interp,
shading='gouraud', vmin=minTemp, vmax=maxTemp, cmap=cmap1, rasterized=True, zorder=1)

ax.grid(zorder=5)

# DRAW SCATTER PLOTS OF TMIX DATA -- TO TRUNCATE DATA TO OMIT DRAWING SCATTER FOR
3PHASE SOLID REPLACE FIRST 4 ARG WITH: z1[0:-3], x1[0:-3], y1[0:-3], c=tmix_colors[0:-
3],
ax.scatter(z1[0:-3], x1[0:-3], y1[0:-3], c=tmix_colors[0:-3], marker="s", s=100,
edgecolors="Black", linewidth=2, zorder=10, clip_on=False)


# UNCOMMENT FOR PLOTTING DIPHYPC DATA WITH MULTIPLE SCATTERS FOR DIFFERENT PHASE
REGIONS

ax.scatter(z2[0:-3], x2[0:-3], y2[0:-3], c=tmix2_colors[0:-3], marker="o", s=100,
edgecolors="Black", linewidth=2, zorder=11, clip_on=False)
ax.scatter(z2[-3:], x2[-3:], y2[-3:], c=tmix2_colors[-3:], marker="o", s=200,
edgecolors="Black", linewidth=2, zorder=11, clip_on=False)    # PLOT 3PHASE CIRCLES
LARGER
ax.scatter(z3, x3, y3, c=tmix3_colors, marker="s", s=50, edgecolors="Black",
linewidth=1, zorder=12, clip_on=False)


# UNCOMMENT TO OUTLINE LIQUID PHASE IN DIPHYPC/DPPE/CHOL, AND 3PHASE REGION SEPARATELY
"""
liqRegion_t = [0.4, 0.3, 0.2, 0.2, 0.3, 0.4]
liqRegion_l = [0.3, 0.4, 0.4, 0.2, 0.1, 0.1]
liqRegion_r = [0.3, 0.3, 0.4, 0.6, 0.6, 0.5]

ax.fill(liqRegion_t, liqRegion_l, liqRegion_r, fc="None", edgecolor="Black",
linewidth=1.5, linestyle='dashed', zorder=3)
```

```
liqRegion_t = [0.3, 0.2, 0.2]
liqRegion_l = [0.1, 0.2, 0.1]
liqRegion_r = [0.6, 0.6, 0.7]

ax.fill(liqRegion_t, liqRegion_l, liqRegion_r, fc="None", edgecolor="Black",
linewidth=2.5, zorder=3)
"""

# SET LABELS
#ax.set_tlabel("Cholesterol (%)")
#ax.set_llabel("DOPC (%)")
#ax.set_rlabel("DPPE (%)")


### Set colorbar axis 1 ###
cax1 = ax.inset_axes([1.05, 0.1, 0.05, 0.9], transform=ax.transAxes)
colorbar1 = fig.colorbar(cs1, cax=cax1)
colorbar1.ax.tick_params(labelsize=14)
#colorbar1.set_label('Temperature (°C)', rotation=270, va='baseline')


### Set colorbar axis 2 *IF NEEDED* INDEPENDENT FROM 2ND DATA SET ###
"""
cax2 = ax.inset_axes([1.12, 0.1, 0.05, 0.9], transform=ax.transAxes)
norm = mpl.colors.Normalize(vmin=minTemp, vmax=maxTemp)
colorbar2 = fig.colorbar(mpl.cm.ScalarMappable(norm=norm, cmap=cmap2), cax=cax2)
colorbar2.ax.tick_params(labelsize=14)
#colorbar2.set_label('Temperature (°C)', rotation=270, va='baseline')
"""



### PLOT BAD SAMPLE / OTHER DATA POINTS ON TERNARY PLOT - UNCOMMENT ONLY 1 SECTION!
###

# VEATCH 2003 DOPC/DPPC/CHOL SOLID PHASE SQUARES, NO TRANSITIONS = OPEN CIRCLES, SOLID
= OPEN SQUARES
"""
chol_s = [0.100, 0.100, 0.100, 0.050, 0.050, 0.050, 0.000]
dopc_s = [0.720, 0.300, 0.090, 0.710, 0.475, 0.320, 0.500]
dppc_s = [0.180, 0.600, 0.810, 0.240, 0.475, 0.630, 0.500]

chol_o = [0.600, 0.550, 0.550, 0.500, 0.500, 0.500, 0.450, 0.450, 0.400, 0.400, 0.400,
0.350, 0.300, 0.250, 0.200, 0.200]
dopc_o = [0.200, 0.113, 0.090, 0.250, 0.167, 0.050, 0.412, 0.367, 0.570, 0.030, 0.000,
0.520, 0.000, 0.712, 0.760, 0.000]
```

```
dppc_o = [0.200, 0.337, 0.360, 0.250, 0.333, 0.450, 0.138, 0.183, 0.030, 0.570, 0.600,
0.130, 0.700, 0.038, 0.040, 0.800]

ax.scatter(chol_s, dopc_s, dppc_s, c= "white", marker="s", s=100, edgecolors='black',
linewidth=2, zorder = 10, clip_on=False)
ax.scatter(chol_o, dopc_o, dppc_o, c= "white", marker="o", s=100, edgecolors='black',
linewidth=2, zorder = 10, clip_on=False)
"""

# DOPC/DPPE/CHOL Xs & CHOL Solubility
"""
chol_x = [0.5, 0.4, 0.3, 0.2, 0.1, 0.0, 0.0, 0.0, 0.1, 0.2, 0.3, 0.4, 0.5]
dopc_x = [0.1, 0.1, 0.1, 0.1, 0.1, 0.1, 0.2, 0.3, 0.0, 0.0, 0.0, 0.0, 0.0]
dppe_x = [0.4, 0.5, 0.6, 0.7, 0.8, 0.9, 0.8, 0.7, 0.9, 0.8, 0.7, 0.6, 0.5]

chol_o = [0.4, 0.3, 0.2, 0.1]
dopc_o = [0.6, 0.7, 0.8, 0.9]
dppe_o = [0.0, 0.0, 0.0, 0.0]

tri_t = [1.0, 0.5, 0.5]
tri_l = [0.0, 0.5, 0.0]
tri_r = [0.0, 0.0, 0.5]

ax.fill(tri_t, tri_l, tri_r, color="white", hatch='...', edgecolor="red", alpha=0.4)
ax.scatter(chol_x, dopc_x, dppe_x, c= "Black", marker="x", s=100, linewidth=4, zorder
= 10, clip_on=False)
ax.scatter(chol_o, dopc_o, dppe_o, c= "white", marker="o", s=100, edgecolors='black',
linewidth=2, zorder = 10, clip_on=False)
"""

# VEATCH 2006 DIPHYPC/DPPC/CHOL SOLID PHASE SQUARES, NO TRANSITIONS = OPEN CIRCLES,
SOLID = OPEN SQUARES
"""
Zoom        = [0.00, 0.00, 0.00, 0.00, 0.00, 0.00]
diphypc_s   = [0.00, 0.20, 0.33, 0.50, 0.66, 0.80]
dppc_s      = [1.00, 0.80, 0.66, 0.50, 0.33, 0.20]

ax.scatter(chol_s, diphypc_s, dppc_s, c= "white", marker="s", s=100,
edgecolors='black', linewidth=2, zorder = 10, clip_on=False)
"""

# DIPHYPC/DPPE/CHOL Xs
"""
chol_x      = [0.0, 0.0, 0.0, 0.1, 0.1, 0.2, 0.3, 0.4, 0.4, 0.5, 0.5, 0.5, 0.5, 0.5]
diphypc_x   = [0.1, 0.2, 0.3, 0.0, 0.1, 0.0, 0.0, 0.0, 0.5, 0.0, 0.1, 0.2, 0.3, 0.4]
dppe_x      = [0.9, 0.8, 0.7, 0.9, 0.8, 0.8, 0.7, 0.6, 0.1, 0.5, 0.4, 0.3, 0.2, 0.1]

chol_o      = [0.4, 0.3, 0.2, 0.1]
```

```
diphypc_o   = [0.6, 0.7, 0.8, 0.9]
dppe_o      = [0.0, 0.0, 0.0, 0.0]

tri_t = [1.0, 0.5, 0.5]
tri_l = [0.0, 0.5, 0.0]
tri_r = [0.0, 0.0, 0.5]

ax.fill(tri_t, tri_l, tri_r, color="white", hatch='...', edgecolor="red", alpha=0.4)
ax.scatter(chol_x, diphypc_x, dppe_x, c= "Black", marker="x", s=100, linewidth=4,
zorder = 10, clip_on=False)
ax.scatter(chol_o, diphypc_o, dppe_o, c= "white", marker="o", s=100,
edgecolors='black', linewidth=2, zorder = 10, clip_on=False)
"""

# NAME, SAVE, and SHOW FIGURE

figName = "DIPHYPC.DPPE_ternary"
fig.savefig(figName + '.svg', format='svg',  transparent=True, dpi=300,
bbox_inches='tight', pad_inches=0)

plt.show()


### END CODE DOCUMENT FOR TERNARY PLOTS ###
```